学位論文

The Size and Luminosity Distributions of Galaxies in the Reionization Era and Their Implications for Galaxy Formation

(再電離期の銀河のサイズと光度および銀河形成へのそれらの示唆)

平成 29 年 12 月博士 (理学) 申請

東京大学大学院理学系研究科
天文学専攻

川俣　良太

The Size and Luminosity Distributions of Galaxies in the Reionization Era and Their Implications for Galaxy Formation

A dissertation submitted in conformity

with the requirements for the degree of Doctor of Philosophy

Ryota Kawamata

Department of Astronomy, Graduate School of Science,
The University of Tokyo

Supervisor:
Associate Prof. Kazuhiro Shimasaku : Department of Astronomy, School of Science, The University of Tokyo

Abstract

The luminosity function and the size–luminosity relation of galaxies are important probes for galaxy formation and evolution. Continuous efforts have been made to investigate these functions and relations at higher redshifts. We construct $z \sim 6-7$, 8, and 9 faint Lyman break galaxy samples (334, 61, and 37 galaxies, respectively) with accurate size measurements with the software `glafic` from the complete *Hubble* Frontier Fields cluster and parallel fields data. Thanks to the strong gravitational lensing effect, these are the largest samples hitherto and reach down to the faint ends of recently obtained deep UV luminosity functions. The gravitational lensing effects are calculated using our own carefully constructed mass models of the clusters. All lensing maps produced from our mass modeling are made available on the STScI website[*1].

At faint magnitudes, however, these samples are highly incomplete for galaxies with large sizes, implying that derivation of the luminosity function sensitively depends on the intrinsic size–luminosity relation. We thus conduct simultaneous maximum-likelihood estimation of luminosity function and size–luminosity relation parameters from the observed distribution of galaxies on the size–luminosity plane with the help of a completeness map as a function of size and luminosity. At $z \sim 6-7$, we find that the intrinsic size–luminosity relation expressed as $r_{\rm e} \propto L^{\beta}$ has a notably steeper slope of $\beta = 0.46^{+0.08}_{-0.09}$ than those at lower redshifts ($\beta \simeq 0.22$–0.25 at $z \sim 4$–5; Huang et al., 2013), which in turn implies that the luminosity function has a relatively shallow faint-end slope of $\alpha = -1.86^{+0.17}_{-0.18}$. This steep β can be reproduced by a simple analytical model in which smaller galaxies have lower specific angular momenta. The β and α values for the $z \sim 8$ and 9 samples are consistent with those for $z \sim 6-7$ but with larger errors. For all three samples, there is a large, positive covariance between β and α, implying that the simultaneous determination of these two parameters is important.

For deeper insights into physical properties of $z \sim 6-9$ galaxies, we investigate their UV colors, multiplicities, and star-formation rate surface densities. We find that the largest ($r_{\rm e} > 0.8$ kpc) galaxies are mostly red in UV color while the smallest ($r_{\rm e} < 0.08$ kpc) ones tend to be blue. We also find that galaxies with multiple cores tend to be brighter. A comparison with various types of local galaxies indicates that our galaxies are similar to circumnuclear star-forming regions of barred galaxies, among the local galaxies compared, in the sense that a sizable amount of stars are forming in a very small area.

[*1] `https://archive.stsci.edu/prepds/frontier/lensmodels/`

Acknowledgments

I would like to express my sincere gratitude to my three advisors, Associate Prof. Kazuhiro Shimasaku, Associate Prof. Masami Ouchi, and Assistant Prof. Masamune Oguri for their invaluable advices and thorough instruction. Special thanks goes to my supervisor, Associate Prof. Kazuhiro Shimasaku for his outstanding guidance on data reductions and analyses, perceptive suggestions during discussions, and feedback during preparations of manuscripts and presentations. This study is owed to his keen and thoughtful insight. I sincerely appreciate all of the time he has spared for every aspect of this project. I would also like to thank Associate Prof. Masami Ouchi for his invaluable advices on scientific and technical problems, particularly those important but easily overlooked. The strong point of this study, exploiting the gravitational lensing effect, is greatly owed to Assistant Prof. Masamune Oguri. I also appreciate his valuable comments that significantly improve qualities of my studies and opportunities he provided to collaborate with other researchers. Without his instructions, I would not be able to accomplish our research goals. I feel especially thankful to my collaborator, Mr. Masafumi Ishigaki, who has suggested lots of efficient analysis methods and has helped me with the data reduction and analysis.

I would like to thank Michael Fall, Rychard Bouwens, Rebecca Bowler, Henry Ferguson, Kentaro Nagamine, Pascal Oesch, Yoshiaki Ono, Takatoshi Shibuya, Tsutomu Takeuchi, Haruka Kusakabe, Taku Okamura, and Kazushi Irikura for their helpful comments. I am grateful to the anonymous referees assigned by ApJ for useful comments that improved our studies.

I greatly appreciate helps by and daily interactions with members of our laboratory, Dr. Kimihiko Nakajima, Dr. Takuya Hashimoto, Mr. Shingo Shinogi, Mr. Ryosuke Goto, Ms. Haruka Kusakabe, Mr. Taku Okamura, Mr. Kazushi Irikura, and Mr. Shingo Tanigawa, and members of our research group, Dr. Masao Hayashi, Dr. Rieko Momose, Assistant Prof. Yoshiaki Ono, Dr. Tomoki Saito, Dr. Takatoshi Shibuya, Dr. Suraphong Yuma, Dr. Akira Konno, Mr. Yoshiaki Naito, Mr. Masafumi Ishigaki, Ms. Hiroko Tamazawa, Mr. Yuichi Harikane, Mr. Seiji Fujimoto, Mr. Takashi Kojima, Mr. Yuma Sugahawa, Mr. Shiro Mukae, Mr. Ryo Higuchi, Mr. Hilmi Miftahul, Mr. Ryohei Itoh, and Mr. Shotaro Kikuchihara. I also wish to thank members of the Department of Astronomy, the University of Tokyo, for daily discussion and encouragement.

I am grateful to Peter Behroozi, Chuanwu Liu, Yoshiaki Ono, and Takatoshi Shibuya for kindly providing us with their results. This work was supported in part by a Grant-in-Aid for JSPS Research Fellow (JP16J01302, JP16J03727) and by a KAKENHI (JP16K05286)

Grant-in-Aid for Scientific Research (C) through the Japan Society for the Promotion of Science (JSPS). This work was supported in part by the World Premier International Research Center Initiative (WPI Initiative), MEXT, Japan, and JSPS KAKENHI Grant Number JP26800093 and JP15H05892. This work used the 2015 public version of the Munich model of galaxy formation and evolution: L-Galaxies. The source code and a full description of the model are available at `http://galformod.mpa-garching.mpg.de/public/LGalaxies/`. The Millennium and Millennium-II simulation databases used in this paper and the web application providing online access to them were constructed as part of the activities of the German Astrophysical Virtual Observatory (GAVO).

Finally, I would like to thank my parents for their great support throughout my entire life.

Contents

List of Figures

List of Tables

Chapter 1

Introduction

"If you gaze long into an abyss, the abyss also gazes into you."
— Friedrich Nietzsche, *Beyond Good and Evil* (1886), Aphorism 146

In 1995, the *Hubble Space Telescope* discovered thousands of galaxies in the empty area called *Hubble* Deep Field. The challenge to probe the abyss of space did not result in a "abyss of wasting time". This is because, contrary to the quotation, it found our ancestors in the abyss watching over us.

1.1 Star-forming Galaxies as a Probe for Galaxy Evolution

Galaxies are systems gravitationally bound in the potential wells generated by their hosting dark matter halos and baryons themselves. Within galaxies are typically 10^{11} stars, the interstellar medium, and dust. Most of the present-day galaxies have clear structures and are classified into two groups: spiral and elliptical galaxies. Besides them, there are galaxies with indistinct shapes classified into irregular galaxies, most of which are forming stars. The beautiful shapes of galaxies and their origins have been of particular interest from their discovery. How did galaxies assemble gas and form stars and how did they acquire clear and attractive shapes as seen today? Galaxy formation is still one of the fundamental mysteries in astronomy.

It has been found that the shape of galaxies, i.e., morphology, is related to their physical quantities. For example, while elliptical galaxies are red with minimal star formation, spiral galaxies are blue and forming stars. As galaxies evolve forming stars from gas, galaxy evolution can be regarded as a history of star formation. From this perspective, one of the best approaches to probe galaxy evolution is to trace star-forming galaxies, such as spiral and irregular galaxies. In addition, star-forming galaxies dominate over elliptical galaxies especially in the past universe and they make it possible to conduct systematic analyses over a wide range of cosmic time.

In order to investigate star-forming galaxies, it would be ideal to conduct spectroscopy to obtain their redshifts and spectral energy distributions. However, spectroscopy is time-consuming. Moreover, faint galaxies are hard to do spectroscopy. Thus, imaging is widely used to construct large samples of galaxies and to study their properties. In particular, samples of star-forming galaxies at high redshifts are necessary to probe changes of

physical properties over cosmic time.

1.2 Physical Quantities of Star-forming Galaxies

Galaxies evolve changing their properties over cosmic time. Their evolution is described in terms of three evolutions: luminosity, kinematics, and chemical evolutions. One of the methods to investigate galaxy evolution is to use the following quantities of star-forming galaxies from the past to the present. These are the most fundamental physical quantities obtained from broad-band observations of star-forming galaxies.

Luminosity function — Since galaxies evolve forming stars, the total luminosity from the formed stars is one of the key parameters. It has been found that the number of bright galaxies is small while that of faint galaxies are large. The abundance of galaxies as a function of luminosity is referred to as the luminosity function, which is a basic statistical quantity. Galaxy evolution can be constrained by examining luminosity functions and their evolution.

Star-formation rate — The evolution of UV luminosity is important also in terms of star formation, because recent star-formations are traced by UV luminosities. This is because UV radiation is mainly emitted from O- and B-type stars, which die quickly and hence reflect only recent star formations. As galaxies convert gas into stars, it is important to clarify which galaxies form more stars and form stars more efficiently. In addition, the amount of star formation in star-forming galaxies in the universe can be calculated from the UV luminosity function given a conversion factor between UV luminosity and star-formation rate.

Galaxy size — Galaxy evolution should be investigated from a kinematics point of view, because galaxies evolve acquiring gas from the intergalactic medium. This gas inflow transports angular momenta from the galactic halos and intergalactic medium to galactic disks. Since most star-forming galaxies have rotation-supported disks, their sizes provide information on the angular momenta in the disks and kinematics such as halo masses and halo spins.

Morphology — According to the hierarchical galaxy formation model, galaxies repeat major and minor mergers throughout their evolution. In particular, during major mergers, the structure of galaxies is largely deformed and their angular momenta are dissipated. In this sense, major mergers strongly affect the kinematics evolution of galaxies. Moreover, mergers are thought to induce bursts of star formation, and hence have a significant effect also on luminosity evolution. Thus, it is important to investigate the frequency of major mergers and physical properties of galaxies under mergers.

Given these physical quantities over cosmic time, we are able to tackle the mysteries of luminosity and kinematical evolutions. The remaining important evolution is chemical evolution, i.e., how and to what degree the heavy elements produced in stars enrich galaxies and the intergalactic medium. Since the cooling rate is enhanced in metal-enriched gas, heavy elements produced through stellar nucleosynthesis recurrently affect succeeding star formations. Furthermore, as these heavy elements compose the earth and our bodies,

chemical evolution is important to probe the origin of the variety of elements that are necessary for life. However, it is difficult to construct large samples with metallicity measurements at the high-redshift universe, because spectroscopic observations are needed to measure metallicities. For these reasons, we do not handle the chemical evolution in this thesis.

1.3 Observations of Galaxies at High-redshifts

Since the speed of light is finite, the distant universe corresponds to the past universe. Thus, in order to construct samples of past galaxies, we should observe distant galaxies. Due to the expansion of the universe, the wavelength of a photon coming from the distant universe is stretched according to the time it is emitted. This shift in wavelength is referred to as redshift. Guhathakurta et al. (1990) and Steidel & Hamilton (1992) have developed a novel method to construct a large sample of distant galaxies from imaging alone, which is called the Lyman-break technique. This method makes use of the steep dimming of galaxy spectra at wavelengths shorter than 91.2–121.6 nm due to significant absorption by the neutral hydrogen in stellar atmospheres, the interstellar medium, and the intergalactic medium. This steep change in spectra is called a break. The position of the break of higher-redshift galaxies is shifted toward longer wavelengths. We are able to identify distant galaxies by selecting galaxies with breaks at a given wavelength. This method requires only broad-band photometry and is suitable to construct large samples of relatively bright galaxies.

There is another technique to select a large number of distant galaxies. This method detects redshifted Lyman alpha emission from distant galaxies using a narrow band. However, this method is not suitable for constructing a large sample of star-forming galaxies over a wide redshift range. Thus, we do not use this method in this thesis.

Recent developments of 8–10 meter telescopes and the *Hubble Space Telescope* enable construction of large samples of $z \lesssim 10$ galaxies. Among the successful survey projects are the *Hubble* Ultra Deep Field 09/12 (HUDF09/12; Beckwith et al., 2006; Oesch et al., 2010b; Ellis et al., 2013; Koekemoer et al., 2013) and the Cosmic Assembly Near-infrared Deep Extragalactic Legacy Survey (CANDELS; Grogin et al., 2011; Koekemoer et al., 2011). Moreover, some projects have probed more distant and fainter galaxies exploiting the power of gravitational lensing by clusters, such as the Cluster Lensing And Supernova survey with *Hubble* (CLASH; Postman et al., 2012), *Hubble* Frontier Fields (HFF; Lotz et al., 2017), and the Reionization Lensing Cluster Survey (D. Coe et al. in prep.). In this thesis, we make full use of the *Hubble Space Telescope* and gravitational lensing effects to investigate very distant galaxies at $z \gtrsim 6$ found in the HFF fields.

1.4 Utilizing the Gravitational Lensing Effects

Studies of faint high-redshift galaxies can be significantly improved by utilizing massive clusters of galaxies as natural telescopes. This is made possible by the so-called gravita-

tional lensing effect, in which the propagation of a light ray is deflected by an intervening matter distribution (Schneider et al., 1992). Although rare, extremely strong lensing events provide an opportunity to study very distant galaxies using their highly magnified images that otherwise cannot even be detected.

The *Hubble* Frontier Fields (HFF; Lotz et al., 2017) is an on-going public *Hubble Space Telescope (HST)* survey to image six massive clusters. The main purpose of the HFF is to study properties and populations of faint high-redshift galaxies behind the cores of these clusters with the help of lensing magnifications. Analyses of early HFF data have already produced useful results on faint-end luminosity functions of high-redshift galaxies (Coe et al., 2015; Atek et al., 2014, 2015b,a; Ishigaki et al., 2015; Oesch et al., 2015; McLeod et al., 2015), size evolution of galaxies (Kawamata et al., 2015), and deep spectroscopy of faint high-redshift galaxies (Vanzella et al., 2014; Zitrin et al., 2015a).

A key ingredient for the analysis of the HFF data is precise mass modeling of the lensing clusters. This is because we need to convert observed quantities, such as apparent magnitudes and angular sizes of galaxies, to physical quantities such as intrinsic luminosities and physical sizes which require corrections of gravitational lensing effects. The mass distribution of the core of a cluster is usually constrained so that it can reproduce the positions of multiple images behind the cluster. A lot of efforts had been made for mass modeling before the HFF observations started, using pre-HFF data, in order to allow prompt analyses of the HFF data by the community (e.g., Richard et al., 2014; Johnson et al., 2014; Zitrin et al., 2015b).

The accuracy of mass modeling relies on the number of multiply imaged background galaxies. Much deeper *HST* images obtained by the HFF in fact allow one to identify many more multiply imaged galaxies and therefore improve strong lensing mass modeling (e.g., Jauzac et al., 2014, 2015a; Lam et al., 2014; Diego et al., 2015a,b; Limousin et al., 2015). In addition, spectroscopy of these multiple images is crucial for robust identification of multiple images as well as constraining the mass distribution, particularly the radial density profile. Significant efforts are being made to collect spectroscopic redshifts of galaxies detected in the HFF (e.g., Schmidt et al., 2014b; Grillo et al., 2015a; Karman et al., 2015; Wang et al., 2015; Treu et al., 2015; Sebesta et al., 2015). In particular, observations by the Multi Unit Spectroscopic Explorer (MUSE) on the *Very Large Telescope* have found a large number of multiple images and obtained their spectroscopic redshifts (Grillo et al., 2015b; Jauzac et al., 2015b; Caminha et al., 2017; Karman et al., 2017; Lagattuta et al., 2017; Mahler et al., 2018).

However, mass models that incorporate positions and spectroscopic redshifts of these new multiple images are not quickly released, even the observations of the field have already completed. Moreover, it limits options of the analyses to use publicly released mass models, because the provided information is restricted. Therefore, we construct our own mass models of the six HFF clusters. At each stage of the HFF observations, we have released one of the most precise mass models (Ishigaki et al., 2015; Kawamata et al., 2016, 2017).

In this thesis, we present our mass modeling results of the all six HFF clusters,

Abell 2744 (Abell, 1958), MACS J0416.1−2403 (Mann & Ebeling, 2012), MACS J0717.5+3745 (Ebeling et al., 2007), MACS J1149.6+2223 (Ebeling et al., 2007), Abell S1063 (Abell et al., 1989), and Abell 370 (Abell, 1958) using the full-depth HFF data as well as the latest follow-up data. In Kawamata et al. (2016), we have constructed version 3 mass models of the first four clusters. In our later study of Kawamata et al. (2017), exploiting the latest MUSE observations, we have updated the first two mass models of Abell 2744 and MACS J1149.6+2223 as well as newly constructed mass models of Abell S1063 and Abell 370. These mass models described in Kawamata et al. (2017) are referred to as version 4 mass models. For each cluster we use more than 100 multiple images to constrain the mass distribution assuming a simply parametrized mass model. We also discuss whether the high-redshift galaxies in our samples are multiply imaged or not.

1.5 Galaxy Sizes and Their Importance on Determining UV Luminosity Functions

Among the four fundamental physical quantities we have listed (luminosity function, star-formation rate, galaxy size, and morphology), we concentrate especially on the luminosity function and galaxy size in this thesis. We discuss the star-formation rate and morphology in Appendix.

Disk sizes of galaxies at very high redshifts are important in two aspects. One is that they provide information on the formation and early evolution of galaxies. The other is that they have a significant effect on the determination of UV luminosity functions because the correction for detection incompleteness sensitively depends on size.

Concerning the first aspect, the size of galaxies is largely determined by their angular momentum (e.g., Fall & Efstathiou, 1980; Mo et al., 1998) as is the case for disk galaxies, and angular momentum is one of the fundamental parameters of galaxies as argued by Fall (1983). Romanowsky & Fall (2012) and Fall & Romanowsky (2013) have discussed galaxy formation and evolution using the specific angular momentum–mass diagram. Indeed, numerous simulations and analytical models of galaxy formation suggest that the size of galaxies changes with a redistribution of the angular momentum in them due to stellar feedback such as galactic winds (e.g., Brooks et al., 2011; Wyithe & Loeb, 2011; Brook et al., 2012; Danovich et al., 2015; Genel et al., 2015; DeFelippis et al., 2017). Recently, high-resolution cosmological simulations have succeeded in increasing sizes at a fixed luminosity or stellar mass of simulated galaxies to reproduce observed sizes by incorporating stellar feedback such as galactic winds of high mass-loading factors (e.g., Brooks et al., 2011; Genel et al., 2015). The luminosity dependence of the size is also affected by stellar feedback as explained by simple analytical models. For example, Wyithe & Loeb (2011) showed that the slope of the size–luminosity relation varies depending on the dominating feedback such as energy-driven and momentum-driven feedback. Larger sizes indicate more efficient feedback, which suggests that the slope of the size–luminosity

relation contains information on the dominant feedback process.

The second aspect concerning UV luminosity functions is also important because luminosity functions are determined by correcting for detection completeness, which depends on the intrinsic size distribution. For a given magnitude, galaxies with larger sizes are less likely to be detected because of their lower surface brightness. Grazian et al. (2011), based on the $z \sim 7$ analysis, have pointed out that the assumed size distribution critically alters the UV luminosity function, especially the faint-end slope.

One of the main goals of recent observational projects targeting $z \gtrsim 6$ galaxies (e.g., HUDF09/12, CANDELS, XDF, GOLDRUSH; Oesch et al., 2010b; Grogin et al., 2011; Koekemoer et al., 2011; Ellis et al., 2013; Illingworth et al., 2013; Ono et al., 2017) is to obtain the faint-end slope of luminosity functions, a key quantity for testing galaxy formation models. In addition, since $z \sim 6 - 10$ is the epoch of reionization and faint galaxies are thought to be major sources of ionizing photons, the abundance of faint galaxies, i.e., the faint-end slope, is important for understanding the reionization of the universe.

Recently, in order to derive luminosity functions at fainter magnitudes, deep observations combined with the power of the gravitational lensing by galaxy clusters have been conducted, such as the CLASH program (see Postman et al., 2012, for more details) and the *Hubble* Frontier Fields program (HFF; Lotz et al., 2017). Utilizing early-stage data from the HFF, the faint limits of luminosity functions reach as faint as UV magnitudes ($M_{\rm UV}$) of $M_{\rm UV} \sim -15.5$, -17, and -17.5 at $z \sim 6-7$, 8, and 9, respectively (Atek et al., 2014, 2015b; Ishigaki et al., 2015; McLeod et al., 2015). More recently, very faint galaxies of $M_{\rm UV} \sim -13$ at $z \sim 6 - 7$ have been detected using one-third of the full HFF data (Castellano et al., 2016; Livermore et al., 2017), half of them (Laporte et al., 2016), two-thirds of them (Kawamata et al., 2016; hereafter K16, Yue et al., 2017), and all of them (Ishigaki et al., 2017). However, the luminosity functions obtained in the previous studies, including those from the HFF, are still highly uncertain, especially at $M_{\rm UV} \gtrsim -18$ and $z \gtrsim 6$, because the size–luminosity relations are not determined well in that magnitude range (see our Figure 4.13, and Figure 2 of Bouwens et al., 2017a) owing to an insufficient number of galaxies with size measurements.

There have been a number of studies that measure sizes of bright ($M_{\rm UV} \lesssim -18$) galaxies (e.g., Ferguson et al., 2004; Bouwens et al., 2004; Curtis-Lake et al., 2016; Laporte et al., 2016; Bowler et al., 2017). At $z \sim 4$ and 5, Huang et al. (2013) have carefully measured the size distributions of Lyman break galaxies (LBGs) with $-22.5 \lesssim M_{\rm UV} \lesssim -17.5$ and find size–luminosity relations of $L \propto r_{\rm e}^{0.22-0.25}$, where L and $r_{\rm e}$ are the luminosity and effective half-light radius, respectively. Oesch et al. (2010a) were among the first to measure the sizes of $z \sim 7$ and 8 galaxies with samples of 16 and five galaxies from HUDF09 (Oesch et al., 2010b) reporting that the decreasing trend of sizes with increasing redshifts continues to these redshifts. This trend has been confirmed by Ono et al. (2013) by careful measurements using the deeper imaging data from HUDF12 (Ellis et al., 2013; Koekemoer et al., 2013). With a larger sample, Grazian et al. (2012) have measured the sizes of $z \sim 7$ LBGs of moderate magnitude ($M_{\rm UV} \lesssim -18.5$). They have found that the

size–luminosity relation is in the form of $L \propto r_{\rm e}^{0.5}$ at this redshift, although their size measurements may suffer from systematic biases due to their measuring method. More recently, Shibuya et al. (2015) have measured sizes for large $z \sim 6-10$ LBG samples with moderate magnitudes of $M_{\rm UV} \lesssim -18$, obtaining a relation of $L \propto r_{\rm e}^{0.25}$, which is not consistent with the result by Grazian et al. (2012). One of the reasons of this discrepancy may be a biased fitting method adopted in Shibuya et al. (2015) (see Section 4.3.1, for more details). Since none of the above studies has reliably determined the size–luminosity relation for $M_{\rm UV} \lesssim -18$ galaxies at $z \gtrsim 6$, a size–luminosity relation of $L \propto r_{\rm e}^{0.25}$ has been commonly adopted in derivations of the luminosity functions, given the results of Huang et al. (2013) obtained for $z \sim 4-5$. This relation is extrapolated and also applied to fainter magnitudes down to $M_{\rm UV} \sim -13$, beyond the magnitude range over which it is determined.

At faint magnitudes of $M_{\rm UV} \gtrsim -18$, Kawamata et al. (2015, hereafter K15) have used the first cluster and parallel fields data from the HFF to find that the sizes of observed faint galaxies ($-18.7 \lesssim M_{\rm UV} \lesssim -16.6$) are considerably smaller than the sizes inferred from the extrapolated size–luminosity relation of $L \propto r_{\rm e}^{0.25}$. This result has subsequently been confirmed by Bouwens et al. (2017a), Laporte et al. (2016), and Bouwens et al. (2017c), who have measured the sizes of faint galaxies using four, three, and four HFF cluster fields data, respectively. In addition, Bouwens et al. (2017a) have indirectly indicated the absence of faint galaxies with large sizes using the dependence of the galaxy surface density on the lensing shear. They have concluded that the intrinsic sizes of the faintest galaxies are small, and the intrinsic size distribution assumed in the calculation of the luminosity function should be close to the observed one. This makes the faint-end slope of the luminosity function shallower. However, since none of Kawamata et al. (2015), Bouwens et al. (2017a,c), and Laporte et al. (2016) have considered an incompleteness correction due to galaxies with large sizes, the slope of the size–luminosity relation may be biased toward a steeper value. In addition, the indirect inference in Bouwens et al. (2017a) is subject to large uncertainties, which may result in weak constraints on the size distribution compared to inferences using direct size measurements.

In this thesis, we provide direct size measurements of $z \sim 6-7$, 8, and 9 LBGs at $-21.6 \lesssim M_{\rm UV} \lesssim -12.3$ using all six HFF cluster and parallel fields data. We show that the incompleteness effect is significant at $z \sim 6-9$ for the first time. We derive incompleteness-corrected intrinsic size–luminosity relations simultaneously with luminosity functions, which enables us to explore the correlation between these two functions. We note that we do not discuss the UV luminosity density and hence the contribution of galaxies to cosmic reionization, because the normalization parameter of UV luminosity functions is not determined in this thesis due to limitations of computing time.

1.6 Overview of this Thesis

In this thesis, we investigate galaxy evolution constructing large galaxy samples at the highest redshifts of $z \sim 6-9$ using the Lyman-break technique. This broadens not only

the redshift range to be traced toward higher redshifts, but also the magnitude ranges toward fainter magnitudes at each redshift. These large samples enable more statistically significant derivations of physical quantities including the above four quantities.

We utilize the complete data by *Hubble Space Telescope* obtained in the Frontier Fields project as described in Chapter 2. This project deeply observes six strongly-lensing clusters, whose gravitational lensing effects enable constructions of large samples of very faint ($M_{\rm UV} \lesssim -12$) galaxies at $z \sim 6-9$. Due to the smaller observed area of the HFF project compared to that of the CANDELS project, brighter and rarer galaxies are not observed in the HFF project. However, thanks to the gravitational lensing effects, fainter galaxies, even fainter than those detected in the deepest ever HUDF12, are discovered in the HFF. Furthermore, HFF goes deeper than the successful previous lensing survey of CLASH, because of the longer exposure times.

In Chapter 3, we carefully construct our own mass models of the six HFF clusters to reliably calculate the lensing effects and evaluate magnification factors. Thanks to the deep imaging by the HFF project, the numbers of multiple images, which are used to constrain the mass models, are large for the HFF clusters ($\sim$ 100–200) compared those for the CLASH clusters ($\simeq$ 50). Additionally, the accuracy of our models are confirmed by our prediction of a reappearance of the lensed supernova SN Refsdal, which is a rare chance to test the accuracy of mass models. The structure of Chapter 3 is as follows. We have described the *HST* data as well as the construction of photometric catalogs in Section 2. Our mass modeling procedure is described in detail in Section 3.1, and the results of the mass modeling are given in Section 3.2. We discuss the multiple image candidates among the $z \sim 6-9$ dropout galaxies in Section 3.3. Finally, we summarize our results in Section 3.4.

In Chapter 4, we measure sizes and magnitudes of the galaxies in our samples to derive size–luminosity relations and luminosity functions. Compared to previous studies at $z \sim 6-9$ (Ono et al., 2013; Holwerda et al., 2015; Shibuya et al., 2015), our samples contains fainter galaxies. In derivations of luminosity functions, previous studies assume size–luminosity relations, which are suggested to strongly affect the resulting luminosity functions (e.g., Grazian et al., 2011; Bouwens et al., 2017a). We, for the first time at $z \sim 6-9$, derive the luminosity functions and size–luminosity relations simultaneously, correcting for detection completeness. These luminosity functions and size–luminosity relations and their implications for galaxy evolution of luminosity and kinematics are discussed. The structure of Chapter 4 is as follows. In Section 4.1, we measure the sizes of the galaxies in the samples constructed in Chapter 2. Our method to correct for systematic biases, which is updated from that in K15 in order to deal with the increased number of galaxies, is also described. In Section 4.2, for each of the three redshift ranges, we simultaneously estimate the intrinsic size–luminosity relation and the UV luminosity function from the observed distribution of galaxies on the size–luminosity plane, taking account of the incompleteness effect. The correlations between the size–luminosity and luminosity function parameters are also obtained. We discuss our findings in Section 4.3 and give a summary in Section 4.4.

In Appendix A, in order to gain insights into physical properties of $z \sim 6-9$ galaxies, we discuss UV colors and multiplicities on the size–luminosity plane for the first time at $z \sim 6-9$. In addition, star-formation rate surface densities of $z \sim 6-9$ galaxies are compared to those of local galaxies for the first time with large samples.

Throughout this thesis, we adopt a flat cosmological model with the matter density $\Omega_M = 0.3$, the cosmological constant $\Omega_\Lambda = 0.7$, and the Hubble constant $H_0 = 70\ \mathrm{km\,s^{-1}Mpc^{-1}}$. Magnitudes are given in the AB system (Oke & Gunn, 1983) and coordinates are given in J2000. Galaxy sizes are measured in the physical scale.

Chapter 2

Data and Sample Selection

Here we describe the data, sample selection, and obtained samples.

2.1 HFF Mosaic Data

We use the reduced image mosaics obtained in the HFF program, which are made publicly available through the STScI website[*1]. This program targets six cluster fields, Abell 2744, MACS J0416.1−2403, MACS J0717.5+3745, MACS J1149.6+2223, Abell S1063, and Abell 370, and their accompanying six parallel fields. Those fields have been observed deeply with the *Hubble Space Telescope* using three bands of the Advanced Camera for Surveys (ACS) and four bands of the IR channel of the Wide Field Camera 3 (WFC3/IR). We utilize the v1.0 standard calibrated (i.e., without 'self-calibration') mosaics for the three ACS bands F435W (B_{435}), F606W (V_{606}), and F814W (i_{814}). For the four WFC3/IR bands F105W (Y_{105}), F125W (J_{125}), F140W (JH_{140}), and F160W (H_{160}), we use the v1.0 standard calibrated mosaics for the Abell 2744 parallel and MACS J0416.1−2403 cluster fields and v1.0 mosaics corrected for 'time-variable sky emission' for the other ten fields. In order to take account of the inhomogeneity of the limiting magnitude due to, e.g., intracluster light, we divide the WFC3/IR field of view of each cluster into 4×4 grid cells and measure limiting magnitudes in individual cells, as shown in Figure 2.1. The 5σ limiting magnitudes of the mosaics are ~ 29 mag on a $0\farcs35$ diameter aperture. All the images have a pixel scale of $0\farcs03$.

Three out of the four clusters have also been observed with *HST* in the CLASH project (see Postman et al., 2012, for more details). Although the CLASH imaging uses many additional bands (F225W, F275W, F336W, F390W, F475W, F625W, F775W, F850LP, and F110W), we do not use these images because they are considerably shallower than the HFF images.

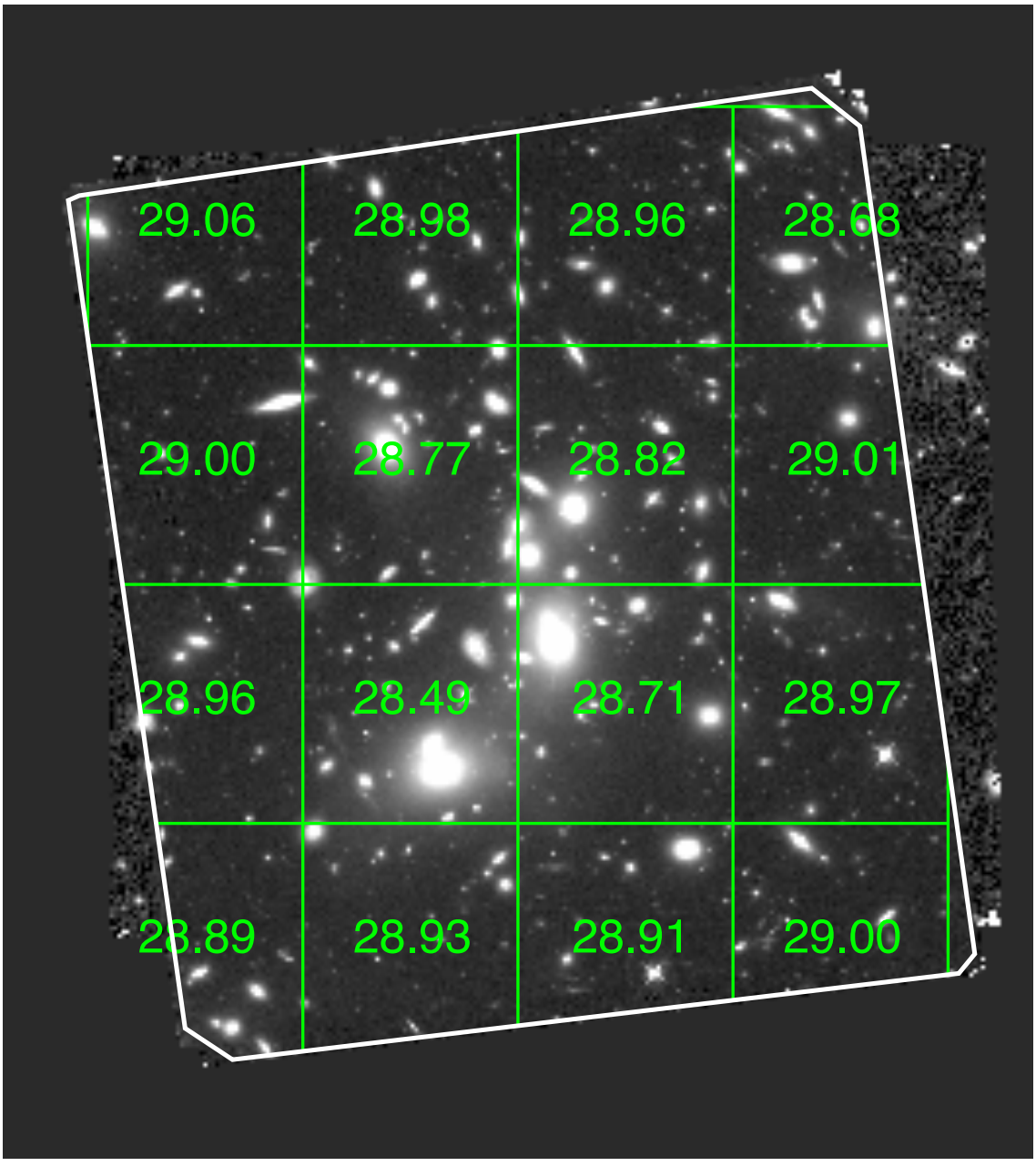

Figure 2.1 Example of the measured 5σ limiting magnitudes in 4×4 grid cells. H_{160} limiting magnitudes are shown on the *HST* H_{160} band image for Abell 2744. Each number shows the limiting magnitude in each cell. We use only the regions within the white lines to search for high-redshift galaxies.

2.2 Sample Selection

We construct two different photometric catalogs specified for the following two purposes, (1) selection of cluster member galaxies and (2) detection of faint high-redshift galaxies.

[*1] http://www.stsci.edu/hst/campaigns/frontier-fields/

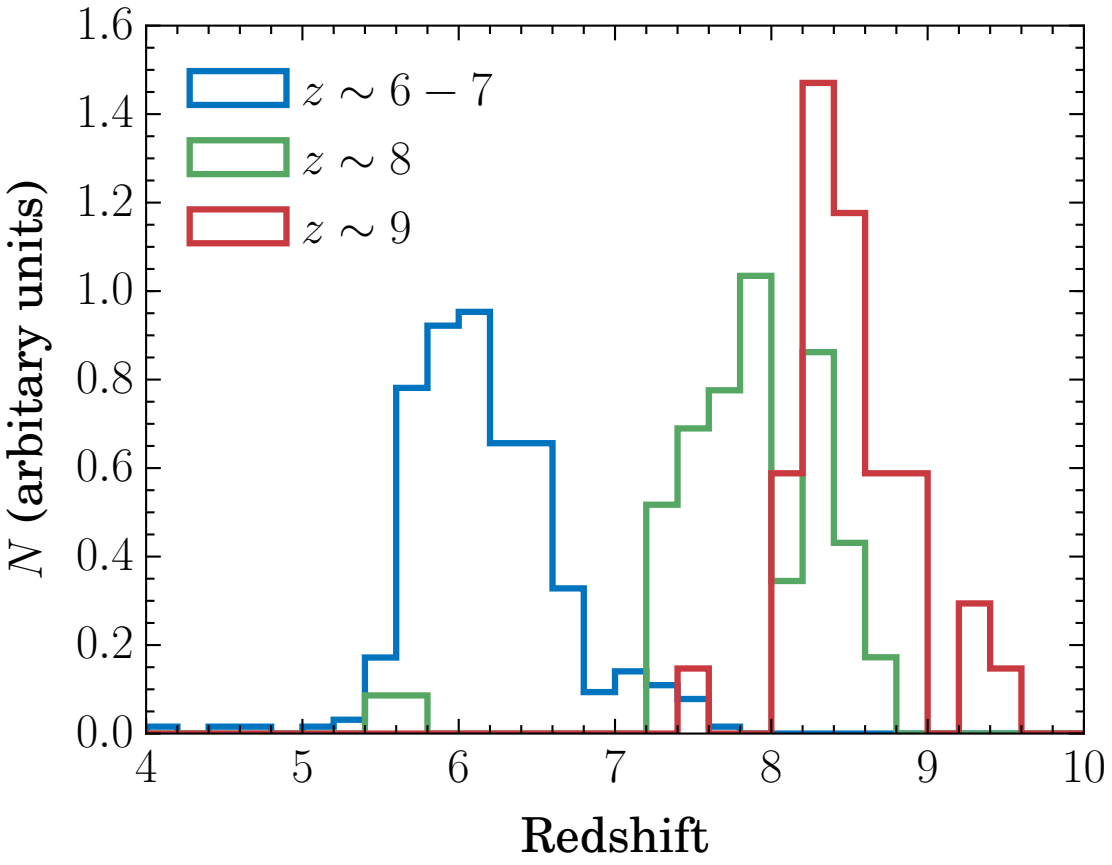

Figure 2.2 Normalized distributions of the photometric redshifts of our dropout galaxy samples for $z \sim 6-7$ (blue), 8 (green), and 9 (red).

2.2.1 Selection of Cluster Member Galaxies

Member galaxies are selected utilizing both the red sequence and photometric redshift techniques. For accurate estimates of galaxy colors, we convolve *HST* images with a Gaussian kernel in order to match the point-spread function (PSF) sizes of all images of interest to the largest one. Then, we run `SExtractor` v2.8.6 (Bertin & Arnouts, 1996) in dual-image mode using the i_{814} image as the detection image setting the parameters `DEBLEND_MINCONT = 0.00005`, `DEBLEND_NTHRESH = 50`, `DETECT_MINAREA = 5`, and `DETECT_THRESH = 2.5`. We estimate photometric redshifts of the galaxies in this catalog using `BPZ` v1.99.3 (Benítez, 2000). We use the $B_{435}-V_{606}$ color-magnitude diagram to identify the red sequence, and extract cluster members with V_{606}-band magnitudes brighter than $\sim 24-25$ mag (see Ishigaki et al., 2015, for more details). We then select galaxies in the vicinity of the red sequence whose photometric redshifts coincide with the cluster redshift as cluster members. After applying these criteria, we refine the member galaxy catalog by adding and removing some galaxies based on their colors, morphologies, and spectroscopic redshifts (Owers et al., 2011; Ebeling et al., 2014).

2.2.2 Selection of Faint High-redshift Galaxies

We make two catalogs with different detection images, which are referred to as the *JJHH* and *JHH* catalogs. The detection image for the former is a J_{125}, JH_{140}, and H_{160} combined image, and for the latter it is a JH_{140} and H_{160} combined image; these are created using `SWarp` v2.38.0 (Bertin et al., 2002). Weight images of these co-added images are also produced from public weight images. Before running `SExtractor` to build photometric catalogs, we again match PSF sizes for reliable color measurements. For the i-dropout selection, images for all the bands are PSF-matched except for B_{435} and V_{606}, and for the other selections all except for B_{435}, V_{606}, and i_{814} are PSF-matched[*2]. Then, we run `SExtractor` in dual-image mode using the co-added images as the detection image with the parameters of `DEBLEND_MINCONT = 0.0005`, `DEBLEND_NTHRESH = 16`, `DETECT_MINAREA = 4`, and `DETECT_THRESH = 3.0`. For measuring colors of galaxies, we use aperture magnitudes (`MAG_APER`) $m_{\rm AP}$ with a aperture diameter of $0\farcs35$ for the convolved images and $0\farcs20$ (B_{435}), $0\farcs19$ (V_{606}), and $0\farcs19$ (i_{814}) for the non-convolved images. We also derive photometric redshifts for the high-redshift galaxies detected in the second photometric catalog using `BPZ`. For reliable color measurements, we PSF-match all the band images. This is because relative fluxes of all of the bands, including those whose wavelengths are shorter than Lyman break, are needed in the SED fittings.

From the catalogs, we select i-, Y-, and YJ-dropout galaxies using the Lyman break technique. For i- and Y-dropout selections, we use the *JJHH* catalog and for YJ-dropout selection, we use the *JHH* catalog. For i-dropouts or $z\sim6-7$ galaxies, we use the criteria used in Atek et al. (2015b) of

$$i_{814}-Y_{105}>0.8, \tag{2.1}$$

$$Y_{105}-J_{125}<0.8, \tag{2.2}$$

$$i_{814}-Y_{105}>2(Y_{105}-J_{125})+0.6, \tag{2.3}$$

those used in Atek et al. (2014, 2015b) for Y-dropouts or $z\sim8$ galaxies,

$$Y_{105}-J_{125}>0.5, \tag{2.4}$$

$$J_{125}-JH_{140}<0.5, \tag{2.5}$$

$$Y_{105}-J_{125}>0.4+1.6(J_{125}-JH_{140}), \tag{2.6}$$

and criteria similar to those used in Oesch et al. (2013); Ishigaki et al. (2015) for YJ-

[*2] Images whose band wavelengths are shorter than Lyman break are not convolved in order for reliable aperture photometries.

dropouts or $z \sim 9$ galaxies,

$$(Y_{105} + J_{125})/2 - JH_{140} > 0.75, \tag{2.7}$$

$$(Y_{105} + J_{125})/2 - JH_{140} > 0.75 + 0.8(JH_{140} - H_{160}), \tag{2.8}$$

$$J_{125} - H_{160} < 1.15, \tag{2.9}$$

$$JH_{140} - H_{160} < 0.6. \tag{2.10}$$

For i-dropouts, we use additional signal-to-noise ratio constraints that require objects not to be detected at $> 2\sigma$ levels in both the B_{435}- and V_{606}-band images or in a B_{435} + V_{606} stacked image. Detections at $> 5\sigma$ levels are also required in both the Y_{105}- and J_{125}-band images. For a conservative selection, i_{814} magnitudes are replaced by the i_{814} 2σ limiting magnitude if the signal is below that level. For Y-dropouts, objects are required to be detected at $> 2\sigma$ levels in none of the B_{435}-, V_{606}-, and i_{814}-band images. In addition, detections at $> 5\sigma$ levels are required in all of the J_{125}-, JH_{140}-, and H_{160}-band images. For YJ-dropouts, objects are required to be detected at $> 2\sigma$ levels in none of the B_{435}-, V_{606}-, and i_{814}-band images. In addition, detections at $> 3\sigma$ levels are required in all of the JH_{140}- and H_{160}-band images and at $> 3.5\sigma$ levels in at least one of these band images. Magnitudes of Y_{105} and J_{125} are replaced by their 0.9σ limiting magnitudes if the signal is below that level[*3]. Finally, we remove objects whose pseudo-χ^2 is larger than 2.8, with $\chi^2 = \sum_i \mathrm{SGN}(f_i)(f_i/\sigma_i)^2$, where the summation runs over all the ACS bands. Here f_i and σ_i are the flux density and its uncertainty in the i-th band image, respectively, and $\mathrm{SGN}(f_i)$ is the sign function, whose definition is $\mathrm{SGN}(x) = 1$ if $x > 0$, $\mathrm{SGN}(x) = 0$ if $x = 0$, and $\mathrm{SGN}(x) = -1$ if $x < 0$. For all of the dropout galaxies, we check that they have `SExtractor` stellarity parameters consistent with being resolved. The selected dropout galaxies are presented in Tables 4–6 in Ishigaki et al. (2017). For each galaxy, the first part of ID represents the field in which it is found; 1, 2, 3, 4, 5, and 6 indicate Abell 2744, MACS J0416.1−2403, MACS J0717.5+3745, MACS J1149.6+2223, Abell S1063, and Abell 370, respectively, and C and P indicate cluster and parallel fields, respectively. The second part of ID represents its coordinates.[*4]

One of the important sources of contamination are evolved galaxies at lower redshifts. However, for $z \sim 6 - 7$ and 8 criteria, Atek et al. (2015b) argued that the chance of contamination is very low. This is because evolved galaxies with a young burst, which may pass the criteria, are very rare. Although other important sources of contamination are brown dwarfs, Atek et al. (2015b) also denied the possibility at these redshifts given the stellarity criterion is adopted. At $z \sim 9$, Oesch et al. (2013) suggested that the contamination is not significant and the estimated contamination fraction is $\gtrsim 10\%$.

[*3] We use the 0.9σ magnitude limit in order to include the $z \sim 9$ candidate in the Abell 2744 field, which seems to be reliable also based on a redshift estimation using model-predicted positions (Zitrin et al., 2014).

[*4] For example, HFF1C-2251-4556 is found in Abell 2744 cluster field and its coordinates are R.A.=00:14:22.51, Decl.= −30:24:55.6.

From the Ishigaki et al. (2017) samples, we remove a Y-dropout galaxy, HFF6P-1733-6559, and a YJ-dropout galaxy, HFF6P-1732-6562, in the Abell 370 parallel field, because they appear to be spurious sources by visual inspection. These are indeed the same object meeting both the Y- and YJ-dropout selections. As a result, the total numbers of the selected galaxies are 350, 64, and 39 for i-, Y-, and YJ-dropouts, respectively. Their photometric redshift distributions are shown in Figure 2.2. The averages of the reliable ($z > 4$) photometric redshifts of the i-, Y-, and YJ-dropouts are $z = 6.2$, 7.8, and 8.5, respectively. Therefore, we use $z = 6$, 8, and 9 in the calculation of the sizes, magnitudes, and magnification factors for i-, Y-, and YJ-dropouts, respectively. Fixing the redshift to these values does not cause any systematic errors in the following results.

Chapter 3

Mass Model Construction

3.1 Mass Modeling Procedure

Here we describe the method to model the mass distributions of the four HFF clusters in detail. We adopt the so-called "parametric lens modeling" approach, in which a simply parametrized mass model consisting of several mass components is assumed and the model parameters are optimized to reproduce observed multiple image properties. Throughout the thesis mass modeling and analysis are performed using the public software `glafic` (Oguri, 2010), which has extensively been used for strong lensing mass modeling of clusters (e.g., Oguri et al., 2012, 2013; Köhlinger & Schmidt, 2014; Ishigaki et al., 2015; Newman et al., 2015). We note that our mass modeling procedure has been highly evaluated in a model comparison project using simulated clusters (Meneghetti et al., 2017).

3.1.1 Mass Components

In this thesis we adopt the following mass components. Details of each mass component are described in Oguri (2010). We give a brief summary below.

A cluster-scale dark halo is modeled by an elliptical extension of the NFW (Navarro et al., 1997) density profile. We introduce an elliptical symmetry in the projected mass density, and compute its lensing properties by numerical integrals (Schramm, 1990). The model parameters include virial mass M, positions, ellipticity $e \equiv 1 - a/b$ (a and b being minor and major axis lengths, respectively) and its position angle θ_e, and concentration parameter c.

Member galaxies are modeled by pseudo-Jaffe ellipsoids (Keeton, 2001). To reduce the number of parameters, in most cases we introduce scaling relations of model parameters with luminosity L, such that velocity dispersion is given by $\sigma/\sigma_* \propto L^{1/4}$ and truncation radius $r_{\rm trun}/r_{\rm trun,*} \propto L^{\eta}$. The ellipticity and position angle of each galaxy are fixed to the values measured by `SExtractor`. All the input quantities for the member galaxies are measured in the i_{814} band. Luminosities are computed from total magnitudes (`MAG_AUTO`) given by `SExtractor`. The model parameters are the normalization of velocity dispersion σ_*, truncation radius $r_{\rm trun,*}$, and dimensionless parameter η. We call this model of a set of member galaxies GALS.

Member galaxies that are located adjacent to multiple images can have significant contributions to the image properties of the multiple images including their locations. For some of these member galaxies we do not apply the scaling relations mentioned above but instead model them independently by pseudo-Jaffe ellipsoid components, to which we refer as PJE. The model parameters are velocity dispersion σ, ellipticity e and its position angle θ_e, and truncation radius $r_{\rm trun}$.

It has been shown that adding an external perturbation on the lens potential and an internal perturbation describing a possible asymmetry of the cluster mass distribution sometimes improves the mass model significantly (e.g., Oguri, 2010; Oguri et al., 2013). Both perturbations are described by a multipole Taylor expansion at the position of the BCG of the form $\phi = (C/m)r^n \cos m(\theta - \theta_*)$, where r is the distance from the BCG, θ is angular coordinate, θ_* is position angle, C is expansion coefficient, and $n, m \geq 0$[*1]. In the case of the external perturbation, the zeroth ($n = 0$, $m = 0$) and the first ($n = 1$, $m = 1$) orders of the Taylor expansion are unobservable. We call the second order term of the external perturbation ($n = 2$, $m = 2$), which is equivalent to the so-called external shear, PERT. We also include higher multipole terms ($m \geq 3$) to approximately model higher-order terms of the external perturbation as well as a possible asymmetry of the cluster mass distribution, which we refer to as MPOLE. Note that a term inducing constant convergence κ ($n = 2$, $m = 0$) is not included in our mass modeling (see Oguri, 2010, for more details).

The amplitudes of the perturbations are defined for a given fiducial source redshift $z_{s,\rm fid}$, and are scaled with the source redshift assuming that the perturbation originates from the structure at the cluster redshift. The model parameters for PERT are external shear γ and its position angle θ_γ, and those for MPOLE are expansion coefficient ϵ, position angle θ_ϵ, m, and n. The values of γ and ϵ are assumed to be constant over the entire field.

3.1.2 Modeling Strategy

We adopt the following unified strategy for conducting our mass modeling. We place several NFW components on the positions of bright cluster member galaxies. When an NFW component has a sufficient number of multiple images around it to constrain the model parameters well, all the NFW model parameters are treated as free parameters. On the other hand, for NFW components located at the edge or outside the strong lensing regions, we fix some model parameters such as positions, ellipticities, and position angles, to observed values. For NFW components lacking strong observational constraints, it is also difficult to reliably constrain the concentration parameter c. In this case we simply assume $c = 10$.

We start with a small number of NFW components, and increase the number of components until we find the least reduced χ^2. We stop adding an NFW component when it begins to increase the reduced χ^2, which is caused because a decrease in the degree of freedom surpasses an improvement in the raw χ^2. Perturbations (PERT and MPOLE) are

[*1] When $m = 0$, i.e., m is sufficiently close to 0, C is selected so that C/m is finite.

also added as long as they improve the mass model significantly. In parallel with building the mass model, we iteratively refine multiple images used as constraints, by validating known multiple image candidates and searching for new multiple image candidates. New multiple image candidates are identified based on consistency with the mass model and on colors, morphologies, and photometric redshifts. Our selection of multiple images is conservative in the sense that we remove any unreliable or suspicious candidates. A final set of multiple images for each cluster is given in Section 3.1.4.

About one fifth of the multiple images have spectroscopic redshifts. The source redshifts are fixed to the spectroscopic redshifts when available. The redshifts of the other multiple images are treated as model parameters and are optimized together with source positions. Some multiple images have a precise photometric redshift estimate. For them, we include this information in the optimization by adding a Gaussian prior centered at the estimated redshift and a conservative standard deviation of $\sigma_z = 0.5$ (see also below). We choose this conservative value in order not to avoid any bias in the best-fitting mass model originating from potential biases in our photometric redshift estimates.

3.1.3 Optimizations and Error Estimates

All the model parameters are simultaneously optimized to reproduce the positions and photometric redshifts of the multiple images. Specifically, the optimization is performed to minimize χ^2

$$\chi^2 = \chi^2_{\rm pos} + \chi^2_z, \tag{3.1}$$

$$\chi^2_{\rm pos} = \sum_i \frac{\left|\mathbf{x}_{i,\rm obs} - \mathbf{x}_i\right|^2}{\sigma^2_{x_i}}, \tag{3.2}$$

$$\chi^2_z = \sum_j \frac{\left(z_{j,\rm obs} - z_j\right)^2}{\sigma^2_z}, \tag{3.3}$$

where $\mathbf{x}_i$ is the position of the i-th image and z_j is the source redshift of the j-th system. The positional uncertainties $\sigma_{x,i}$ can be different for different images and are given in Section 3.1.4. For Abell 2744, we include an additional term $\chi^2_\mu = (\mu_{\rm obs} - \mu)^2/\sigma^2_\mu$ from the observation of a Type Ia supernova behind this cluster (see Section 3.1.4 for more details).

Formally we need to solve a non-linear lens equation to estimate the position χ^2 (Equation 3.2), which is time-consuming. We adopt the so-called source plane minimization which evaluates Equation (3.2) in the source plane. Once a distance in the source plane is converted to a corresponding distance in the image plane using the full magnification tensor, this provides a very good approximation for the image plane position χ^2 (see Appendix 2 of Oguri, 2010).

We derive the best-fitting mass model for each cluster that minimizes the total χ^2 (Equation 3.1) by a standard downhill simplex method. In addition, we run Markov Chain Monte Carlo (MCMC) to estimate errors in the mass models. When deriving the best-fitting mass model and running MCMC, the parameter ranges of ellipticity, concen-

Table 3.1. Summary of Mass Modeling

Cluster	No. of Multiple Image Systems (with spec-z)	No. of Multiple Images	χ^2/dof	Image Plane rms (arcsec)
Abell 2744 v4	45 (24)	132	130.2/134	0.42
MACS J0416.1−2403 v4	75 (34)	202	240.0/196	0.50
MACS J0717.5+3745 v3	60 (8)	173	144.5/144	0.52
MACS J1149.6+2223 v3	36 (16)	108	100.1/103	0.31
Abell S1063 v4	53 (19)	141	136.2/138	0.38
Abell 370 v4	49 (19)	135	99.5/140	0.50

Table 3.2. Mass Model Parameters for Abell 2744

Component	Model	Mass ($10^{14}\ h^{-1}M_\odot$)	e	θ_e (deg)	c	Δx[a] (arcsec)	Δy[a] (arcsec)
Cluster halo 1	NFW	$4.53^{+0.88}_{-0.80}$	$0.37^{+0.03}_{-0.03}$	$165.05^{+4.04}_{-2.88}$	$4.04^{+0.36}_{-0.33}$	$-0.21^{+0.41}_{-0.37}$	$3.30^{+0.53}_{-0.52}$
Cluster halo 2	NFW	$1.41^{+0.21}_{-0.22}$	$0.38^{+0.02}_{-0.02}$	$129.42^{+1.79}_{-2.02}$	$9.49^{+0.88}_{-0.69}$	$-18.69^{+0.18}_{-0.18}$	$-17.91^{+0.16}_{-0.17}$
Cluster halo 3	NFW	$0.21^{+0.07}_{-0.08}$	$0.76^{+0.03}_{-0.08}$	$107.61^{+9.78}_{-3.94}$	[10.00]	[−26.97]	[30.91]
		σ_*[b] (km s^{-1})	$r_{\mathrm{trun},*}$ (arcsec)	η			
Member galaxies	GALS	$190.76^{+9.69}_{-9.94}$	$71.98^{+31.40}_{-19.06}$	$1.42^{+0.06}_{-0.11}$			
		$z_{s,\mathrm{fid}}$	$\gamma \times 10^2$	θ_γ (deg)			
External perturbation	PERT	[2.00]	$8.97^{+0.85}_{-0.88}$	$139.31^{+2.05}_{-2.24}$			
		$z_{s,\mathrm{fid}}$	$\epsilon \times 10^2$	θ_ϵ (deg)	m	n	
Multipole perturbation 1	MPOLE	[2.00]	$0.22^{+0.19}_{-0.11}$	$52.37^{+17.80}_{-12.16}$	[3.00]	[2.00]	
Multipole perturbation 2	MPOLE	[2.00]	$1.22^{+0.26}_{-0.21}$	$93.97^{+1.96}_{-2.24}$	[4.00]	[2.00]	

Note. — Numbers in square brackets are fixed during the model optimization.

[a]Coordinates are relative to the brightest cluster galaxy position in the Abell 2744 field (R.A. = 3.58611, decl. = −30.40024).

[b]The normalization luminosity L^* corresponds to $i_{814} = 18.33$.

tration parameter, and index η for GALS are restricted to [0, 0.8], [1, 40], and [0.2, 1.5], respectively.

3.1.4 Input Data for each Cluster

Abell 2744

Multiple images for this cluster have been identified in Merten et al. (2011), Atek et al. (2014), Richard et al. (2014), Zitrin et al. (2014), Lam et al. (2014), Ishigaki et al. (2015), Jauzac et al. (2015a), Kawamata et al. (2016), and Mahler et al. (2018). Spectroscopic redshifts of multiple images have been presented in Richard et al. (2014), Johnson et al. (2014), Wang et al. (2015), and Mahler et al. (2018). Lam et al. (2014) and Wang et al. (2015) regarded systems 55 and 56 as a part of systems 1 and 2, respectively, and assigned

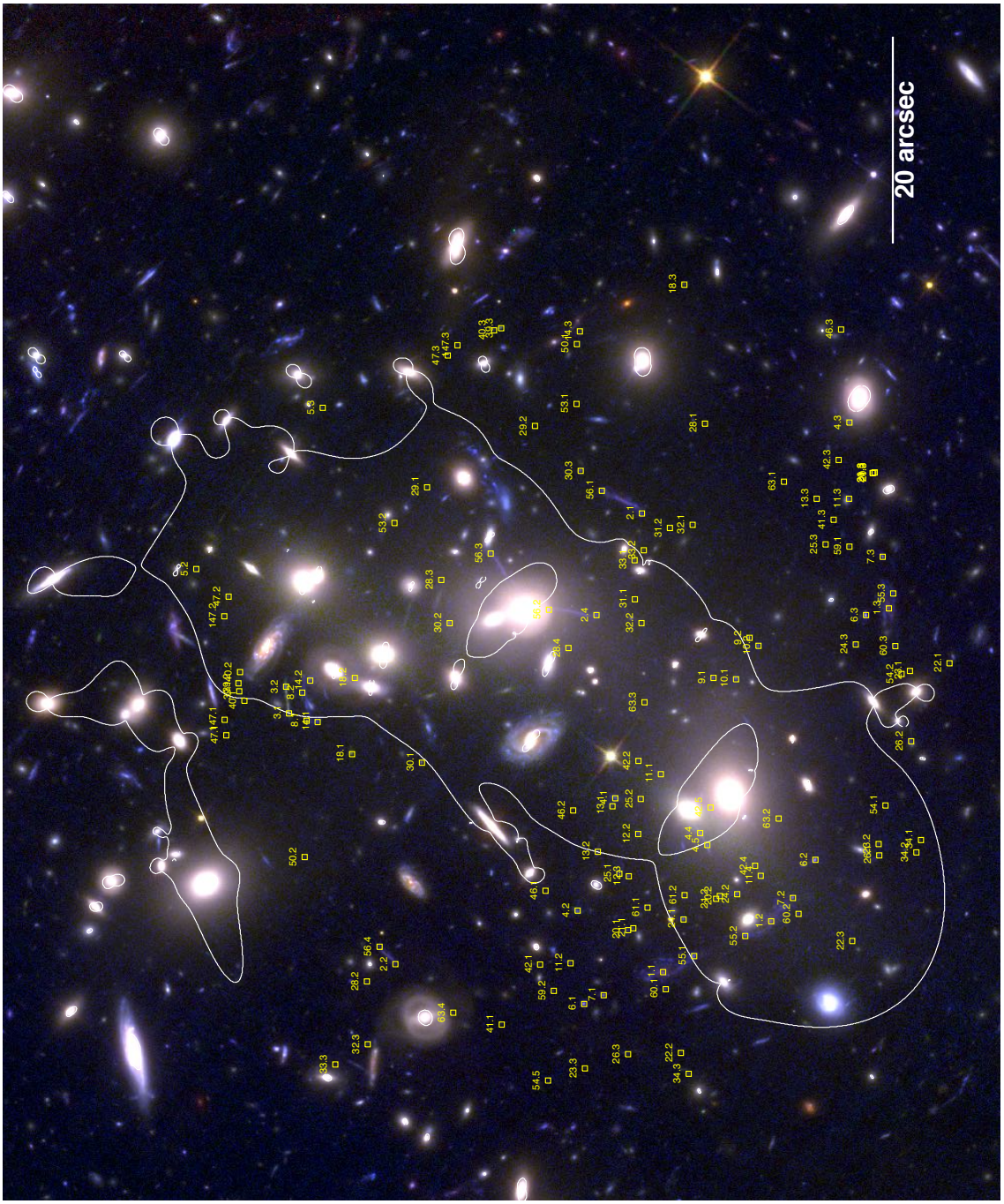

Figure 3.1 Multiple image systems used for mass modeling and critical curve of the best-fitting models for Abell 2744. Underlying color-composite image is created from the *HST* B_{435}+V_{606}-, i_{814}+Y_{105}-, and J_{125}+JH_{140}+H_{160}-band images. Small yellow squares show the positions of multiple images (see Appendix B for the coordinates). Critical curves for a source redshift of $z = 8$ are shown with solid lines.

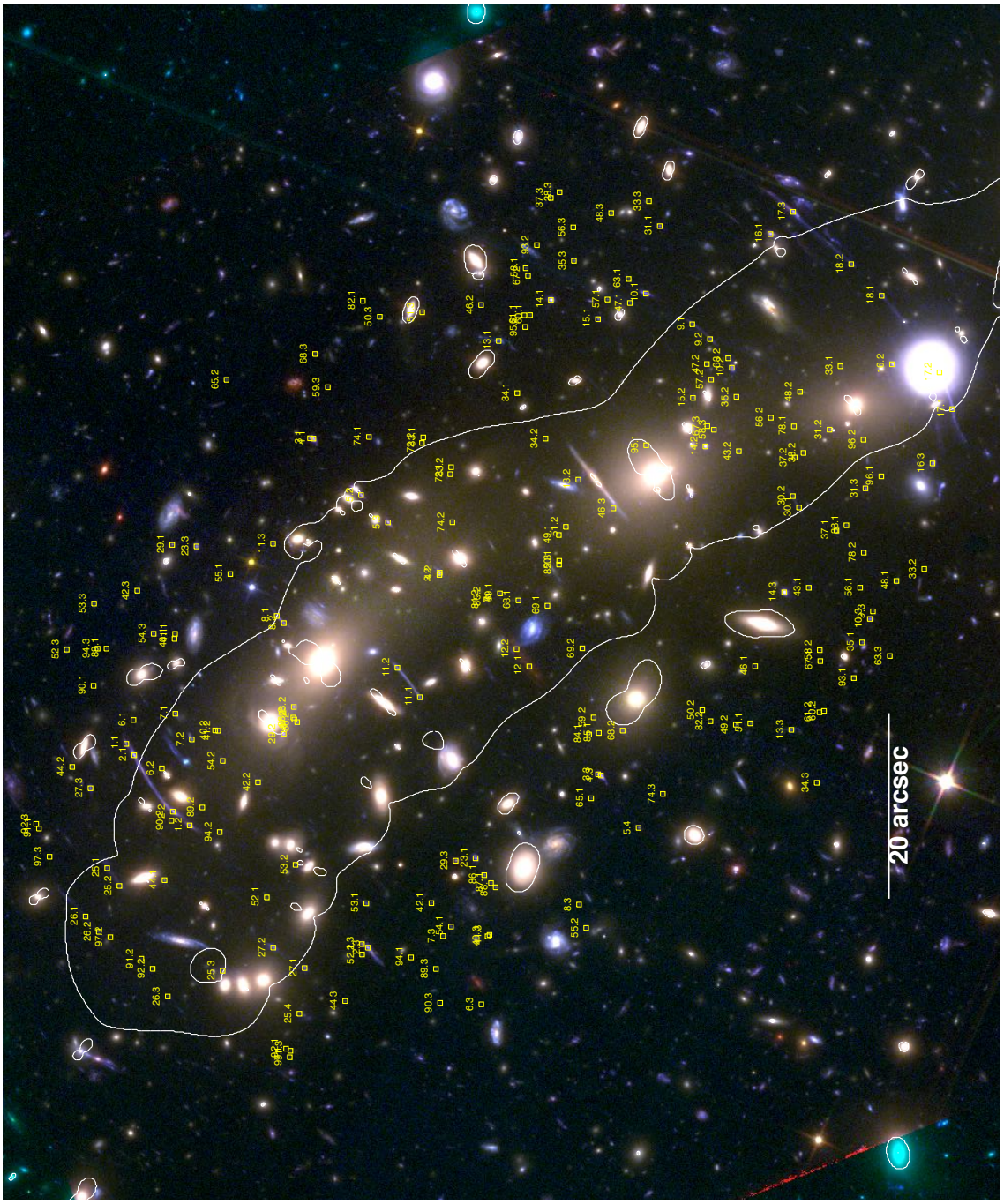

Figure 3.2 Same as Figure 3.1 but for MACS J0416.1−2403.

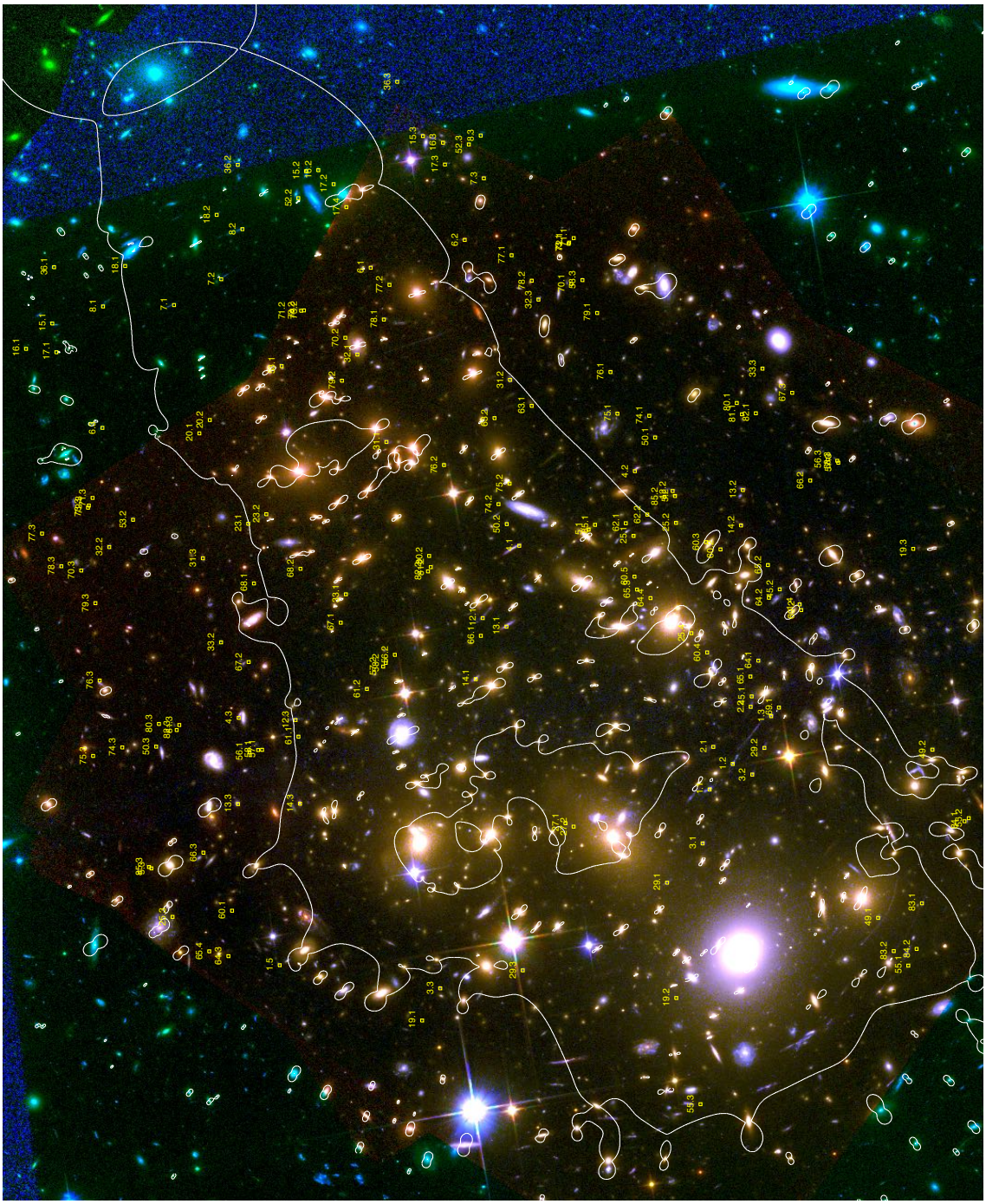

Figure 3.3 Same as Figure 3.1 but for MACS J0717.5+3745.

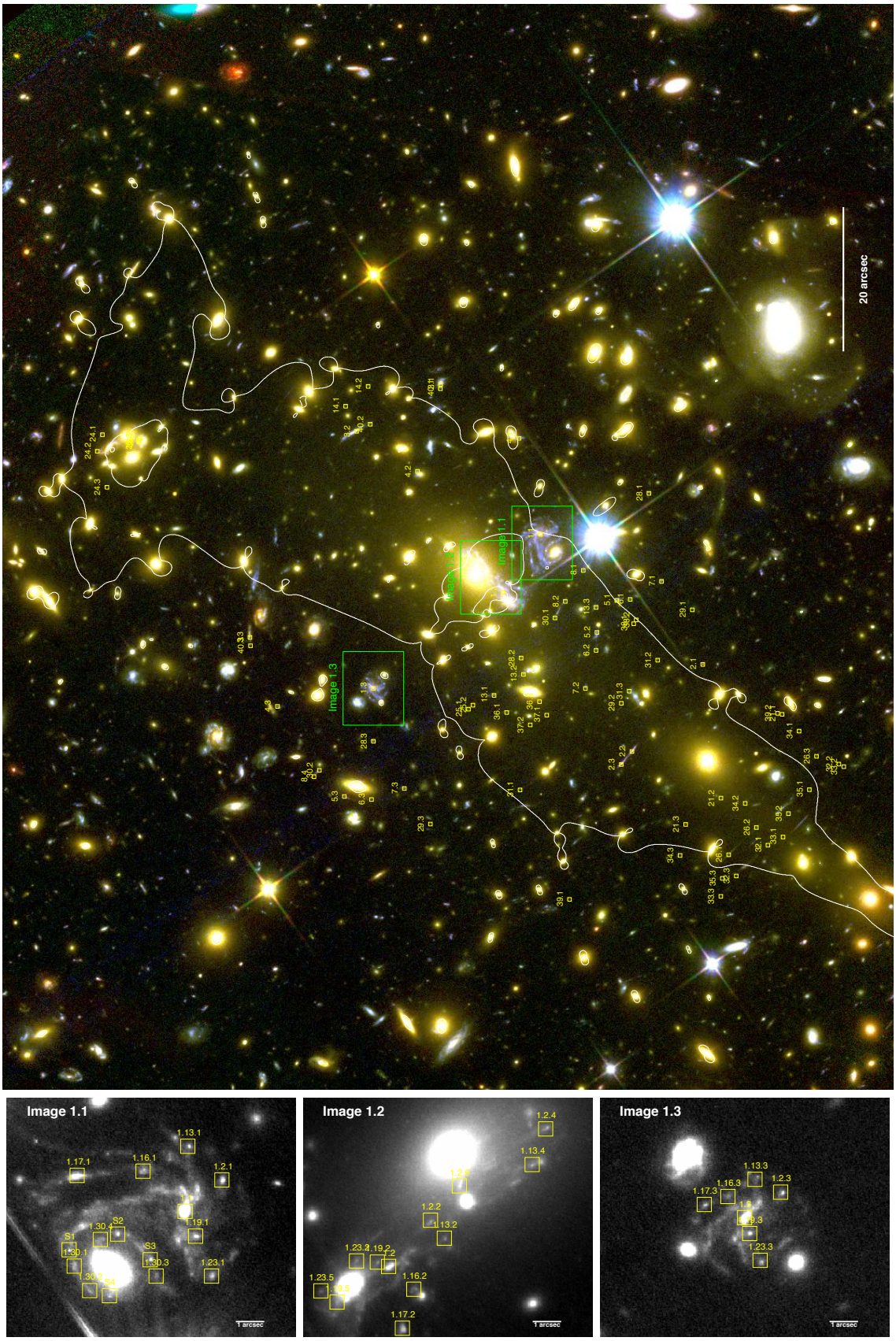

Figure 3.4 Same as Figure 3.1 but for MACS J1149.6+2223. Bottom panels show zoomed-in *HST* i_{814}-band images of System 1 in the MACS J1149.6+2223 field. Small yellow squares represent the positions of multiply imaged knots that are used as constraints in mass modeling.

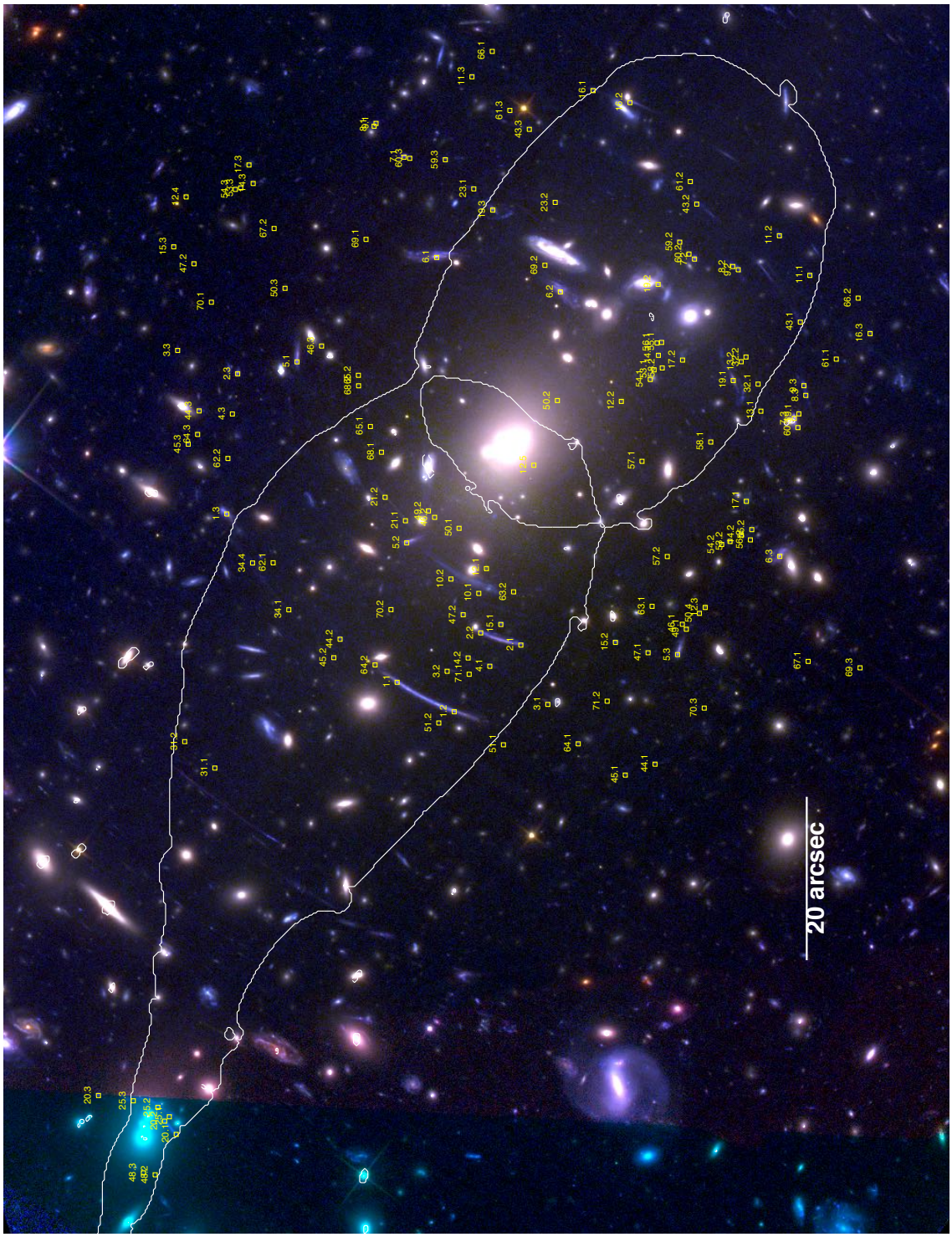

Figure 3.5 Same as Figure 3.1 but for Abell S1063.

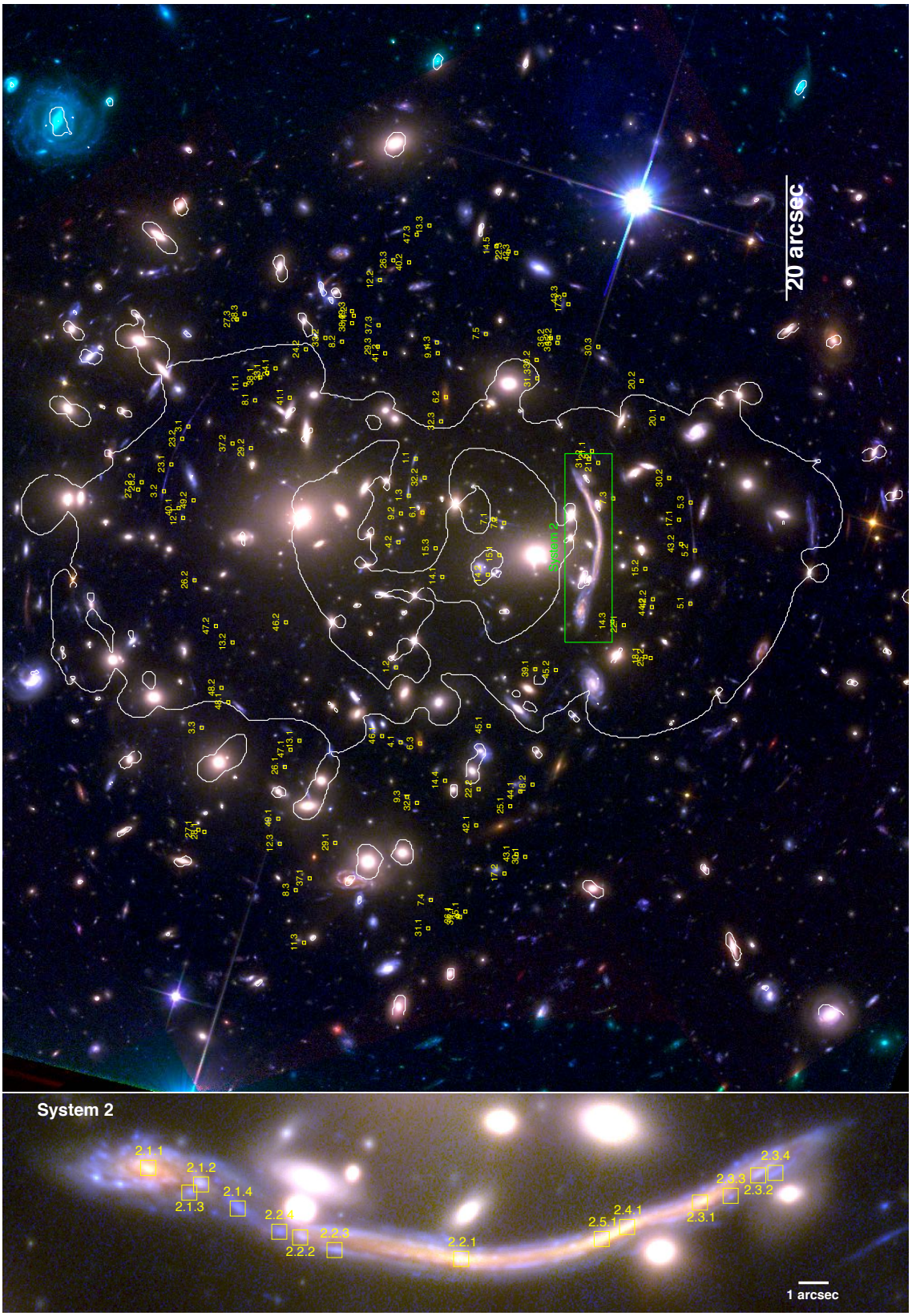

Figure 3.6 Same as Figure 3.1 but for Abell 370. Bottom panel shows zoomed-in image of System 2 in the Abell 370 field. Small yellow squares represent the positions of multiply imaged knots that are used as constraints in mass modeling.

Table 3.3. Mass Model Parameters for MACS J0416.1−2403

Component	Model	Mass ($10^{14}\ h^{-1}M_\odot$)	e	θ_e (deg)	c	Δx[a] (arcsec)	Δy[a] (arcsec)
Cluster halo 1	NFW	$2.78^{+0.37}_{-0.29}$	$0.66^{+0.01}_{-0.01}$	$60.58^{+0.65}_{-1.07}$	$4.18^{+0.33}_{-0.26}$	$-1.98^{+0.65}_{-0.49}$	$1.69^{+0.29}_{-0.37}$
Cluster halo 2	NFW	$2.23^{+0.71}_{-0.58}$	$0.69^{+0.02}_{-0.02}$	$42.93^{+0.97}_{-1.10}$	$4.45^{+0.77}_{-0.42}$	$21.95^{+0.58}_{-0.48}$	$-34.32^{+0.39}_{-0.41}$
Cluster halo 3	NFW	$1.18^{+0.52}_{-0.31}$	$0.61^{+0.04}_{-0.04}$	$37.66^{+2.24}_{-1.61}$	$4.19^{+0.63}_{-0.55}$	$24.40^{+0.57}_{-0.56}$	$-53.79^{+0.85}_{-0.95}$
		σ_*[b] (km s^{-1})	$r_{\rm trun,*}$ (arcsec)	η			
Member galaxies	GALS	$291.59^{+19.70}_{-16.41}$	$16.39^{+4.89}_{-3.13}$	$1.40^{+0.06}_{-0.10}$			
		σ (km s^{-1})	e	θ_e (deg)	$r_{\rm trun}$ (arcsec)	Δx[a] (arcsec)	Δy[a] (arcsec)
Member galaxy	PJE	$118.69^{+46.15}_{-13.90}$	[0.27]	[166.70]	$1.81^{+3.48}_{-1.27}$	[−14.56]	[15.28]
		$z_{s,\rm fid}$	$\gamma\times10^2$	θ_γ (deg)			
External perturbation	PERT	[2.00]	$3.49^{+0.95}_{-1.02}$	$27.89^{+4.62}_{-6.26}$			
		$z_{s,\rm fid}$	$\epsilon\times10^2$	θ_ϵ (deg)	m	n	
Multipole perturbation	MPOLE	[2.00]	$1.10^{+0.25}_{-0.22}$	$57.36^{+4.31}_{-3.56}$	[3.00]	[2.00]	

Note. — Numbers in square brackets are fixed during the model optimization.

[a]Coordinates are relative to the brightest cluster galaxy position in the MACS J0416.1−2403 field (R.A. = 64.0380981, decl. = −24.0674834).

[b]The normalization luminosity L^* corresponds to $i_{814} = 18.73$.

their redshifts accordingly. To avoid introducing biases, we do not fix the redshifts but treat them as model parameters. While Wang et al. (2015) reported the redshift of system 56 to be $z = 1.2$ with a rating of probable, Johnson et al. (2014) estimated it to be $z = 2.2$ and Lam et al. (2014) adopted this value in their mass modeling. In our mass modeling, we do not assume any spectroscopic redshift on this system and find a model-predicted redshift of $z = 1.97^{+0.07}_{-0.07}$, which is closer to that of Johnson et al. (2014). Due to a controversy over the position of the counterimage of system 3 (see e.g. Lam et al., 2014; Jauzac et al., 2015a, for more details), we do not use its position as a constraint in our mass modeling. For system 5, we find one new counterimage. While Wang et al. (2015) recently reported the redshift of system 22 to be $z = 4.84$, we use $z = 5.284$ by Mahler et al. (2018). Although we have identified a new set of multiple images (system 62) in the northwest part of this cluster in the construction of the version 3 model, we remove this system in the version 4 model because it is not secure (see also Mahler et al., 2018).

Here we describe what has been updated from the version 3 model. Considering the results of the MUSE observation by Mahler et al. (2018), we incorporate and remove 25 and six positions of multiple images, respectively. Specifically, we incorporate multiple image systems 39, 40, 42, 47, 50, 61, 63, and 147 and remove IDs 2.3, 5.1, 5.4, and 8.3 and system 62. The positions of IDs 33.3 and 34.3 are corrected. In addition, we incorporate 20 MUSE spectroscopic redshifts that are considered to be reliable based on their qualities

Table 3.4. Mass Model Parameters for MACS J0717.5+3745

Component	Model	Mass ($10^{14}\ h^{-1} M_\odot$)	e	θ_e (deg)	c	Δx[a] (arcsec)	Δy[a] (arcsec)
Cluster halo 1	NFW	$4.78^{+1.02}_{-0.59}$	$0.63^{+0.03}_{-0.03}$	$135.70^{+1.43}_{-1.09}$	$3.97^{+0.36}_{-0.53}$	$8.09^{+1.05}_{-0.62}$	$3.44^{+1.11}_{-0.79}$
Cluster halo 2	NFW	$2.02^{+0.20}_{-0.39}$	$0.73^{+0.02}_{-0.02}$	$135.60^{+0.95}_{-1.46}$	$3.96^{+0.23}_{-0.31}$	$35.81^{+1.13}_{-0.79}$	$-9.95^{+0.97}_{-0.89}$
Cluster halo 3	NFW	$2.23^{+0.25}_{-0.29}$	$0.56^{+0.02}_{-0.02}$	$142.09^{+0.97}_{-1.32}$	$6.98^{+1.02}_{-1.49}$	$-2.12^{+0.52}_{-0.48}$	$30.13^{+1.11}_{-0.79}$
Cluster halo 4	NFW	$3.18^{+0.48}_{-0.28}$	$0.31^{+0.04}_{-0.04}$	$152.04^{+2.86}_{-1.97}$	$3.85^{+0.31}_{-0.39}$	$67.18^{+0.58}_{-0.61}$	$49.61^{+0.61}_{-0.57}$
Cluster halo 5	NFW	$1.51^{+0.08}_{-0.13}$	[0.32]	[174.30]	[10.00]	[129.13]	[77.20]
Cluster halo 6	NFW	$0.56^{+0.13}_{-0.13}$	$0.19^{+0.23}_{-0.12}$	$105.68^{+1.57}_{-2.84}$	$2.39^{+0.53}_{-0.55}$	[−19.33]	[−21.66]
Cluster halo 7	NFW	$1.20^{+0.16}_{-0.19}$	$0.55^{+0.04}_{-0.04}$	$129.81^{+1.33}_{-1.61}$	$3.56^{+0.49}_{-0.53}$	[108.64]	[45.46]
Cluster halo 8	NFW	$0.14^{+0.02}_{-0.03}$	$0.78^{+0.02}_{-0.02}$	$146.46^{+4.24}_{-1.51}$	$2.69^{+0.56}_{-0.68}$	[−10.32]	[−42.04]
Cluster halo 9	NFW	$0.06^{+0.05}_{-0.02}$	$0.76^{+0.03}_{-0.04}$	$133.99^{+4.15}_{-4.48}$	$12.40^{+5.93}_{-4.83}$	$29.63^{+2.05}_{-2.53}$	$-32.35^{+1.20}_{-0.99}$
		σ_*[b] (km s^{-1})	$r_{\mathrm{trun},*}$ (arcsec)	η			
Member galaxies	GALS	$518.64^{+35.12}_{-43.24}$	$7.06^{+2.25}_{-2.08}$	$0.43^{+0.07}_{-0.09}$			
		$z_{s,\mathrm{fid}}$	γ	θ_γ (deg)			
External perturbation	PERT	[2.00]	$0.12^{+0.00}_{-0.01}$	$51.13^{+1.49}_{-0.90}$			
		$z_{s,\mathrm{fid}}$	ϵ	θ_ϵ (deg)	m	n	
Multipole perturbation 1	MPOLE	[2.00]	$0.02^{+0.00}_{-0.00}$	$42.99^{+2.36}_{-7.54}$	[3.00]	[2.00]	
Multipole perturbation 2	MPOLE	[2.00]	$0.01^{+0.00}_{-0.00}$	$8.54^{+2.99}_{-1.74}$	[4.00]	[2.00]	
Multipole perturbation 3	MPOLE	[2.00]	$0.01^{+0.00}_{-0.00}$	$20.00^{+1.44}_{-1.75}$	[5.00]	[2.00]	

Note. — Numbers in square brackets are fixed during the model optimization.

[a]Coordinates are relative to the brightest cluster galaxy position in the MACS J0717.5+3745 field (R.A. = 109.3982391, decl. = +37.7457307).

[b]The normalization luminosity L^* corresponds to $i_{814} = 17.16$.

and consistency with our mass model. The spectroscopic redshift of system 1 is updated, and 19 redshifts are newly determined for systems 2, 5, 8, 10, 22, 24, 26, 30, 31, 33, 34, 39, 40, 41, 42, 47, 61, 63, and 147. We add a mass component representing a multipole perturbation in order to better fit the observations. While the image plane rms increases by 0.″05, the reduced χ^2 slightly decreases by 0.01 compared to our version 3 model.

As noted above, we conservatively exclude some multiple images in the literature. As a result, we have 45 multiple image systems from the literature for our mass modeling. The total number of multiple images is 132. The positional uncertainty of $\sigma_x = 0.''4$ is assumed for all of them.

In addition we include a magnification constraint at the position of the type Ia supernova HFF14Tom at $z = 1.3457$ (Rodney et al., 2015). The magnification of the HFF14Tom is estimated by a careful cosmology-independent analysis to be $\mu = 2.03 \pm 0.29$. We use this constraint by adding a term to the total χ^2 (Equation 3.1).

Table 3.5. Mass Model Parameters for MACS J1149.6+2223

Component	Model	Mass ($10^{14}\ h^{-1}M_\odot$)	e	θ_e (deg)	c	Δx[a] (arcsec)	Δy[a] (arcsec)
Cluster halo 1	NFW	$8.26^{+1.52}_{-1.83}$	$0.49^{+0.02}_{-0.02}$	$126.37^{+1.31}_{-1.28}$	$3.82^{+0.34}_{-0.25}$	$-0.21^{+0.15}_{-0.16}$	$-0.12^{+0.10}_{-0.10}$
Cluster halo 2	NFW	$1.61^{+0.59}_{-0.46}$	$0.67^{+0.09}_{-0.14}$	$76.36^{+7.39}_{-6.88}$	$6.66^{+2.75}_{-2.16}$	[16.38]	[47.36]
Cluster halo 3	NFW	$0.64^{+0.75}_{-0.34}$	$0.70^{+0.05}_{-0.06}$	$158.13^{+3.19}_{-4.23}$	$2.57^{+1.50}_{-0.85}$	$-22.93^{+1.04}_{-0.68}$	$-32.21^{+1.31}_{-1.26}$
Cluster halo 4	NFW	$0.16^{+0.04}_{-0.03}$	$0.68^{+0.08}_{-0.10}$	$150.23^{+2.05}_{-2.71}$	[10.00]	[−44.77]	[−54.86]
		σ_*[b] (km s^{-1})	$r_{\rm trun,*}$ (arcsec)	η			
Member galaxies	GALS	$233.07^{+21.42}_{-16.80}$	$2.88^{+1.07}_{-0.65}$	$0.26^{+0.08}_{-0.04}$			
		σ (km s^{-1})	e	θ_e (deg)	$r_{\rm trun}$ (arcsec)	Δx[a] (arcsec)	Δy[a] (arcsec)
Member galaxy[c]	PJE	$232.08^{+25.96}_{-17.38}$	[0.30]	[47.50]	$1.26^{+0.54}_{-0.38}$	[3.22]	[−11.11]
		$z_{s,\rm fid}$	γ	θ_γ (deg)			
External perturbation	PERT	[2.00]	$0.04^{+0.02}_{-0.01}$	$82.76^{+9.28}_{-7.17}$			
		$z_{s,\rm fid}$	ϵ	θ_ϵ (deg)	m	n	
Multipole perturbation	MPOLE	[2.00]	$0.02^{+0.00}_{-0.00}$	$165.09^{+4.04}_{-3.37}$	[3.00]	[2.00]	

Note. — Numbers in square brackets are fixed during the model optimization.

[a]Coordinates are relative to the brightest cluster galaxy position in the MACS J1149.6+2223 field (R.A. = 177.3987491, decl. = +22.3985308).

[b]The normalization luminosity L^* corresponds to $i_{814} = 18.80$.

[c]This component corresponds to the member galaxy that produces four multiple images S1–S4 of SN Refsdal.

Table 3.6. Mass Model Parameters for Abell S1063

Component	Model	Mass ($10^{14}\ h^{-1}M_\odot$)	e	θ_e (deg)	c	Δx[a] (arcsec)	Δy[a] (arcsec)
Cluster halo 1	NFW	$11.47^{+0.99}_{-1.05}$	$0.46^{+0.01}_{-0.01}$	$53.38^{+0.33}_{-0.35}$	$5.15^{+0.25}_{-0.19}$	$-0.53^{+0.16}_{-0.15}$	$0.27^{+0.20}_{-0.17}$
Cluster halo 2	NFW	$0.47^{+0.14}_{-0.16}$	$0.77^{+0.02}_{-0.06}$	$70.84^{+2.30}_{-2.03}$	$2.92^{+1.57}_{-0.61}$	[−84.67]	[45.07]
Cluster halo 3	NFW	$0.04^{+0.02}_{-0.01}$	$0.62^{+0.06}_{-0.11}$	$102.80^{+5.63}_{-5.38}$	$7.94^{+2.48}_{-2.11}$	$16.02^{+1.23}_{-0.89}$	$-17.23^{+0.66}_{-0.54}$
		σ_*[b] (km s^{-1})	$r_{\rm trun,*}$ (arcsec)	η			
Member galaxies	GALS	$130.39^{+8.45}_{-7.39}$	$173.91^{+186.37}_{-72.16}$	$0.57^{+0.51}_{-0.22}$			
		$z_{s,\rm fid}$	$\gamma \times 10^2$	θ_γ (deg)			
External perturbation	PERT	[2.00]	$3.93^{+0.72}_{-0.69}$	$37.58^{+3.16}_{-4.20}$			

Note. — Numbers in square brackets are fixed during the model optimization.

[a]Coordinates are relative to the brightest cluster galaxy position in the Abell S1063 field (R.A. = 342.1832095, decl. = −44.5308829).

[b]The normalization luminosity L^* corresponds to $i_{814} = 18.19$.

Table 3.7. Mass Model Parameters for Abell 370

Component	Model	Mass ($10^{14}\ h^{-1}M_\odot$)	e	θ_e (deg)	c	Δx[a] (arcsec)	Δy[a] (arcsec)
Cluster halo 1	NFW	$0.70^{+0.22}_{-0.18}$	$0.50^{+0.06}_{-0.06}$	$5.80^{+4.00}_{-3.40}$	$10.05^{+3.42}_{-2.00}$	$3.69^{+0.69}_{-0.66}$	$-5.24^{+1.42}_{-1.93}$
Cluster halo 2	NFW	$16.57^{+6.82}_{-6.27}$	$0.28^{+0.06}_{-0.07}$	$154.22^{+11.20}_{-21.52}$	$1.62^{+0.31}_{-0.28}$	$-17.10^{+2.97}_{-3.63}$	$-4.55^{+2.37}_{-2.13}$
Cluster halo 3	NFW	$0.40^{+0.82}_{-0.27}$	$0.43^{+0.19}_{-0.32}$	$15.44^{+9.03}_{-6.18}$	$6.85^{+3.50}_{-1.84}$	$-6.55^{+0.82}_{-0.82}$	$-24.14^{+1.14}_{-1.11}$
Cluster halo 4	NFW	$1.52^{+0.67}_{-0.43}$	$0.15^{+0.05}_{-0.05}$	$164.13^{+15.39}_{-38.20}$	$8.80^{+2.11}_{-1.60}$	[−5.88]	[−37.21]
		σ_*[b] (km s^{-1})	$r_{\rm trun,*}$ (arcsec)	η			
Member galaxies	GALS	$235.92^{+35.58}_{-26.20}$	$23.60^{+17.36}_{-9.86}$	$1.41^{+0.07}_{-0.15}$			
		$z_{s,\rm fid}$	$\gamma \times 10^2$	θ_γ (deg)			
External perturbation	PERT	[2.00]	$6.55^{+2.25}_{-2.35}$	$177.71^{+4.13}_{-5.64}$			
		$z_{s,\rm fid}$	$\epsilon \times 10^2$	θ_ϵ (deg)	m	n	
Multipole perturbation 1	MPOLE	[2.00]	$1.69^{+0.29}_{-0.30}$	$43.57^{+3.32}_{-2.85}$	[3.00]	[2.00]	
Multipole perturbation 2	MPOLE	[2.00]	$0.85^{+0.17}_{-0.19}$	$12.21^{+3.84}_{-3.00}$	[4.00]	[2.00]	

Note. — Numbers in square brackets are fixed during the model optimization.

[a]Coordinates are relative to the brightest cluster galaxy position in the Abell 370 field (R.A. = 39.969704, decl. = −1.571899).

[b]The normalization luminosity L^* corresponds to $i_{814} = 18.42$.

MACS J0416.1−2403

Multiple images for this cluster have been identified in Zitrin et al. (2013), Jauzac et al. (2014), Diego et al. (2015a), Kawamata et al. (2016), and Caminha et al. (2017). Spectroscopic redshifts of multiple images have been presented in Christensen et al. (2012), Grillo et al. (2015a), Caminha et al. (2017), and Rodney et al. (2017). We also use new spectroscopic redshifts from GLASS (Hoag et al. in prep.; see also Schmidt et al. 2014b and Treu et al. 2015). While Jauzac et al. (2014) estimated the redshift of system 14 to be $z = 2.0531$, Grillo et al. (2015a) reported that its correct redshift is $z = 1.637$. We adopt the latter as it reproduces its image positions well. We correct the positions of five counterimages, 29.2, 37.3, 40.3, 41.3, and 55.2, and add nine new systems, 74, 78, 82, 83, 89, 90, 91, 93, and 97, and identify four new counterimages, 6.3, 8.3, 34.3, and 50.3.

Here we describe what has been updated from the version 3 model. Considering the results of the MUSE observation by Caminha et al. (2017), we update our model by incorporating 22 positions of multiple images. Specifically, we incorporate systems 26, 58, 67, 92, 94, 95, 96, and 97, among which system 97 is found for the first time in this work. The position of ID 91.3 are corrected. In addition, we incorporate 18 MUSE spectroscopic redshifts that are considered to be reliable based on their qualities and consistency with our mass model. The spectroscopic redshifts incorporated are for systems 26, 33, 25, 38, 44, 47, 48, 49, 51, 55, 58, 67, 86, 91, 94, 95, 96. The image plane rms increases by 0.″06,

and the reduced χ^2 increases by 0.30 compared to our version 3 model.

As a result, we have 66 multiple image systems from the literature and nine new systems for our mass modeling. The total number of multiple images is 202. The positional uncertainty of $\sigma_x = 0\farcs4$ is assumed for all of them.

MACS J0717.5+3745

Multiple images for this cluster have been identified in Zitrin et al. (2009), Limousin et al. (2012), Vanzella et al. (2014), Richard et al. (2014), and Diego et al. (2015b). Spectroscopic redshifts of multiple images have been presented in Limousin et al. (2012), Schmidt et al. (2014b), Vanzella et al. (2014), and Treu et al. (2015). The redshift of system 5 was newly confirmed and those of systems 12 and 13 were updated by GLASS (Schmidt et al., 2014b; Treu et al., 2015). While we use the updated redshift of system 12, we do not use that of system 5 as it is significantly different from our model prediction and that of system 13 as it is less precise than that estimated in Limousin et al. (2012). We assign image 25.4 to system 25, which was regarded as a part of system 5 in Diego et al. (2015b). We add six new counterimages, 25.4, 55.3, 64.3, 64.4, 65.3, and 65.4, and 20 new systems, $66-85$. As a result, we have 40 multiple image systems from the literature and 20 new systems for our mass modeling. The total number of multiple images is 173. As a foreground galaxy located at (R.A. $= 109.405027$, decl. $= +37.739714$) makes a significant contribution to the lensing effect, we independently model this galaxy by an NFW, but at the cluster redshift (Cluster halo 6) because `glafic` does not support multiple lens planes. We assume a positional uncertainty of $\sigma_x = 0\farcs6$, which is larger than those for the other HFF clusters, for all multiple images. The larger positional uncertainty and the large number of mass components are due to the fact that the mass distribution of this cluster appears to be considerably more complicated than the other clusters, presumably due to ongoing multiple mergers (see, e.g., Limousin et al., 2012).

MACS J1149.6+2223

Multiple images for this cluster have been identified in Zitrin & Broadhurst (2009), Smith et al. (2009), Zheng et al. (2012), Rau et al. (2014), Richard et al. (2014), Jauzac et al. (2015b), and Treu et al. (2016). Spectroscopic redshifts of multiple images have been presented in Smith et al. (2009), Jauzac et al. (2015b), Grillo et al. (2015b), and Brammer et al. (in prep.). While Smith et al. (2009) estimated the redshift of system 3 to be $z = 2.497$, a recent study using GMOS and MUSE data (Jauzac et al., 2015b; Grillo et al., 2015b) revised its redshift to be $z = 3.129$, which we adopt in our analysis. The new spectroscopic redshifts of system 13 by GLASS (Brammer et al. in prep.) and systems 4, 14, and 29 by MUSE (Grillo et al., 2015b) are used in our mass modeling (see also Treu et al., 2016). As a result, we have 10 multiple image systems from the literature and 18 new systems, $21-40$, for our mass modeling. We also include additional positional constraints from multiple images of seven knots in a lensed face-on spiral galaxy at $z = 1.488$ as well as four supernova images of SN Refsdal in the lensed spiral galaxy (Kelly et al., 2015). The total number of multiple images is 108 from 36 systems.

In order to accurately predict the reappearance of SN Refsdal image (Oguri, 2015;

Sharon & Johnson, 2015; Diego et al., 2016a; Jauzac et al., 2015b; Grillo et al., 2015b) and its magnification, we follow Oguri (2015) to adopt different positional errors for different multiple images. Specifically, we assume the standard positional error of $\sigma_x = 0\farcs4$ for most multiple images, but use a smaller error of $\sigma_x = 0\farcs2$ for the core and knots of the lensed spiral galaxy, and an even smaller error of $\sigma_x = 0\farcs05$ for the four SN images. A member galaxy located at R.A. = 177.397784, decl. = +22.395446 clearly has a significant impact on the prediction of the quadruple images S1–S4 of SN Refsdal. Thus we model this galaxy separately by a PJE.

Abell S1063

In order to construct a mass model for Abell S1063, we use multiple images identified in Balestra et al. (2013), Monna et al. (2014), Richard et al. (2014), Johnson et al. (2014), Karman et al. (2015), Caminha et al. (2016a,b), Diego et al. (2016a), and Karman et al. (2017). Spectroscopic redshifts of multiple images were obtained in Balestra et al. (2013), Richard et al. (2014), Johnson et al. (2014), Karman et al. (2015), Caminha et al. (2016a), Karman et al. (2017), and the GLASS program (Schmidt et al., 2014b; Treu et al., 2015). In addition, we find three new counterimages and 13 new systems, which sums up to 35 new multiple images. As a result, we use 40 systems from the literature and 13 new systems; the total number of multiple images is 141. The positional uncertainty in the multiple images is assumed to be $\sigma_x = 0\farcs4$ for all of them.

Abell 370

In order to construct a mass model for Abell 370, we use multiple images identified in Richard et al. (2010), Richard et al. (2014), Johnson et al. (2014), Diego et al. (2016b), and Lagattuta et al. (2017). Spectroscopic redshifts of multiple images were obtained in Richard et al. (2010, 2014), Lagattuta et al. (2017), and the GLASS program (Schmidt et al., 2014b; Treu et al., 2015). We correct the positions of four multiple images of IDs 3.3, 8.3, 13.3, and 26.3. In addition, we find two new counterimages and 16 new systems, which sums up to 40 new multiple images. As a result, we use 33 systems from the literature and 16 new systems; the total number of multiple images is 135. The positional uncertainty in the multiple images is assumed to be $\sigma_x = 0\farcs4$ for all of them.

3.2 Mass Modeling Results

3.2.1 The Best-fitting Mass Models

The numbers of input multiple images and mass modeling results of the four HFF clusters are summarized in Table 3.1, and the critical curves of the best-fitting models are shown in Figures 3.1–3.6. Figure 3.7 shows magnification maps for sources at $z = 9$ and the positions of the NFW and PJE components. We provide lists of all multiple images used as constraints in Tables B.1–B.6 in Appendix B. Model parameters and errors from the MCMC for individual clusters are shown in Tables 3.2−3.7. Parameters in square brackets are fixed during the model optimization. Maps of magnification factor, lens

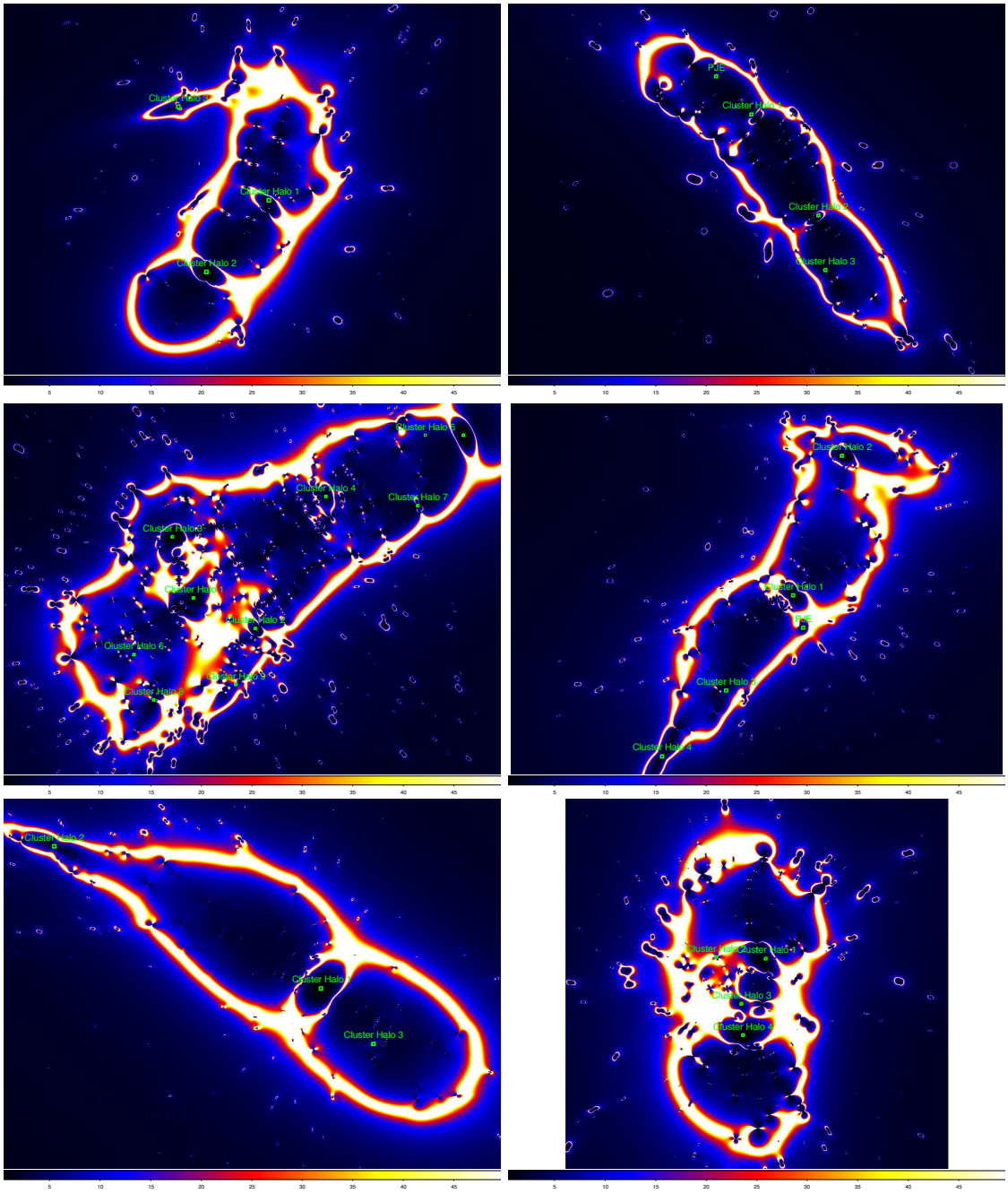

Figure 3.7 Positions of model components are shown on a magnification map for $z = 9$ sources for Abell 2744 (*upper left*), MACS J0416.1−2403 (*upper right*), MACS J0717.5+3745 (*middle left*), MACS J1149.6+2223 (*middle right*), Abell S1063 (*lower left*), and Abell 370 (*lower right*).

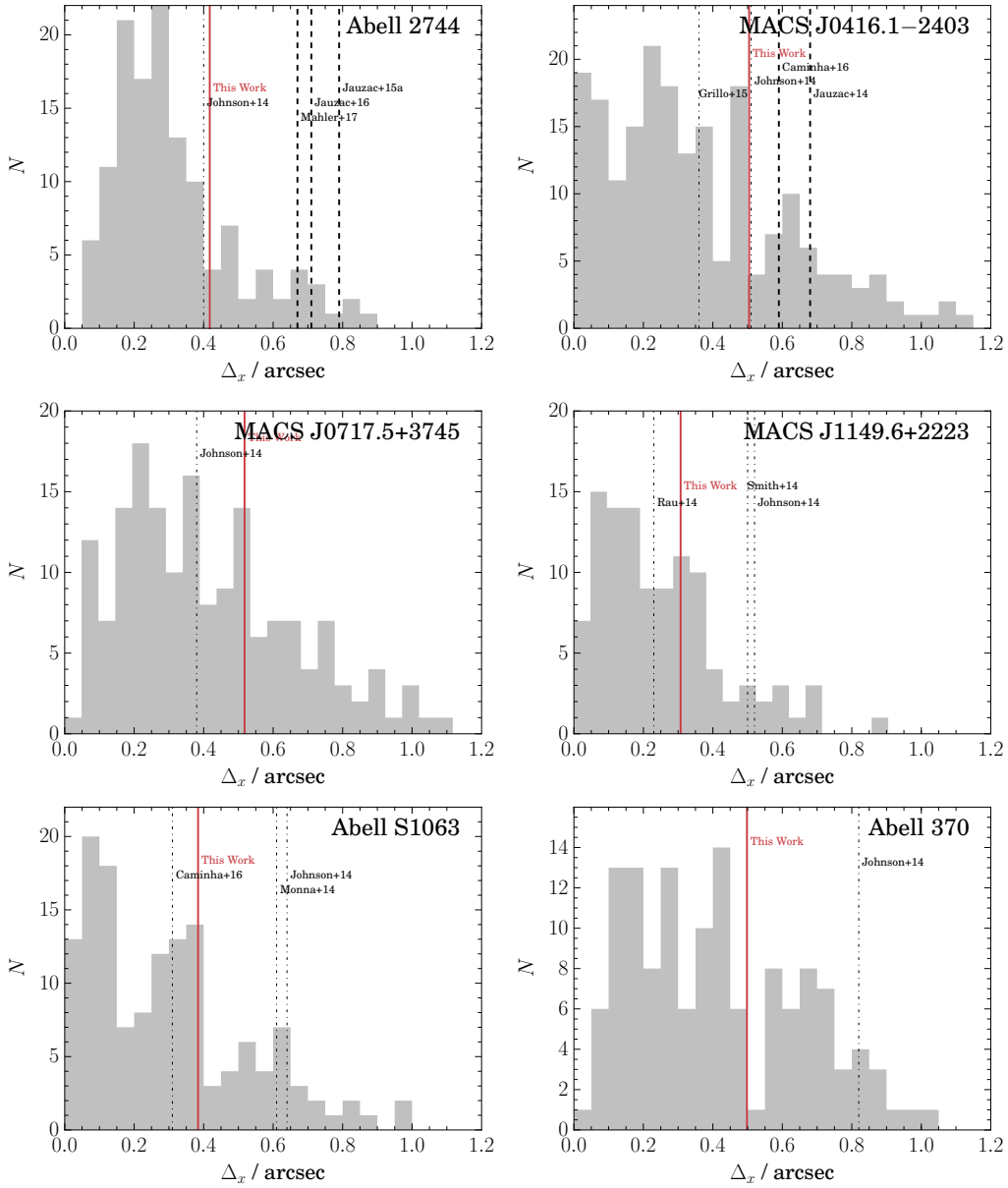

Figure 3.8 The distribution of the distances between observed and model-predicted image positions, $\Delta_x \equiv |\mathbf{x}_{\rm obs} - \mathbf{x}_{\rm model}|$, for all the multiple images used for mass modeling for Abell 2744 (*upper left*), MACS J0416.1−2403 (*upper right*), MACS J0717.5+3745 (*middle left*), MACS J1149.6+2223 (*middle right*), Abell S1063 (*lower left*), and Abell 370 (*lower right*). See Appendix B for lists of multiple images for individual clusters. The red solid, black long-dashed, and black dash-dotted vertical lines show root square means of Δ_x calculated from our models, previous mass models that used more than 100 multiple images, and previous mass models that used less than 100 multiple images, respectively. The root square means of Δ_x for all the clusters are summarized in Table 3.1.

potential, kappa, and shear from our mass modeling will be made available on the STScI website[*2].

Table 3.1 indicates that all of our best-fitting models have reduced chi-square values, χ^2/dof, close to unity. In fact this is expected, because we have chosen the positional errors of multiple images to reproduce $\chi^2/\mathrm{dof} \sim 1$ (see Section 3.1.4 for the specific values). In cluster strong lensing modeling, the positional errors usually originate from the complexity of the lens potential due to, e.g., substructures that is not included by a simply parametrized model, rather than from measurement uncertainties in multiple image positions. A proper choice of positional uncertainties is important for the MCMC to estimate model uncertainties.

It is found that our best-fitting mass models reproduce the positions of multiple images with rms errors of $\sim 0''.4$ (see Table 3.1), which is a significant improvement over previous strong lens modeling (e.g., Broadhurst et al., 2005) and is comparable or even better than other mass models constructed for HFF. For instance, this number should be compared with rms errors of $0''.68$ for MACS J0416.1−2403 (Jauzac et al., 2014) and $0''.79$ for Abell 2744 (Jauzac et al., 2015a) by the CATS team, both of which used more than 100 multiple images as constraints. Grillo et al. (2015a) modeled MACS J0416.1−2403 with rms errors of $0''.36$, but only 30 multiple images were used as constraints. Our mass modeling satisfies both a large number of multiple images and a good accuracy in their reproduced positions.

To illustrate this point further, in Figure 3.8 we plot the distributions of $\Delta_x \equiv |\mathbf{x}_{\rm obs} - \mathbf{x}_{\rm model}|$, the distance between the observed and model-predicted image positions for each multiple image. We find that for any cluster Δ_x is indeed small for most of the multiple images, with a distribution peaking around $0''.2$ and most multiple images having $\Delta_x < 0''.6$, which again indicates the success of our mass modeling.

The accuracy of our mass models may be tested further by observations of other than image positions. For Abell 2744, our model yields a magnification $\mu = 2.38 \pm 0.06$ at the position of the lensed Type Ia supernova HFF14Tom (Rodney et al., 2015). This is fully consistent with the observed magnification $\mu = 2.03 \pm 0.29$, although we note that this may not be a fair comparison as we have explicitly included the observed magnification as a constraint in mass modeling. On the other hand, the time delays and flux ratios of the lensed supernova SN Refsdal (Kelly et al., 2015) in MACS J1149.6+2223 can provide a useful blind test of our mass model. We will discuss this blind test in Section 3.2.3.

As shown in Tables 3.2−3.7, some NFW components have high ellipticities ($e > 0.7$). There are presumably two reasons for this. The first reason is that the intrinsic mass distribution is indeed highly elongated, which is not surprising given the axis-ratio distribution of simulated dark matter halos (e.g., Jing & Suto, 2002). In some cases, such as Cluster halos 2 and 9 in MACS J0717.5+3745, such a high elongation is also implied by aligned positions of nearby member galaxies. The second reason may be an insufficient number of multiple images around the position of the NFW component. If multiple images are unevenly distributed around an NFW component, the model parameters can

[*2] `https://archive.stsci.edu/prepds/frontier/lensmodels/`

sometimes be biased toward the local potential, around where the multiple images are observed. This is the case for Cluster halo 3 in the Abell 2744 field and Cluster halo 8 in the MACS J0717.5+3745 field. In the case of Cluster halo 3 in the Abell 2744 field, an additional NFW component is required besides the GALS component so that the positions of the multiple images located 20 arcsec southwest are well reproduced. However, this component is optimized to have a higher ellipticity than the actual galaxy light distribution presumably because of the small number of multiple images around it to constrain its parameters.

3.2.2 Model Comparison

Some teams have also constructed precise mass models exploiting the full-depth HFF data and more than 100 multiple images. We here compare our best-fitting mass models with those obtained in previous work. A thorough comparison between mass models of Abell 2744 and MACS J0416.1−2403 by all modeling teams has been conducted in Priewe et al. (2017).

Abell 2744 — We place three cluster-scale NFW components to model the cluster mass distribution. The positions of Cluster halos 1 and 2 are consistent with those in Jauzac et al. (2015a) and Mahler et al. (2018). Wang et al. (2015), who adopt a free-form modeling method, also predict mass peaks at these positions. In addition, we assume a third NFW component, Cluster halo 3, as described above, where there is also a mass peak in Wang et al.'s (2015) model.

MACS J0416.1−2403 — We place three cluster-scale NFW components and one PJE component. The PJE component is for better modeling of the member galaxy near systems 1, 2, 6, 89, and 90, as this member has a significant effect on these multiple image systems. The positions of Cluster halos 1 and 2 are consistent with those in Jauzac et al. (2014), Diego et al. (2015a), and Caminha et al. (2017), but the PJE component is included only in our model. While Jauzac et al. (2014), Diego et al. (2015a), and Caminha et al. (2017) assume only two halo components, there is a "soft component" in the model of Diego et al. (2015a) at the position of our Cluster halo 3.

MACS J0717.5+3745 — Limousin et al. (2015) use four halo-scale profiles. Diego et al. (2015b) also identify four mass peaks in their free-form model. While we place nine cluster-scale NFW components, only four, Cluster halos 1+3, 2, 4, and 5, have a significant mass peak. This is consistent with their results. Limousin et al. (2015) report very shallow mass profiles for this cluster, which is consistent with our NFW components having relatively smaller concentration parameters. We note that the position of Cluster halo 9 is consistent with an X-ray emission peak from *Chandra* (see Figure 4 in Diego et al., 2015b). Interestingly, our PERT component has been recently suggested to describe line of sight structure at $z > 2$ by Williams et al. (2017).

MACS J1149.6+2223 — We place four cluster-scale NFW components and one PJE component. The positions of Cluster halos 1, 2, and 3 are consistent with those in Jauzac et al. (2015b). They do not place a component at the position of Cluster halo 4. On the other hand, they place a halo component at the position of a bright member galaxy

located ~ 100 arcsec north from the BCG and is out of the region of the HFF WFC3/IR observation.

Abell S1063 — We place three cluster-scale NFW components. The position of Cluster halo 1 is consistent with that in Caminha et al. (2016a), who utilize only 48 multiple images. They do not place components at the positions of Cluster halos 2 and 3. On the other hand, they place a dual pseudo-isothermal elliptical component at the position of the BCG. Diego et al. (2016a) also identify moderate three mass peaks in their free-form model, which is consistent with our NFW components.

Abell 370 — We place four cluster-scale NFW components. The position of Cluster halo 4 is consistent with that in Lagattuta et al. (2017), who utilize only 75 multiple images. They also place two halo components around the positions of Cluster halos 1 and 2. They do not have a mass peak at the position of Cluster halo 3. On the other hand, Diego et al. (2016b) identify a mass peak in their free-form model at the position of Cluster halos 3.

3.2.3 Predictions for SN Refsdal

In our mass modeling of MACS J1149.6+2223, we only use positions of the multiple images S1–S4 of SN Refsdal as observational constraints. Importantly, when our mass modeling was completed, any relative time delays and magnifications had not been measured yet, which indicates that observations of relative time delays and magnifications serve as an important *blind* test of our mass model. Treu et al. (2016) made a detailed comparison of predictions of our best-fitting model (corresponding to the short name "Ogu-a" in Treu et al. 2016) with those from other mass modeling teams. Treu et al. (2016) also compared predictions of relative magnifications and time delays between images S1–S4 with preliminary measurements, finding a good agreement between our best-fit model predictions and observations. Updated measurements and comparisons are available in Rodney et al. (2016).

Most mass models of MACS J1149.6+2223 predict two additional images of SN Refsdal around images 1.2 and 1.3, which we call SX and SY following Oguri (2015). SX is predicted to appear approximately one year after S1–S4, whereas SY is predicted to have appeared a decade ago. Our refined model predictions for the time delay, position, and magnification factor of SX are $\Delta t_{\rm SX} = 336^{+22}_{-20}$ days, $x_{\rm SX} = -4.16^{+0.08}_{-0.07}$ arcsec, $y_{\rm SX} = -6.50^{+0.08}_{-0.08}$ arcsec, and $\mu_{\rm SX} = 4.23^{+0.32}_{-0.31}$, where $\Delta t_{\rm SX}$ is the relative time delay from the image S1, $x_{\rm SX}$ and $y_{\rm SX}$ are coordinates relative to the BCG. The predicted time delay, position, and magnification factor of SY are $\Delta t_{\rm SY} = -6229^{+209}_{-227}$ days, $x_{\rm SY} = -16.7^{+0.08}_{-0.08}$ arcsec, $y_{\rm SY} = 12.8^{+0.12}_{-0.12}$ arcsec, and $\mu_{\rm SY} = 3.52^{+0.19}_{-0.17}$.

While Kawamata et al. (2016), where we have made the predictions for SN Refsdal, was under review, a new SN image was discovered in *HST* images taken on 2015 December 11 (Kelly et al., 2016). The observed position of the image is $x = -4.43$ arcsec and $y = -6.62$ arcsec, which is fully consistent with the predicted position of SX with offsets from the predicted position only 0.27 arcsec to the east and 0.12 arcsec to the south. Furthermore, as can be seen in Figure 2 in Kelly et al. (2016), our time delay and magnification predictions on SX are fully consistent with the observed values. We again emphasize that these

predictions are made before the reappearance of the new image. These blind test results support the validity and accuracy of our mass modeling method.

3.3 Multiple Image Candidates

Our analysis suggests that some dropout galaxies are multiply imaged. Among them, reliable ones have been included in our mass modeling; systems 28, 46, and 54 in Abell 2744 field; systems 6, 90, 91, 92, and 97 in MACS J0416.1−2403 field; systems 19 and 66 in MACS J0717.5+3745 field; systems 33, 38, and 39 in MACS J1149.6+2223 field; systems 11, 34, 47, and 48 in Abell S1063 field; and systems 14, 18, and 38 in Abell 370 field (see Section 3.2). Here we discuss several interesting reliable multiple images and multiple image candidates at $z \sim 9$.

HFF2C-i2, -i3, -i7, and -i16 — We refer to the galaxies of HFF2C-1148-3434, -1131-3400, -1220-3595, and -1045-3324 as HFF2C-i2, -i3, -i7, and -i16, respectively, following Kawamata et al. (2016). These are newly identified multiple images in MACS J0416.1−2403 field. HFF2C-i2 and -i16 compose system 91, and HFF2C-i3 and -i7 compose system 92. They are placed in the most northeast part of this cluster and improve mass modeling in this region.

HFF4C-YJ1 and HFF4C-YJ3 — We refer to the galaxies of HFF4C-3358-4457 and HFF4C-3373-4483 as HFF4C-YJ1 and HFF4C-YJ3, respectively, following Kawamata et al. (2016). HFF4C-YJ1 is a bright $z \sim 9$ galaxy candidate in MACS J1149.6+2223 discovered by Zheng et al. (2012). We find a faint $z \sim 9$ galaxy candidate, HFF4C-YJ3, close to this galaxy (see Figure 3.9). Our best-fitting mass model has a critical curve that is placed near these galaxies. Therefore, it is possible that these two galaxies are in fact multiple images of a $z \sim 9$ galaxy. The reliability of this multiple image system is not very high, because there are not many known multiple images around this system, and therefore our mass model in this region includes relatively large uncertainties. The $JH_{140} - H_{160}$ colors of YJ1 and YJ3 are 0.24 ± 0.04 and 0.16 ± 0.23, respectively, and are consistent with being multiple images.

HFF4C-YJ4 — We refer to the galaxies of HFF4C-3617-3327 as HFF4C-YJ4 following Kawamata et al. (2016). This is a $z \sim 9$ galaxy in MACS J1149.6+2223 near the critical curve. We find another faint red galaxy nearby this galaxy (see Figure 3.9). The color of this faint red galaxy is consistent with being at $z \sim 9$, but it is below the detection limit used for the dropout selection. The relative positions of these two galaxies are fully consistent with being multiple images of a single $z \sim 9$ galaxy. Given its high reliability, we include the positions of these galaxies as constraints in our mass modeling as system 38. The $JH_{140} - H_{160}$ colors of YJ4 and the faint red galaxy are -0.15 ± 0.24 and 0.19 ± 0.24, respectively. This is consistent with being multiple images.

Even if these galaxy pairs are not real multiple images of single galaxies, the close separations are interesting in term of galaxy formation and evolution.

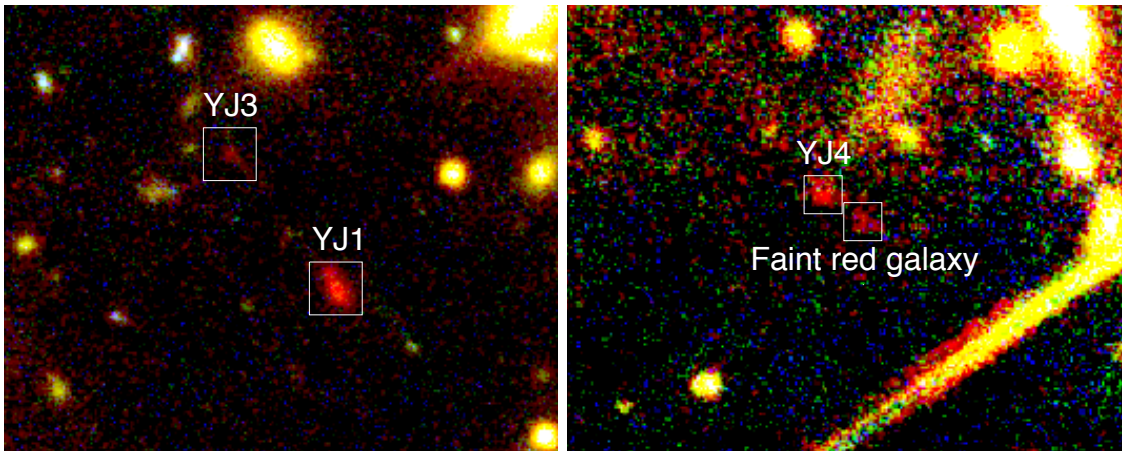

Figure 3.9 Color-composite images of the multiple image candidates, HFF4C-YJ1 and HFF4C-YJ3 (*left panel*), and of HFF4C-YJ4 and its companion (*right panel*). *Left*: HFF4C-YJ1 and HFF4C-YJ3 may be distorted in the direction of the shear at that position. *Right*: A faint red galaxy is located very close to HFF4C-YJ4, and its position is consistent with being a counterimage of HFF4C-YJ4.

3.4 Summary

We have conducted precise mass modeling of all six HFF clusters, exploiting the full depth HFF data and the latest spectroscopic follow-up results, including those by MUSE observations, on multiple images. We have used the positions of 132, 202, 173, 108, 141, and 135 multiple images to constrain the matter distributions of Abell 2744, MACS J0416.1−2403, MACS J0717.5+3745, MACS J1149.6+2223, Abell S1063, and Abell 370, respectively. Among them, 182 multiple images are new systems identified in this thesis. We assume simply parametrized mass models and optimize model parameters with the public software `glafic` (Oguri, 2010). We have found that our best-fitting mass models reproduce the observed positions of multiple images quite well, with image plane rms of $\sim 0\farcs4$ (see Table 3.1). For Abell 2744, our best-fitting mass model recovers the observed magnification at the position of the Type Ia supernova HFF14Tom (Rodney et al., 2015), although we note that we have explicitly included this magnification as a constraint in mass modeling. We have found that the predicted time delays and flux ratios of the quadruple images of SN Refsdal (Kelly et al., 2015) in MACS J1149.6+2223 are consistent with observations (Treu et al., 2016). A thorough comparison between mass models of Abell 2744 and MACS J0416.1−2403 by all modeling teams can be found in Priewe et al. (2017).

Chapter 4

Simultaneous Derivation of the Size–luminosity Relations and UV Luminosity Functions

4.1 Size and Magnitude Measurements

4.1.1 Two-dimensional Profile Fitting

In this subsection, we estimate lensing-corrected, i.e., intrinsic, sizes and magnitudes of the dropout galaxies.

The lensing effects are calculated using the software `glafic` v1.2.7 (Oguri, 2010). For the mass distributions of Abell 2744, MACS J0416.1−2403, Abell S1063, and Abell 370, we use our version 4 mass models, while for MACS J0717.5+3745 and MACS J1149.6+2223, we use our version 3 mass models. Modeling details are described in Chapter 3. All of the mass models are available on the Space Telescope Science Institute website[*1]. The uncertainty in each magnification factor is calculated from ten-thousand models sampled from a Markov chain Monte Carlo (MCMC) chain (see Section 4.1.2). This uncertainty is smaller than the scatter in magnification factors among all modeling teams' models. The typical scatters are 30% at $\mu \sim 2$ and 70% at $\mu \sim 40$ as reported in Priewe et al. (2017), who have conducted a thorough comparison between the mass maps of Abell 2744 and MACS J0416.1−2403 by all modeling teams (see also Meneghetti et al., 2017). The smaller uncertainties in our models are due to limited flexibilities inherent in parametric modeling methods, while the predicted magnification factors are consistent with those by the other teams (see Figures 10–11 and 12–13 in Priewe et al., 2017).

The method to measure intrinsic sizes and magnitudes is identical to that in K15. However, while the measurements in K15 were conducted only for bright galaxies, here we deal with all the galaxies in the samples. We fit a Sérsic profile to a galaxy image in an $8\farcs4 \times 8\farcs4$ cutout image using a two-dimensional fitting algorithm conducted by the

[*1] `https://archive.stsci.edu/prepds/frontier/lensmodels/`

command `optimize` in `glafic`, which simultaneously corrects for the lensing and point-spread function (PSF) effects. In order to correct for the lensing effects, an ellipsoidal Sérsic profile on the source plane is lensed onto the image plane, and the galaxy image is fitted with the lensing-distorted Sérsic profile. In order to correct for the PSF effects, the lensing-distorted Sérsic profile is convolved with an average stellar image on the image plane, which is generated by stacking 5–20 stars found in each field. The Sérsic profile is defined as

$$\Sigma(x, y; e, \theta) = \Sigma_0 \exp\left[-b_n \left(\frac{\sqrt{\tilde{x}^2/(1-e) + (1-e)\tilde{y}^2}}{r_{\rm e}}\right)^{1/n}\right], \tag{4.1}$$

where $\Sigma(r)$, Σ_0, b_n, $r_{\rm e}$, and n represent the surface brightness profile, surface brightness at $r = 0$, parameter to convert the scale radius to the half-light radius, circularized half-light radius, and Sérsic index, respectively. The ellipticity e and position angle θ are introduced by a simple variable transformation (see Oguri, 2010, for details) and

$$\tilde{x} = x\cos\theta + y\sin\theta \tag{4.2}$$

$$\tilde{y} = -x\sin\theta + y\cos\theta. \tag{4.3}$$

In what follows, $r_{\rm e}$ means the circularized half-light radius, $r_{\rm e}^{\rm maj}\sqrt{1-e}$, where $r_{\rm e}^{\rm maj}$ is the radius along the major axis. The magnitude is calculated from $r_{\rm e}$ and Σ_0. During the fitting, the Sérsic index is fixed to $n = 1$ and the maximum ellipticity is set to 0.9. A uniform sky background is assumed, and the normalization is optimized at the same time. When nearby objects may introduce any bias to the fitting result, we mask these objects or add additional profiles to fit the nearby objects simultaneously. The fittings are conducted using the *YJJH*, *JJHH*, and *JHH* combined images at $z \sim 6-7$, 8, and 9, respectively. Although we have already constructed in K15 size samples from the Abell 2744 cluster and parallel fields, we conduct the fittings again because there are updates on the mass map of the cluster. The obtained morphological properties and magnitudes are presented in Tables C.1–C.3 in Appendix C. The fitting results for galaxies fainter than -18 mag are also graphically shown in Figures C.1 and C.2 in Appendix C.

4.1.2 Error Estimations

In this subsection, we evaluate errors in the measured sizes and magnitudes following the method in K15, but in a more efficient way. We consider two sources of errors: errors in the fitting procedure and errors in the mass map.

There are two types of errors in the fitting procedure. One is a systematic bias, by which the sizes and magnitudes of larger (smaller) galaxies are underestimated (overestimated). The other is a random error, which arises from random sky noise that disperses the estimated size and magnitude. In order to estimate these errors, we conduct a Monte Carlo simulation, in which we bury simulated galaxies in a real image and perform the same fitting procedure as for real dropout galaxies. Since these systematic and random errors are primarily dependent on the galaxy apparent magnitude, apparent radius, and

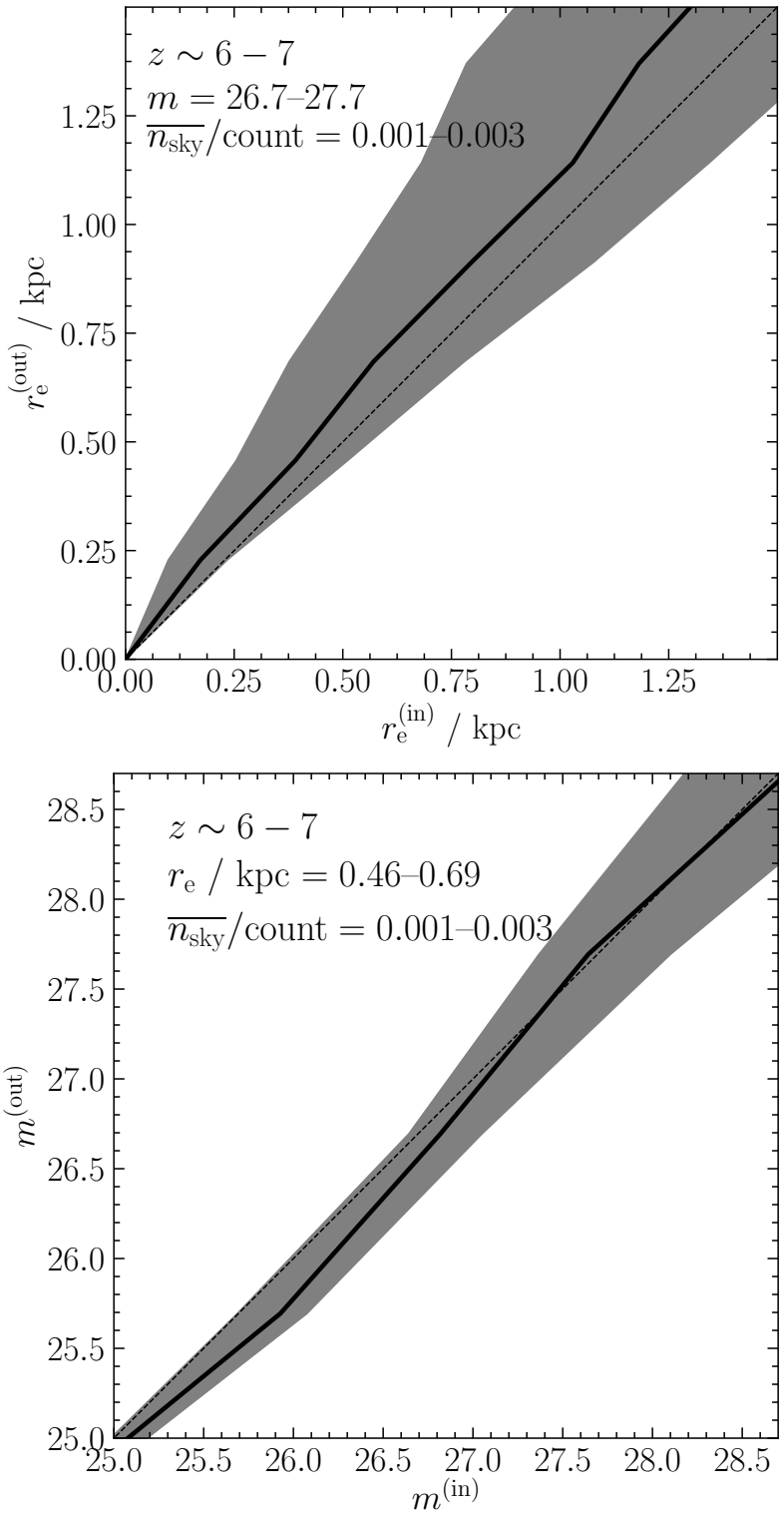

Figure 4.1 Examples of the Monte Carlo simulations to estimate the systematic and random errors in size and magnitude measurements. The top panel shows the median and 1σ distribution of output radii as a function of input radius for galaxies with an apparent magnitude of $m/\mathrm{mag} = 26.7$–27.7 and for a sky value of $\overline{n_{\rm sky}}/\mathrm{count} = 0.001$–$0.003$. The bottom panel shows the median and 1σ distribution of output magnitudes as a function of input magnitude for galaxies with $r_{\rm e}/\mathrm{kpc} = 0.46$–$0.69$ and for a sky value of $\overline{n_{\rm sky}}/\mathrm{count} = 0.001$–$0.003$. The dashed lines are lines of equality.

sky value in the vicinity, we estimate the two errors as a function of the three parameters. We use the Abell 2744 cluster field image for this derivation and apply the relation to all twelve fields. In detail, first, we select a random position in the image and bury an $n = 1$ Sérsic profile, whose magnitude, radius, ellipticity, and position angle are chosen randomly. Second, we conduct the same procedure on this pseudo-galaxy as for real galaxies. We repeat these two processes until we obtain a sufficient number of measurements in each parameter bin. Third, for each real dropout galaxy, we choose a set of simulated galaxies whose apparent magnitudes, apparent radii, and sky values in the vicinity are close to those of the dropout galaxy. Using the intrinsic magnitudes and radii of the simulated galaxies in this set, we estimate the random errors and correct for the systematic errors in size and magnitude. Examples of the Monte Carlo simulations are presented in Figure 4.1.

Systematic errors in mass maps also affect measurement results. Since the apparent magnitudes and sizes of lensed galaxies are converted into intrinsic values using mass maps, an overestimate of the magnification factor results in an underestimate of the intrinsic sizes and magnitudes, and vice versa. In order to estimate the errors in magnification, we generate an MCMC chain of the mass model parameters using the command `mcmc` in `glafic`. From ten-thousand samples in the chain, we estimate the error in magnification factor at the positions of each dropout galaxy with the `mcmc_calcim` command. For each cluster, one hundred mass maps generated from randomly selected MCMC samples are available on the Space Telescope Science Institute website.

The random errors in size and magnitude due to the fitting procedure and random errors in magnification factor are presented in Tables C.1–C.3.

4.2 Size–luminosity Distributions at $z \sim 6 - 9$

In this section, we first present the distribution of our galaxies on the size–luminosity plane. Then, detection incompleteness is calculated as a function of absolute magnitude and size for each field and redshift range. Finally, we use these incompleteness maps on the size–luminosity plane to simultaneously derive intrinsic size–luminosity relations and luminosity functions for the first time at these redshift ranges.

4.2.1 Galaxy Distribution on the Size–luminosity Plane

Figures 4.2–4.4 show the size–luminosity distributions of our galaxies at $z \sim 6-7$, 8, and 9, together with those from previous studies that adopt two-dimensional profile fittings in size measurements. The error bars include the errors in the fitting process and our mass maps. Our samples occupy either the same regions as the previous samples or their reasonable extrapolations toward much fainter magnitudes.

As summarized in Tables C.1–C.3, some galaxies are multiply imaged on the image plane. The physical parameters of these galaxies are calculated by averaging over the multiple images. The numbers of independent galaxies with size measurements are thus reduced to 334, 61, and 37 at $z \sim 6-7$, 8, and 9, respectively. Among them, the numbers of faint ($M_{\rm UV} \gtrsim -18$) galaxies are 83, six, and three, respectively. These numbers should

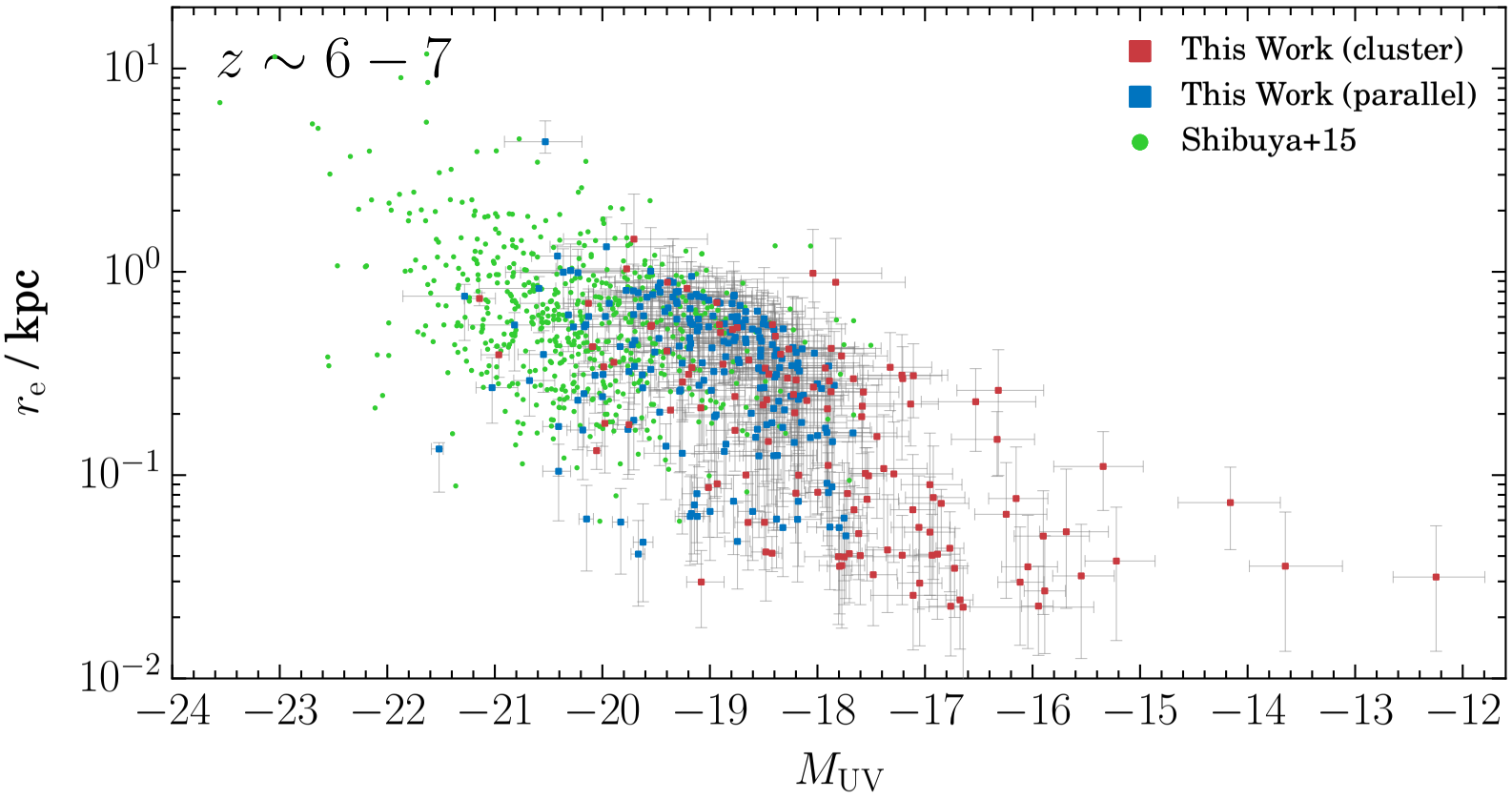

Figure 4.2 Galaxy distributions on the size–luminosity plane at $z \sim 6-7$. The red and blue points represent our galaxies from the cluster fields and parallel fields, respectively. The green points represent galaxies at $z \sim 6-7$ in Shibuya et al. (2015).

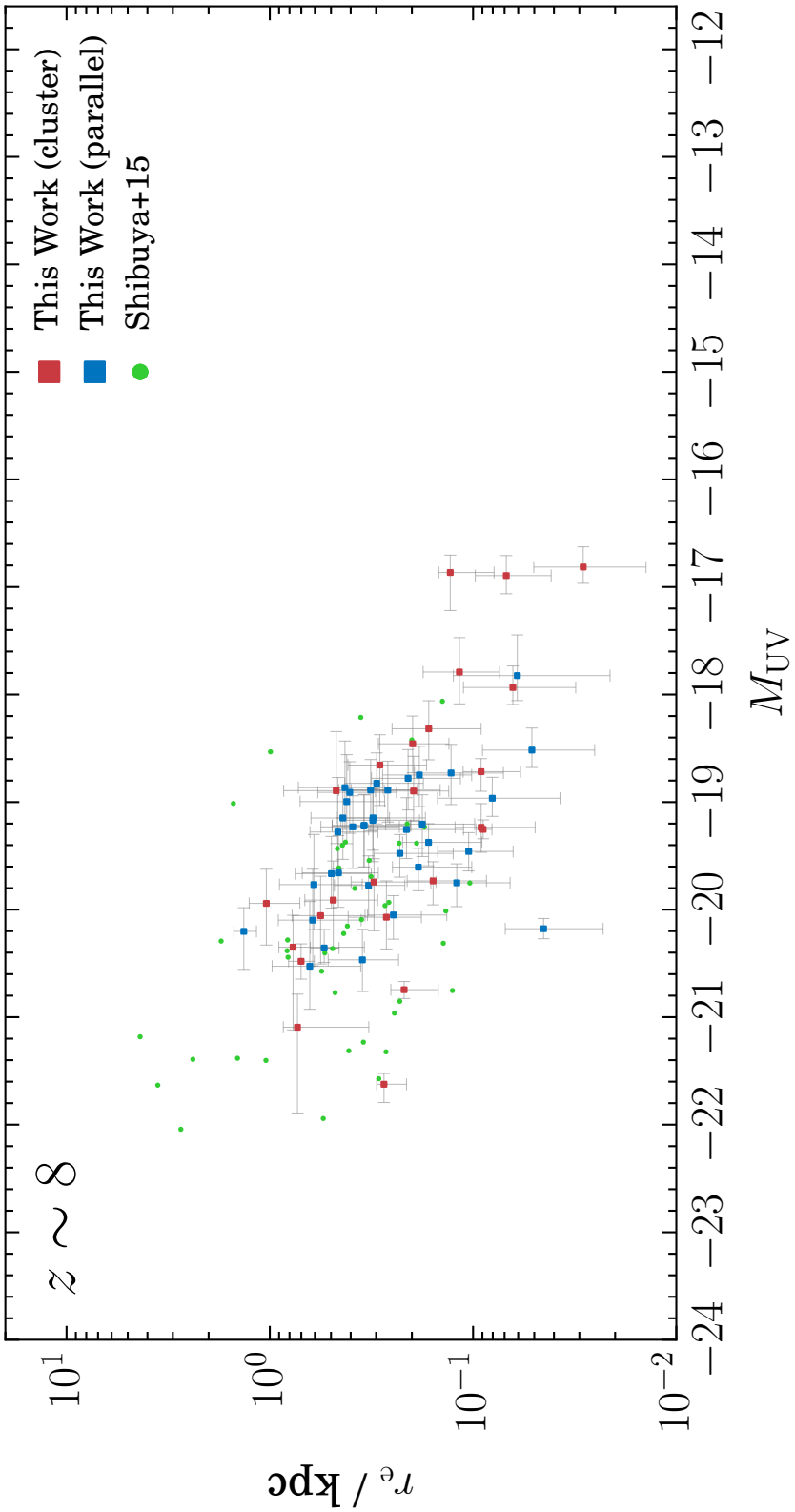

Figure 4.3 Same as Figure 4.2 but for $z \sim 8$.

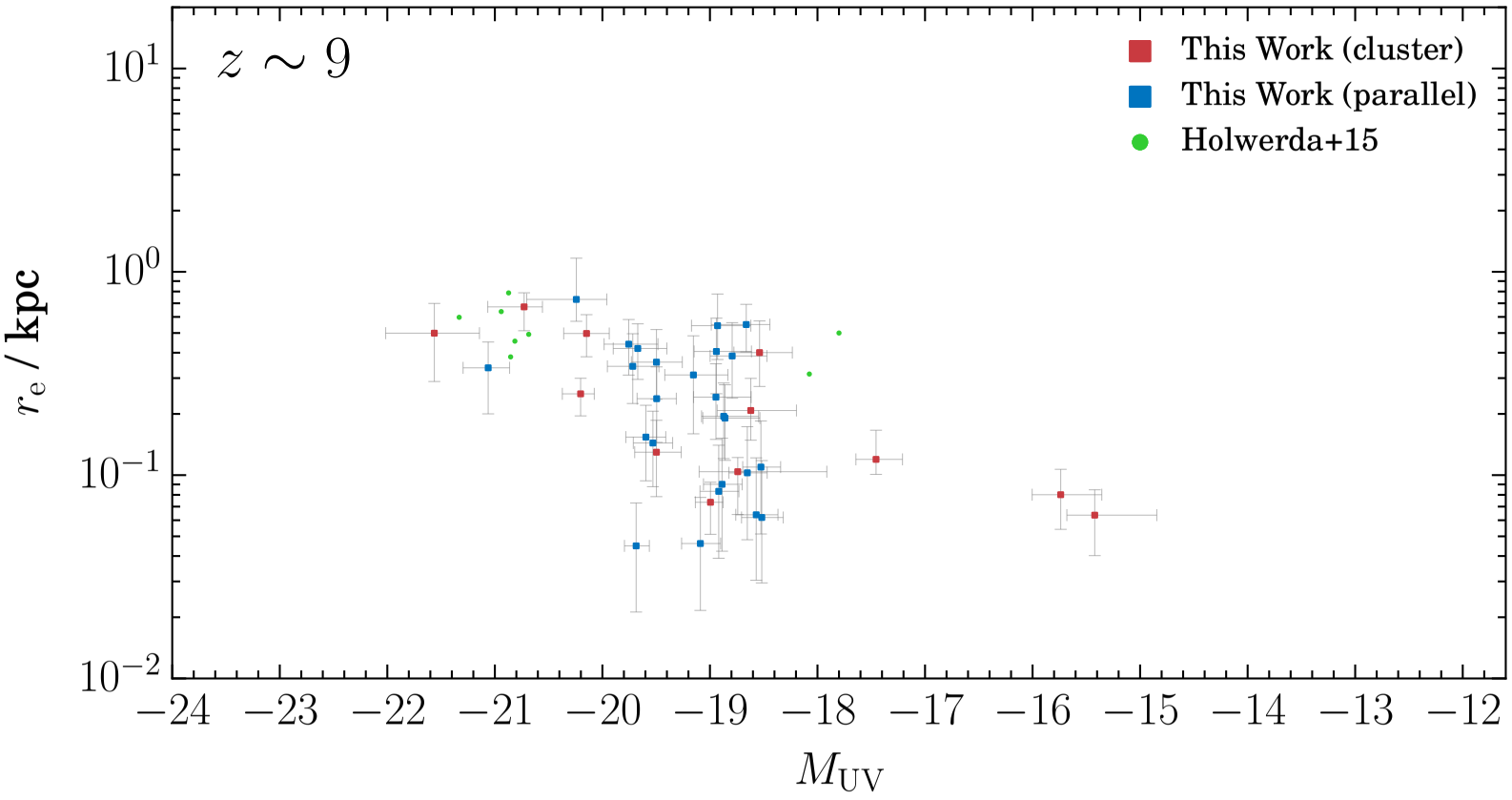

Figure 4.4 Same as Figure 4.2 but for $z \sim 9$. The green points represent galaxies at $z \sim 9$ in Holwerda et al. (2015).

Table 4.1. Number of $M_{\rm UV} \gtrsim -18$ galaxies in the present and previous samples

References	$z \sim 6-7$	$z \sim 8$	$z \sim 9$	Data
This work	91 (350)	7 (64)	3 (39)	Six HFF cluster and parallel fields
Ono et al. (2013)	0 (9)	0 (6)	—	HUDF12
Holwerda et al. (2015)	—	—	1 (8)	XDF and CANDELS
Kawamata et al. (2015)	4 (31)	0 (8)	—	First HFF cluster and parallel fields
Shibuya et al. (2015)	$7+1$ $(422+173)^{a}$	0 (46)	—	CANDELS, HUDF09/12, and first two HFF parallel fields
Bouwens et al. (2017a)	47 (76)	—	—	First two HFF cluster fields

Note. — The number of galaxies in the full sample is shown in parentheses.

[a]Numbers at $z \sim 6$ and 7 are presented.

be compared only with those from previous studies that adopt parametric size measurements such as `GALFIT` (Peng et al., 2002, 2010), not with those based on nonparametric methods such as "curve-of-growth." This is because these two methods rely on different assumptions, which may introduce different biases and therefore make comparisons of the results difficult. At faint magnitude ranges, as investigated in this work, previous studies that adopt parametric size measurements are Ono et al. (2013), K15, Holwerda et al. (2015), Shibuya et al. (2015), and Bouwens et al. (2017a) (see also Oesch et al., 2010a). The numbers of galaxies in our samples and in the previous studies are presented in Table 4.1. For $z \sim 6-7$ and 9, the addition of our samples increases the numbers of faint ($M_{\rm UV} \gtrsim -18$) galaxies with size measurements about 2.5 and 4 times, respectively. For $z \sim 8$, our sample is the first that contains faint galaxies with size measurements. The faintest objects among the previous samples have $M_{\rm UV} \simeq -14.48$ (Bouwens et al., 2017a), -18.1 (Shibuya et al., 2015), and -17.8 (Holwerda et al., 2015) at $z \sim 6-7$, 8, and 9, respectively. We push the faint limits down to $M_{\rm UV} \simeq -12.3$, -16.8, and -15.4 at $z \sim 6-7$, 8, and 9, respectively.

4.2.2 Completeness Estimation

For a given total magnitude, galaxies with larger sizes are less likely to be detected in observations because of their low surface brightnesses. Since this effect is more prominent for fainter objects, observed size–luminosity relations can become significantly steeper than intrinsic ones. We conduct the following Monte Carlo simulations to calculate detection completeness as a function of absolute magnitude and size. The detection completeness is defined as the fraction of galaxies that are detected and pass the dropout selection described in Section 2.2.2. (1) We select random positions uniformly on the source plane. (2) For each position, we generate an artificial galaxy with a certain size and magnitude and place it, taking the lensing and PSF effects into account, into the combined image, which is used as the detection image in the catalog construction. The galaxy is modeled with a Sérsic profile of the index $n = 1$. The ellipticity is randomly chosen from a uniform distribution between 0 and 0.9. (3) We run `SExtractor` on the image with artificial

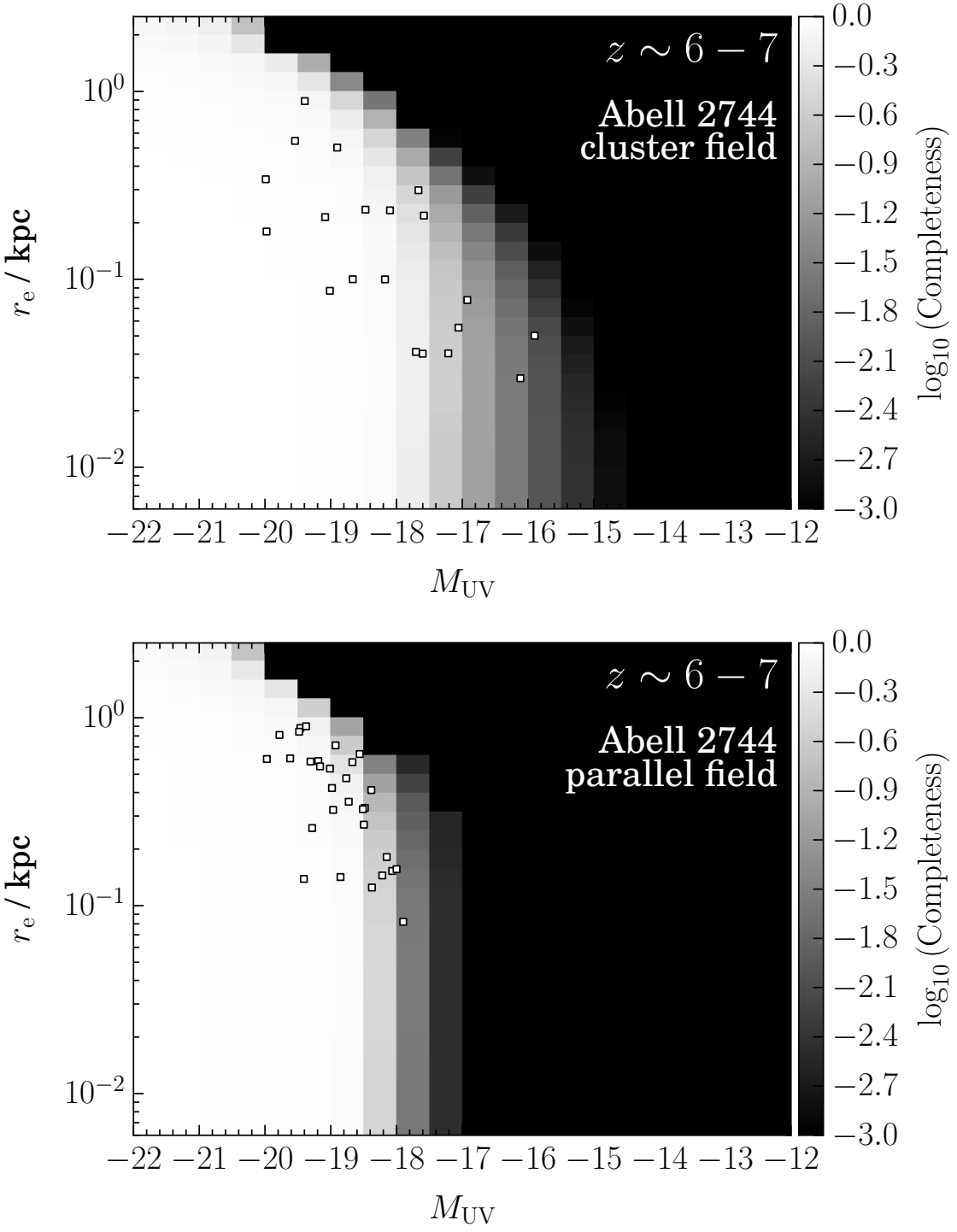

Figure 4.5 Detection completeness at $z \sim 6-7$ as a function of absolute magnitude and size for the Abell 2744 cluster (*top*) and parallel (*bottom*) fields, shown on a logarithmic scale. Galaxies detected in each field are plotted with squares.

galaxies and calculate the fraction of artificial galaxies that are detected by `SExtractor` and bright enough to meet the criteria of dropout selection. (4) We repeat steps (1)–(3), changing the size and magnitude of artificial galaxies. It should be noted that we do not assume any specific spectral energy distribution (SED) shape. This is because, primarily, the completeness is not dependent on the SED shape but only on size and magnitude. As an example, the obtained completeness maps at $z \sim 6-7$ in the Abell 2744 cluster and parallel fields are shown in Figure 4.5. Note that although faint galaxies are bright enough to be detected if highly magnified, their completeness is significantly low because they rarely fall onto highly magnified regions.

As seen in Figure 4.6, the observed size–luminosity distributions can be significantly deformed by incompleteness, which depends on size and luminosity. We discuss the impact of incompleteness on the estimation of the intrinsic size–luminosity relations in Section 4.3.1. In the cluster fields, even galaxies fainter than ~ -18 mag are detected, but with low completeness. For example, at $M_{\rm UV} = -16$, only those with $r_{\rm e} < 0.1$ kpc are included in the samples. This means that while the HFF has opened a window to faint galaxies, it is open only to very small objects. On the other hand, galaxies detected in the parallel fields are limited to ~ -18 mag, but with a relatively high completeness over a wide size range because completeness drops sharply at $M_{\rm UV} \sim -18$. Therefore, the cluster fields require a more careful consideration of incompleteness effects.

4.2.3 Maximum-likelihood Estimation of the Intrinsic Size–luminosity Distribution

In this subsection, we obtain for each of the three redshift ranges the incompleteness-corrected or intrinsic bivariate size–luminosity distribution of galaxies, which is a product of the intrinsic size–luminosity relation and the luminosity function. We model the size–luminosity relation by a log-normal distribution with three free parameters while modeling the luminosity function by a Schechter function with two free parameters; the total number of free parameters is thus five. Then, by multiplying the intrinsic distribution by the incompleteness map, we model the observed size–luminosity distribution of galaxies. Maximum-likelihood estimation (MLE) is used to obtain the best-fit values of these parameters that best reproduce the observed bivariate distribution.

This bivariate method has been exploited in de Jong & Lacey (2000) and Huang et al. (2013) to simultaneously derive the size–luminosity relation and UV luminosity function for local spiral galaxies and LBGs at $z \sim 4-5$, respectively. A similar method has also been adopted in Schmidt et al. (2014a). This method has two advantages over binning methods conventionally adopted as described in Schmidt et al. (2014a); one is that no information is lost because data are not binned, and the other is that photometric errors in magnitude are also considered. In addition, by determining the size–luminosity relation and luminosity function simultaneously, we are able to evaluate the degeneracy between those two relations. Furthermore, in most previous studies, size–luminosity relations have been determined to minimize the residuals in size, which is equivalent to MLE that assumes

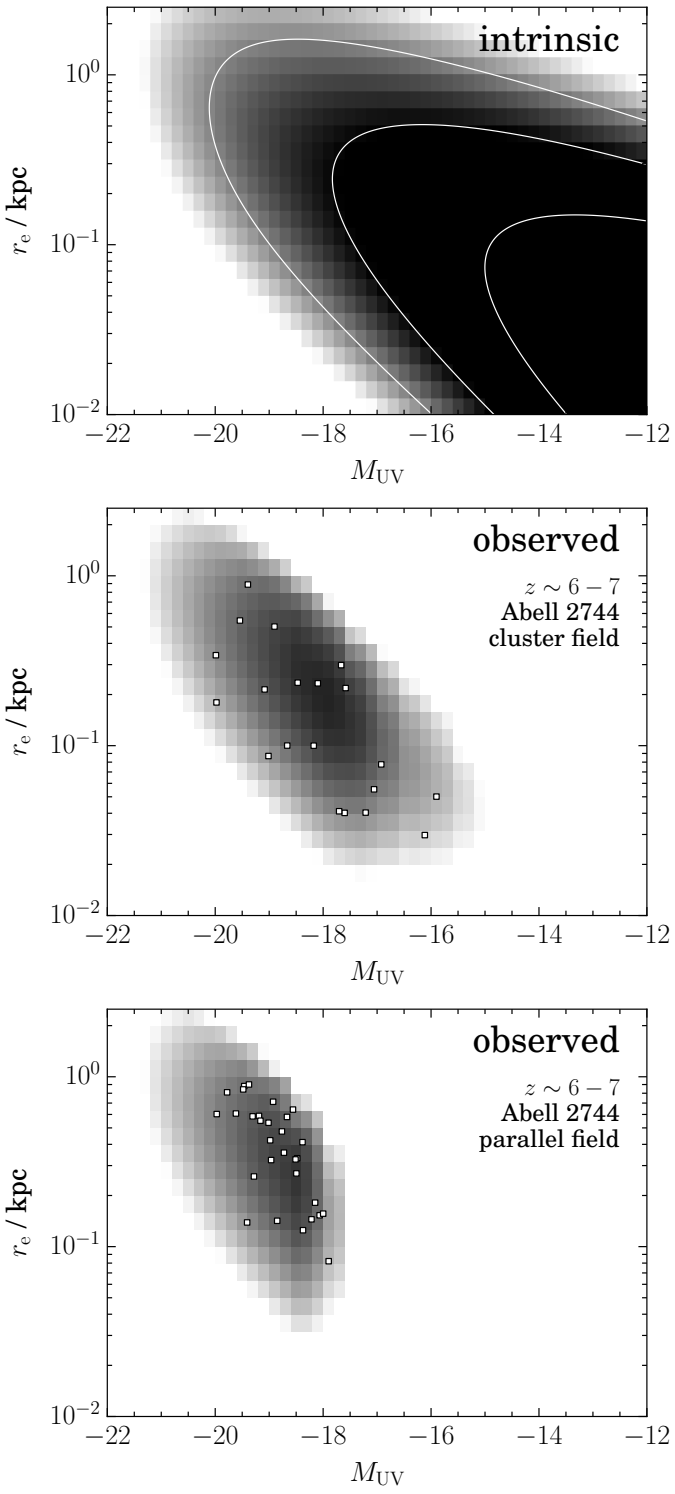

Figure 4.6 Bivariate probability distributions of $z \sim 6-7$ galaxies on the size–luminosity plane shown on a logarithmic scale. The top panel shows the intrinsic distribution with an arbitrary normalization. The contour levels are logarithmically equidistant with 1 dex steps. The middle and bottom panels are for the observed distributions in the Abell 2744 cluster and parallel fields, respectively, calculated by multiplying the intrinsic distribution by the completeness map for each field. Galaxies detected in each field are shown with squares in the lower two panels. The parameters of the intrinsic bivariate distribution presented here are the best-fit parameters obtained in Section 4.2.3.

observed galaxies have a flat distribution in luminosity. On the other hand, our method correctly derives the size–luminosity relation and, consequently, the luminosity function because the luminosity distribution is also modeled using luminosity functions.

The probability density function (PDF) of the intrinsic galaxy distribution on the size–luminosity plane $\Psi(r_{\rm e}, M_{\rm UV})$ is modeled as

$$\begin{aligned}&\Psi(r_{\rm e}, M_{\rm UV}; r_0, \sigma, \beta, M^*, \alpha)\\ &= P(r_{\rm e}, M_{\rm UV}; r_0, \sigma, \beta)\, \phi(M_{\rm UV}; M^*, \alpha),\end{aligned} \tag{4.4}$$

where $P(r_{\rm e}, M_{\rm UV})$ is the PDF of size and $\phi(M_{\rm UV})$ is that of luminosity. As $P(r_{\rm e}, M_{\rm UV})$, we adopt a log-normal distribution described as

$$P(r_{\rm e}, M_{\rm UV}; r_0, \sigma, \beta) = \frac{1}{\sigma r_{\rm e}\sqrt{2\pi}} \exp\left[-\frac{\ln^2(r_{\rm e}/\overline{r_{\rm e}})}{2\sigma^2}\right], \tag{4.5}$$

where

$$\overline{r_{\rm e}}(L) = r_0 \left(\frac{L}{L_0}\right)^{\beta}, \tag{4.6}$$

and r_0, σ, β, and L_0 are the modal radius at $M_{\rm UV} = -21$, width of the log-normal distribution, slope of the size–luminosity relation, and luminosity corresponding to $M_{\rm UV} = -21$, respectively. As $\phi(M_{\rm UV})$, we adopt a Schechter function described as

$$\begin{aligned}&\phi(M_{\rm UV}; M^*, \alpha)\\ &= 10^{-0.4(\alpha+1)(M_{\rm UV}-M^*)} \exp\left[-10^{-0.4(M_{\rm UV}-M^*)}\right],\end{aligned} \tag{4.7}$$

where M^* and α are the characteristic magnitude and power-law slope at the faint end. Note that we do not determine the normalization parameter ϕ_* of the Schechter function because we are interested not in the absolute number of galaxies but only in their relative distribution on the size–luminosity plane.

The observed size–luminosity distribution Ψ' in the i-th field is modeled by multiplying the parameterized intrinsic size–luminosity distribution and the completeness map in that field $\mathcal{C}_i$ obtained in Section 4.2.2,

$$\Psi'_i(r_{\rm e}, M_{\rm UV}; r_0, \sigma, \beta, M^*, \alpha) \equiv \mathcal{N}_i\, \Psi(r_{\rm e}, M_{\rm UV})\, \mathcal{C}_i(r_{\rm e}, M_{\rm UV}), \tag{4.8}$$

where $\mathcal{N}_i$ is the normalization parameter to make the volume unity, and i corresponds to the six cluster and six parallel fields. The probability that a galaxy with $(r_{\rm e}, r_{\rm e} + dr_{\rm e})$ and $(M_{\rm UV}, M_{\rm UV} + dM_{\rm UV})$ is found is $\Psi'(r_{\rm e}, M_{\rm UV})\, dr_{\rm e}\, dM_{\rm UV}$. In order to calculate the probability of the j-th galaxy in the i-th field $f_{i,j}$ considering the observed errors in size and magnitude, we convolve the modeled observed size–luminosity distribution Ψ' with a two-dimensional gaussian centered on the observed size and magnitude, whose variances are equal to their observed errors:

$$\begin{aligned}f_{i,j} = &\int dr'_{\rm e}\, dM'_{\rm UV}\\ &\times \Psi'_i(r'_{\rm e}, M'_{\rm UV})\, g(r'_{\rm e}, M'_{\rm UV}; r_{{\rm e},j}, M_{{\rm UV},j}, \delta r_{{\rm e},j}, \delta M_{{\rm UV},j}),\end{aligned} \tag{4.9}$$

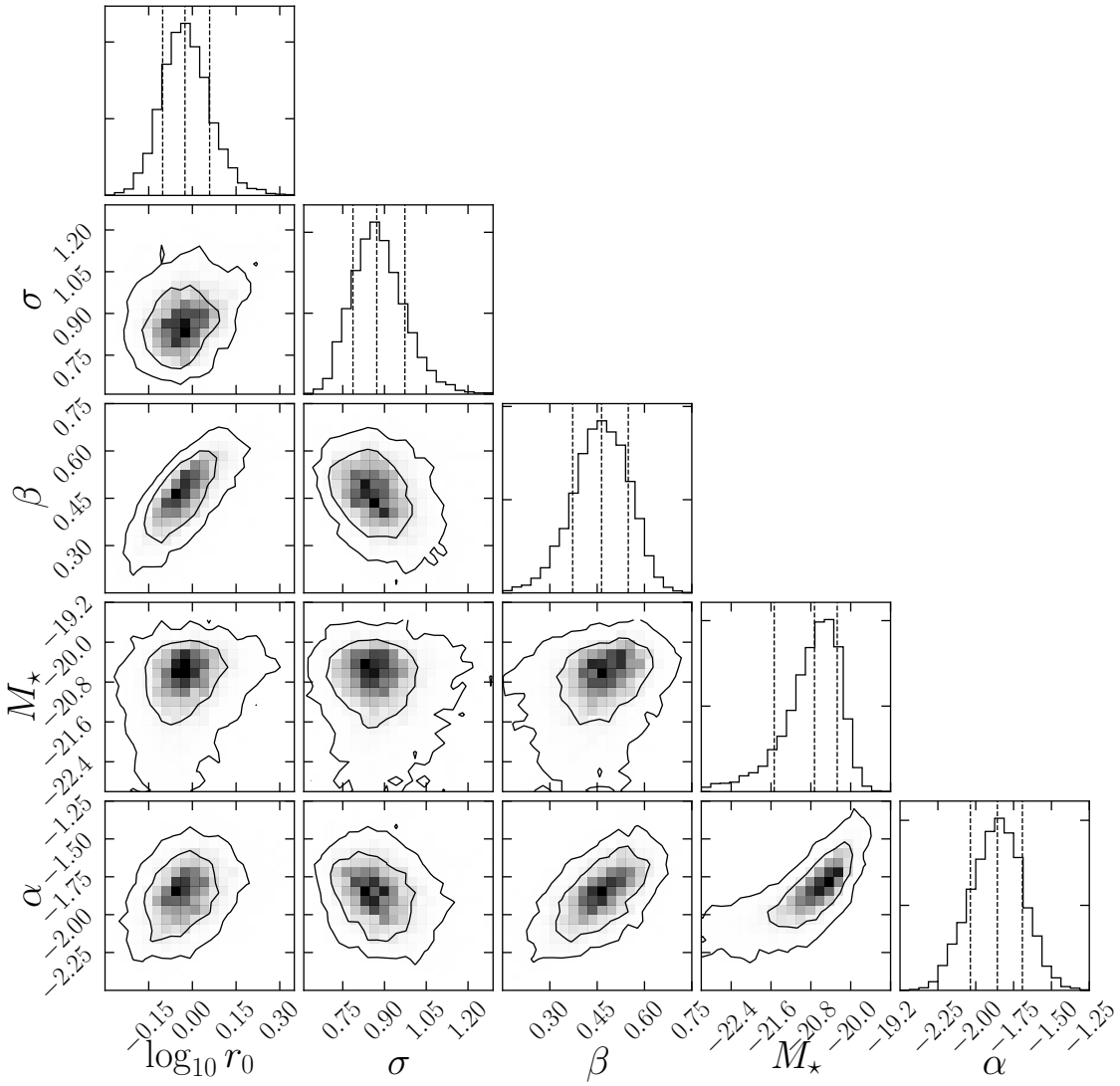

Figure 4.7 Two-dimensional projections of the MCMC samples at $z \sim 6-7$. The inner and outer contours represent 68% and 95% confidence intervals. The three vertical dashed lines on the histograms show the 16th, 50th, and 84th percentiles. Plotted using the `corner.py` module (Foreman-Mackey, 2016).

where $g(r'_{\rm e}, M'_{\rm UV}; r_{{\rm e},j}, M_{{\rm UV},j}, \delta r_{{\rm e},j}, \delta M_{{\rm UV},j})$ is a gaussian function whose peak is at the observed size and magnitude $(r_{{\rm e},j}, M_{{\rm UV},j})$ and the variances are equal to their observed errors $(\delta r_{{\rm e},j}, \delta M_{{\rm UV},j})$. The likelihood in the i-th field $\mathcal{L}_i$ is given by

$$\mathcal{L}_i(r_0, \sigma, \beta, M^*, \alpha) = \prod_j f_{i,j}(r_0, \sigma, \beta, M^*, \alpha). \tag{4.10}$$

The total likelihood $\mathcal{L}$ is the product of the likelihood in each field,

$$\mathcal{L} \equiv \prod_i \mathcal{L}_i. \tag{4.11}$$

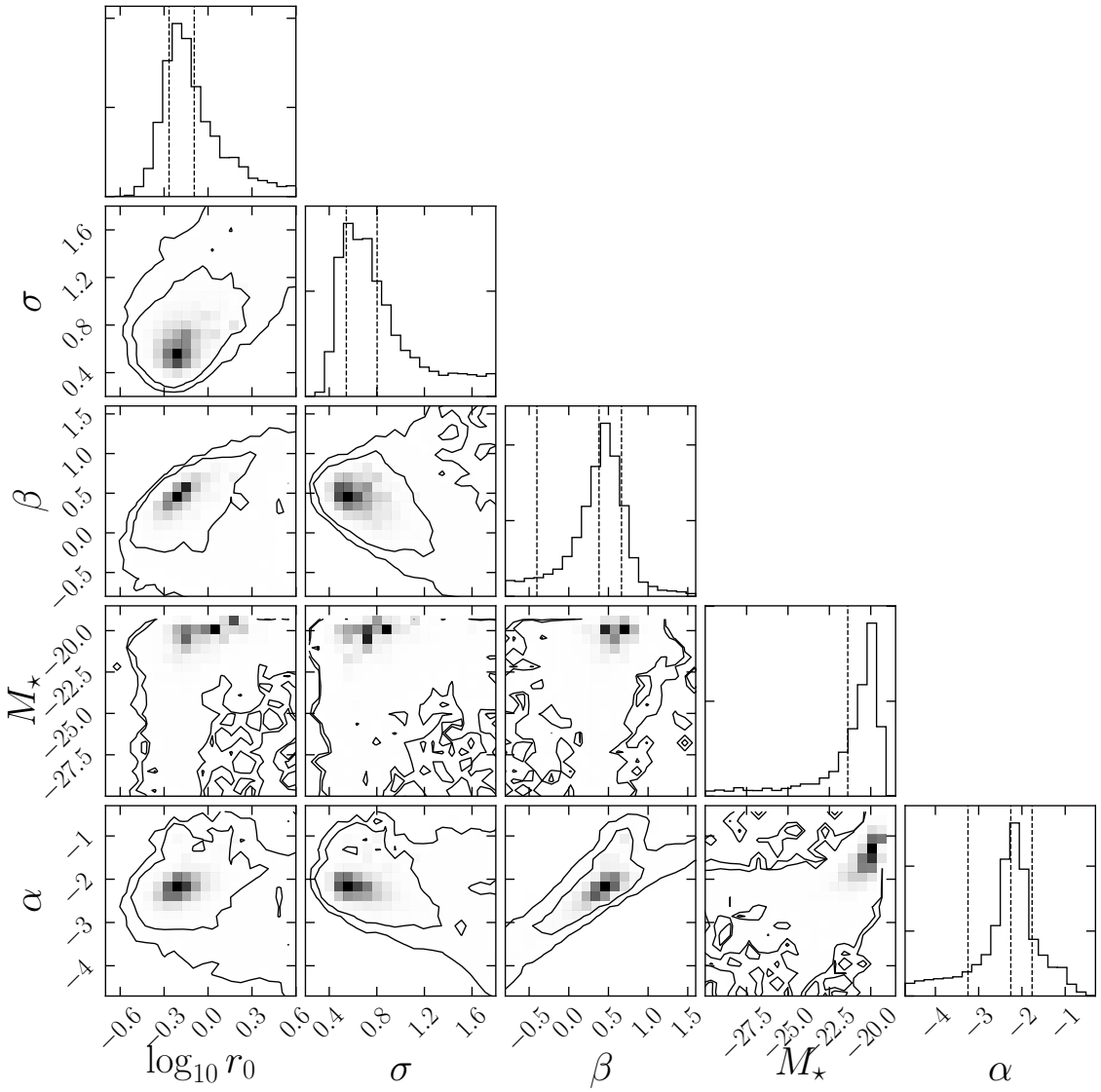

Figure 4.8 Same as Figure 4.7 but for $z \sim 8$.

We use the MCMC procedure to estimate the best-fit values and uncertainties for the five parameters and the degeneracy between them. We assume flat priors on all five parameters. Note that we do not use the galaxies HFF5P-1940-3315 at $z \sim 6-7$ and HFF5P-2129-2064 at $z \sim 8$ in the Abell S1063 parallel field because they are outliers. For the MCMC sampling, we use the public software `emcee` (Foreman-Mackey et al., 2013). The MCMC results are shown in Table 4.2 and Figures 4.7–4.9. As an example, the obtained intrinsic bivariate size–luminosity distribution at $z \sim 6-7$ is presented in the top panel of Figure 4.6.

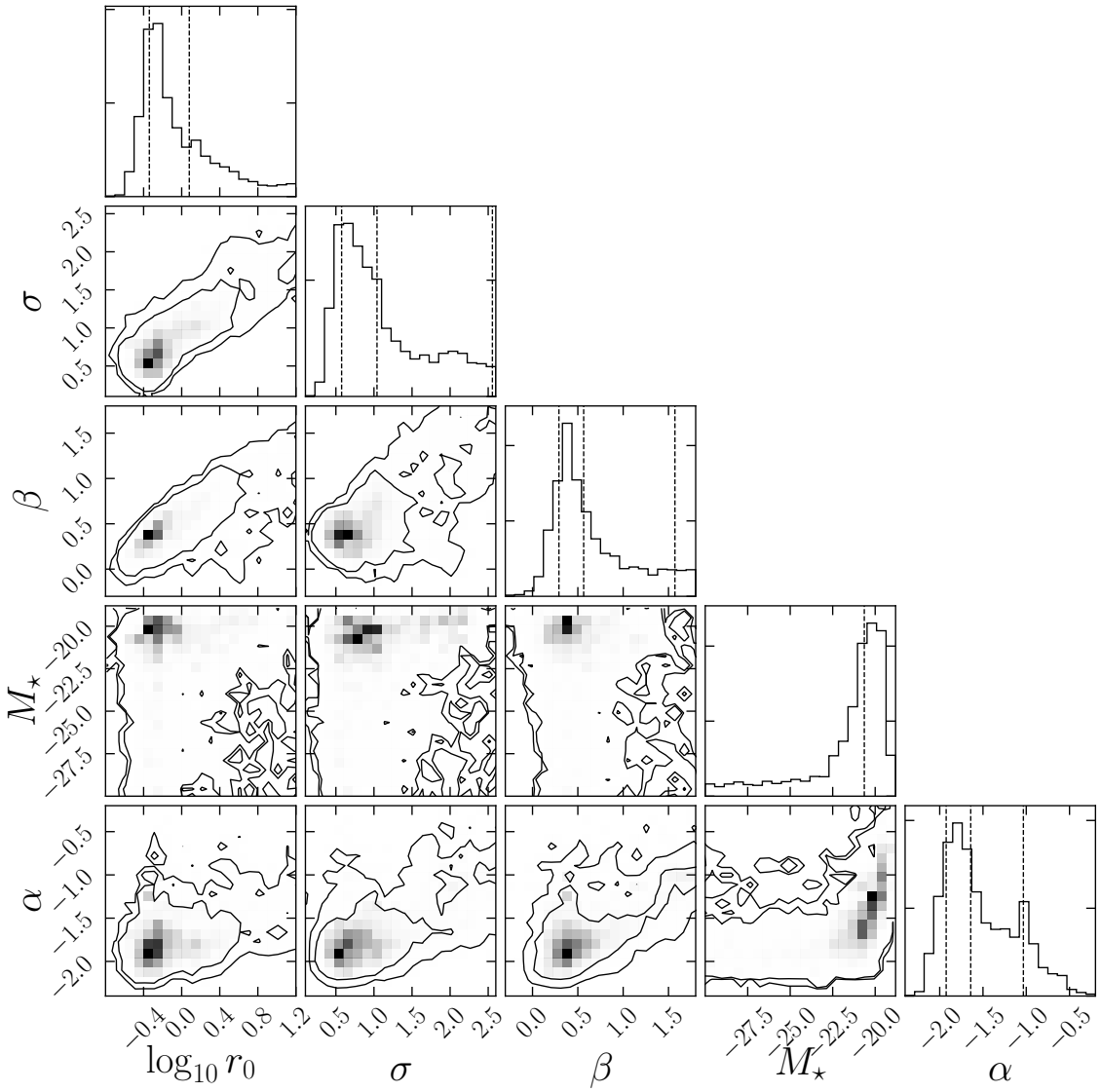

Figure 4.9 Same as Figure 4.7 but for $z \sim 9$.

4.3 Discussion

In this section, we first discuss the intrinsic size–luminosity relations and luminosity functions at $z \sim 6-9$. Second, we construct a model to reproduce the steep size–luminosity relation at $z \sim 6-7$ using the result of the abundance matching in Behroozi et al. (2013). Third, we show that there are large uncertainties in the $z > 6$ luminosity functions derived in previous studies because of a large variance in the assumed size–luminosity relations and that those uncertainties are greatly reduced at least for $z \sim 6-7$ by using the size–luminosity relation obtained in this work. Finally, we discuss the redshift evolution of size.

Table 4.2. Best-fit parameters of size–luminosity relations and luminosity functions

References	r_0/kpc	σ	β	M^*	α
$z \sim 6-7$					
This work	$0.94^{+0.20}_{-0.15}$	$0.87^{+0.10}_{-0.09}$	$0.46^{+0.08}_{-0.09}$	$-20.73^{+0.46}_{-0.81}$	$-1.86^{+0.17}_{-0.18}$
This work (mode)	0.94	0.86	0.44	-20.56	-1.86
This work (LF fixed)	$0.95^{+0.18}_{-0.14}$	$0.86^{+0.09}_{-0.07}$	$0.47^{+0.06}_{-0.06}$	[−20.73]	[−1.86]
This work (apparent)	0.75	0.66	0.52	—	—
Atek et al. (2015a)	[0.81]	[0.90]	[0.25]	$-20.89^{+0.60}_{-0.72}$	$-2.04^{+0.17}_{-0.13}$
Bouwens et al. (2015)	—[a]	—[a]	[∼ 0.25][a,b]	$-20.94^{+0.20}_{-0.20}$	$-1.87^{+0.10}_{-0.10}$
Laporte et al. (2016)	[0.81]	[0.90]	[0]	$-20.33^{+0.37}_{-0.47}$	$-1.91^{+0.26}_{-0.27}$
Livermore et al. (2017)	[0.5]	[0]	[0]	$-20.819^{+0.044}_{-0.034}{}^{+0.001}_{-0.031}$	$-2.10^{+0.03}_{-0.03}{}^{+0.07}_{-0.01}$
Ishigaki et al. (2017)	—[c]	—[c]	[∼ 0.25][b,c]	$-20.89^{+0.17}_{-0.13}$	$-2.15^{+0.08}_{-0.06}$
Bouwens et al. (2017b)	[0.80]	[0.69]	[0.27]	[−20.94]	$-1.92^{+0.04}_{-0.04}$
$z \sim 8$					
This work	$0.81^{+5.28}_{-0.26}$	$0.80^{+1.07}_{-0.26}$	$0.38^{+0.28}_{-0.78}$	$-151.98^{+130.60}_{-314.19}$	$-2.26^{+0.49}_{-0.99}$
This work (mode)	0.58	0.56	0.44	-19.95	-2.14
This work (M_* fixed)	$0.75^{+0.53}_{-0.16}$	$0.65^{+0.35}_{-0.14}$	$0.50^{+0.16}_{-0.21}$	[−20.73]	$-1.80^{+0.22}_{-0.30}$
This work (LF fixed)	$0.69^{+0.24}_{-0.14}$	$0.62^{+0.18}_{-0.12}$	$0.49^{+0.13}_{-0.14}$	[−20.73]	[−1.86]
This work (apparent)	0.57	0.48	0.52	—	—
Bouwens et al. (2015)	—[a]	—[a]	[∼ 0.25][a,b]	$-20.63^{+0.36}_{-0.36}$	$-2.02^{+0.23}_{-0.23}$
Laporte et al. (2016)	[0.81]	[0.90]	[0]	$-20.32^{+0.49}_{-0.26}$	$-1.95^{+0.43}_{-0.40}$
Livermore et al. (2017)	[0.5]	[0]	[0]	$-20.742^{+0.195}_{-0.152}{}^{+0.006}_{-0.014}$	$-2.02^{+0.08}_{-0.07}{}^{+0.01}_{-0.03}$
Ishigaki et al. (2017)	—[c]	—[c]	[∼ 0.25][b,c]	$-20.35^{+0.20}_{-0.30}$	$-1.96^{+0.18}_{-0.15}$
$z \sim 9$					
This work	$1.20^{+367.64}_{-0.74}$	$1.04^{+1.52}_{-0.46}$	$0.56^{+1.01}_{-0.27}$	$-82.74^{+62.10}_{-763.40}$	$-1.64^{+0.61}_{-0.28}$
This work (mode)	0.42	0.54	0.40	-19.80	-1.82
This work (M_* fixed)	$0.59^{+0.61}_{-0.16}$	$0.69^{+0.40}_{-0.20}$	$0.42^{+0.17}_{-0.15}$	[−20.73]	$-1.59^{+0.19}_{-0.18}$
This work (LF fixed)	$0.53^{+0.27}_{-0.13}$	$0.68^{+0.27}_{-0.18}$	$0.34^{+0.13}_{-0.14}$	[−20.73]	[−1.86]
This work (apparent)	0.43	0.47	0.39	—	—
Oesch et al. (2013)	—	—	—	$-18.8^{+0.3}_{-0.3}$	[−1.73]
Laporte et al. (2016)	[0.81]	[0.90]	[0]	[−20.45]	$-2.17^{+0.41}_{-0.43}$

Note. — Numbers in square brackets are fixed during the fitting.

[a]Size–luminosity relation is presented in their Appendix D.

[b]Effective slope of the size–luminosity relation, although its parameterization is different from ours.

[c]Size–luminosity relation is presented in their paper and the bottom panel of our Figure 4.13.

4.3.1 The Intrinsic Size–luminosity Relation and Luminosity Function at $z \sim 6-7$

We discuss here the intrinsic size–luminosity relation and UV luminosity function at $z \sim 6-7$, which are reliably estimated because of the large sample. The best-fit size–luminosity relation and its 1σ uncertainty are presented in the top panel of Figure 4.10, together with the results of previous work.

First, to evaluate the impact of detection incompleteness on the estimation of the size–luminosity relation, we fit the apparent size–luminosity distribution without correcting for completeness. In this process, as an alternative to Ψ'_i in Equation (4.8), we use a

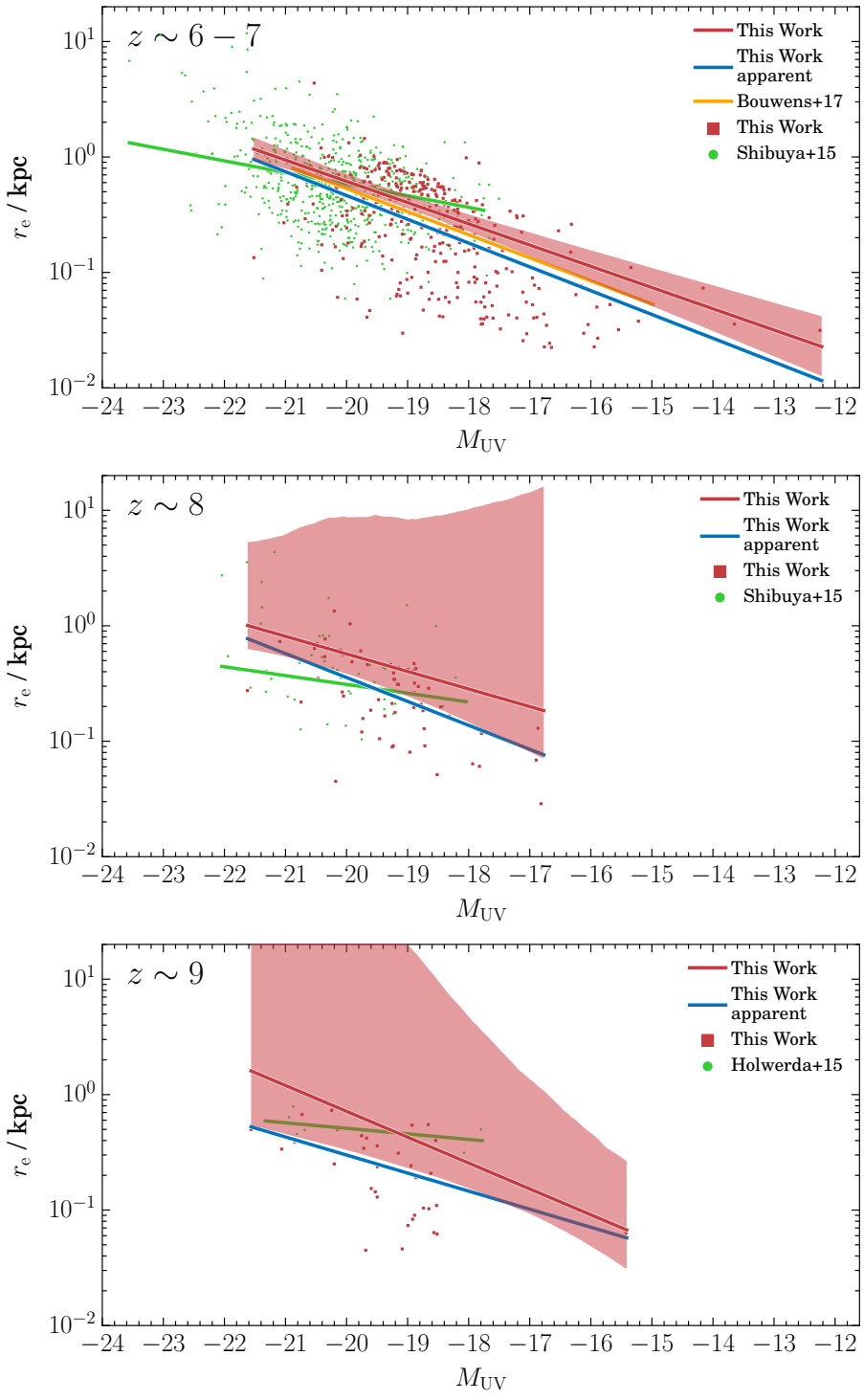

Figure 4.10 Galaxy distributions on the size–luminosity plane at $z \sim 6-7$ (*top*), 8 (*middle*), and 9 (*bottom*), respectively. The red and green points represent, respectively, our galaxies and those from previous studies (Shibuya et al. 2015, for $z \sim 6-7$ and 8; Holwerda et al. 2015 for $z \sim 9$). The red and blue solid lines represent the size–luminosity relations by the completeness-corrected and completeness-uncorrected fittings to our samples, respectively. The 1σ distribution of the completeness-corrected size–luminosity relation is shown by the red shaded region. While the green solid lines show the best-fit power laws obtained by Shibuya et al. (2015) and Holwerda et al. (2015), the orange solid line is for the result obtained by Bouwens et al. (2017a) based on two-dimensional size measurements.

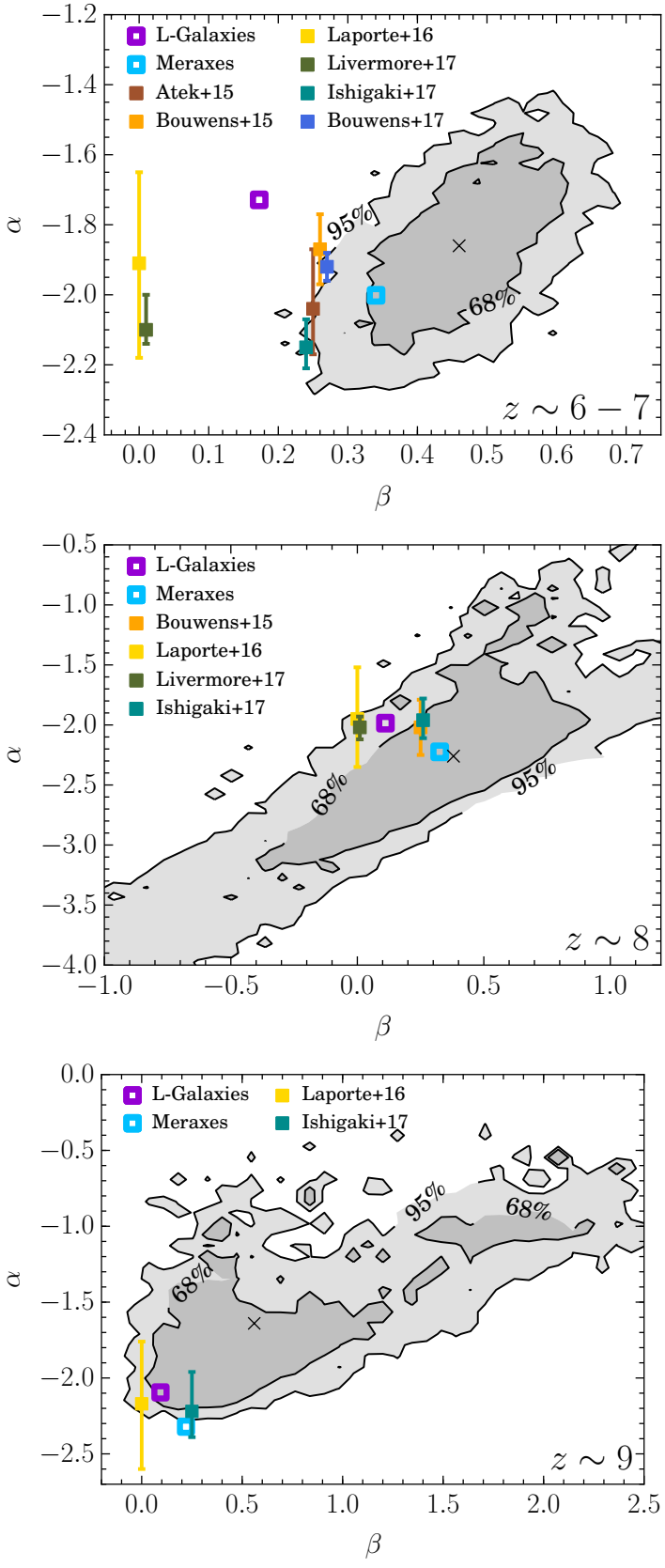

Figure 4.11 Correlations between the faint-end slope of the luminosity function, α, and the slope of the size–luminosity relation, β, overplotted with our median values (crosses), the observational results presented in Table 4.2 (filled squares) and simulation results (open squares). The top, middle, and bottom panels show the results at $z \sim 6-7$, 8, and 9, respectively.

distribution model of

$$\begin{aligned}&\Psi_{\rm apparent}(r_{\rm e}, M_{\rm UV}; r_0, \sigma, \beta)\\ &= P(r_{\rm e}, M_{\rm UV}; r_0, \sigma, \beta),\end{aligned} \tag{4.12}$$

where $P(r_{\rm e}, M_{\rm UV})$ is described in Equation (4.5). This implies that we assume a flat distribution for the magnitude distribution. The best-fit parameter sets estimated using MLE are presented in Table 4.2 as "This work (apparent)". We find that the modal sizes are ~ 0.15 dex underestimated, on average, and as large as ~ 0.2 dex at $M_{\rm UV} = -16$. The slope of the intrinsic size–luminosity relation is overestimated by $\Delta\beta = 0.06$. This suggests that incompleteness has a slight contribution to the apparent steepness. In contrast, we find that the variance of the size–luminosity relation σ is $\sim 25\%$ underestimated if incompleteness is not corrected for.

Then, we discuss the incompleteness-corrected results. Concerning the size–luminosity relation, the marginalized value of the slope is $\beta = 0.46^{+0.08}_{-0.09}$. This slope is steeper than $\beta = 0.25^{+0.25}_{-0.14}$ at $z \sim 5$ by Huang et al. (2013) (with incompleteness correction) and $\beta = 0.25^{+0.05}_{-0.05}$ at $z \sim 6$ by Shibuya et al. (2015) (without incompleteness correction), both of them utilizing brighter ($M_{\rm UV} \lesssim -18$) samples. This is the first time to confirm the steepness of the intrinsic size–luminosity relation of $z \sim 6-7$ galaxies. Although a steep slope for galaxies at this redshift range was first reported by K15 based on reliable size measurements of the first HFF sample and then confirmed with larger samples by Bouwens et al. (2017a,c), none of these studies has applied incompleteness correction. The differences in the slope from Huang et al. (2013) and Shibuya et al. (2015) can be due to the differences in the magnitude range and hence in the physics dominating in galaxies. We further investigate this physical origin of the steepness in Section 4.3.3 using the result of the abundance matching by Behroozi et al. (2013). As described in the next paragraph, the difference from Shibuya et al. (2015) can also be explained by the differences in methods to measure magnitudes and to fit the size–luminosity relation. We note that although it has a steep slope, the best-fit intrinsic bivariate distribution predicts the existence of faint galaxies with large sizes, for instance, $M_{\rm UV} = -16$ galaxies with $r_{\rm e} \sim 1$ kpc, (see the top panel of Figure 4.6).

Shibuya et al. (2015) have found remarkably shallower slopes of $\beta \simeq 0.25 \pm 0.05$ for brighter galaxies at $z \sim 6$ and 7 even without correcting for incompleteness. Interestingly, in Figures 4.2–4.3 and 4.10, their galaxies appear to have a similar slope to ours. In fact, while their samples made public and plotted here use `GALFIT` magnitudes based on profile fittings, they have used `SExtractor` magnitudes based on Kron photometries to derive the slope (T. Shibuya 2017, private communication). Applying the same method (Equation 4.12) to their sample, we find that using `SExtractor` magnitudes gives slopes 0.13 and 0.21 shallower than those based on `GALFIT` magnitudes at $z \sim 6$ and 7, respectively. This may suggest that using `SExtractor` magnitudes leads them to derive the shallower slopes. In addition, our fitting method is different from theirs. They use a least-squares method that minimizes residuals only in size, which can bias the slope toward shallower values.

The modal size at $M_{\rm UV} = -21$ is $0.94^{+0.20}_{-0.15}$ kpc at $z \sim 6-7$. This size can be slightly larger than the incompleteness-uncorrected sizes by the previous studies (Bouwens et al., 2004; Oesch et al., 2010a; Shibuya et al., 2015). We note that the sizes in Bouwens et al. (2004) and Oesch et al. (2010a) are averages in the range of $-21 \leq M_{\rm UV} \leq -19.7$, which means the sizes at $M_{\rm UV} = -21$ should be larger (see also Figure 4.16).

The variance of the log-normal size distribution is $\sigma = 0.87^{+0.10}_{-0.09}$. This is in good accordance with the values of $\sigma = 0.83^{+0.046}_{-0.044}$ and $0.90^{+0.15}_{-0.065}$ at $z \sim 4$ and 5, respectively, in Huang et al. (2013). According to the analytical model by Mo et al. (1998) (see also Fall & Efstathiou, 1980), galaxy sizes are basically proportional to their halo sizes and spin parameters. The distribution of the spin parameter is log-normal at a fixed halo mass and thus also approximately log-normal at a fixed luminosity. Its variance was estimated to be $\sigma_{\rm h} = 0.60$ at $z = 0$ and revealed to scarcely evolve toward higher redshifts by Zjupa & Springel (2017) with the dark matter-only Illustris simulation. Since the observed variance of the galaxy-size distribution is larger than that of the spin parameter, there may be some elements that broaden the galaxy-size distribution. For example, a scatter in halo mass at fixed luminosity would result in a broader size distribution. This scatter was recently suggested at low redshifts in Charlton et al. (2017). Another explanation is a disk-to-halo ratio of specific angular momentum depending on the spin parameter, which means the galaxy size is no longer proportional to the spin parameter. We note that the derived variance σ has been corrected for errors in size and magnitude measurements as described in Equation (4.9).

We find a shallow faint-end slope of the luminosity function of $\alpha = -1.86^{+0.17}_{-0.18}$, consistent with the slopes in Bouwens et al. (2015, 2017b) and Laporte et al. (2016) but slightly incompatible with recently suggested steep slopes of $\alpha \simeq -2.00$ to -2.15 (e.g., Livermore et al., 2017; Ishigaki et al., 2017). The reason for this is that our size–luminosity relation is steeper than those utilized in the previous studies. With a steeper size–luminosity relation, galaxies are easier to detect and a smaller amount of incompleteness correction is needed in luminosity function derivation, especially at faint magnitude ranges. Thus, the faint-end slope becomes shallower. The effects of the size–luminosity relation on the luminosity function are further discussed in Section 4.3.4.

The characteristic magnitude, $M^* = -20.73^{+0.46}_{-0.81}$ is consistent with those of previous work. Since the marginalized distribution has a long tail toward the brighter magnitude, the mode of it is slightly larger, $M^* \simeq -20.56$. The uncertainty in M^* is relatively large, probably because we do not use bright-galaxy samples from large-area surveys.

The parameters of the size–luminosity relation strongly correlate with those of the luminosity function. The most important may be the correlation between α and β, which has been pointed out by several works, including Grazian et al. (2011) and Bouwens et al. (2017a,b). The top panel of Figure 4.11 shows the correlation between α and β obtained in this work together with the previous measurements of these parameters presented in Table 4.2. We find that the steeper α in Atek et al. (2015a) and Ishigaki et al. (2017) will become further consistent with ours if steeper size–luminosity relations are assumed. Even with our large and deep sample, at $z \sim 6-7$ there still remains a moderate uncertainty

in α due to the uncertainty in the size–luminosity relation. This uncertainty in α is propagated to the UV luminosity density, a key quantity to calculating the number density of ionizing photons, although no previous studies on cosmic reionization have considered this uncertainty. We note that although the values of α obtained in Laporte et al. (2016) and Livermore et al. (2017) are consistent with our value, their α–β combinations are outside (with a large margin) of the 95% confidence ellipse obtained in this study. This demonstrates that these parameters must not be determined independently.

We also compare our α and β measurements with the results of the semi-analytical model of galaxy formation L-Galaxies (Henriques et al., 2015). We run the L-Galaxies code on two N-body dark matter simulations of different resolutions, the Millennium (Springel et al., 2005) and Millennium-II (Boylan-Kolchin et al., 2009), and combine the two galaxy catalogs to probe a wide halo mass range. Applying Equation (4.4) to the combined catalog finds that the L-Galaxies predicts an α consistent with our value but a significantly flatter β. Results of the semi-analytical model of galaxy formation meraxes (Mutch et al., 2016; Liu et al., 2017) are also compared. We find a good agreement with our results for $z \sim 6-7$ and 8 and an acceptable agreement for $z \sim 9$. Note that the values of β obtained here are different from those obtained in Liu et al. (2017) because of different fitting methods.

However, we find that the two models tend to predict relatively flatter size–luminosity relations, especially at $z \sim 6-7$ and 9. Their sizes are calculated essentially based on the analytical model by Mo et al. (1998). The flatter size–luminosity relations than observed may suggest the importance of careful calculations of the exchange of angular momentum between the dark matter halo and the stellar disk. Indeed, meraxes assumes a constant specific angular momentum of $j_{\rm d}/m_{\rm d} = 1$, which disagrees with our result in Section 4.3.3. In L-Galaxies, specific angular momenta are calculated and compared with those by other semi-analytical models and hydrodynamical simulations (e.g. Guo et al., 2016; Hou et al., 2017). However, we do not discuss their results because they provide only the specific angular momenta of cooled gas, which may be systematically different from the specific angular momenta of disks, $j_{\rm d}/m_{\rm d}$. Further comparison between the observations and simulations is beyond the scope of this thesis.

Another parameter set that shows a strong correlation is α and M^*, as seen in Figure 4.7 and as has been reported in previous studies. We confirm that the uncertainty in α decreases from ~ 0.2 to $\lesssim 0.1$ if M^* is virtually fixed to, for instance, $M^* = -21$. The slope β also correlates with the modal size r_0 and weakly with the width of the size distribution σ; both correlations originate from a requirement to reproduce small faint galaxies (except for the β–σ correlation at $z \sim 9$).

Since α strongly correlates with M^* and β, a more accurate measurement of α requires a larger sample containing bright objects (to better constrain M^*) accompanied by a completeness estimation on the size–luminosity plane (to obtain an unbiased β value).

4.3.2 The Intrinsic Size–luminosity Relation and Luminosity Function at $z \sim 8$ and 9

The fitting results of the intrinsic size–luminosity distributions at $z \sim 8$ and 9 are presented in the middle and bottom panels of Figure 4.10, respectively. Since the samples are smaller than that at $z \sim 6-7$, the uncertainties in the parameters are typically $\gtrsim 2-3$ times larger.

Similar to that at $z \sim 6-7$, we find steep slopes of the size–luminosity relations of $\beta = 0.38^{+0.28}_{-0.78}$ and $0.56^{+1.01}_{-0.27}$ at $z \sim 8$ and 9, respectively. These are steeper than the slope of $\beta = 0.19^{+0.25}_{-0.25}$ at $z \sim 8$ by Shibuya et al. (2015), although the differences are within the 1σ errors. However, the distributions of our galaxies on the size–luminosity plane appear to be consistent with theirs, as is the case for $z \sim 6-7$.

The modal sizes at $M_{\rm UV} = -21$ are $0.81^{+5.28}_{-0.26}$ kpc and $1.20^{+367.64}_{-0.74}$ kpc at $z \sim 8$ and 9, respectively. If incompleteness is not corrected for, the sizes become 0.2–0.3 dex smaller at $z \sim 8$ and 9, a slightly larger amount of decrease than that at $z \sim 6-7$. These are consistent with the incompleteness-uncorrected sizes of $r_{\rm e} = 0.419^{+1.981}_{-0.262}$ at $z \sim 8$ by Shibuya et al. (2015) and $r_{\rm e} = 0.6^{+0.3}_{-0.3}$ at $z \sim 9$ by Holwerda et al. (2015).

The variance of the size distribution σ is $0.80^{+1.07}_{-0.26}$ and $1.04^{+1.52}_{-0.46}$ at $z \sim 8$ and 9, respectively, being almost constant at $z \sim 6-9$. While we do not find any indication of the evolution of σ over this redshift range, the modal value of the variance distribution may decrease with redshift. Further discussion needs larger samples.

While the faint-end slope of the luminosity function at $z \sim 9$ is relatively shallow ($\alpha = -1.64^{+0.61}_{-0.28}$), that at $z \sim 8$ may be steep ($\alpha = -2.26^{+0.49}_{-0.99}$). However, both values are consistent with the value at $z \sim 6-7$ due to the large uncertainties.

At $z \sim 8-9$, the probability distributions of M^* have tails toward the brighter magnitudes, and thus the median values are remarkably brighter than that at $z \sim 6-7$. This is because our samples do not have enough bright galaxies due to the small cosmic volume the HFF program is probing. We note that the M^* values at $z \sim 8-9$ are close to typical magnitudes at these redshifts of $M^* \sim -21$ within the uncertainties. Furthermore, the modes are $M^* = -19.95$ at $z \sim 8$ and -19.80 at $z \sim 9$.

We also calculate r_0, σ, β, and α by fixing M^* to -20.73, the best-fit value at $z \sim 6-7$, and obtain $(r_0/{\rm kpc}, \sigma, \beta, \alpha) = (0.75^{+0.53}_{-0.16}, 0.65^{+0.35}_{-0.14}, 0.50^{+0.16}_{-0.21}, -1.80^{+0.22}_{-0.30})$ at $z \sim 8$ and $(0.59^{+0.61}_{-0.16}, 0.69^{+0.40}_{-0.20}, 0.42^{+0.17}_{-0.15}, -1.59^{+0.19}_{-0.18})$ at $z \sim 9$, as presented in Table 4.2. These α values are even shallower than those from the full modeling, with the uncertainties being reduced to be comparable to those of previous studies.

The middle and bottom panels of Figure 4.11 are the same as the top panel but for $z \sim 8$ and 9, respectively. In contrast to the case for $z \sim 6-7$, all the α–β combinations from previous observations and L-Galaxies are within the 95% confidence contour of our results. Besides the parameter sets of (α, β), (α, M^*), (r_0, β), and (σ, β) that show correlations at $z \sim 6-7$, r_0 and σ also correlate strongly at $z \sim 8-9$. This correlation is to reproduce the smaller galaxies and may indicate that we still do not trace the peak

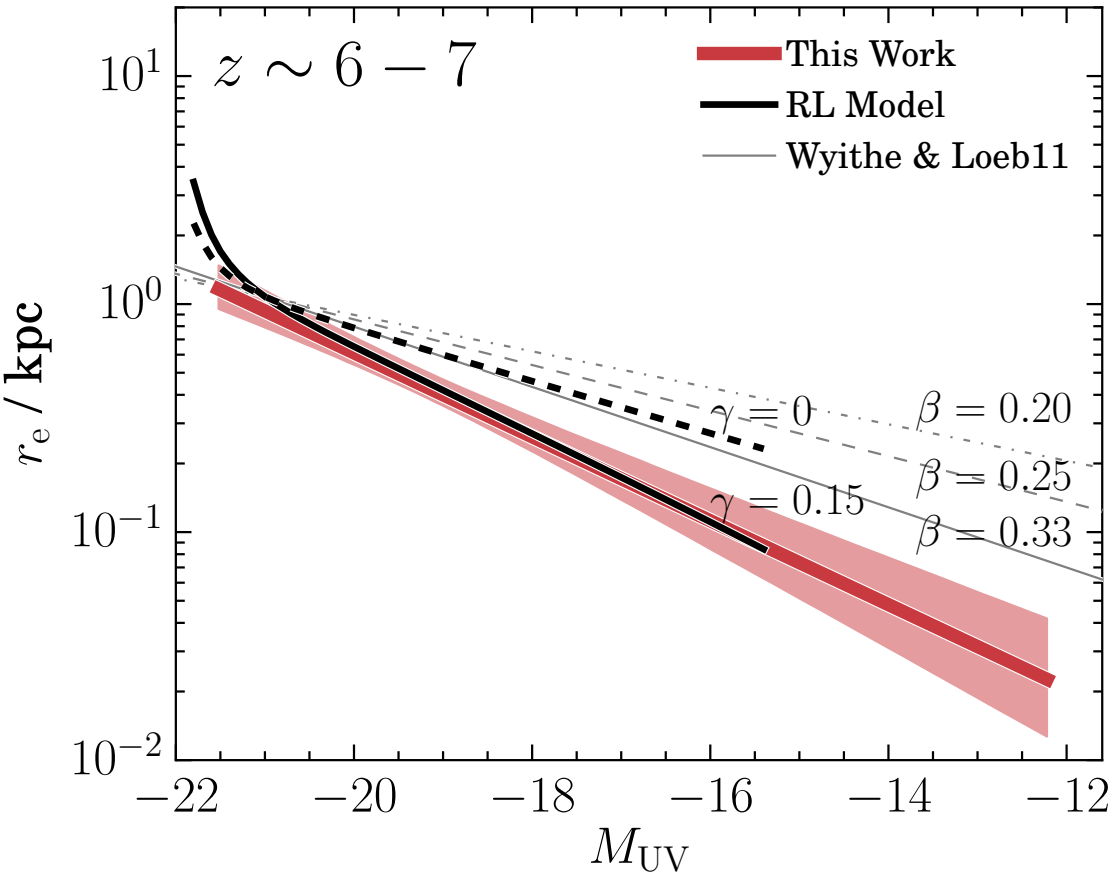

Figure 4.12 Model predictions of the size–luminosity relation at $z \sim 6-7$, overplotted with the fitting result to the observation. The black solid and dashed lines show the predictions by the RL model with $\gamma = 0.15$ and 0, respectively. The gray dash-dotted, dashed, and solid lines represent the predictions by the Wyithe & Loeb (2011) model with $\beta = 0.20$, 0.25, and 0.33, respectively, normalized to agree with those by the RL model at $M_{UV} = -21$.

of the size distributions at $z \gtrsim 8$.

We find that the parameters of the size–luminosity relations and luminosity functions at $z \sim 8-9$ are still not well constrained. Thus, there are significant uncertainties in the luminosity function the faint-end slope of the luminosity function α and hence in discussions of reionization based on the UV luminosity density.

4.3.3 The Modeling of the Size–luminosity Relation

We construct a model to predict the normalization and slope of the size–luminosity relation at $z \sim 6-7$ in the following process. Hereafter, we call this model RL model. (1) We calculate the average stellar mass of galaxies as a function of luminosity using the stellar mass–luminosity relation by González et al. (2011). (2) Combining step (1) with the stellar mass–halo mass relation by Behroozi et al. (2013), we evaluate the average halo

mass of galaxies as a function of luminosity[*2]. Note that an extrapolated relation covering a wider mass range than that presented in their paper is utilized (P. Behroozi 2016, private communication). (3) We calculate the virial radius of halos by

$$r_{\rm vir} = \left[\frac{2GM_{\rm vir}}{\Delta_{\rm vir}H(z)^2}\right]^{1/3}. \tag{4.13}$$

In the calculation of the virial overdensity $\Delta_{\rm vir}$, we use the fitted form of $\Delta_{\rm vir} = 18\pi^2 + 82x - 39x^2$ with $x = \Omega_{\rm m}(z) - 1$ by Bryan & Norman (1998). (4) From the halo radius, we calculate the galaxy size based on the equation in Mo et al. (1998),

$$r_{\rm e} = \frac{1.678}{\sqrt{2}} f_j \lambda f_{\rm c}^{-1/2} f_{\rm R} r_{\rm vir}, \tag{4.14}$$

where λ is the spin parameter of the halo defined in Peebles (1969). The factor $f_j(M_{\rm vir})$ represents the ratio of the specific angular momentum in the galaxy against that in the halo,

$$f_j(M_{\rm vir}) = \frac{j_{\rm d}}{m_{\rm d}}(M_{\rm vir}) \tag{4.15}$$

$$= \left(\frac{j_{\rm d}}{m_{\rm d}}\right)_{M_{\rm UV}=-21} \left(\frac{M_{\rm vir}}{M_{\rm vir,0}}\right)^{\gamma}, \tag{4.16}$$

where $j_{\rm d}$ and $m_{\rm d}$ are the ratio of the angular momentum and mass, respectively, in the galaxy against those in the halo. In contrast to the original equation in Mo et al. (1998), we allow $j_{\rm d}/m_{\rm d}$ to vary as a function of the halo mass, whose dependence was suggested in several observational studies (e.g., Somerville et al., 2017) and simulations of galaxy formation (e.g., Sales et al., 2010). The factor $(j_{\rm d}/m_{\rm d})_{M_{\rm UV}=-21}$ and $M_{\rm vir,0}$ represent the $j_{\rm d}/m_{\rm d}$ and the halo mass of galaxies with $M_{\rm UV} = -21$, respectively. The index γ is the exponent of the mass dependence of $j_{\rm d}/m_{\rm d}$. The factor f_j equates to the original constant $j_{\rm d}/m_{\rm d}$ when $\gamma = 0$. The factor $f_{\rm c}(c)$, depending only on the concentration parameter of the halo c, is to correct for the effect caused by the change in the density profile from the isothermal sphere to the NFW profile. The other factor $f_{\rm R}(j_{\rm d}/m_{\rm d}, m_{\rm d}, \lambda, c)$ is to correct for effects caused by the change in the density profile and the gravitational effect by the disk. We need the factor of 1.678 to convert the scale length of the exponential profile to the half-light radius $r_{\rm e}$. Thus, we obtain the model of the size–luminosity relation.

Except for γ, there are four parameters that are needed to calculate the size; while λ and c are reliably determined in simulations (e.g., Bullock et al., 2001; Vitvitska et al., 2002; Davis & Natarajan, 2009; Prada et al., 2012), the parameters $j_{\rm d}$ and $m_{\rm d}$, depending on baryonic physics, are difficult to predict. In the calculation of the size, we assume $\lambda = 0.04$ that is independent of redshift, which is consistent with the recent result in Zjupa & Springel (2017). For the concentration parameter c, we utilize the fitting function for the

[*2] There may be a logical inconsistency that we model the steep size–luminosity relation using the results in Behroozi et al. (2013), where a luminosity function derived assuming a shallower size–luminosity relation is used. However, we consider this effect to be of secondary importance.

c–$M_{\rm vir}$ relation for Planck cosmology in Correa et al. (2015). We assume the typical values of $(j_{\rm d}/m_{\rm d})_{M_{\rm UV}=-21} = 1.0$ (e.g., Fall & Efstathiou, 1980; Mo et al., 1998; Romanowsky & Fall, 2012; Fall & Romanowsky, 2013) and $m_{\rm d} = 0.05$ (e.g., Sales et al., 2010). These values of $j_{\rm d}$ and $m_{\rm d}$ are shown to be consistent with observations in Section 4.3.5.

The calculated size–luminosity relation at $z \sim 6-7$ is presented in Figure 4.12 as the RL model. We find that the RL model predicts a shallow slope of $\beta \simeq 0.3$ when $\gamma = 0$. While this shallow slope is consistent with observed slopes at lower redshifts of $\beta \sim 0.25$ (e.g., de Jong & Lacey, 2000; Huang et al., 2013; Shibuya et al., 2015, see also Figure 4.15), it is inconsistent with our steep slope at $z \sim 6-7$. However, when we change f_j as a function of halo mass with $\gamma = 0.15$, the model predicts a steeper slope that is consistent with the observed value at $z \sim 6-7$. This may suggests that $j_{\rm d}/m_{\rm d}$, that is, the fraction of the specific angular momentum in the galaxy, is smaller in fainter galaxies at higher redshifts. In the beginning stage of galaxy formation, stars are formed preferentially from gas with lower angular momenta. The halo mass dependence of f_j obtained here may suggest that the faint galaxies are indeed in such a stage.

Stellar feedback may be another explanation because it redistributes the angular momentum between the galaxy and the halo, thus changing f_j. Genel et al. (2015) have used the Illustris cosmological simulation to find that stellar feedback increases the specific angular momentum of galaxies, although the halo mass dependence is equivalent to $\gamma < 0$, opposite to what we find here (see also Sales et al. 2010 for a contradictory result).

Another possibility is that in low-mass halos, only those with relatively small spin parameters can form disks, thus making the slope steeper even with $\gamma = 0$. If this is the case, the shape and variance of the log-normal size distribution at faint magnitudes can be different from those at bright magnitudes.

We also compare the obtained intrinsic slope with analytical predictions by Wyithe & Loeb (2011), which are shown in Figure 4.12 with gray lines. They construct a simple analytical model that describes the relation between the size and luminosity (see also Liu et al., 2017). The predicted relation depends on the feedback that dominates in galaxies. They test three kinds of feedback: energy conserving, momentum conserving, and no feedback. The predicted slopes are $\beta = 0.20$, 0.25, and 0.33, respectively, all of which are shallower than the observed value at $> 1\sigma$ levels. We note that they assume a constant f_j, which corresponds to $\gamma = 0$.

Very recently, Ma et al. (2017) have suggested that UV light does not necessarily trace the main part of galaxies using high-resolution cosmological zoom-in simulations from the FIRE project. This observational bias might affect our discussion presented here.

4.3.4 The Size–luminosity Relations for Derivations of Luminosity Functions

In this subsection, we examine the effects of the size–luminosity relation on the estimation of the detected fraction of galaxies, and thus of the luminosity function.

The top panel of Figure 4.13 shows the detected fraction against UV magnitude for $z \sim 6-7$ calculated for all of the HFF cluster and parallel fields using the best-fit size–luminosity relation. As shown in this figure, the detected fraction at the faintest

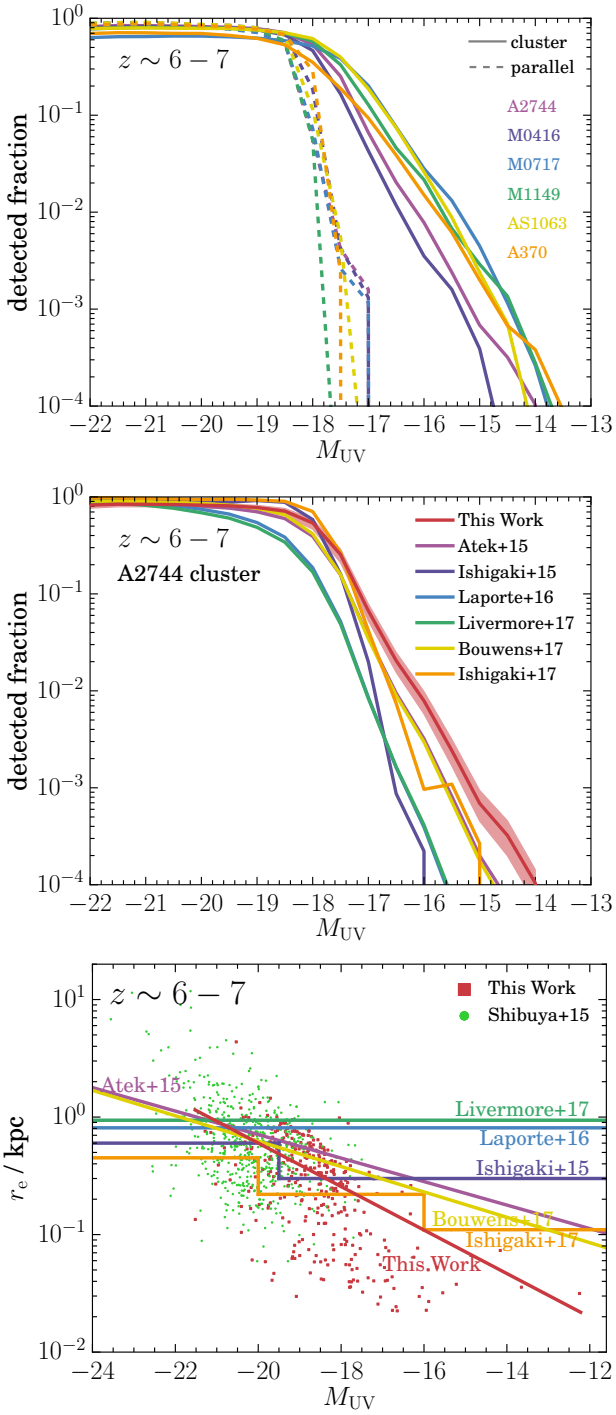

Figure 4.13 (*Top*) Detected fraction against UV absolute magnitude in each field at $z \sim 6-7$ calculated using the completeness map of the field and the best-fit size–luminosity relation at $z \sim 6-7$. The solid and dashed lines correspond to the cluster and parallel fields, respectively. (*Middle*) Variation in the detected fractions at $z \sim 6-7$ in the Abell 2744 cluster field calculated with size–luminosity relations given in previous studies. The uncertainty estimated in this work is also plotted by the red shaded region. (*Bottom*) Size–luminosity relations in the previous studies utilized to calculate the detected fractions in the middle panel, overplotted with the galaxy distributions from this work (red points) and Shibuya et al. (2015) (green points).

Table 4.3. Luminosities Where the Average Sizes in Figure 4.16 Are Calculated

References	$\overline{M_{\rm UV}}$
This work	-21
Bouwens et al. (2004)	-20.35
Oesch et al. (2010a)	-20.35
Grazian et al. (2012)	-20.50
Huang et al. (2013)	-21
Ono et al. (2013) at $z \sim 7$	-20.2
Ono et al. (2013) at $z \sim 8$	-20.15
Kawamata et al. (2015) at $z \sim 6-7$	-20.2
Kawamata et al. (2015) at $z \sim 8$	-20.30
Holwerda et al. (2015)	-20.87
Shibuya et al. (2015)	-21
Laporte et al. (2016)	-20.35

magnitudes $M_{\rm UV} \simeq -15$ to -14 is extremely low. This implies that the luminosity function is calculated from only a small part of galaxies in the field of view with a large ($\sim 10^3$) incompleteness correction.

We calculate the detected fractions, as an example, in the Abell 2744 cluster field assuming the six size–luminosity relations utilized in the previous studies at $z \sim 6-7$ (Atek et al., 2015a; Ishigaki et al., 2015, 2017; Laporte et al., 2016; Livermore et al., 2017; Bouwens et al., 2017b). These fractions, together with that calculated assuming our size–luminosity relation considering its uncertainty, are shown in the middle panel of Figure 4.13. The assumed size–luminosity relations are presented in the bottom panel of Figure 4.13. Whereas the relations in Ishigaki et al. (2015) and Ishigaki et al. (2017) have delta-function-like size distributions, those in Atek et al. (2015a), Laporte et al. (2016), Livermore et al. (2017), and Bouwens et al. (2017b) have variances of $\sigma \simeq 0.9$, 0.9, 1.0, and 0.69, respectively. As shown in the bottom panel, all of the size–luminosity relations in the previous studies are considerably flatter than ours, which results in underestimation of the detected fraction and a steeper faint-end slope of the luminosity function. Furthermore, there is a considerable difference between the relations, which introduces a significant uncertainty in the detected fraction and, consequently, in the luminosity function. In contrast, the uncertainty in the detected fraction calculated by our size–luminosity relation is smaller than the scatter of the detected fractions by the relations in the previous studies. This means that we reduce the uncertainty in the luminosity function that originates from the size–luminosity relation (the middle panel of Figure 4.13).

Our size–luminosity relations are more accurate than those in previous studies at $z \sim 6-9$ for three reasons: they are not extrapolations from low-redshift results but are determined directly from large samples with accurate size measurements, they are corrected for detection incompleteness, and proper statistics are utilized.

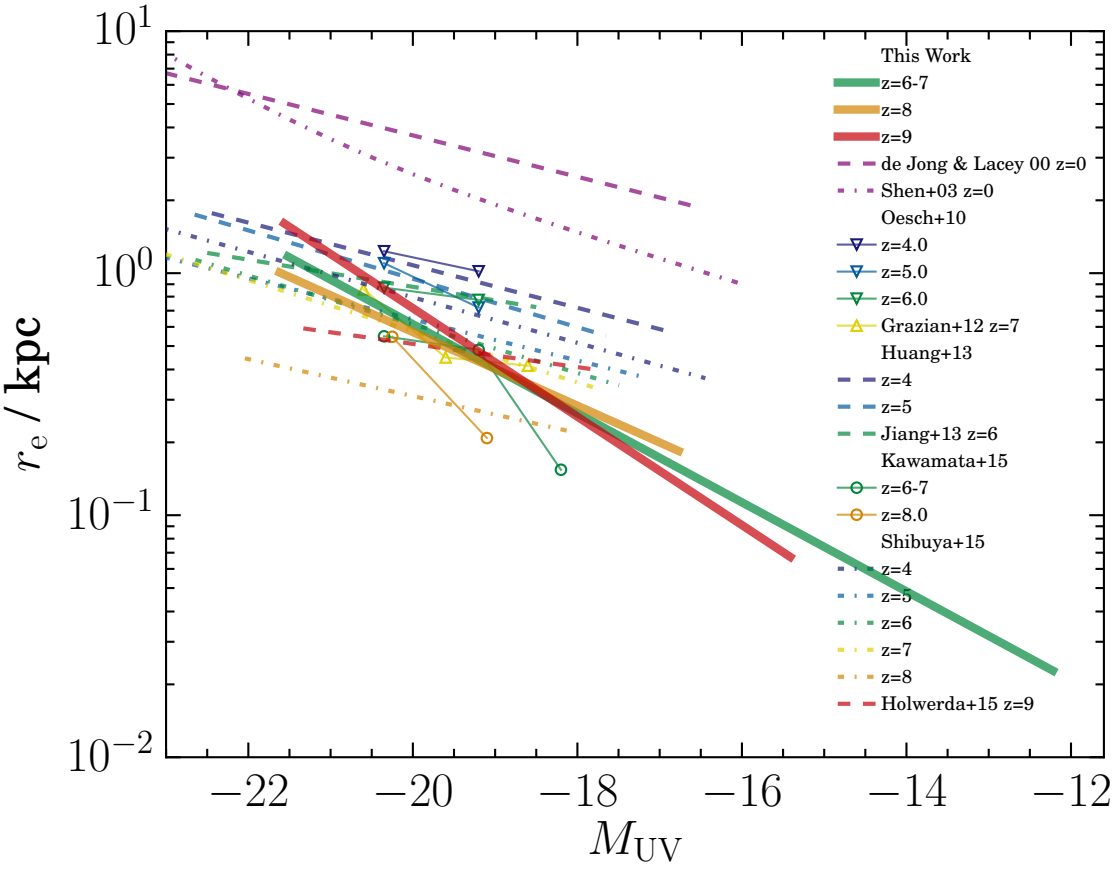

Figure 4.14 Compilation of size–luminosity relations of LBGs from $z \sim 4$ to $z \sim 9-10$ (Huang et al. 2013, Jiang et al. 2013 [LAEs+LBGs], Oesch et al. 2010a, Grazian et al. 2012, Kawamata et al. 2015, Shibuya et al. 2015, and Holwerda et al. 2015) and spiral galaxies at $z = 0$ (de Jong & Lacey 2000, Shen et al. 2003), with our results plotted by thick solid lines. Redshift is coded by color: purple, $z = 0$; violet, $z \sim 4$; blue, $z \sim 5$; green, $z \sim 6$ ($z \sim 6-7$ for our result); yellow, $z \sim 7$; orange, $z \sim 8$; and red, $z \sim 9-10$ ($z \sim 9$ for our result). Different symbols represent the average absolute magnitudes and sizes of different samples: inverse triangles, $z \sim 4-6$ samples by Oesch et al. (2010a); triangles, $z \sim 7$ sample by Grazian et al. (2012); and circles, $z \sim 6-8$ samples by Kawamata et al. (2015). The purple dashed and dot-dashed lines represent the relations of $z \sim 0$ disk galaxies obtained by the measurements in the i band by de Jong & Lacey (2000) and r band by Shen et al. (2003), respectively. The violet, blue, and green dashed lines represent the fitting results to the sample of $z \sim 4$ and 5 LBGs by Huang et al. (2013) and $z \sim 5.7-6.5$ Lyα emitters and LBGs by Jiang et al. (2013), respectively.

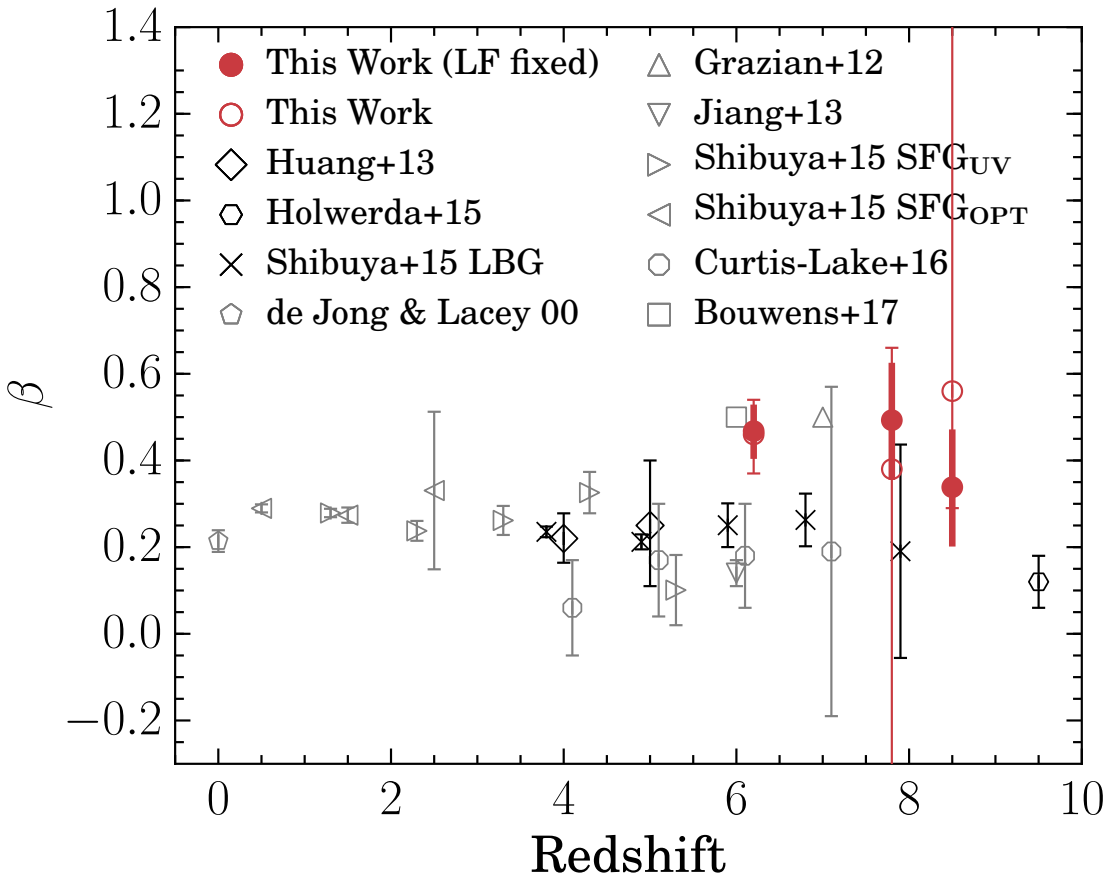

Figure 4.15 Redshift evolution of the slope of the size–luminosity relation. The red circles show our measurements, while black symbols show those of LBGs obtained by previous studies with two-dimensional profile fitting. The gray symbols represent results for non-LBG samples or those not based on two-dimensional profile fitting. The error bars correspond to the 1σ standard errors. The bold error bars of our samples show the 1σ standard errors where the parameters of the luminosity functions are fixed to the $z \sim 6-7$ best-fit values.

4.3.5 Redshift Evolution of Size

Figure 4.14 shows the redshift evolution of the size–luminosity relation. While Oesch et al. (2010a), Grazian et al. (2012), Huang et al. (2013), Holwerda et al. (2015), Kawamata et al. (2015), and Shibuya et al. (2015) showed the relations of LBGs, Roche et al. (1996), de Jong & Lacey (2000), and Jiang et al. (2013) showed those of irregular galaxies, local spiral galaxies, and a combined sample of Lyα emitters (LAEs) and LBGs, respectively. The slopes at $z \sim 6-9$ are slightly steeper than those at $z \lesssim 5$ and those derived from bright samples at $z \gtrsim 6$. This may suggest that physical processes that affect the slopes, such as the formation stage, feedback, and transfers and redistributions of angular momentum, differ at around $z \sim 6$, especially for faint galaxies.

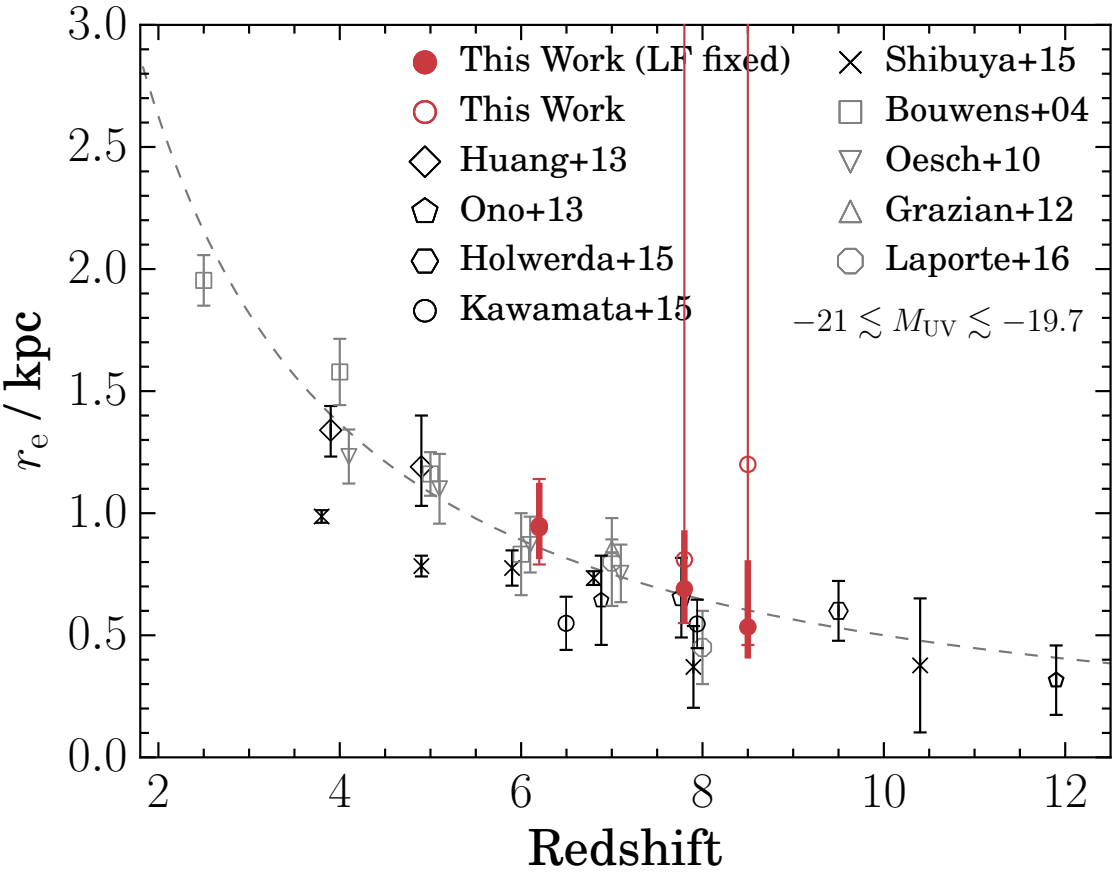

Figure 4.16 Redshift evolution of the average size of bright galaxies at $-21 \lesssim M_{\rm UV} \lesssim -19.7$. The red circles show our measurements, while the black symbols show those of LBGs obtained by previous studies. The gray dashed line represents the best-fit function of $r_{\rm e} \propto (1+z)^{-m}$ with $m = 1.28$. The error bars correspond to the 1σ standard errors. The bold error bars of our samples show the 1σ standard errors where the parameters of the luminosity functions are fixed to the $z \sim 6-7$ best-fit values.

Figure 4.15 shows the redshift evolution of β based on LBG samples by two-dimensional profile size measurements. While our fiducial values, where all uncertainties are considered, are plotted with red open circles and thin error bars, values where the parameters of the luminosity functions are fixed to the $z \sim 6-7$ best-fit values are plotted with red filled circles and bold error bars and presented in Table 4.2. For comparison, we also plot results from samples of non-LBGs and samples based on other size measurement methods. This figure shows that the slopes of our faint LBGs at $z \gtrsim 6$ are steeper than those of bright or lower-redshift galaxies, which are almost constant at $\beta \simeq 0.2$–0.3.

The redshift evolution of sizes at $-21 \lesssim M_{\rm UV} \lesssim -19.7$ ($(0.3-1)L^*_{z=3}$) is presented in Figure 4.16, where $L^*_{z=3}$ is the characteristic UV luminosity of $z \sim 3$ LBGs obtained in Steidel et al. (1999). Similar to Figure 4.15, we plot our fiducial values and values where the parameters of the luminosity functions are fixed. Our samples give consistent

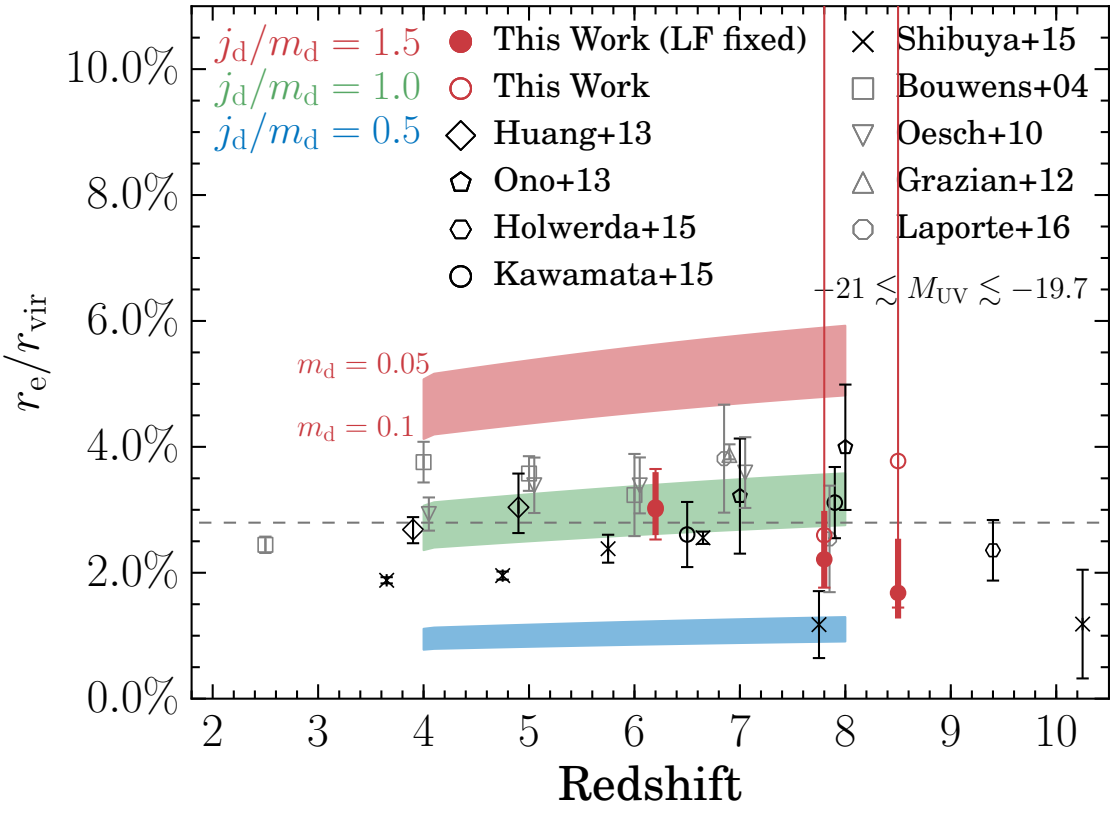

Figure 4.17 Redshift evolution of the galaxy size–halo size ratio. Our samples are shown with red circles, and those from previous studies are in black. The errors in disk sizes only (plotted in Figure 4.16) are considered. The gray dashed line shows the average size ratio. The red, green, and blue shaded bands represent the ratio predicted by the model described in Section 4.3.5 with $(j_d/m_d)_{M_{UV}=-21} = 1.5$, 1.0, and 0.5, respectively, where the width of each band indicates a weak dependence of the ratio on m_d and the upper and lower edges of each band correspond to $m_d = 0.05$ and 0.1, respectively.

results with previous measurements. We fit $r_e \propto (1+z)^{-m}$ to data that are based on two-dimensional size measurements at $4 < z < 9.5$ (except for those by Shibuya et al. 2015, because they seem to be considerably smaller than the others). For our data, we use the ones where the parameters of the luminosity functions are fixed for consistency with the previous studies. We obtain $m = 1.28 \pm 0.11$, which is consistent within the errors with previous work (Bouwens et al., 2004; Oesch et al., 2010a; Ono et al., 2013; Kawamata et al., 2015; Holwerda et al., 2015; Shibuya et al., 2015). The index is predicted by analytical models to be $m = 1.0$ for halos with a fixed mass and $m = 1.5$ for halos with a fixed circular velocity (e.g., Ferguson et al., 2004). We find that we trace halos in the middle of the two states, as reported in previous work.

We note that the difference in the luminosity range makes the comparison between the samples difficult. The average luminosities of individual samples plotted in Figure 4.14 have some variance, as shown in Table 4.3. For instance, at $z = 7$, a difference of 0.5 mag

in luminosity corresponds to a difference in stellar mass of $\Delta M^*/M^* = 54\%$, assuming the mass-luminosity relation in González et al. (2011). Based on the stellar mass–halo mass relation by Behroozi et al. (2013), the difference in stellar mass at $M_{\rm UV} = -21$ is equivalent to those in halo mass and halo radius of $\Delta M_{\rm vir}/M_{\rm vir} = 52\%$ and $\Delta r_{\rm vir}/r_{\rm vir} = 21\%$, respectively. Since the galaxy size is fundamentally proportional to the halo size, the expected galaxy size would differ $\Delta r_{\rm e}/r_{\rm e} = 21\%$. This means that the difference between samples in the luminosity range introduces a systematic uncertainty into the discussion of the evolution of the average size, which is conventional in previous studies.

In order to resolve the above problem and further investigate the size evolution of galaxies, we calculate the evolution of the galaxy size–halo size ratio following K15 (see also Shibuya et al., 2015). We calculate size ratios with a similar method to that for the model construction described in Section 4.3.3. In order to estimate the average halo size of each sample from its average luminosity, we make use of the stellar mass–luminosity relation in Reddy & Steidel (2009) at $z \sim 2.5$ and that in González et al. (2011) at $z \sim 4 - 9.5$, the stellar mass–halo mass relation (Behroozi et al., 2013), and Equation (4.13). Then, we obtain the size ratio by dividing the galaxy size by the halo size. The stellar mass–luminosity relation in González et al. (2011) is originally obtained at $z \sim 4-7$, but we also apply the relation at $z \sim 8-9.5$. In the above process, the variance in luminosity between the samples is corrected for because fainter samples are assigned smaller halo sizes. The result is shown in Figure 4.17. We confirm that the size ratio is roughly constant over the wide redshift range of $2.5 \lesssim z \lesssim 7.0$, and the average ratio is $2.80\% \pm 0.10\%$ over this redshift range. This value is in good agreement with those obtained in previous studies (Kawamata et al., 2015; Shibuya et al., 2015; Huang et al., 2017; Okamura et al., 2017; Somerville et al., 2017).

It appears from Figure 4.16 that the average size continues to decrease with redshift at $z \gtrsim 7$. This trend, if true, predicts that the size ratio starts to decrease at $z \gtrsim 7$ because the denominator (halo mass and hence halo size of $M_{\rm UV} \simeq -21$ galaxies) increases with redshift at $z \gtrsim 7$ according to the stellar mass–halo mass relation by Behroozi et al. (2013). This prediction is consistent with our size ratio measurements at $z \sim 8$ and 9 within the errors. This decreasing trend in the size ratio was not observed in our previous work, K15, because K15 linearly extrapolated the stellar mass–halo mass relation at $M_{\rm h} \simeq 10^{11} M_\odot$, while in reality, it has a knee at $M_{\rm h} \simeq 10^{11.3} M_\odot$, thus resulting in underestimation of the halo masses.

We compare the observed size ratios with those predicted by the model constructed in Section 4.3.3 with $\gamma = 0$,

$$\frac{r_{\rm e}}{r_{\rm vir}} = \frac{1.678}{\sqrt{2}} \left(\frac{j_{\rm d}}{m_{\rm d}} \right)_{M_{\rm UV}=-21} \lambda f_{\rm c}^{-1/2} f_{\rm R}. \tag{4.17}$$

Since $f_{\rm R}$ strongly depends on $j_{\rm d}/m_{\rm d}$ and weakly on $m_{\rm d}$, the only uncertain parameter to calculate the size ratio is $(j_{\rm d}/m_{\rm d})_{M_{\rm UV}=-21}$. Following K15, we change $(j_{\rm d}/m_{\rm d})_{M_{\rm UV}=-21}$ with the updated size measurements and simulation results of λ and c. Model-predicted size ratios are presented in Figure 4.17. Since they weakly depend on $m_{\rm d}$, we show with bands the uncertainty due to $m_{\rm d}$ within the range of $0.05 - 0.1$. If we assume the typical

value of 0.05 for $m_{\rm d}$ (e.g., Sales et al., 2010), we confirm that the observed size ratios are in good accordance with the model ratios premised on $j_{\rm d} \sim m_{\rm d}$ at $M_{\rm UV} = -21$. This is why we have assumed $(j_{\rm d}/m_{\rm d})_{M_{\rm UV}=-21} = 1.0$ and $m_{\rm d} = 0.05$, when modeling the size–luminosity relation in Section 4.3.3.

Using a mass-complete sample at $z \sim 1-7$ from the FourStar Galaxy Evolution Survey, Allen et al. (2017) have found a slower size evolution of $r_{\rm e} \propto (1+z)^{-0.97\pm0.02}$. Since the size evolution of LBGs is faster, they have concluded that LBGs do not represent the entire galaxy population. Considering their results, it should be noted that this study also might not be tracing the entire galaxy population at $z \sim 6-9$.

4.4 Summary

We have measured the intrinsic sizes and magnitudes of 334, 61, and 37 faint dropout galaxies at $z \sim 6-7$, 8, and 9, respectively, from the complete HFF data, properly correcting for the lensing effects by fitting the lensed images with lensing-distorted Sérsic profiles. These represent the largest samples, especially at faint magnitudes of $M_{\rm UV} = -18$ to -12, where luminosity function measurements have been made possible only recently. Systematic and random errors in sizes and magnitudes have been carefully estimated using Monte Carlo simulations.

Although the HFF observations reach the faintest galaxies with the help of cluster lensing, our samples still suffer from the incompleteness that faint but large galaxies are not detected in observations. Since the degree of incompleteness strongly depends on the intrinsic size–luminosity relation, we have conducted simultaneous maximum-likelihood estimation of the luminosity function and size–luminosity relation from the observed distribution of galaxies on the size–luminosity plane and examined correlations between the luminosity function and size–luminosity relation.

The following are the main results of this chapter.

i. We have found that the slope of the intrinsic size–luminosity relation of faint galaxies at $z \sim 6-7$ is considerably steeper ($\beta \simeq 0.46$) than those ($\beta \simeq 0.22$–0.25) at $z \sim 4-5$ and those ($\beta \simeq 0.25$) assumed in previous studies of the luminosity function at $z \sim 6-7$. As a result of the steep size–luminosity relation, a shallow faint-end slope of the luminosity function of $\alpha = -1.86^{+0.17}_{-0.18}$ has been derived. The values of β and α at $z \sim 8$ and 9 are consistent with those at $z \sim 6-7$ but have large errors due to small sample sizes. Thus, at $z \sim 8$ and 9, the UV luminosity density is still highly uncertain, which has to be taken into account in the discussion of cosmic reionization.
ii. We have quantified the correlation between the parameters of the size–luminosity relation and luminosity function. Among the parameter pairs, we have found strong correlations between the faint-end slope of the luminosity function and the slope of the size–luminosity relation, (α, β), and between the faint-end slope and the characteristic magnitude of the luminosity function, (α, $M_\star$). Although the values of α in several previous studies are consistent with our measurements, some of the previous results have been found to be located outside our confidence region in the α–β plane.

iii. We have constructed an analytical model to reproduce the steep slope of the size–luminosity relation at $z \sim 6-7$ utilizing the result of the abundance matching in Behroozi et al. (2013). We have found that the steepness is not reproduced when $j_{\rm d}/m_{\rm d}$ is constant within the magnitude range studied here. One possible explanation for the steepness is that a smaller fraction of the specific angular momentum is transferred to the disk from its halo at fainter magnitudes. Another possible explanation is that low-mass halos can host galaxies only when they have relatively small halo spin parameters.

iv. The average size at $(0.3-1)L^*_{z=3}$ gradually decreases with redshift with $(1+z)^{-m}$, where $m = 1.28 \pm 0.11$ over a redshift range of $4 \lesssim z \lesssim 9.5$. However, we have pointed out that this conventional discussion of the size evolution suffers from systematic biases due to a variance in average luminosity between the samples. In order to overcome this issue, we have calculated the disk-to-halo size ratio to find $j_{\rm d}/m_{\rm d} \sim 1$ at $M_{\rm UV} = -21$.

Chapter 5

Conclusion

In this thesis, we have investigated galaxies at $z \sim 6-9$ in order to probe for galaxy formation and evolution. We have constructed samples of faint Lyman break galaxies (334, 61, and 37 galaxies at $z \sim 6-7$, 8, and 9, respectively) from the complete *Hubble* Frontier Fields data. Our samples include very faint galaxies detected thanks to the strong gravitational lensing effects by the Frontier Fields clusters. The sizes and magnitudes of the galaxies in the samples have been carefully measured by a two-dimensional fitting algorithm using a lensing-distorted Sérsic profile. Using the sample, we have approached the galaxy luminosity evolution and kinematics evolution by determining luminosity functions and size–luminosity relations. In addition, we have discussed physical properties of $z \sim 6-9$ galaxies exploiting information on the size for the first time at these redshifts. The followings are the main results of this thesis.

i. In Chapter 3, we have conducted precise mass modeling of all six HFF clusters. We have used the positions of 132, 202, 173, 108, 141, and 135 multiple images to constrain the matter distributions of Abell 2744, MACS J0416.1−2403, MACS J0717.5+3745, MACS J1149.6+2223, Abell S1063, and Abell 370, respectively. Among them, 182 multiple images are new systems identified in this thesis. We have found that our best-fitting mass models reproduce the observed positions of multiple images quite well, with image plane RMS of $\sim 0\farcs4$. For Abell 2744, our best-fitting mass model recovers the observed magnification at the position of the Type Ia supernova HFF14Tom (Rodney et al., 2015). We have found that the predicted time delays and flux ratios of the quadruple images of SN Refsdal (Kelly et al., 2015) in MACS J1149.6+2223 are consistent with observations (Treu et al., 2016). All of our mass models are publicly available through the STScI website.

ii. In Sections 4.3.1 and 4.3.2, we have found that the slope of the intrinsic size–luminosity relation of faint galaxies at $z \sim 6$–7 is considerably steeper ($\beta \simeq 0.46$) than those ($\beta \simeq 0.22$–0.25) at $z \sim 4$–5 and those ($\beta \simeq 0.25$) assumed in previous studies of the luminosity function at $z \sim 6-7$. As a result of the steep size–luminosity relation, a shallow faint-end slope of the luminosity function of $\alpha = -1.86^{+0.17}_{-0.18}$ has been derived. The values of β and α at $z \sim 8$ and 9 are consistent with those at $z \sim 6$–7, but have large errors due to small sample sizes. Thus, at $z \sim 8$ and 9, the UV luminosity density is still highly uncertain, which has to be taken into account in the discussion

of cosmic reionization. We have also found strong correlations between the faint-end slope of the luminosity function and the slope of the size–luminosity relation, (α, β). When compared on the size–luminosity plane, although the values of α in several previous studies are consistent with our measurements, some of the previous results have been found to be located outside our confidence region in the α–β plane.

iii. In Section 4.3.3, we have constructed an analytical model to reproduce the steep slope of the size–luminosity relation at $z \sim 6-7$, utilizing the result of the abundance matching in Behroozi et al. (2013). We have found that the steepness is not reproduced when $j_{\rm d}/m_{\rm d}$ is constant within the magnitude range studied here. One possible explanation for the steepness is that a smaller fraction of the specific angular momentum is transferred to the disk from its halo at fainter magnitudes. Another possible explanation is that low-mass halos can host galaxies only when they have relatively small halo spin parameters.

iv. As described in Section 4.3.5, the average size at $(0.3-1)L^*_{z=3}$ gradually decreases with redshift with $(1+z)^{-m}$, where $m = 1.28 \pm 0.11$ over a redshift range of $4 \lesssim z \lesssim 9.5$. However, we have pointed out that this conventional discussion of the size evolution suffers from systematic biases due to a variance in average luminosity between the samples. In order to overcome this issue, we have calculated the disk-to-halo size ratio to find $j_{\rm d}/m_{\rm d} \sim 1$ at $M_{\rm UV} = -21$. This discussion of the specific angular momentum is made possible, because the luminosity dependency of the average sizes is cancelled out by dividing the sizes by luminosity-dependent halo sizes.

As summarized above, we have obtained observational constraints on the three aspects of galaxy evolution: luminosity, kinematics, and chemical evolutions.

We have found that the faint-end slope α of the luminosity function at $z \sim 6-7$ is shallower than previously suggested. The slope does not strongly evolve from lower redshifts around $z \sim 2$ (e.g., Reddy & Steidel, 2009). This implies that there is no significant luminosity evolution at faint magnitudes.

On the other hand, the sizes provide information on the kinematic evolution. We have found that the steep size–luminosity relation at $z \sim 6-7$ implies that disks of fainter galaxies have smaller amount of specific angular momenta. However, Huang et al. (2013) have reported that the slope of the relation at $z \sim 4-5$ is shallower at $\beta \sim 0.25$. This implies that, at $z \sim 4$–5, disks of fainter galaxies have almost the same amount of specific angular momenta as those of brighter galaxies have. This slope evolutions may suggests that disks of fainter galaxies at $z \sim 6-7$ acquire specific angular momenta more quickly than those of brighter galaxies. On the other hand, the size evolution toward smaller sizes with increasing redshifts has been confirmed with larger samples in this thesis. While $j_{\rm d}/m_{\rm d}$ of $(0.3-1)L^*_{z=3}$ galaxies at $2.5 \lesssim z \lesssim 7.0$ has found to be virtually constant at $j_{\rm d}/m_{\rm d} = 1.0$, it may decrease at $z \gtrsim 8$. This implies that, at a fixed magnitude of $M_{\rm UV} \simeq -21$, disks of galaxies acquire specific angular momenta probably because of stellar feedbacks or that galaxies start to form in halos with larger spin parameters from $z \gtrsim 8$ to $z \sim 7$. At $2.5 \lesssim z \lesssim 7.0$ on the other hand, disks of galaxies preserve the amount of specific angular momenta.

In Appendix A, we further investigate properties of galaxies in our sample from the perspectives of the evolution stage, merger rate, and mode of star formation.

One of the important goals of the HFF is to provide prior information on very faint high-redshift galaxies that will be observed by the *James Webb Space Telescope (JWST)*. Our findings, especially the shallower faint-end slope α and smaller galaxy sizes at fainter magnitudes than previously suggested, are very important in terms of building effective observing strategies of the *JWST*.

Appendix A

Properties of $z \sim 6-9$ Galaxies

A.1 Introduction

In Chapter 4, we have intensively discussed the galaxy distributions on the size–luminosity plane and the evolution of average galaxy sizes. In this chapter, we discuss their evolution stage, merger rate, and efficiency of star-formation combining the information of sizes and magnitudes obtained in Chapter 4. To do so, we calculate galaxy UV continuum slopes β ($f_\lambda \propto \lambda^\beta$), multiplicities, and star-formation surface densities $\Sigma_{\rm SFR}$. Since our galaxies are too faint to conduct spectroscopy, we are not able to obtain detailed galaxy properties from their spectral energy distributions. On the other hand, the above three parameters are relatively easy to derive because only broad-band imaging is needed.

Galaxy UV continuum slopes are affected mainly by dust extinction, age, and metallicity. Galaxies with higher dust extinction, older ages, and higher metallicities have redder UV continuum slopes. These galaxies are typically thought to be more evolved and mature. Measurements of UV continuum slopes at $z \sim 6-9$ are conducted in several studies (e.g., Dunlop et al., 2013; Bouwens et al., 2014). They have reported modest slopes of $\beta \simeq -2.1$ at $M_{\rm UV} = -18$, being slightly bluer at fainter magnitudes. They have concluded that these slopes are interpreted by star-forming galaxies with $\simeq$ solar metallicity and zero dust, or modest sub-solar metallicity and moderate dust extinction. Significantly large scatters in the measured slope have also been found in their samples. Dunlop et al. (2013) have attributed the scatter to observational biases and shown that the measured slopes are consistent with $\beta = -2$ using a end-to-end simulation.

However, no previous study at $z \gtrsim 6$ has compared UV slopes with galaxy sizes, although both the size and UV slope may be tracers of the evolution stage of a galaxy. The reason for the size being a tracer is that, at a fixed luminosity or stellar mass, more evolved galaxies can experience more stellar feedbacks, which results in larger specific angular momenta in the disks and hence in larger sizes (e.g., DeFelippis et al., 2017). If there is a strong correlation between sizes and UV slopes, then the scatter in the size at a fixed luminosity may be one of reasons of the large scatter in the UV slope.

Galaxies with multiple cores can be identified using only imaging data by visual inspection. Multiple cores can be regarded as a sign of a recent merging event. Many papers have estimated the fraction of galaxies with multiple cores at high redshift (e.g. Ravin-

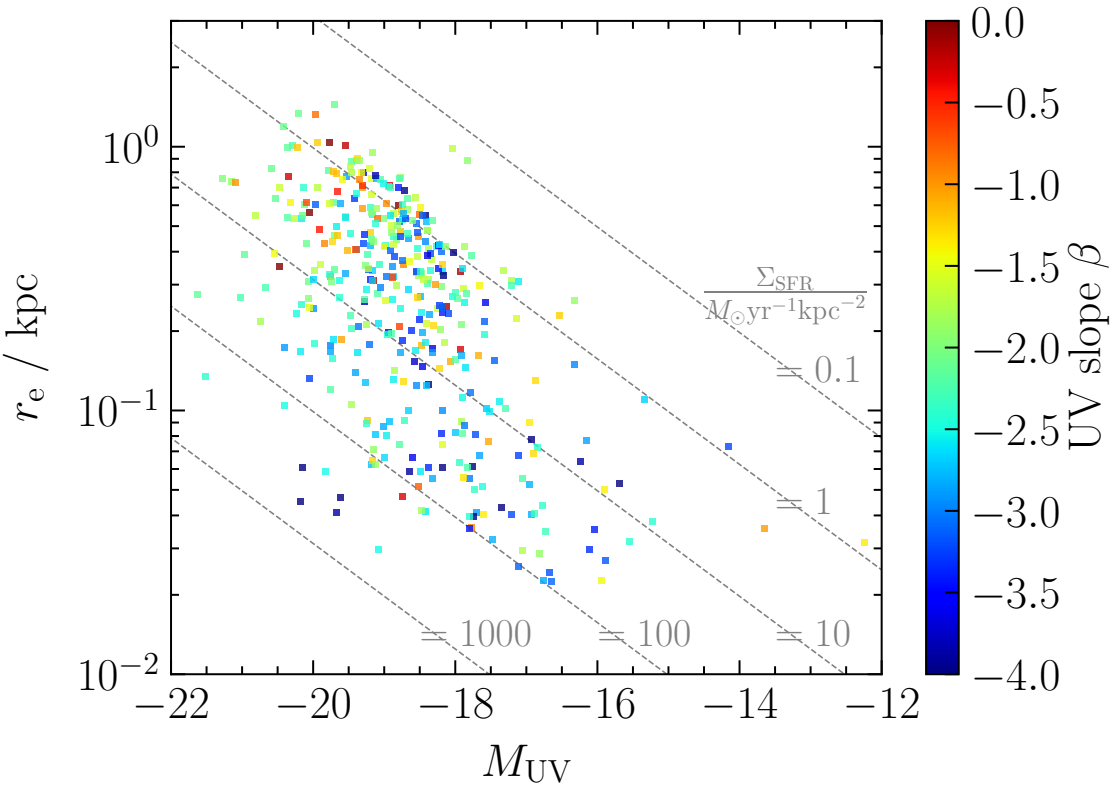

Figure A.1 Size–luminosity relation for the merged sample of $z \sim 6-8$. Galaxies are color-coded by the UV power-law index, β. The solid lines correspond to constant star formation surface densities of $\Sigma_{SFR}/(M_\odot yr^{-1} kpc^{-2}) = 0.1, 1, 10, 100$, and 1000.

dranath et al., 2006; Lotz et al., 2008; Oesch et al., 2010a; Law et al., 2012; Guo et al., 2012; Jiang et al., 2013). For example, Ravindranath et al. (2006) have reported that 30% of $z \sim 3$ LBGs have multiple cores, and Jiang et al. (2013) have found that 40%–50% of bright ($M_{UV} \leq -20.5$) galaxies at $5.7 \leq z \leq 7.0$ have multiple cores.

The physical state of star formation of a galaxy is effectively described by the total *SFR* and the Σ_{SFR}. While the former is just the scale of star formation, the latter corresponds to the intensity of star formation and is useful for discussing the mode of star formation. Since $z \gtrsim 6$ LBGs have higher *SFR*s and small sizes, their Σ_{SFR}s are considerably higher than those of local normal galaxies (e.g., Oesch et al., 2010a; Ono et al., 2013). It is informative to compare the state of star formation of the LBGs in our samples with those of local galaxies, which are well investigated.

The structure of this chapter is as follows. In Sections A.2 and A.3, we discuss the UV slopes and multiplicities of our galaxies on the size–luminosity plane, respectively. The state of star formation of our galaxies is compared with those of local galaxies in Section A.4. Finally, we summarize our results in Section A.5.

A.2 UV Color

Figure A.2 plots half-light radii against UV luminosities for all the galaxies in the combined sample, colored according to the UV slope β that is defined as $f_\lambda \propto \lambda^\beta$ with f_λ being the UV continuum flux density with respect to wavelength λ. We calculate β using the equations given in Bouwens et al. (2013): $\beta = -2.0 + 4.39(J_{125} - H_{160})$ for $z \sim 6-7$ and $\beta = -2.0 + 8.98(JH_{140} - H_{160})$ for $z \sim 8$. The UV slope β for $z \sim 9$ galaxies cannot be calculated from the *HST* images obtained in the HFF project. For each redshift, the range of β in our sample is consistent with those of Bouwens et al. (2013) and Dunlop et al. (2013).

We also find that largest (> 0.8 kpc) galaxies are mostly red and smallest (< 0.08 kpc) galaxies are mostly blue, while the remainings do not show a very strong trend. There are mainly three factors that make galaxies red: high dust extinction, old age, and high metallicity. Since these three characteristics are often seen in evolved galaxies, selecting largest galaxies may lead to effectively picking out evolved galaxies at the redshifts studied here.

A.3 Multiplicity

We also examine if galaxies with multiple cores have any preference in size or luminosity. We identify galaxies with multiple cores in our sample by visual inspection, considering the claim by Jiang et al. (2013) that while galaxies at $z \gtrsim 6$ are too small and faint for quantitative morphological analysis, visual inspection is still valid for examining whether or not a galaxy has multiple cores. Galaxies with multiple cores are marked in red in Figure A.2. Forty-three galaxies, or 10% of the sample, are found to have multiple cores. This fraction is similar to that derived by Oesch et al. (2010a) at similar redshifts. As seen in the galaxy images summarized in Appendix, for most of the galaxies with multiple cores, the primary cores are distinct compared to the secondary or later cores, which perhaps implies relatively minor mergers.

As can be seen from Figure A.2, most of the galaxies with multiple cores are bright ($M_{\rm UV} \lesssim -20$), qualitatively consistent with the trend seen in the sample of Oesch et al. (2010a) that brighter galaxies tend to have multiple cores. More specifically, in the sample of Oesch et al. (2010a), the brightest and fourth brightest galaxies have multiple cores among the 16 $z \sim 7$ galaxies. In our sample, five of the eight galaxies ($M_{\rm UV} \leq -21$) at $z \sim 6-9$ have multiple cores. On the other hand, we find that the sizes of galaxies with multiple cores are distributed widely from 0.03 kpc to 1.2 kpc.

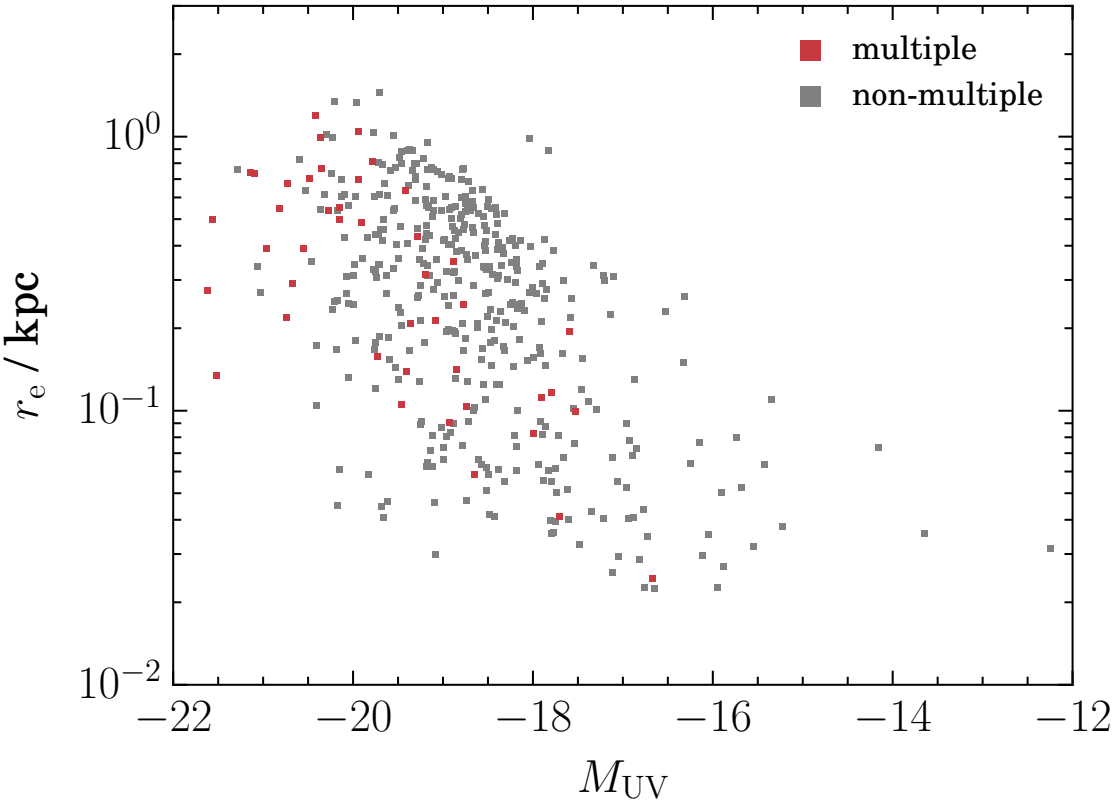

Figure A.2 Size–luminosity relation for the merged sample of $z \sim 6-9$. Galaxies with multiple cores are plotted in red.

A.4 *SFR* Surface Density

We calculate the *SFR* and $\Sigma_{\rm SFR}$ for our galaxies with equations (3) from Kennicutt (1998) and (4) from Ono et al. (2013), respectively:

$$\frac{SFR}{M_\odot {\rm yr}^{-1}} = 1.4 \times 10^{-28} \frac{L_\nu}{{\rm erg\ s^{-1}\ Hz^{-1}}} \tag{A.1}$$

$$\Sigma_{\rm SFR} = \frac{SFR/2}{\pi {r_e}^2}. \tag{A.2}$$

The log-average $\Sigma_{\rm SFR}$s of $(0.3-1)L^*_{z=3}$ galaxies are 6.2 $M_\odot {\rm yr}^{-1}{\rm kpc}^{-2}$ at $z \sim 6-7$, 7.4 $M_\odot {\rm yr}^{-1}{\rm kpc}^{-2}$ at $z \sim 8$, and 5.2 $M_\odot {\rm yr}^{-1}{\rm kpc}^{-2}$ at $z \sim 9$, slightly higher than 3.5 $M_\odot {\rm yr}^{-1}{\rm kpc}^{-2}$ at $z \sim 7$ and 3.2 $M_\odot {\rm yr}^{-1}{\rm kpc}^{-2}$ at $z \sim 8$ by Ono et al. (2013).

As found from Figure A.2, our galaxies are forming stars with a rate of $SFR \sim 0.1-10$ $M_\odot {\rm yr}^{-1}$ and with a surface intensity of $\Sigma_{\rm SFR} \sim 1-100$ $M_\odot {\rm yr}^{-1}{\rm kpc}^{-2}$. This $\Sigma_{\rm SFR}$ range is slightly wider toward higher values than reported by Ono et al. (2013) based on HUDF12, reflecting the fact that our galaxies are distributed over a wider area in the size–luminosity plane than those of Ono et al. (2013). Our sample extends especially toward smaller half-light radii.

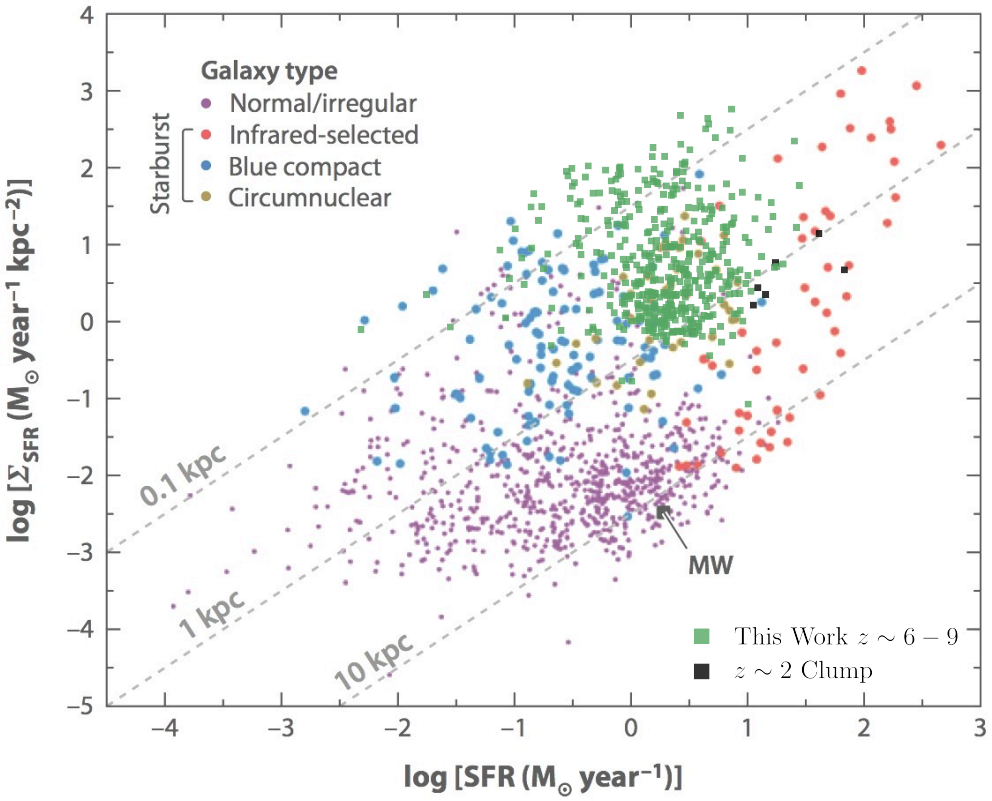

Figure A.3 Distribution of our galaxies in the *SFR*–$\Sigma_{\rm SFR}$ plane, overplotted with a various types of local galaxies and star-forming clumps of $z \sim 2$ galaxies (Genzel et al., 2011). Plotted on Fig. 9 in Kennicutt & Evans (2012).

We show in Figure A.3 the distribution in the *SFR*–$\Sigma_{\rm SFR}$ plane of our galaxies and various types of local galaxies, in order to examine in what sense the state of star formation of $z \sim 6-9$ galaxies are similar or dissimilar to local ones. Comparison to normal galaxies finds that our galaxies have much higher (typically three orders of magnitude higher) $\Sigma_{\rm SFR}$s than normal galaxies in spite of having modest *SFR*s similar to that of the Milky Way. In other words, $z \sim 6-9$ galaxies are forming stars at similar rates to local normal galaxies but in 10^3 times smaller areas.

Our galaxies are roughly comparable in $\Sigma_{\rm SFR}$ to average infrared-selected galaxies and to blue compact galaxies, while falling between these two galaxy populations in *SFR*. It is circumnuclear regions that resembles our galaxies most. Circumnuclear regions are not the whole bodies of galaxies but starbursting rings at the center of a certain type of galaxies in which gas is effectively fed along bars. This resemblance may suggest that $z \sim 6-9$ galaxies have a similar amount of cold gas of a similarly high density to that of circumnuclear regions.

Ono et al. (2013) have found that the $\Sigma_{\rm SFR}$s of $z \sim 7-8$ galaxies are comparable to those of infrared-selected galaxies and circumnuclear regions. While we confirm this finding above, we also find that infrared-selected galaxies are scaled-up systems in terms

of *SFR*.

Finally, we find that our galaxies have similar $\Sigma_{\rm SFR}$s but slightly lower *SFR*s than star-forming clumps of $z \sim 2$ galaxies taken from Genzel et al. (2011) (black dots in Figure A.3). In this sense, $z \sim 6-9$ galaxies may be considered to be scaled-down systems of clumps.

In this subsection we have neglected dust extinction. If we use UV slope to calculate the extinction at 1600Å, A_{1600}, according to Meurer et al. (1999)'s formula, we find a median $A_{1600} = 1.2$ in our sample, corresponding to a factor 2.9 increase in *SFR* (and $\Sigma_{\rm SFR}$). Therefore, if Meurer et al. (1999)'s formula is still applicable to $z \sim 6-9$ galaxies (although they could have very different stellar populations and dust properties from local starbursts), then a significant fraction of our galaxies enter the region in the *SFR*–$\Sigma_{\rm SFR}$ plane occupied by local infrared-selected galaxies.

A.5 Summary

We have measured the UV colors, multiplicities, and star-formation surface densities of the galaxies in the $z \sim 6-9$ samples constructed in Chapter 2. These parameters indicate, respectively, the degree of chemical evolution, recent mergers, and the efficiency of star formation. The UV colors are calculated from aperture magnitudes of two bands and the multiplicities are identified by visual inspection. These analyses are the first to incorporate the information of size into discussions of the two parameters at $z \sim 6-9$. The efficiencies of star formation are calculated from their UV magnitudes and sizes. Comparing these efficiencies to those of local galaxies have been conducted also for the first time in this thesis.

The followings are the main results of this chapter.

i. We have found that largest ($r_{\rm e} > 0.8$ kpc) galaxies are mostly bright and red in UV color while smallest ($r_{\rm e} < 0.08$ kpc) ones mostly blue, and that galaxies with multiple cores tend to be bright.
ii. The $\Sigma_{\rm SFR}$s of $z \sim 6-9$ galaxies are typically three orders of magnitude higher than those of local normal spiral galaxies. The distribution of our galaxies in the *SFR*–$\Sigma_{\rm SFR}$ plane is largely overlapped with that of circumnuclear star-forming regions in local barred galaxies, which may suggest a similarity in the environment of star formation.

Size measurements for high-redshift samples help advance our understanding of galaxy formation and evolution through galaxy size studies, which provide complementary information to luminosity and color studies.

The $z \sim 6-9$ galaxies in our samples have higher *SFR*s than those of normal galaxies in the local universe on average. Furthermore, because of their smaller sizes, they have turned out to form stars very efficiently, that is, have higher $\Sigma_{\rm SFR}$s. This means that they grow rapidly despite their small physical sizes.

We have also found that most of the brightest galaxies have multiple cores, which imply major mergers, and the fraction of galaxies with multiple cores is $\sim 10\%$. This

may suggest that UV magnitudes, i.e., *SFR* are enhanced for $\sim 10\%$ of all galaxies. In order to investigate evolution of merger rate, which is related to both luminosity and kinematics evolutions, we should compare merger rates at each magnitude with those at lower redshifts, but the sizes of our samples at $z \sim 6-9$ are not large enough for that analysis.

Appendix B

Lists of Multiple Images Used for Mass Modeling

Table B.1. Abell 2744 Multiple Image Systems

ID	R.A.	Decl.	$z_{\rm spec}$	$z_{\rm model}$	Photo-z Prior	References[a]
1.1	3.597542	−30.403917	1.688	···	···	JM, GM
1.2	3.595958	−30.406822		···	···	JM
1.3	3.586208	−30.409986		···	···	JM
2.1	3.583250	−30.403350	1.888	···	···	JM, GM
2.2	3.597292	−30.396725		···	···	JM
2.4	3.586417	−30.402128		···	···	JM
3.1	3.589480	−30.393867	3.980	···	···	JM, TJ
3.2	3.588647	−30.393788		···	···	JM
4.1	3.592125	−30.402633	3.580	···	···	JM, JR
4.2	3.595625	−30.401622		···	···	JM
4.3	3.580417	−30.408925		···	···	JM
4.4	3.593208	−30.404914		···	···	JR
4.5	3.593583	−30.405106		···	···	JR
5.2	3.584982	−30.391374	4.022	···	···	JM, GM
5.3	3.579959	−30.394772		···	···	JM
6.1	3.598535	−30.401797	2.019	···	···	JM, JR
6.2	3.594042	−30.408011		···	···	JM
6.3	3.586417	−30.409372		···	···	JM
7.1	3.598261	−30.402322	···	$2.65^{+0.13}_{-0.12}$	3.25 ± 0.5	JM
7.2	3.595233	−30.407407	···			JM
7.3	3.584601	−30.409818	···			JM
8.1	3.589708	−30.394339	3.975	···	···	JM
8.2	3.588834	−30.394222		···	···	JM, GM
9.1	3.588375	−30.405272	···	$2.46^{+0.36}_{-0.30}$	···	JM
9.2	3.587125	−30.406242	···		···	JM
10.1	3.588417	−30.405878	2.656	···	···	JM, GM
10.2	3.587375	−30.406481		···	···	JM
11.1	3.591375	−30.403858	···	$2.57^{+0.12}_{-0.11}$	···	JM
11.2	3.597264	−30.401431	···		···	JM
11.3	3.582792	−30.408914	···		···	JM
11.4	3.594542	−30.406542	···		···	JR
12.2	3.593239	−30.403249	···	$3.12^{+0.46}_{-0.42}$	2.80 ± 0.5	JR
12.3	3.594555	−30.402996	···			JR
13.1	3.592375	−30.402558	···	$1.41^{+0.04}_{-0.04}$	···	JR
13.2	3.593792	−30.402164	···		···	JR
13.3	3.582792	−30.408044	···		···	JR
14.1	3.589750	−30.394636	···	$2.58^{+0.12}_{-0.12}$	···	JR
14.2	3.588458	−30.394436	···		···	JR
14.3	3.577577	−30.401682	···		···	MJ
18.1	3.590750	−30.395561	5.660	···	···	JR, XW
18.2	3.588375	−30.395636		···	···	JR
18.3	3.576123	−30.404489		···	···	DL
20.1	3.596234	−30.402976	···	$2.55^{+0.12}_{-0.11}$	···	DL
20.2	3.595172	−30.405442	···		···	DL
20.3	3.581992	−30.409550	···		···	MJ
21.1	3.596176	−30.403117	···	$2.55^{+0.12}_{-0.11}$	···	DL
21.2	3.595259	−30.405342	···		···	DL
21.3	3.581973	−30.409600	···		···	MJ
22.1	3.587919	−30.411613	5.284	···	···	DL, GM
22.2	3.600059	−30.404395		···	···	HA14
22.3	3.596572	−30.409000		···	···	HA14
23.1	3.588157	−30.410550	···	$4.53^{+0.38}_{-0.32}$	···	DL
23.2	3.593552	−30.409709	···		···	HA14
23.3	3.600541	−30.401816	···		···	HA14

Table B.1 (cont'd)

ID	R.A.	Decl.	$z_{\rm spec}$	$z_{\rm model}$	Photo-z Prior	References[a]
24.1	3.595902	−30.404467	1.043	···	···	MJ, GM
24.2	3.595114	−30.405909		···	···	MJ
24.3	3.587332	−30.409095		···	···	MJ
25.1	3.594476	−30.402742	···	$1.22^{+0.03}_{-0.03}$	···	MJ
25.2	3.592147	−30.403317	···		···	MJ
25.3	3.584215	−30.408284	···		···	MJ
26.1	3.593906	−30.409726	3.054	···	···	DL, GM
26.2	3.590350	−30.410584		···	···	DL
26.3	3.600099	−30.402976		···	···	DL
28.1	3.580452	−30.405043	···	$6.67^{+0.43}_{-0.42}$	6.70 ± 0.5	HA14
28.2	3.597831	−30.395958	···			HA14
28.3	3.585321	−30.397958	···			HA14
28.4	3.587442	−30.401376	···			DL
29.1	3.582437	−30.397575	···	$3.31^{+0.43}_{-0.38}$	···	MJ
29.2	3.580524	−30.400475	···		···	MJ
30.1	3.591016	−30.397439	1.025	···	···	MJ, GM
30.2	3.586669	−30.398184		···	···	MJ
30.3	3.581923	−30.401704		···	···	MJ
31.1	3.585925	−30.403159	4.760	···	···	DL, GM
31.2	3.583703	−30.404100		···	···	DL
32.1	3.583605	−30.404712	···	$4.46^{+0.40}_{-0.32}$	···	MJ
32.2	3.586667	−30.403337	···		···	MJ
32.3	3.599789	−30.395980	···		···	MJ
33.1	3.584708	−30.403152	5.726	···	···	HA14, GM
33.2	3.584396	−30.403400		···	···	HA14
33.3	3.600418	−30.395110		···	···	GM
34.1	3.593427	−30.410847	3.785	···	···	MJ, GM
34.2	3.593813	−30.410723		···	···	MJ
34.3	3.600711	−30.404604		···	···	MJ
39.1	3.588792	−30.392530	4.015	···	···	MJ, GM
39.2	3.588542	−30.392508		···	···	MJ
39.3	3.577479	−30.399568		···	···	JM
40.1	3.589086	−30.392668	4.000	···	···	MJ, GM
40.2	3.588193	−30.392551		···	···	MJ
40.3	3.577544	−30.399376		···	···	JM
41.1	3.599176	−30.399582	4.911	···	···	MJ, GM
41.2	3.593558	−30.407769		···	···	MJ
41.3	3.583446	−30.408500		···	···	MJ
41.4	3.590617	−30.404459		···	···	GM
42.1	3.597306	−30.400612	3.692	···	···	MJ, GM
42.2	3.590961	−30.403255		···	···	MJ
42.3	3.581584	−30.408635		···	···	MJ
42.4	3.594229	−30.406390		···	···	MJ
42.5	3.592413	−30.405194		···	···	GM
46.1	3.595007	−30.400759	···	$9.52^{+0.45}_{-0.41}$	9.50 ± 0.5	AZ
46.2	3.592505	−30.401500	···			AZ
46.3	3.577519	−30.408700	···			AZ
47.1	3.590162	−30.392181	4.022	···	···	GM, GM
47.2	3.585842	−30.392244		···	···	MJ
47.3	3.578329	−30.398133		···	···	MJ
50.1	3.577973	−30.401600	···	$5.65^{+0.53}_{-0.47}$	···	MJ
50.2	3.593956	−30.394287	···		···	MJ
53.1	3.579838	−30.401592	···	$5.54^{+0.82}_{-0.72}$	···	DL
53.2	3.583548	−30.396700	···		···	DL

Table B.1 (cont'd)

ID	R.A.	Decl.	$z_{\rm spec}$	$z_{\rm model}$	Photo-z Prior	References[a]
54.1	3.592350	−30.409892	···	$5.98^{+0.70}_{-0.55}$	···	DL
54.2	3.588254	−30.410325	···		···	DL
54.5	3.600920	−30.400825	···		···	DL
55.1	3.597042	−30.404753	···	$1.70^{+0.05}_{-0.05}$	···	DL
55.2	3.596417	−30.406125	···		···	DL
55.3	3.585744	−30.410100	···		···	DL
56.1	3.582542	−30.402272	···	$1.97^{+0.07}_{-0.07}$	···	DL
56.2	3.586250	−30.400850	···		···	DL
56.3	3.584500	−30.399286	···		···	DL
56.4	3.596750	−30.396300	···		···	DL
59.1	3.584284	−30.408925	···	$2.49^{+0.13}_{-0.12}$	···	MI
59.2	3.598125	−30.400981	···		···	MI
60.1	3.598075	−30.403989	···	$1.71^{+0.06}_{-0.06}$	1.70 ± 0.5	DL
60.2	3.595729	−30.407558	···			DL
60.3	3.587384	−30.410158	···			DL
61.1	3.595533	−30.403499	2.951	···	···	GM, GM
61.2	3.595143	−30.404495		···	···	MJ
63.1	3.582261	−30.407166	5.662	···	···	GM, GM
63.2	3.592758	−30.407022		···	···	GM
63.3	3.589134	−30.403419		···	···	GM
63.4	3.598805	−30.398279		···	···	XW
147.1	3.589679	−30.392136	4.022	···	···	MJ, GM
147.2	3.586454	−30.392128		···	···	MJ
147.3	3.578009	−30.398392		···	···	GM

[a]JM—Merten et al. (2011), HA14—Atek et al. (2014), JR—Richard et al. (2014), AZ—Zitrin et al. (2014), DL—Lam et al. (2014), TJ—Johnson et al. (2014), MI—Ishigaki et al. (2015), MJ—Jauzac et al. (2015a), XW—Wang et al. (2015), GM—Mahler et al. (2018).

Table B.2. MACS J0416.1−2403 Multiple Image Systems

ID	R.A.	Decl.	$z_{\rm spec}$	$z_{\rm model}$	Photo-z Prior	References[a]
1.1	64.040797	−24.061616	1.896	···	···	AZ, LC
1.2	64.043472	−24.063514		···	···	AZ
1.3	64.047367	−24.068673		···	···	AZ
2.1	64.041168	−24.061851	1.893	···	···	AZ, CG
2.2	64.043021	−24.063010		···	···	AZ
2.3	64.047484	−24.068851		···	···	AZ
3.1	64.030772	−24.067118	1.989	···	···	AZ, CG
3.2	64.035254	−24.070993		···	···	AZ
3.3	64.041797	−24.075743		···	···	AZ
4.1	64.030782	−24.067218	1.989	···	···	AZ, CG
4.2	64.035181	−24.071001		···	···	AZ
4.3	64.041834	−24.075826		···	···	AZ
5.2	64.032637	−24.068647	2.095	···	···	AZ, AH
5.3	64.033531	−24.069452		···	···	AZ
5.4	64.043554	−24.076957		···	···	AZ
6.1	64.040013	−24.061830	···	$6.37^{+0.33}_{-0.33}$	6.30 ± 0.5	AZ
6.2	64.041600	−24.062680	···			AZ
6.3	64.049342	−24.072247	···			RK16
7.1	64.039808	−24.063085	2.086	···	···	AZ, CG
7.2	64.040652	−24.063578		···	···	AZ
7.3	64.047101	−24.071103		···	···	AZ
8.1	64.036602	−24.066122	···	$2.01^{+0.06}_{-0.07}$	···	AZ
8.2	64.036837	−24.066332	···		···	AZ
8.3	64.046069	−24.075174	···		···	RK16
9.1	64.027032	−24.078564	···	$2.04^{+0.06}_{-0.06}$	···	AZ
9.2	64.027521	−24.079095	···		···	AZ
9.3	64.036450	−24.083976	···		···	MJ
10.1	64.026027	−24.077175	2.298	···	···	AZ, CG
10.2	64.028458	−24.079749		···	···	AZ
10.3	64.036698	−24.083885		···	···	AZ
11.1	64.039269	−24.070410	1.006	···	···	AZ, SR
11.2	64.038302	−24.069735		···	···	AZ
11.3	64.034232	−24.066012		···	···	AZ
12.1	64.038256	−24.073685	···	$1.68^{+0.12}_{-0.09}$	···	AZ
12.2	64.037690	−24.073301	···		···	AZ
13.1	64.027579	−24.072768	3.223	···	···	AZ, CG
13.2	64.032132	−24.075151		···	···	AZ
13.3	64.040336	−24.081532		···	···	AZ
14.1	64.026237	−24.074330	1.637	···	···	AZ, CG
14.2	64.031038	−24.078958		···	···	AZ
14.3	64.035826	−24.081317		···	···	AZ
15.1	64.026865	−24.075740	2.336	···	···	MJ, AH
15.2	64.029449	−24.078585		···	···	AZ
16.1	64.024075	−24.080905	1.964	···	···	AZ, AH
16.2	64.028342	−24.084548		···	···	AZ
16.3	64.031596	−24.085759		···	···	AZ
17.1	64.029814	−24.086351	2.218	···	···	AZ, CG
17.2	64.028609	−24.085968		···	···	AZ
17.3	64.023343	−24.081585		···	···	AZ
18.1	64.026096	−24.084238	···	$2.03^{+0.08}_{-0.07}$	···	AZ
18.2	64.025061	−24.083325	···		···	AZ
23.1	64.044550	−24.072075	2.091	···	···	AZ, AH
23.2	64.039586	−24.066633		···	···	AZ
23.3	64.034321	−24.063719		···	···	AZ

Table B.2 (cont'd)

ID	R.A.	Decl.	$z_{\rm spec}$	$z_{\rm model}$	Photo-z Prior	References[a]
25.1	64.044873	−24.061043	···	$2.40^{+0.09}_{-0.08}$	···	AZ
25.2	64.045457	−24.061410	···		···	AZ
25.3	64.048241	−24.064501	···		···	MJ
25.4	64.049650	−24.066800	···		···	AZ
26.1	64.046460	−24.060396	3.238	···	···	MJ, GC
26.2	64.046962	−24.060792		···	···	MJ
26.3	64.049083	−24.062857		···	···	MJ
27.1	64.048153	−24.066957	2.107	···	···	MJ, AH
27.2	64.047480	−24.066017		···	···	MJ
27.3	64.042253	−24.060543		···	···	MJ
29.1	64.034270	−24.062989	2.285	···	···	MJ, AH
29.2	64.040469	−24.066330		···	···	RK16
29.3	64.044631	−24.071479		···	···	MJ
30.1	64.033043	−24.081763	···	$2.76^{+0.87}_{-0.63}$	···	MJ
30.2	64.032671	−24.081576	···		···	MJ
31.1	64.023814	−24.077592	···	$1.81^{+0.05}_{-0.05}$	1.85 ± 0.5	MJ
31.2	64.030489	−24.082676	···			MJ
31.3	64.032415	−24.083751	···			MJ
33.1	64.028409	−24.083001	5.365	···	···	MJ, GC
33.2	64.035060	−24.085512		···	···	MJ
33.3	64.022992	−24.077267		···	···	MJ
34.1	64.029291	−24.073323	···	$5.74^{+0.36}_{-0.35}$	5.25 ± 0.5	MJ
34.2	64.030782	−24.074169	···			MJ
34.3	64.042074	−24.082294	···			RK16
35.1	64.037471	−24.083651	3.492	···	···	MJ, GC
35.2	64.029412	−24.079887		···	···	MJ
35.3	64.024950	−24.075019		···	···	MJ
37.1	64.033800	−24.082883	···	$2.99^{+0.12}_{-0.11}$	···	MJ
37.2	64.031403	−24.081635	···		···	MJ
37.3	64.022888	−24.074327	···		···	RK16
38.1	64.033627	−24.083182	3.440	···	···	MJ, GC
38.2	64.031252	−24.081896		···	···	MJ
38.3	64.022698	−24.074590		···	···	MJ
40.1	64.037353	−24.063060	···	$2.40^{+0.08}_{-0.08}$	···	MJ
40.2	64.040356	−24.064276	···		···	MJ
40.3	64.047109	−24.072435	···		···	RK16
41.1	64.037189	−24.063076	···	$2.42^{+0.09}_{-0.08}$	···	MJ
41.2	64.040365	−24.064368	···		···	MJ
41.3	64.047064	−24.072493	···		···	RK16
42.1	64.046020	−24.070753	···	$2.53^{+0.09}_{-0.09}$	···	MJ
42.2	64.042057	−24.065560	···		···	MJ
42.3	64.035772	−24.061944	···		···	MJ
43.1	64.035675	−24.082055	···	$2.76^{+0.30}_{-0.25}$	2.80 ± 0.5	MJ
43.2	64.031197	−24.079960	···			MJ
44.1	64.045266	−24.062760	3.290	···	···	MJ, GC
44.2	64.041552	−24.059996		···	···	MJ
44.3	64.049232	−24.068171		···	···	MJ
46.1	64.038250	−24.080450	···	$2.21^{+0.07}_{-0.06}$	···	MJ
46.2	64.026399	−24.072241	···		···	MJ
46.3	64.033072	−24.076201	···		···	MJ
47.1	64.026334	−24.076699	3.253	···	···	MJ, GC
47.2	64.028336	−24.079001		···	···	MJ
48.1	64.035452	−24.084679	4.122	···	···	MJ, GC
48.2	64.029248	−24.081793		···	···	MJ

Table B.2 (cont'd)

ID	R.A.	Decl.	$z_{\rm spec}$	$z_{\rm model}$	Photo-z Prior	References[a]
48.3	64.023385	−24.076135		···	···	MJ
49.1	64.033945	−24.074570	3.871	···	···	MJ, GC
49.2	64.040168	−24.079871		···	···	MJ
50.1	64.034793	−24.074581	···	$2.79^{+0.12}_{-0.11}$	···	MJ
50.2	64.039689	−24.078864	···		···	MJ
50.3	64.026788	−24.069208	···		···	RK16
51.1	64.040124	−24.080303	4.103	···	···	MJ, GC
51.2	64.033678	−24.074780		···	···	MJ
51.3	64.026638	−24.070476		···	···	MJ
52.1	64.045834	−24.065825	···	$4.26^{+0.26}_{-0.35}$	···	MJ
52.2	64.047707	−24.068677	···		···	MJ
52.3	64.037706	−24.059832	···		···	MJ
53.1	64.046027	−24.068803	···	$2.98^{+0.15}_{-0.13}$	2.90 ± 0.5	MJ
53.2	64.044764	−24.066685	···			MJ
53.3	64.036196	−24.060650	···			MJ
54.1	64.046792	−24.071339	···	$2.30^{+0.08}_{-0.07}$	···	MJ
54.2	64.041356	−24.064504	···		···	MJ
54.3	64.037185	−24.062435	···		···	MJ
55.1	64.035226	−24.064730	3.292	···	···	MJ, GC
55.2	64.046837	−24.075387		···	···	RK16
56.1	64.035673	−24.083593	···	$3.27^{+0.15}_{-0.14}$	···	MJ
56.2	64.030097	−24.080918	···		···	MJ
56.3	64.023854	−24.075001	···		···	MJ
57.1	64.026221	−24.076024	···	$3.06^{+0.36}_{-0.36}$	3.15 ± 0.5	MJ
57.2	64.028847	−24.079126	···			MJ
58.1	64.025193	−24.073576	3.081	···	···	MJ, GC
58.2	64.037723	−24.082384		···	···	MJ
58.3	64.030491	−24.079212		···	···	MJ
59.1	64.035862	−24.072805	···	$1.94^{+0.05}_{-0.05}$	···	MJ
59.2	64.039932	−24.075610	···		···	MJ
59.3	64.029096	−24.067650	···		···	MJ
60.1	64.026732	−24.073705	···	$3.84^{+0.26}_{-0.25}$	···	MJ
60.2	64.039717	−24.082510	···		···	MJ
61.1	64.026737	−24.073536	···	$3.81^{+0.21}_{-0.19}$	···	MJ
61.2	64.039762	−24.082376	···		···	MJ
63.1	64.025548	−24.076658	···	$4.08^{+0.24}_{-0.24}$	3.90 ± 0.5	MJ
63.2	64.028146	−24.079641	···			MJ
63.3	64.037916	−24.084480	···			MJ
65.1	64.042583	−24.075535	···	$5.11^{+0.54}_{-0.31}$	···	MJ
65.2	64.028854	−24.064618	···		···	MJ
67.1	64.038083	−24.082401	3.111	···	···	MJ, GC
67.2	64.025442	−24.073646		···	···	MJ
67.3	64.030371	−24.079018		···	···	MJ
68.1	64.036092	−24.073358	···	$2.59^{+0.09}_{-0.08}$	···	MJ
68.2	64.040362	−24.076479	···		···	MJ
68.3	64.028008	−24.067271	···		···	MJ
69.1	64.036267	−24.074226	···	$1.68^{+0.11}_{-0.09}$	···	MJ
69.2	64.037663	−24.075272	···		···	MJ
72.1	64.031950	−24.071318	···	$3.09^{+0.38}_{-0.30}$	···	MJ
72.2	64.030927	−24.070470	···		···	MJ
74.1	64.030730	−24.068882	···	$2.28^{+0.07}_{-0.07}$	2.40 ± 0.5	RK16
74.2	64.033526	−24.071381	···			RK16
74.3	64.042442	−24.077683	···			RK16
78.1	64.030380	−24.081610	···	$2.43^{+0.37}_{-0.27}$	···	RK16

Table B.2 (cont'd)

ID	R.A.	Decl.	$z_{\rm spec}$	$z_{\rm model}$	Photo-z Prior	References[a]
78.2	64.034524	−24.083701	···		···	RK16
82.1	64.026265	−24.068699	···	$3.77^{+0.27}_{-0.21}$	···	RK16
82.2	64.040054	−24.079110	···		···	RK16
82.3	64.034916	−24.074576	···		···	RK16
83.1	64.030745	−24.070510	···	$4.26^{+0.65}_{-0.52}$	···	RK16
83.2	64.031722	−24.071343	···		···	RK16
84.1	64.040492	−24.075476	···	$1.98^{+0.09}_{-0.08}$	···	JD
84.2	64.036063	−24.072404	···		···	JD
85.1	64.040438	−24.075768	···	$2.02^{+0.09}_{-0.08}$	···	JD
85.2	64.035960	−24.072461	···		···	JD
86.1	64.045104	−24.072335	3.292	···	···	JD, GC
86.2	64.040084	−24.066734		···	···	JD
87.1	64.045363	−24.072537	···	$3.76^{+0.58}_{-0.55}$	···	JD
87.2	64.040000	−24.066651	···		···	JD
88.1	64.045503	−24.072676	···	$3.76^{+0.43}_{-0.48}$	···	JD
88.2	64.039936	−24.066618	···		···	JD
89.1	64.037673	−24.061023	···	$4.04^{+0.23}_{-0.21}$	···	RK16
89.2	64.042884	−24.063891	···		···	RK16
89.3	64.048181	−24.070889	···		···	RK16
90.1	64.038892	−24.060636	···	$6.58^{+0.38}_{-0.32}$	6.40 ± 0.5	RK16
90.2	64.043317	−24.062964	···			RK16
90.3	64.049296	−24.071014	···			RK16
91.1	64.043575	−24.059000	6.145	···	···	RK16, GC
91.2	64.047846	−24.062066		···	···	RK16
91.3	64.050865	−24.066531		···	···	GC
92.1	64.050797	−24.066401	6.145	···	···	GC, GC
92.2	64.048176	−24.062404		···	···	GC
92.3	64.043422	−24.058918		···	···	GC
93.1	64.038639	−24.083404	···	$6.82^{+0.83}_{-0.46}$	···	RK16
93.2	64.024434	−24.073911	···		···	RK16
94.1	64.047803	−24.070143	3.607	···	···	GC, GC
94.2	64.043690	−24.064415		···	···	GC
95.3	64.037674	−24.060757		···	···	GC
95.1	64.031001	−24.077185	3.923	···	···	GC, GC
95.2	64.027122	−24.073560		···	···	GC
96.1	64.032020	−24.084227	5.973	···	···	GC, GC
96.2	64.030818	−24.083693		···	···	GC
97.1	64.047138	−24.061138	···	$6.06^{+0.32}_{-0.31}$	6.00 ± 0.5	···
97.2	64.051077	−24.066511	···			···
97.3	64.044499	−24.059318	···			···

[a]LC—Christensen et al. (2012), AZ—Zitrin et al. (2013), MJ—Jauzac et al. (2014), CG—Grillo et al. (2015a), JD—Diego et al. (2015a), RK16—Kawamata et al. (2016), AH—Hoag et al. (2016), GC—Caminha et al. (2017), SR—Rodney et al. (2017).

Table B.3. MACS J0717.5+3745 Multiple Image Systems

ID	R.A.	Decl.	$z_{\rm spec}$	$z_{\rm model}$	Photo-z Prior	References[a]
1.1	109.395338	+37.741175	2.963	···	···	AZ, ML
1.2	109.393826	+37.740092		···	···	AZ
1.3	109.390988	+37.738286		···	···	AZ
1.4	109.384352	+37.736947		···	···	AZ
1.5	109.405784	+37.761374		···	···	EV
2.1	109.392813	+37.741003	···	$2.82^{+0.18}_{-0.11}$	···	AZ
2.2	109.390434	+37.739247	···		···	AZ
3.1	109.398546	+37.741503	1.855	···	···	AZ, ML
3.2	109.394459	+37.739172		···	···	AZ
3.3	109.407155	+37.753830		···	···	ML
4.1	109.380870	+37.750119	1.855	···	···	AZ, KS
4.2	109.376438	+37.744689		···	···	AZ
4.3	109.391094	+37.763300		···	···	AZ
5.1	109.379908	+37.746861	···	$4.45^{+0.18}_{-0.19}$	5.10 ± 0.5	AZ
5.2	109.377917	+37.742803	···			AZ
5.3	109.400034	+37.767403	···			ML
6.1	109.364357	+37.757097	···	$2.04^{+0.04}_{-0.03}$	···	AZ
6.2	109.362705	+37.752681	···		···	AZ
6.3	109.373863	+37.769703	···		···	AZ
7.1	109.366570	+37.766339	···	$2.07^{+0.04}_{-0.04}$	···	AZ
7.2	109.365037	+37.764119	···		···	AZ
7.3	109.359047	+37.751781	···		···	AZ
8.1	109.366652	+37.769674	···	$2.61^{+0.07}_{-0.07}$	···	AZ
8.2	109.362062	+37.763125	···		···	AZ
8.3	109.356509	+37.751928	···		···	AZ
12.1	109.385165	+37.751836	1.710	···	···	AZ, TT
12.2	109.377617	+37.742914		···	···	AZ
12.3	109.391219	+37.760630		···	···	AZ
13.1	109.385674	+37.750722	2.547	···	···	AZ, ML
13.2	109.377564	+37.739614		···	···	AZ
13.3	109.396212	+37.763333		···	···	AZ
14.1	109.388791	+37.752164	1.855	···	···	ML, ML
14.2	109.379664	+37.739703		···	···	ML
14.3	109.396192	+37.760419		···	···	ML
15.1	109.367663	+37.772058	2.405	···	···	ML, ML
15.2	109.358624	+37.760133		···	···	ML
15.3	109.356540	+37.754641		···	···	ML
16.1	109.369170	+37.773291	···	$3.03^{+0.06}_{-0.06}$	···	ML
16.2	109.358561	+37.759558	···		···	ML
16.3	109.356930	+37.753699	···		···	ML
17.1	109.369371	+37.771866	···	$2.48^{+0.05}_{-0.05}$	···	ML
17.2	109.359393	+37.758839	···		···	ML
17.3	109.358227	+37.753608	···		···	ML
17.4	109.360754	+37.758241	···		···	JD
18.1	109.364249	+37.768633	···	$2.04^{+0.06}_{-0.06}$	···	ML
18.2	109.361215	+37.764333	···		···	ML
19.1	109.409067	+37.754682	6.387	···	···	EV
19.2	109.407728	+37.742741		···	···	EV
19.3	109.381057	+37.731611		···	···	JR
20.1	109.374191	+37.765149	···	$2.58^{+0.24}_{-0.25}$	···	JD
20.2	109.373400	+37.764658	···		···	JD
23.1	109.379564	+37.762852	···	$3.84^{+0.40}_{-0.35}$	3.50 ± 0.5	JD
23.2	109.378995	+37.762003	···			JD
25.1	109.380288	+37.744750	···	$4.53^{+0.18}_{-0.23}$	5.00 ± 0.5	JD

Table B.3 (cont'd)

ID	R.A.	Decl.	$z_{\rm spec}$	$z_{\rm model}$	Photo-z Prior	References[a]
25.2	109.379513	+37.742756	···			JD
25.3	109.402914	+37.766408	···			JD
25.4	109.386063	+37.742033	···			···
27.1	109.397351	+37.747949	···	$2.25^{+0.64}_{-0.75}$	···	JD
27.2	109.397551	+37.747566	···		···	JD
29.1	109.400879	+37.743175	···	$1.61^{+0.02}_{-0.02}$	···	JD
29.2	109.392875	+37.738603	···		···	JD
29.3	109.406088	+37.749953	···		···	JD
31.1	109.374705	+37.756359	···	$1.55^{+0.02}_{-0.02}$	···	JD
31.2	109.371020	+37.750555	···		···	JD
31.3	109.381612	+37.764983	···		···	JD
32.1	109.369513	+37.757724	···	$2.43^{+0.04}_{-0.05}$	3.00 ± 0.5	JD
32.2	109.380947	+37.769383	···			JD
32.3	109.366249	+37.749216	···			JD
33.1	109.383753	+37.758266	···	$3.87^{+0.08}_{-0.10}$	···	JD
33.2	109.386605	+37.764129	···		···	JD
33.3	109.370353	+37.738692	···		···	JD
36.1	109.364321	+37.771974	···	$2.59^{+0.08}_{-0.07}$	···	JD
36.2	109.358243	+37.763341	···		···	JD
36.3	109.353315	+37.755850	···		···	JD
45.1	109.389817	+37.739200	···	$3.06^{+0.25}_{-0.20}$	···	JD
45.2	109.383456	+37.737881	···		···	JD
49.1	109.402967	+37.733258	···	$4.00^{+0.36}_{-0.36}$	···	JD
49.2	109.392978	+37.730708	···		···	JD
50.1	109.374442	+37.743736	···	$2.97^{+0.08}_{-0.07}$	···	JD
50.2	109.379582	+37.750708	···		···	JD
50.3	109.392803	+37.767181	···		···	JD
52.2	109.360222	+37.760497	···	$3.02^{+0.27}_{-0.18}$	···	JD
52.3	109.357034	+37.752486	···		···	JD
53.1	109.370197	+37.761283	···	$2.55^{+0.06}_{-0.07}$	···	JD
53.2	109.379324	+37.768266	···		···	JD
53.3	109.365095	+37.747151	···		···	JD
55.1	109.405801	+37.731841	···	$4.79^{+0.26}_{-0.24}$	4.60 ± 0.5	JD
55.2	109.397047	+37.729001	···			JD
55.3	109.414033	+37.741602	···			···
56.1	109.393140	+37.762794	···	$3.92^{+0.13}_{-0.14}$	···	JD
56.2	109.387349	+37.755964	···		···	JD
56.3	109.375753	+37.735622	···		···	JD
57.1	109.392990	+37.762203	···	$3.91^{+0.12}_{-0.12}$	···	JD
57.2	109.388044	+37.756514	···		···	JD
57.3	109.375941	+37.735131	···		···	JD
58.1	109.393003	+37.762389	···	$4.01^{+0.10}_{-0.10}$	···	JD
58.2	109.387824	+37.756392	···		···	JD
58.3	109.375824	+37.735178	···		···	JD
60.1	109.402547	+37.763613	···	$2.85^{+0.06}_{-0.07}$	3.00 ± 0.5	JD
60.2	109.381086	+37.740666	···			JD
60.3	109.380654	+37.741346	···			JD
60.4	109.387206	+37.741291	···			JD
60.5	109.382704	+37.744707	···			JD
61.1	109.392209	+37.760494	···	$2.67^{+0.13}_{-0.13}$	3.15 ± 0.5	JD
61.2	109.389374	+37.757278	···			JD
62.1	109.379533	+37.745114	···	$3.85^{+0.44}_{-0.38}$	3.60 ± 0.5	JD
62.2	109.379020	+37.744105	···			JD
63.1	109.372561	+37.749536	···	$2.93^{+0.21}_{-0.19}$	3.40 ± 0.5	JD

Table B.3 (cont'd)

ID	R.A.	Decl.	$z_{\rm spec}$	$z_{\rm model}$	Photo-z Prior	References[a]
63.2	109.373289	+37.751282	···			JD
64.1	109.387693	+37.738889	···	$3.79^{+0.15}_{-0.10}$	3.85 ± 0.5	JD
64.2	109.383957	+37.738396	···			JD
64.3	109.405246	+37.763783	···			···
64.4	109.383980	+37.743955	···			···
65.1	109.388637	+37.739259	···	$4.40^{+0.14}_{-0.26}$	4.10 ± 0.5	JD
65.2	109.382017	+37.738436	···			JD
65.3	109.383471	+37.744588	···			···
65.4	109.404961	+37.764683	···			···
66.1	109.386218	+37.751924	···	$5.78^{+0.26}_{-0.21}$	6.20 ± 0.5	···
66.2	109.376999	+37.736450	···			···
66.3	109.399102	+37.764959	···			···
67.1	109.385440	+37.758508	···	$4.19^{+0.14}_{-0.12}$	4.50 ± 0.5	···
67.2	109.387777	+37.762834	···			···
67.3	109.371791	+37.737295	···			···
68.1	109.383107	+37.762585	···	$4.04^{+0.27}_{-0.26}$	4.00 ± 0.5	···
68.2	109.382235	+37.760399	···			···
69.1	109.390481	+37.737919	···	$3.13^{+0.11}_{-0.22}$	···	···
69.2	109.384688	+37.736875	···		···	···
70.1	109.365316	+37.747671	···	$3.40^{+0.12}_{-0.10}$	4.00 ± 0.5	···
70.2	109.368518	+37.758292	···			···
70.3	109.382338	+37.770699	···			···
71.1	109.362599	+37.747559	···	$3.26^{+0.10}_{-0.08}$	···	···
71.2	109.366909	+37.760808	···		···	···
71.3	109.378027	+37.770166	···		···	···
72.1	109.362867	+37.747774	···	$3.24^{+0.07}_{-0.08}$	···	···
72.2	109.366909	+37.760366	···		···	···
72.3	109.378480	+37.770341	···		···	···
73.1	109.362941	+37.747799	···	$3.26^{+0.07}_{-0.08}$	···	···
73.2	109.366888	+37.760233	···		···	···
73.3	109.378606	+37.770383	···		···	···
74.1	109.373152	+37.744011	···	$3.80^{+0.17}_{-0.15}$	4.50 ± 0.5	···
74.2	109.378399	+37.751095	···			···
74.3	109.392850	+37.768771	···			···
75.1	109.373027	+37.745508	···	$4.49^{+0.19}_{-0.22}$	···	···
75.2	109.377178	+37.750574	···		···	···
75.3	109.393355	+37.770141	···		···	···
76.1	109.370552	+37.745834	···	$3.60^{+0.11}_{-0.11}$	4.50 ± 0.5	···
76.2	109.376077	+37.753657	···			···
76.3	109.388875	+37.769833	···			···
77.1	109.363617	+37.750477	···	$3.43^{+0.17}_{-0.14}$	···	···
77.2	109.365372	+37.756216	···		···	···
77.3	109.380145	+37.772541	···		···	···
78.1	109.367431	+37.756481	···	$3.32^{+0.11}_{-0.11}$	4.00 ± 0.5	···
78.2	109.365128	+37.749532	···			···
78.3	109.382085	+37.771633	···			···
79.1	109.367048	+37.746459	···	$3.38^{+0.11}_{-0.10}$	4.10 ± 0.5	···
79.2	109.371065	+37.758450	···			···
79.3	109.384278	+37.770033	···			···
80.1	109.372394	+37.739899	···	$4.62^{+0.16}_{-0.15}$	5.10 ± 0.5	···
80.2	109.381475	+37.754354	···			···
80.3	109.391454	+37.767049	···			···
81.1	109.373064	+37.739655	···	$3.87^{+0.08}_{-0.10}$	4.00 ± 0.5	···
81.2	109.382140	+37.754277	···			···

Table B.3 (cont'd)

ID	R.A.	Decl.	$z_{\rm spec}$	$z_{\rm model}$	Photo-z Prior	References[a]
81.3	109.391518	+37.766093	···			···
82.1	109.373004	+37.739002	···	$4.53^{+0.22}_{-0.17}$	5.00 ± 0.5	···
82.2	109.382391	+37.754409	···			···
82.3	109.391816	+37.766214	···			···
83.1	109.402100	+37.731199	···	$2.49^{+0.10}_{-0.10}$	2.60 ± 0.5	···
83.2	109.404937	+37.732524	···			···
84.1	109.397229	+37.729200	···	$4.67^{+0.32}_{-0.36}$	···	···
84.2	109.404811	+37.731449	···		···	···
85.1	109.379628	+37.746559	···	$4.33^{+0.16}_{-0.20}$	4.50 ± 0.5	···
85.2	109.377965	+37.743293	···			···
85.3	109.399954	+37.767516	···			···

[a]AZ—Zitrin et al. (2009), ML—Limousin et al. (2012), KS—Schmidt et al. (2014b), EV—Vanzella et al. (2014), JR—Richard et al. (2014), JD—Diego et al. (2015b), TT—Treu et al. (2015)

Table B.4. MACS J1149.6+2223 Multiple Image Systems

ID	R.A.	Decl.	$z_{\rm spec}$	$z_{\rm model}$	Photo-z Prior	References[a]
1.1	177.397003	+22.396003	1.488	···	···	AZ, GS
1.2	177.399420	+22.397442		···	···	AZ
1.3	177.403420	+22.402442		···	···	AZ
2.1	177.402419	+22.389753	1.894	···	···	AZ, GS
2.2	177.406044	+22.392480		···	···	AZ
2.3	177.406586	+22.392889		···	···	AZ
3.1	177.390753	+22.399850	3.129	···	···	AZ, MJ, CG
3.2	177.392711	+22.403083		···	···	AZ
3.3	177.401295	+22.407191		···	···	AZ
4.1	177.393003	+22.396828	2.949	···	···	AZ, CG
4.2	177.394378	+22.400739		···	···	AZ
4.3	177.404170	+22.406130		···	···	AZ
5.1	177.399753	+22.393064	2.800	···	···	AZ, GB
5.2	177.401086	+22.393828		···	···	AZ
5.3	177.407920	+22.403555		···	···	AZ
6.1	177.399711	+22.392547	···	$2.79^{+0.07}_{-0.06}$	···	AZ
6.2	177.401836	+22.393861	···		···	AZ
6.3	177.408045	+22.402508	···		···	AZ
7.1	177.398961	+22.391342	···	$2.67^{+0.08}_{-0.08}$	···	AZ
7.2	177.403420	+22.394272	···		···	AZ
7.3	177.407586	+22.401244	···		···	AZ
8.1	177.398503	+22.394353	···	$2.84^{+0.08}_{-0.08}$	···	AZ
8.2	177.399794	+22.395047	···		···	AZ
8.4	177.407092	+22.404722	···		···	WZ
13.1	177.403711	+22.397789	1.240	···	···	WZ, GB
13.2	177.402836	+22.396658		···	···	WZ
13.3	177.400045	+22.393861		···	···	WZ
14.1	177.391667	+22.403506	3.703	···	···	JR, GB, CG
14.2	177.390842	+22.402639		···	···	JR
21.1	177.404496	+22.386697	···	$3.04^{+0.12}_{-0.12}$	···	MJ
21.2	177.407986	+22.389053	···		···	MJ
21.3	177.409082	+22.390411	···		···	MJ
23.1	177.393012	+22.411422	···	$1.26^{+1.27}_{-0.52}$	···	TT
23.2	177.393083	+22.411458	···		···	TT
23.3	177.393154	+22.411475	···		···	TT
24.1	177.392853	+22.412872	···	$2.05^{+0.44}_{-0.45}$	3.50 ± 0.5	GS
24.2	177.393541	+22.413069	···			GS
24.3	177.395042	+22.412697	···			GS
25.1	177.404283	+22.398775	···	$3.18^{+2.25}_{-1.58}$	···	TT
25.2	177.404117	+22.398603	···		···	TT
26.1	177.410345	+22.388753	···	$3.72^{+0.20}_{-0.18}$	3.30 ± 0.5	MJ
26.2	177.409211	+22.387689	···			MJ
26.3	177.406245	+22.385372	···			MJ
28.1	177.395296	+22.391825	···	$3.03^{+0.13}_{-0.11}$	3.15 ± 0.5	MJ
28.2	177.402154	+22.396747	···			MJ
28.3	177.405621	+22.402436	···			MJ
29.1	177.400146	+22.390156	3.214	···	···	MJ, CG
29.2	177.404037	+22.392889		···	···	MJ
29.3	177.409067	+22.400242		···	···	MJ
30.1	177.400483	+22.395444	···	$2.92^{+0.11}_{-0.11}$	···	TT
30.2	177.406829	+22.404517	···		···	TT
31.1	177.407646	+22.396789	···	$1.75^{+0.03}_{-0.03}$	···	TT
31.2	177.402242	+22.391489	···		···	TT
31.3	177.403533	+22.392586	···		···	TT

Table B.4 (cont'd)

ID	R.A.	Decl.	$z_{\rm spec}$	$z_{\rm model}$	Photo-z Prior	References[a]
32.1	177.409945	+22.387244	···	$5.03^{+0.22}_{-0.22}$	4.80 ± 0.5	MJ
32.2	177.406570	+22.384511	···			MJ
32.3	177.411228	+22.388461	···			MJ
33.1	177.409607	+22.386661	···	$6.66^{+0.28}_{-0.30}$	6.50 ± 0.5	MJ
33.2	177.406678	+22.384322	···			MJ
33.3	177.412078	+22.389056	···			MJ
34.1	177.405196	+22.386042	···	$3.62^{+0.15}_{-0.14}$	···	MJ
34.2	177.408208	+22.388119	···		···	MJ
34.3	177.410374	+22.390625	···		···	MJ
35.1	177.407636	+22.385647	···	$3.82^{+0.18}_{-0.25}$	···	TT
35.2	177.408632	+22.386453	···		···	TT
35.3	177.411328	+22.388997	···		···	TT
36.1	177.404421	+22.397303	···	$1.34^{+0.05}_{-0.04}$	···	TT
36.2	177.403971	+22.396039	···		···	TT
37.1	177.404533	+22.395761	···	$1.37^{+0.04}_{-0.04}$	···	TT
37.2	177.404937	+22.396397	···		···	TT
38.1	177.400725	+22.392411	···	$8.39^{+0.46}_{-0.54}$	8.40 ± 0.5	···
38.2	177.400567	+22.392317	···			···
39.1	177.412204	+22.394883	···	$5.63^{+0.34}_{-0.34}$	6.50 ± 0.5	···
39.2	177.404455	+22.386872	···			···
40.1	177.390938	+22.399858	···	$3.15^{+0.09}_{-0.09}$	···	···
40.2	177.392417	+22.402561	···		···	···
40.3	177.401642	+22.407169	···		···	···
SN Refsdal						
S1	177.398225	+22.395628	1.488	···	···	PK, GS
S2	177.397713	+22.395781		···	···	PK
S3	177.397371	+22.395531		···	···	PK
S4	177.397800	+22.395181		···	···	PK
Knot in System 1						
1.2.1	177.396615	+22.396308	1.488	···	···	GS, GS
1.2.2	177.398978	+22.397892		···	···	GS
1.2.3	177.403041	+22.402689		···	···	GS
1.2.4	177.397765	+22.398780		···	···	GS
1.2.6	177.398674	+22.398225		···	···	SR
1.13.1	177.396974	+22.396636	1.488	···	···	GS, GS
1.13.2	177.398832	+22.397717		···	···	GS
1.13.3	177.403311	+22.402814		···	···	GS
1.13.4	177.397907	+22.398433		···	···	GS
1.16.1	177.397446	+22.396394	1.488	···	···	GS
1.16.2	177.399154	+22.397219		···	···	GS
1.16.3	177.403596	+22.402647		···	···	GS
1.17.1	177.398140	+22.396353	1.488	···	···	GS, GS
1.17.2	177.399274	+22.396839		···	···	GS
1.17.3	177.403845	+22.402569		···	···	GS
1.19.1	177.396892	+22.395761	1.488	···	···	SR
1.19.2	177.399538	+22.397483		···	···	SR
1.19.3	177.403367	+22.402286		···	···	SR
1.19.5	177.399962	+22.397094		···	···	SR
1.23.1	177.396724	+22.395372	1.488	···	···	GS, GS
1.23.2	177.399757	+22.397494		···	···	GS
1.23.3	177.403257	+22.402025		···	···	GS
1.23.5	177.400133	+22.397203		···	···	SR

Table B.4 (cont'd)

ID	R.A.	Decl.	$z_{\rm spec}$	$z_{\rm model}$	Photo-z Prior	References[a]
1.30.1	177.398171	+22.395469	1.488	···	···	SR, GS
1.30.2	177.398008	+22.395231		···	···	SR
1.30.3	177.397308	+22.395372		···	···	SR
1.30.4	177.397896	+22.395728		···	···	SR

[a] AZ—Zitrin & Broadhurst (2009), GS—Smith et al. (2009), WZ—Zheng et al. (2012), SR—Rau et al. (2014), JR—Richard et al. (2014), PK—Kelly et al. (2015), MJ—Jauzac et al. (2015b), TT—Treu et al. (2016), CG—Grillo et al. (2015b), GB—Brammer et al. (in prep.).

[*] We note that in the identification of the multiple images, we do not refer to Jauzac et al. (2015b), which was posted to arXiv very recently. All of the multiple images labeled Jauzac et al. (2015b) in this table are also presented in Treu et al. (2016).

Table B.5. Abell S1063 Multiple Image Systems

ID	R.A.	Decl.	$z_{\rm spec}$	$z_{\rm model}$	Photo-z Prior	References[a]
1.1	342.194460	−44.526987	1.228	···	···	JR, WK16
1.2	342.195863	−44.528929		···	···	JR
1.3	342.186429	−44.521196		···	···	JR
2.1	342.192683	−44.531195	1.259	···	···	JR, WK16
2.2	342.192103	−44.529830		···	···	JR
2.3	342.179742	−44.521566		···	···	JR
3.1	342.195513	−44.532112	···	$2.15^{+0.05}_{-0.05}$	···	TJ
3.2	342.193934	−44.528687	···		···	TJ
3.3	342.178629	−44.519524	···		···	···
4.1	342.193694	−44.530139	1.258	···	···	TJ, WK16
4.2	342.193298	−44.529402		···	···	TJ
4.3	342.181657	−44.521385		···	···	···
5.1	342.179174	−44.523584	1.397	···	···	JR, WK16
5.2	342.187807	−44.527313		···	···	JR
5.3	342.193140	−44.536522		···	···	JR
6.1	342.174191	−44.528332	1.428	···	···	JR, WK15
6.2	342.175834	−44.532538		···	···	JR
6.3	342.188451	−44.540000		···	···	JR
7.1	342.169407	−44.527224	1.837	···	···	JR, GC
7.2	342.174267	−44.537099		···	···	JR
7.3	342.181867	−44.540491		···	···	JR
8.1	342.167930	−44.526204	···	$2.72^{+0.07}_{-0.07}$	2.80 ± 0.5	TJ
8.2	342.174621	−44.538403	···			TJ
8.3	342.180771	−44.540884	···			TJ
9.1	342.167797	−44.526269	···	$2.74^{+0.10}_{-0.09}$	2.80 ± 0.5	JR
9.2	342.174777	−44.538587	···			JR
9.3	342.180308	−44.540821	···			JR
10.1	342.190218	−44.529764	···	$0.73^{+0.01}_{-0.01}$	···	JD
10.2	342.189531	−44.528818	···		···	JD
11.1	342.175044	−44.541022	3.117	···	···	JR, GC
11.2	342.173153	−44.539985		···	···	JR
11.3	342.165571	−44.529530		···	···	JR
12.1	342.189034	−44.530024	6.110	···	···	JR, IB
12.2	342.181057	−44.534611		···	···	JR
12.3	342.190890	−44.537464		···	···	JR
12.4	342.171304	−44.519812		···	···	JR
12.5	342.184103	−44.531637		···	···	GC
13.1	342.181524	−44.539357	4.113	···	···	GC, WK15
13.2	342.179164	−44.538688		···	···	GC
14.1	342.178859	−44.535871	3.118	···	···	JR, GC
14.2	342.187426	−44.538691		···	···	JR
14.3	342.170662	−44.522092		···	···	JR
15.1	342.191700	−44.530514	3.060	···	···	JR, WK16
15.2	342.192557	−44.534409		···	···	JR
15.3	342.173685	−44.519391		···	···	GC
16.1	342.166229	−44.533650	···	$3.14^{+0.11}_{-0.10}$	3.00 ± 0.5	JR
16.2	342.166801	−44.534904	···			TJ
16.3	342.177823	−44.543070	···			JR
17.1	342.185825	−44.538863	3.606	···	···	JR, WK16
17.2	342.179086	−44.536691		···	···	JR
17.3	342.169780	−44.521950		···	···	JR
19.1	342.180062	−44.538416	1.035	···	···	JR, WK15
19.2	342.175475	−44.535862		···	···	JR
19.3	342.171930	−44.530240		···	···	JR

Table B.5 (cont'd)

ID	R.A.	Decl.	$z_{\rm spec}$	$z_{\rm model}$	Photo-z Prior	References[a]
20.1	342.216022	−44.519471	···	$2.16^{+0.49}_{-0.47}$	···	JD
20.2	342.215390	−44.519079	···		···	JD
20.3	342.214167	−44.516827	···		···	JD
21.1	342.186752	−44.527270	···	$0.74^{+0.01}_{-0.01}$	···	JD
21.2	342.185633	−44.526578	···		···	JD
23.1	342.170920	−44.529593	···	$3.39^{+0.34}_{-0.29}$	···	JD
23.2	342.171562	−44.532362	···		···	JD
25.1	342.215180	−44.519237	···	$1.22^{+0.17}_{-0.18}$	···	JD
25.2	342.214731	−44.518847	···		···	JD
25.3	342.214420	−44.518012	···		···	JD
31.1	342.198547	−44.520788	···	$3.10^{+0.21}_{-0.19}$	3.00 ± 0.5	JD
31.2	342.197287	−44.519763	···			JD
32.1	342.180231	−44.539262	···	$3.33^{+0.22}_{-0.22}$	3.00 ± 0.5	JD
32.2	342.178939	−44.538851	···			JD
34.1	342.190999	−44.523304	···	$1.62^{+0.05}_{-0.05}$	···	JD
34.4	342.188767	−44.522071	···		···	JD
43.1	342.177274	−44.540697	···	$1.65^{+0.03}_{-0.04}$	2.00 ± 0.5	GC
43.2	342.171644	−44.537175	···			GC
43.3	342.168078	−44.531482	···			JD
44.1	342.198367	−44.535758	2.976	···	···	JD, WK16
44.2	342.192403	−44.525047		···	···	JD
44.3	342.181513	−44.520255		···	···	JD
45.1	342.198886	−44.534745	···	$2.71^{+0.08}_{-0.08}$	2.50 ± 0.5	JD
45.2	342.193286	−44.524834	···			JD
45.3	342.183098	−44.519884	···			JD
46.1	342.191691	−44.536685	···	$1.28^{+0.02}_{-0.02}$	1.10 ± 0.5	JD
46.2	342.186589	−44.528263	···			JD
46.3	342.178417	−44.524419	···			JD
47.1	342.193051	−44.535521	···	$2.90^{+0.10}_{-0.10}$	···	JD
47.2	342.174495	−44.520080	···		···	JD
47.2	342.191236	−44.529232	···		···	JD
48.2	342.217950	−44.518754	···	$2.84^{+0.99}_{-1.00}$	···	JD
48.3	342.217856	−44.518354	···		···	JD
49.1	342.191928	−44.536821	···	$1.23^{+0.03}_{-0.03}$	1.10 ± 0.5	JD
49.2	342.186284	−44.528052	···			JD
50.1	342.187113	−44.529094	···	$1.63^{+0.03}_{-0.03}$	1.60 ± 0.5	JD
50.2	342.181017	−44.532437	···			JD
50.3	342.175664	−44.523176	···			JD
50.4	342.191171	−44.537266	···			···
51.1	342.197440	−44.530602	···	$2.66^{+0.20}_{-0.15}$	···	JD
51.2	342.196400	−44.528404	···		···	JD
53.1	342.179551	−44.535725	···	$3.17^{+0.13}_{-0.11}$	3.00 ± 0.5	JD
53.2	342.187740	−44.538308	···			JD
53.3	342.170875	−44.521668	···			JD
54.1	342.180011	−44.535595	···	$3.10^{+0.11}_{-0.11}$	3.00 ± 0.5	JD
54.2	342.187886	−44.538025	···			JD
54.3	342.170944	−44.521484	···			JD
55.1	342.178244	−44.535982	···	$3.13^{+0.28}_{-0.20}$	3.00 ± 0.5	JD
55.2	342.187175	−44.539048	···			JD
56.1	342.178271	−44.535826	···	$3.16^{+0.23}_{-0.22}$	3.00 ± 0.5	JD
56.2	342.187666	−44.539000	···			JD
57.1	342.188756	−44.522771	5.237	···	···	WK16, WK16
57.2	342.183780	−44.521233		···	···	WK16
58.1	342.190836	−44.535657	5.051	···	···	WK16, WK16

Table B.5 (cont'd)

ID	R.A.	Decl.	$z_{\rm spec}$	$z_{\rm model}$	Photo-z Prior	References[a]
58.2	342.190144	−44.530948		···	···	WK16
59.1	342.181653	−44.540650	1.875	···	···	··· , GLASS
59.2	342.173460	−44.536597		···	···	···
59.3	342.169528	−44.528625		···	···	···
60.1	342.182308	−44.540617	···	$1.92^{+0.05}_{-0.04}$	1.65 ± 0.5	···
60.2	342.174028	−44.536912	···			···
60.3	342.169461	−44.527416	···			···
61.1	342.179041	−44.541921	···	$2.26^{+0.07}_{-0.06}$	···	···
61.2	342.170567	−44.536957	···		···	···
61.3	342.167176	−44.530820	···		···	···
62.1	342.183917	−44.535313	6.108	···	···	··· , WK16
62.2	342.188460	−44.536174		···	···	···
63.1	342.182996	−44.537653	···	$1.46^{+0.07}_{-0.06}$	···	···
63.2	342.179461	−44.536002	···		···	···
64.1	342.197395	−44.533146	···	$1.92^{+0.04}_{-0.04}$	···	···
64.2	342.193629	−44.526237	···		···	···
64.3	342.182633	−44.520203	···		···	···
65.1	342.182256	−44.526079	···	$8.26^{+0.39}_{-0.44}$	8.30 ± 0.5	···
65.2	342.179813	−44.525671	···			···
66.1	342.164359	−44.530220	···	$5.07^{+0.32}_{-0.34}$	6.00 ± 0.5	···
66.2	342.176130	−44.542664	···			···
67.1	342.193465	−44.540965	···	$6.80^{+0.60}_{-0.49}$	···	···
67.2	342.172810	−44.522804	···		···	···
68.1	342.183484	−44.526454	···	$2.60^{+0.24}_{-0.18}$	···	···
68.2	342.180313	−44.525677	···		···	···
69.1	342.173329	−44.525929	···	$5.91^{+1.01}_{-0.50}$	···	···
69.2	342.174564	−44.532012	···		···	···
69.3	342.193771	−44.542729	···		···	···
70.1	342.176327	−44.520671	3.713	···	···	··· , WK16
70.2	342.190991	−44.526777		···	···	···
70.3	342.195692	−44.537430		···	···	···
71.1	342.194074	−44.529437	···	$7.59^{+1.18}_{-1.46}$	···	···
71.2	342.195361	−44.534129	···		···	···

[a]IB—Balestra et al. (2013), JR—Richard et al. (2014), WK15—Karman et al. (2015), TJ—Johnson et al. (2014), GC—Caminha et al. (2016a), JD—Diego et al. (2016a), WK16—Karman et al. (2017), GLASS—Schmidt et al. (2014b), Treu et al. (2015)

Table B.6. Abell 370 Multiple Image Systems

ID	R.A.	Decl.	$z_{\rm spec}$	$z_{\rm model}$	Photo-z Prior	References[a]
1.1	39.967071	−1.576914	0.806	···	···	JR10, JR10
1.2	39.976292	−1.576042		···	···	JR10
1.3	39.968704	−1.576606		···	···	JR10
3.1	39.965647	−1.566871	1.950	···	···	JR10, DL
3.2	39.968504	−1.565792		···	···	JR10
3.3	39.978958	−1.567461		···	···	···
4.1	39.979604	−1.576245	1.273	···	···	JR10, DL
4.2	39.970758	−1.576147		···	···	JR10
4.3	39.961929	−1.577847		···	···	JR10
5.1	39.973475	−1.589043	1.278	···	···	JR10, DL
5.2	39.971124	−1.589242		···	···	JR10
5.3	39.969004	−1.589055		···	···	JR10
6.1	39.969450	−1.577208	1.063	···	···	JR10, JR14
6.2	39.964346	−1.578247		···	···	JR10
6.3	39.979654	−1.577103		···	···	JR10
7.1	39.969763	−1.580356	2.751	···	···	JR10, DL
7.2	39.969904	−1.580814		···	···	JR10
7.3	39.968825	−1.585633		···	···	JR10
7.4	39.961554	−1.580008		···	···	JR10
7.5	39.986571	−1.577578		···	···	JD
8.1	39.964488	−1.569817	···	$3.18^{+0.14}_{-0.15}$	2.90 ± 0.5	JR10
8.2	39.961896	−1.573656	···			JR10
8.3	39.986137	−1.571614	···			···
9.1	39.962402	−1.577887	1.520	···	···	JR10, DL
9.2	39.969486	−1.576259		···	···	JR10
9.3	39.982021	−1.576527		···	···	JR10
11.1	39.963789	−1.569381	···	$8.22^{+0.46}_{-0.44}$	7.80 ± 0.5	JR14
11.2	39.960749	−1.574176	···			JR14
11.3	39.988463	−1.571978	···			···
12.1	39.969684	−1.566640	···	$3.65^{+0.20}_{-0.18}$	3.40 ± 0.5	JR14
12.2	39.959169	−1.575330	···			JR14
12.3	39.984089	−1.570908	···			JR14
13.1	39.979532	−1.571778	···	$3.62^{+0.21}_{-0.17}$	4.10 ± 0.5	JR14
13.2	39.975189	−1.568824	···			JR14
13.3	39.956763	−1.577517	···			···
14.1	39.972293	−1.578084	3.131	···	···	JD, DL
14.2	39.972192	−1.580097		···	···	DL
14.3	39.974267	−1.585595		···	···	JD
14.4	39.981300	−1.578206		···	···	JD
14.5	39.957679	−1.580475		···	···	JD
15.1	39.971328	−1.580604	3.708	···	···	DL, DL
15.2	39.971935	−1.587051		···	···	DL
15.3	39.971027	−1.577791		···	···	DL
17.1	39.969768	−1.588539	4.257	···	···	DL, DL
17.2	39.985403	−1.580831		···	···	DL
17.3	39.960239	−1.583653		···	···	DL
18.1	39.975824	−1.587055	4.430	···	···	DL, DL
18.2	39.981474	−1.582072		···	···	DL
20.1	39.965288	−1.587814	5.751	···	···	JD, DL
20.2	39.963629	−1.586889		···	···	JD
21.1	39.966733	−1.584694	1.257	···	···	JD, DL
21.2	39.967252	−1.584969		···	···	JD
22.1	39.974425	−1.586103	3.131	···	···	JD, DL
22.2	39.981675	−1.579686		···	···	JD

Table B.6 (cont'd)

ID	R.A.	Decl.	$z_{\rm spec}$	$z_{\rm model}$	Photo-z Prior	References[a]
22.3	39.957905	−1.581013		···	···	DL
23.1	39.967321	−1.566119	1.950	···	···	JD, DL
23.2	39.966188	−1.566597		···	···	JD
24.1	39.963077	−1.570721	···	$3.81^{+0.38}_{-0.38}$	4.00 ± 0.5	JD
24.2	39.962232	−1.572062	···			JD
25.1	39.976373	−1.582191	···	$1.07^{+0.02}_{-0.02}$	0.75 ± 0.5	JD
25.2	39.962701	−1.582252	···			JD
26.1	39.980692	−1.571131	···	$2.93^{+0.13}_{-0.12}$	2.90 ± 0.5	JD
26.2	39.972442	−1.567144	···			JD
26.3	39.958296	−1.575922	···			···
27.1	39.987325	−1.578867	···	$3.96^{+0.23}_{-0.21}$	3.90 ± 0.5	JD
27.2	39.961950	−1.583169	···			JD
28.1	39.987084	−1.579103	···	$3.97^{+0.23}_{-0.20}$	3.90 ± 0.5	JD
28.2	39.961704	−1.583214	···			JD
29.1	39.984050	−1.573356	···	$1.98^{+0.06}_{-0.06}$	1.85 ± 0.5	JD
29.2	39.966600	−1.569636	···			JD
29.3	39.962117	−1.575239	···			JD
30.1	39.987279	−1.578761	···	$3.99^{+0.25}_{-0.22}$	3.90 ± 0.5	JD
30.2	39.961733	−1.582881	···			JD
31.1	39.963513	−1.582281	···	$3.22^{+0.13}_{-0.12}$	3.00 ± 0.5	JD
31.2	39.967075	−1.584556	···			JD
31.3	39.987825	−1.577461	···			···
32.1	39.982280	−1.576966	···	$1.26^{+0.03}_{-0.03}$	1.15 ± 0.5	JD
32.2	39.967908	−1.577306	···			JD
32.3	39.965417	−1.578031	···			JD
33.1	39.963271	−1.570358	···	$4.89^{+0.50}_{-0.42}$	5.10 ± 0.5	JD
33.2	39.961729	−1.572922	···			JD
34.1	39.983471	−1.567314	···	$4.86^{+0.28}_{-0.25}$	4.60 ± 0.5	···
34.2	39.968433	−1.564653	···			···
34.3	39.960909	−1.569017	···			···
35.1	39.983563	−1.567578	···	$4.89^{+0.32}_{-0.28}$	4.60 ± 0.5	···
35.2	39.968108	−1.564811	···			···
35.3	39.960667	−1.569353	···			···
36.1	39.984667	−1.581744	···	$2.83^{+0.12}_{-0.11}$	2.80 ± 0.5	···
36.2	39.967925	−1.588103	···			···
36.3	39.962125	−1.584975	···			···
37.1	39.985617	−1.572228	···	$2.99^{+0.13}_{-0.11}$	3.00 ± 0.5	···
37.2	39.966396	−1.568822	···			···
37.3	39.961167	−1.575269	···			···
38.1	39.963472	−1.570047	···	$7.61^{+0.41}_{-0.47}$	7.50 ± 0.5	···
38.2	39.961076	−1.574099	···			···
39.1	39.982428	−1.581085	···	$8.14^{+0.45}_{-0.46}$	8.20 ± 0.5	···
39.2	39.975879	−1.587287	···			···
40.1	39.969254	−1.566439	···	$6.49^{+0.45}_{-0.45}$	6.15 ± 0.5	···
40.2	39.958391	−1.576619	···			···
41.1	39.964372	−1.571347	···	$4.92^{+0.44}_{-0.40}$	4.80 ± 0.5	···
41.2	39.962409	−1.575561	···			···
42.1	39.983274	−1.579580	···	$4.19^{+0.24}_{-0.23}$	4.50 ± 0.5	···
42.2	39.973279	−1.587386	···			···
42.3	39.957971	−1.581345	···			···
43.1	39.984554	−1.581364	···	$3.88^{+0.23}_{-0.20}$	4.00 ± 0.5	···
43.2	39.970841	−1.588630	···			···
43.3	39.959819	−1.583475	···			···
44.1	39.981774	−1.581531	···	$2.77^{+0.17}_{-0.16}$	3.00 ± 0.5	···

Table B.6 (cont'd)

ID	R.A.	Decl.	$z_{\rm spec}$	$z_{\rm model}$	Photo-z Prior	References[a]
44.2	39.973626	−1.587340	···			···
45.1	39.978879	−1.580130	···	$4.32^{+1.12}_{-0.64}$	···	···
45.2	39.976408	−1.583100	···		···	···
46.1	39.979327	−1.575426	···	$2.24^{+0.19}_{-0.16}$	3.00 ± 0.5	···
46.2	39.974299	−1.571179	···			···
47.1	39.979935	−1.571383	···	$3.53^{+0.20}_{-0.19}$	3.80 ± 0.5	···
47.2	39.974465	−1.568088	···			···
47.3	39.957165	−1.576956	···			···
48.1	39.977829	−1.568634	···	$4.42^{+0.39}_{-0.44}$	4.00 ± 0.5	···
48.2	39.977197	−1.568334	···			···
49.1	39.982981	−1.570840	···	$2.45^{+0.09}_{-0.08}$	2.75 ± 0.5	···
49.2	39.968907	−1.567101	···			···
49.3	39.960544	−1.574095	···			···
Knot in System 2						
2.1.1	39.973846	−1.584200	0.725	···	···	JR10, JR10
2.2.1	39.970963	−1.585039		···	···	JR10
2.3.1	39.968763	−1.584519		···	···	JR10
2.4.1	39.969433	−1.584745		···	···	JR10
2.5.1	39.969667	−1.584856		···	···	JR10
2.1.2	39.973359	−1.584353	0.725	···	···	JD, JR10
2.2.2	39.972446	−1.584842		···	···	JD
2.3.2	39.968225	−1.584269		···	···	JD
2.1.3	39.973467	−1.584428	0.725	···	···	JD, JR10
2.2.3	39.972129	−1.584958		···	···	JD
2.3.3	39.968479	−1.584458		···	···	JD
2.1.4	39.973021	−1.584575	0.725	···	···	JD, JR10
2.2.4	39.972638	−1.584789		···	···	JD
2.3.4	39.968067	−1.584247		···	···	JD

[a]JR10—Richard et al. (2010), JR14—Richard et al. (2014), JD—Diego et al. (2016b), DL—Lagattuta et al. (2017).

Appendix C

Fitting Results

The obtained morphological properties and magnitudes are presented in Tables C.1–C.3. The fitting results for galaxies fainter than −18 mag are graphically shown in Figures C.1 and C.2.

Table C.1. Fitting results for dropouts at $z \sim 6-7$

ID[a]	R.A.	Decl.	$m_{\rm UV}$[b,c]	$M_{\rm UV}$[c]	$r_{\rm e}$ / kpc[c,d]	e	$\mu_{\rm best}$[e]	μ[f]	$z_{\rm photo}$
HFF1C									
2251-4556	3.593804	−30.415447	$27.68^{+0.10}_{-0.14}$	$-19.01^{+0.10}_{-0.14}$	$0.09^{+0.03}_{-0.04}$	0.38	3.44	$3.85^{+0.38}_{-0.32}$	$6.6^{+0.8}_{-0.7}$
1695-4527	3.570654	−30.414659	$26.72^{+0.11}_{-0.14}$	$-19.98^{+0.11}_{-0.14}$	$0.18^{+0.06}_{-0.08}$	0.81	1.41	$1.53^{+0.09}_{-0.06}$	$6.0^{+0.7}_{-0.7}$
2549-3119	3.606222	−30.386644	$26.71^{+0.18}_{-0.23}$	$-19.99^{+0.18}_{-0.23}$	$0.34^{+0.11}_{-0.12}$	0.24	1.48	$1.64^{+0.08}_{-0.06}$	$5.8^{+0.7}_{-0.7}$
1930-4181[s1]	3.580453	−30.405043	$28.52^{+0.10}_{-0.13}$	$-18.17^{+0.10}_{-0.13}$	$0.09^{+0.03}_{-0.04}$	0.45	4.21	$4.81^{+0.41}_{-0.35}$	$6.8^{+0.8}_{-0.8}$
2516-4570	3.604865	−30.415839	$27.15^{+0.36}_{-0.41}$	$-19.54^{+0.36}_{-0.41}$	$0.55^{+0.19}_{-0.18}$	0.65	2.31	$2.97^{+0.24}_{-0.22}$	$5.6^{+0.7}_{-0.6}$
2348-3454[s1]	3.597834	−30.395961	$28.54^{+0.11}_{-0.13}$	$-18.15^{+0.11}_{-0.13}$	$0.03^{+0.02}_{-0.01}$	0.90	3.08	$3.42^{+0.26}_{-0.20}$	$7.0^{+0.8}_{-0.8}$
2178-2458	3.590761	−30.379409	$27.61^{+0.17}_{-0.22}$	$-19.08^{+0.17}_{-0.22}$	$0.21^{+0.07}_{-0.07}$	0.90	1.94	$1.77^{+0.12}_{-0.09}$	$5.8^{+0.7}_{-0.6}$
2047-3526[s1]	3.585322	−30.397958	$28.49^{+0.30}_{-0.15}$	$-18.20^{+0.30}_{-0.15}$	$0.18^{+0.08}_{-0.05}$	0.41	3.63	$3.79^{+0.36}_{-0.34}$	$6.8^{+0.7}_{-0.8}$
2425-4143	3.601072	−30.403991	$28.99^{+0.11}_{-0.13}$	$-17.70^{+0.11}_{-0.13}$	$0.04^{+0.02}_{-0.02}$	0.90	3.79	$3.82^{+0.31}_{-0.21}$	$6.0^{+0.6}_{-0.7}$
2414-4370	3.600619	−30.410296	$29.77^{+0.28}_{-0.25}$	$-16.92^{+0.28}_{-0.25}$	$0.08^{+0.06}_{-0.05}$	0.77	6.89	$11.72^{+1.69}_{-1.56}$	$6.4^{+0.7}_{-0.7}$
2482-2595	3.603426	−30.383219	$28.03^{+0.32}_{-0.34}$	$-18.67^{+0.32}_{-0.34}$	$0.10^{+0.08}_{-0.06}$	0.39	1.47	$1.57^{+0.08}_{-0.06}$	$5.8^{+0.7}_{-0.7}$
2477-4372	3.603214	−30.410351	$27.79^{+0.37}_{-0.50}$	$-18.90^{+0.37}_{-0.50}$	$0.50^{+0.15}_{-0.17}$	0.53	3.40	$4.07^{+0.32}_{-0.25}$	$6.3^{+0.7}_{-0.7}$
2230-4479	3.592944	−30.413328	$29.64^{+0.28}_{-0.25}$	$-17.06^{+0.28}_{-0.25}$	$0.06^{+0.04}_{-0.03}$	0.48	5.87	$7.12^{+0.82}_{-0.70}$	$6.1^{+0.7}_{-0.7}$
1845-3107	3.576889	−30.386328	$29.48^{+0.11}_{-0.12}$	$-17.21^{+0.11}_{-0.12}$	$0.04^{+0.02}_{-0.02}$	0.85	3.96	$7.57^{+1.75}_{-1.08}$	$6.1^{+0.8}_{-0.7}$
2040-4471	3.585016	−30.413084	$29.09^{+0.11}_{-0.13}$	$-17.60^{+0.11}_{-0.13}$	$0.04^{+0.02}_{-0.02}$	0.76	3.37	$3.06^{+0.23}_{-0.19}$	$5.7^{+0.6}_{-4.7}$
1911-4242	3.579635	−30.406723	$29.03^{+0.26}_{-0.43}$	$-17.67^{+0.26}_{-0.43}$	$0.30^{+0.13}_{-0.11}$	0.42	3.22	$3.69^{+0.30}_{-0.24}$	$5.6^{+0.6}_{-5.3}$
2616-3070	3.609003	−30.385283	$28.22^{+0.31}_{-0.27}$	$-18.47^{+0.31}_{-0.27}$	$0.23^{+0.19}_{-0.14}$	0.73	1.38	$1.52^{+0.07}_{-0.05}$	$6.1^{+0.7}_{-0.7}$
2509-4337	3.604563	−30.409364	$29.11^{+0.29}_{-0.26}$	$-17.58^{+0.29}_{-0.26}$	$0.22^{+0.17}_{-0.13}$	0.40	2.85	$3.15^{+0.24}_{-0.16}$	$6.1^{+0.8}_{-0.8}$
2274-2562	3.594752	−30.382305	$27.30^{+0.45}_{-0.49}$	$-19.39^{+0.45}_{-0.49}$	$0.89^{+0.31}_{-0.30}$	0.42	1.99	$1.97^{+0.13}_{-0.11}$	$0.1^{+3.5}_{-0.1}$
2364-4454	3.598515	−30.412612	$30.58^{+0.19}_{-0.19}$	$-16.12^{+0.19}_{-0.19}$	$0.03^{+0.03}_{-0.02}$	0.70	6.57	$15.68^{+4.68}_{-3.31}$	$6.6^{+0.8}_{-1.2}$
1991-3429	3.582960	−30.395261	$30.79^{+0.41}_{-0.24}$	$-15.90^{+0.41}_{-0.24}$	$0.05^{+0.03}_{-0.03}$	0.90	15.49	$10.35^{+1.00}_{-0.97}$	$1.3^{+5.5}_{-1.1}$
2172-2471	3.590518	−30.379763	$28.59^{+0.31}_{-0.33}$	$-18.10^{+0.31}_{-0.33}$	$0.23^{+0.19}_{-0.14}$	0.90	2.00	$1.83^{+0.12}_{-0.09}$	$6.1^{+0.8}_{-1.1}$
HFF1P									
5395-1452	3.474803	−30.362578	$27.29^{+0.13}_{-0.11}$	$-19.41^{+0.13}_{-0.11}$	$0.14^{+0.04}_{-0.06}$	0.90	1.07	$1.05^{+0.01}_{-0.01}$	$7.3^{+0.8}_{-0.8}$
5292-4021	3.470509	−30.400605	$26.72^{+0.32}_{-0.29}$	$-19.97^{+0.32}_{-0.29}$	$0.60^{+0.22}_{-0.21}$	0.42	1.08	$1.01^{+0.01}_{-0.01}$	$5.8^{+0.6}_{-0.7}$
5793-1536	3.491388	−30.364890	$26.91^{+0.19}_{-0.14}$	$-19.78^{+0.19}_{-0.14}$	$0.81^{+0.15}_{-0.10}$	0.65	1.08	$1.07^{+0.02}_{-0.01}$	$7.3^{+0.9}_{-0.8}$
5398-1451	3.474918	−30.362542	$27.84^{+0.17}_{-0.18}$	$-18.85^{+0.17}_{-0.18}$	$0.14^{+0.06}_{-0.06}$	0.89	1.07	$1.05^{+0.01}_{-0.01}$	$7.5^{+0.8}_{-1.5}$
5535-2162	3.480643	−30.371175	$27.41^{+0.32}_{-0.28}$	$-19.28^{+0.32}_{-0.28}$	$0.26^{+0.20}_{-0.16}$	0.48	1.08	$1.05^{+0.01}_{-0.01}$	$6.3^{+0.7}_{-0.7}$
5701-1517	3.487575	−30.364380	$27.21^{+0.20}_{-0.18}$	$-19.48^{+0.20}_{-0.18}$	$0.84^{+0.14}_{-0.12}$	0.35	1.08	$1.07^{+0.01}_{-0.01}$	$5.7^{+0.6}_{-4.8}$
5734-3406	3.488924	−30.394630	$27.68^{+0.28}_{-0.46}$	$-19.01^{+0.28}_{-0.46}$	$0.54^{+0.23}_{-0.20}$	0.62	1.10	$1.03^{+0.02}_{-0.01}$	$6.8^{+0.7}_{-0.8}$
5581-2176	3.482550	−30.371559	$27.39^{+0.32}_{-0.53}$	$-19.31^{+0.32}_{-0.53}$	$0.58^{+0.18}_{-0.23}$	0.27	1.09	$1.05^{+0.01}_{-0.01}$	$5.8^{+0.6}_{-1.0}$
5615-3497	3.483960	−30.397152	$27.50^{+0.28}_{-0.46}$	$-19.19^{+0.28}_{-0.46}$	$0.59^{+0.26}_{-0.22}$	0.75	1.09	$1.02^{+0.02}_{-0.01}$	$6.3^{+0.7}_{-0.7}$
5221-3488	3.467581	−30.396908	$27.08^{+0.32}_{-0.29}$	$-19.62^{+0.32}_{-0.29}$	$0.61^{+0.22}_{-0.21}$	0.51	1.08	$1.01^{+0.01}_{-0.01}$	$6.8^{+0.7}_{-0.8}$
5748-3582	3.489519	−30.399527	$27.73^{+0.31}_{-0.28}$	$-18.96^{+0.31}_{-0.28}$	$0.32^{+0.26}_{-0.19}$	0.65	1.09	$1.03^{+0.02}_{-0.01}$	$6.6^{+0.8}_{-0.7}$
5210-3156	3.467097	−30.387685	$27.53^{+0.28}_{-0.46}$	$-19.16^{+0.28}_{-0.46}$	$0.55^{+0.24}_{-0.21}$	0.48	1.08	$1.02^{+0.01}_{-0.01}$	$6.1^{+0.7}_{-0.7}$
5185-3398	3.466056	−30.394409	$27.71^{+0.28}_{-0.46}$	$-18.98^{+0.28}_{-0.46}$	$0.42^{+0.18}_{-0.16}$	0.83	1.08	$1.02^{+0.01}_{-0.01}$	$5.9^{+0.7}_{-0.6}$
5573-2343	3.482238	−30.376221	$27.93^{+0.27}_{-0.45}$	$-18.76^{+0.27}_{-0.45}$	$0.48^{+0.21}_{-0.18}$	0.57	1.09	$1.05^{+0.01}_{-0.01}$	$1.3^{+3.7}_{-1.1}$
4940-1588	3.455844	−30.366359	$27.77^{+0.32}_{-0.52}$	$-18.93^{+0.32}_{-0.52}$	$0.71^{+0.23}_{-0.28}$	0.45	1.07	$1.03^{+0.01}_{-0.01}$	$5.6^{+0.7}_{-4.7}$
5327-2576	3.471985	−30.382683	$28.31^{+0.27}_{-0.44}$	$-18.38^{+0.27}_{-0.44}$	$0.41^{+0.18}_{-0.16}$	0.71	1.09	$1.03^{+0.01}_{-0.01}$	$6.7^{+0.8}_{-2.1}$
5054-1587	3.460588	−30.366320	$28.69^{+0.42}_{-0.33}$	$-18.00^{+0.42}_{-0.33}$	$0.16^{+0.13}_{-0.09}$	0.90	1.07	$1.04^{+0.01}_{-0.01}$	$5.8^{+0.6}_{-1.3}$
5587-3058	3.482833	−30.384961	$28.18^{+0.31}_{-0.27}$	$-18.51^{+0.31}_{-0.27}$	$0.33^{+0.26}_{-0.20}$	0.64	1.09	$1.04^{+0.01}_{-0.01}$	$1.1^{+5.1}_{-0.9}$
5687-3584	3.486987	−30.399579	$27.23^{+0.42}_{-0.55}$	$-19.46^{+0.42}_{-0.55}$	$0.88^{+0.42}_{-0.34}$	0.35	1.09	$1.02^{+0.02}_{-0.01}$	$5.9^{+0.7}_{-1.2}$
5691-3514	3.487147	−30.397615	$28.20^{+0.31}_{-0.27}$	$-18.50^{+0.31}_{-0.27}$	$0.27^{+0.21}_{-0.16}$	0.60	1.09	$1.03^{+0.02}_{-0.01}$	$4.2^{+1.9}_{-4.1}$
5638-2369	3.484920	−30.376917	$28.32^{+0.36}_{-0.32}$	$-18.37^{+0.36}_{-0.32}$	$0.12^{+0.09}_{-0.07}$	0.90	1.09	$1.05^{+0.01}_{-0.01}$	$6.0^{+0.7}_{-0.8}$
5429-2542	3.476220	−30.381741	$27.97^{+0.31}_{-0.28}$	$-18.73^{+0.31}_{-0.28}$	$0.36^{+0.28}_{-0.22}$	0.87	1.09	$1.03^{+0.01}_{-0.01}$	$5.8^{+0.8}_{-5.5}$
5509-1488	3.479546	−30.363580	$28.48^{+0.36}_{-0.31}$	$-18.22^{+0.36}_{-0.31}$	$0.14^{+0.11}_{-0.08}$	0.90	1.07	$1.06^{+0.01}_{-0.01}$	$4.7^{+0.9}_{-4.3}$
5453-3095	3.477238	−30.385997	$28.21^{+0.31}_{-0.27}$	$-18.48^{+0.31}_{-0.27}$	$0.33^{+0.26}_{-0.20}$	0.89	1.09	$1.03^{+0.01}_{-0.01}$	$6.5^{+0.7}_{-0.8}$
4938-2422	3.455764	−30.378410	$28.63^{+0.42}_{-0.33}$	$-18.07^{+0.42}_{-0.33}$	$0.15^{+0.13}_{-0.09}$	0.90	1.08	$1.02^{+0.01}_{-0.01}$	$6.1^{+1.3}_{-5.2}$
5381-3517	3.474215	−30.397703	$28.02^{+0.31}_{-0.52}$	$-18.67^{+0.31}_{-0.52}$	$0.58^{+0.18}_{-0.23}$	0.82	1.08	$1.02^{+0.01}_{-0.01}$	$6.3^{+0.9}_{-5.7}$
5566-3224	3.481928	−30.389557	$28.55^{+0.42}_{-0.33}$	$-18.15^{+0.42}_{-0.33}$	$0.18^{+0.15}_{-0.11}$	0.90	1.09	$1.03^{+0.01}_{-0.01}$	$6.2^{+0.7}_{-0.8}$
5467-2421	3.477807	−30.378362	$28.80^{+0.21}_{-0.21}$	$-17.90^{+0.21}_{-0.21}$	$0.08^{+0.07}_{-0.04}$	0.89	1.09	$1.04^{+0.01}_{-0.01}$	$5.8^{+1.1}_{-5.2}$
5445-2223	3.476915	−30.372887	$27.32^{+0.67}_{-0.50}$	$-19.38^{+0.67}_{-0.50}$	$0.90^{+0.44}_{-0.36}$	0.35	1.08	$1.05^{+0.01}_{-0.01}$	$5.8^{+1.0}_{-5.2}$
5588-2288	3.482860	−30.374682	$28.13^{+0.45}_{-0.58}$	$-18.56^{+0.45}_{-0.58}$	$0.64^{+0.28}_{-0.31}$	0.52	1.09	$1.05^{+0.01}_{-0.01}$	$1.1^{+3.7}_{-1.0}$

Table C.1 (cont'd)

ID[a]	R.A.	Decl.	$m_{\rm UV}$[b,c]	$M_{\rm UV}$[c]	$r_{\rm e}$ / kpc[c,d]	e	$\mu_{\rm best}$[e]	μ[f]	$z_{\rm photo}$
HFF2C									
0949-5187	64.039545	−24.088540	$26.60^{+0.32}_{-0.29}$	$-20.09^{+0.32}_{-0.29}$	$0.43^{+0.16}_{-0.15}$	0.39	1.53	$1.60^{+0.05}_{-0.04}$	$5.9^{+0.7}_{-0.7}$
1148-3434[s1]	64.047846	−24.062066	$29.19^{+0.28}_{-0.25}$	$-17.51^{+0.28}_{-0.25}$	$0.15^{+0.06}_{-0.05}$	0.86	14.13	$14.46^{+0.63}_{-0.60}$	$6.2^{+0.7}_{-0.7}$
1131-3400[s2]	64.047138	−24.061138	$29.87^{+0.28}_{-0.25}$	$-16.83^{+0.28}_{-0.25}$	$0.04^{+0.03}_{-0.02}$	0.90	11.12	$11.28^{+0.62}_{-0.60}$	$5.9^{+0.7}_{-0.7}$
0899-3404	64.037485	−24.061238	$28.43^{+0.18}_{-0.13}$	$-18.27^{+0.18}_{-0.13}$	$0.42^{+0.08}_{-0.05}$	0.55	3.15	$3.21^{+0.15}_{-0.13}$	$6.0^{+0.7}_{-0.6}$
0828-5386	64.034514	−24.094074	$27.14^{+0.31}_{-0.28}$	$-19.55^{+0.31}_{-0.28}$	$0.54^{+0.20}_{-0.18}$	0.50	1.49	$1.55^{+0.04}_{-0.03}$	$5.9^{+0.7}_{-0.7}$
0960-3425	64.040012	−24.061829	$29.12^{+0.32}_{-0.37}$	$-17.57^{+0.32}_{-0.37}$	$0.26^{+0.09}_{-0.09}$	0.69	8.86	$8.91^{+0.69}_{-0.55}$	$6.3^{+0.7}_{-0.7}$
1147-4580	64.047818	−24.082800	$27.90^{+0.42}_{-0.55}$	$-18.79^{+0.42}_{-0.55}$	$0.52^{+0.31}_{-0.25}$	0.72	1.40	$1.45^{+0.04}_{-0.03}$	$6.8^{+0.7}_{-0.8}$
1220-3595[s1]	64.050865	−24.066531	$28.84^{+0.30}_{-0.26}$	$-17.85^{+0.30}_{-0.26}$	$0.08^{+0.07}_{-0.05}$	0.90	3.54	$3.56^{+0.12}_{-0.13}$	$5.9^{+0.7}_{-0.6}$
1156-3446	64.048176	−24.062404	$30.65^{+0.27}_{-0.24}$	$-16.04^{+0.27}_{-0.24}$	$0.04^{+0.03}_{-0.02}$	0.81	18.55	$19.09^{+1.28}_{-1.09}$	$6.2^{+0.7}_{-0.7}$
1181-3480	64.049226	−24.063349	$31.15^{+0.26}_{-0.23}$	$-15.55^{+0.26}_{-0.23}$	$0.03^{+0.03}_{-0.02}$	0.90	35.85	$36.95^{+5.96}_{-4.75}$	$6.3^{+0.7}_{-0.7}$
0768-5032	64.032020	−24.084227	$29.48^{+0.41}_{-0.38}$	$-17.21^{+0.41}_{-0.38}$	$0.31^{+0.18}_{-0.19}$	0.17	7.22	$8.28^{+0.66}_{-0.67}$	$5.5^{+0.6}_{-5.1}$
1030-3258	64.042942	−24.057182	$28.94^{+0.11}_{-0.11}$	$-17.75^{+0.11}_{-0.11}$	$0.04^{+0.02}_{-0.02}$	0.89	2.72	$2.82^{+0.12}_{-0.11}$	$5.7^{+0.7}_{-0.7}$
0743-3348	64.030960	−24.059683	$28.49^{+0.41}_{-0.54}$	$-18.20^{+0.41}_{-0.54}$	$0.29^{+0.18}_{-0.14}$	0.41	1.74	$1.76^{+0.04}_{-0.04}$	$1.4^{+6.0}_{-0.6}$
0778-3204	64.032450	−24.055671	$28.24^{+0.31}_{-0.27}$	$-18.46^{+0.31}_{-0.27}$	$0.15^{+0.12}_{-0.09}$	0.90	1.66	$1.67^{+0.04}_{-0.04}$	$6.0^{+0.7}_{-0.7}$
1105-5392	64.046063	−24.094241	$28.20^{+0.11}_{-0.11}$	$-18.49^{+0.11}_{-0.11}$	$0.06^{+0.03}_{-0.02}$	0.90	1.23	$1.26^{+0.02}_{-0.02}$	$6.5^{+0.7}_{-0.7}$
0829-5229	64.034556	−24.089700	$28.48^{+0.30}_{-0.27}$	$-18.21^{+0.30}_{-0.27}$	$0.20^{+0.16}_{-0.12}$	0.15	1.78	$1.88^{+0.06}_{-0.05}$	$6.0^{+0.7}_{-0.9}$
1045-3324[s1]	64.043574	−24.059000	$29.39^{+0.29}_{-0.25}$	$-17.30^{+0.29}_{-0.25}$	$0.07^{+0.05}_{-0.04}$	0.90	4.68	$4.86^{+0.24}_{-0.22}$	$6.1^{+0.7}_{-0.7}$
0856-4435	64.035702	−24.078765	$30.38^{+0.39}_{-0.36}$	$-16.32^{+0.39}_{-0.36}$	$0.26^{+0.15}_{-0.16}$	0.74	13.28	$15.92^{+1.99}_{-1.84}$	$1.1^{+5.1}_{-0.8}$
0933-3382	64.038890	−24.060637	$28.28^{+0.36}_{-0.49}$	$-18.42^{+0.36}_{-0.49}$	$0.55^{+0.17}_{-0.19}$	0.75	3.63	$3.72^{+0.19}_{-0.15}$	$6.4^{+0.7}_{-0.7}$
1051-5500	64.043800	−24.097245	$26.99^{+0.68}_{-0.65}$	$-19.71^{+0.68}_{-0.65}$	$1.45^{+0.96}_{-0.41}$	0.64	1.23	$1.26^{+0.02}_{-0.02}$	$1.3^{+5.0}_{-0.8}$
1330-3565	64.055426	−24.065698	$28.79^{+0.31}_{-0.33}$	$-17.91^{+0.31}_{-0.33}$	$0.21^{+0.17}_{-0.13}$	0.89	2.27	$2.27^{+0.06}_{-0.07}$	$5.8^{+0.6}_{-1.1}$
1225-3594[s2]	64.051077	−24.066511	$29.65^{+0.20}_{-0.20}$	$-17.04^{+0.20}_{-0.20}$	$0.04^{+0.04}_{-0.02}$	0.89	3.45	$3.47^{+0.12}_{-0.12}$	$6.0^{+0.7}_{-0.6}$
1308-3431	64.054524	−24.061998	$29.81^{+0.21}_{-0.20}$	$-16.88^{+0.21}_{-0.20}$	$0.04^{+0.04}_{-0.02}$	0.48	4.03	$4.04^{+0.12}_{-0.13}$	$5.8^{+0.6}_{-0.7}$
0771-3205	64.032155	−24.055706	$28.92^{+0.21}_{-0.21}$	$-17.77^{+0.21}_{-0.21}$	$0.04^{+0.03}_{-0.02}$	0.59	1.68	$1.70^{+0.04}_{-0.04}$	$5.8^{+0.7}_{-0.9}$
0924-5133	64.038512	−24.087044	$28.77^{+0.26}_{-0.43}$	$-17.93^{+0.26}_{-0.43}$	$0.34^{+0.15}_{-0.13}$	0.61	1.70	$1.78^{+0.06}_{-0.04}$	$6.2^{+0.8}_{-0.9}$
HFF2P									
3165-7300	64.131878	−24.125007	$27.03^{+0.06}_{-0.07}$	$-19.67^{+0.06}_{-0.07}$	$0.04^{+0.02}_{-0.02}$	0.79	1.00	$1.00^{+0.00}_{-0.00}$	$7.5^{+0.9}_{-0.8}$
2773-7107	64.115582	−24.119644	$26.63^{+0.18}_{-0.23}$	$-20.07^{+0.18}_{-0.23}$	$0.31^{+0.10}_{-0.11}$	0.58	1.00	$1.00^{+0.00}_{-0.00}$	$6.4^{+0.8}_{-0.7}$
3552-5571	64.148028	−24.099201	$26.94^{+0.17}_{-0.23}$	$-19.75^{+0.17}_{-0.23}$	$0.32^{+0.10}_{-0.11}$	0.17	1.00	$1.00^{+0.01}_{-0.01}$	$6.3^{+1.0}_{-0.7}$
2912-7330	64.121366	−24.125856	$27.91^{+0.17}_{-0.21}$	$-18.78^{+0.17}_{-0.21}$	$0.07^{+0.03}_{-0.03}$	0.86	1.00	$1.00^{+0.00}_{-0.00}$	$7.6^{+0.9}_{-0.8}$
3660-5583	64.152507	−24.099529	$27.41^{+0.28}_{-0.47}$	$-19.29^{+0.28}_{-0.47}$	$0.43^{+0.19}_{-0.16}$	0.56	1.00	$1.00^{+0.01}_{-0.01}$	$5.8^{+0.7}_{-0.6}$
3011-7264	64.125486	−24.124020	$27.59^{+0.32}_{-0.28}$	$-19.10^{+0.32}_{-0.28}$	$0.28^{+0.22}_{-0.17}$	0.54	1.00	$1.00^{+0.00}_{-0.00}$	$5.9^{+0.7}_{-0.6}$
3514-6214	64.146433	−24.105965	$26.76^{+0.36}_{-0.42}$	$-19.94^{+0.36}_{-0.42}$	$0.70^{+0.25}_{-0.23}$	0.63	1.00	$1.00^{+0.01}_{-0.01}$	$6.4^{+0.7}_{-0.8}$
3809-6184	64.158737	−24.105133	$26.98^{+0.32}_{-0.29}$	$-19.71^{+0.32}_{-0.29}$	$0.62^{+0.23}_{-0.21}$	0.22	1.00	$1.00^{+0.01}_{-0.01}$	$5.8^{+0.6}_{-0.7}$
3597-6014	64.149902	−24.100413	$27.83^{+0.31}_{-0.28}$	$-18.87^{+0.31}_{-0.28}$	$0.32^{+0.26}_{-0.19}$	0.17	1.00	$1.00^{+0.01}_{-0.01}$	$7.2^{+0.8}_{-0.8}$
3378-6338	64.140776	−24.109396	$27.52^{+0.42}_{-0.54}$	$-19.18^{+0.42}_{-0.54}$	$0.76^{+0.36}_{-0.29}$	0.18	1.00	$1.00^{+0.01}_{-0.00}$	$5.4^{+0.6}_{-5.0}$
2796-7156	64.116512	−24.121026	$27.28^{+0.32}_{-0.54}$	$-19.42^{+0.32}_{-0.54}$	$0.64^{+0.20}_{-0.25}$	0.89	1.00	$1.00^{+0.00}_{-0.00}$	$6.0^{+0.7}_{-0.7}$
3253-6121	64.135552	−24.103380	$27.40^{+0.42}_{-0.55}$	$-19.29^{+0.42}_{-0.55}$	$0.80^{+0.38}_{-0.31}$	0.33	1.00	$1.00^{+0.01}_{-0.01}$	$6.6^{+0.8}_{-0.7}$
3316-7571	64.138174	−24.132532	$27.90^{+0.27}_{-0.45}$	$-18.79^{+0.27}_{-0.45}$	$0.60^{+0.26}_{-0.23}$	0.45	0.99	$0.99^{+0.00}_{-0.00}$	$5.3^{+0.6}_{-4.8}$
3241-7291	64.135067	−24.124757	$28.34^{+0.42}_{-0.34}$	$-18.35^{+0.42}_{-0.34}$	$0.34^{+0.28}_{-0.20}$	0.90	1.00	$1.00^{+0.00}_{-0.00}$	$1.4^{+4.9}_{-1.2}$
3084-7172	64.128510	−24.121451	$28.31^{+0.43}_{-0.34}$	$-18.38^{+0.43}_{-0.34}$	$0.31^{+0.26}_{-0.19}$	0.41	1.00	$1.00^{+0.00}_{-0.00}$	$5.8^{+0.7}_{-0.6}$
2909-7142	64.121231	−24.120634	$28.50^{+0.42}_{-0.34}$	$-18.20^{+0.42}_{-0.34}$	$0.40^{+0.34}_{-0.24}$	0.58	1.00	$1.00^{+0.00}_{-0.00}$	$6.1^{+0.9}_{-0.8}$
3088-5573	64.128688	−24.099261	$28.46^{+0.42}_{-0.34}$	$-18.24^{+0.42}_{-0.34}$	$0.35^{+0.29}_{-0.21}$	0.13	1.01	$1.00^{+0.01}_{-0.01}$	$5.8^{+0.7}_{-0.7}$
3151-6300	64.131331	−24.108356	$28.15^{+0.31}_{-0.27}$	$-18.54^{+0.31}_{-0.27}$	$0.33^{+0.26}_{-0.20}$	0.53	1.00	$1.00^{+0.01}_{-0.00}$	$6.1^{+0.7}_{-0.7}$
3216-6167	64.134030	−24.104666	$28.56^{+0.42}_{-0.33}$	$-18.13^{+0.42}_{-0.33}$	$0.25^{+0.21}_{-0.15}$	0.90	1.00	$1.00^{+0.01}_{-0.01}$	$6.5^{+0.9}_{-5.4}$
3429-6045	64.142896	−24.101276	$27.95^{+0.31}_{-0.52}$	$-18.74^{+0.31}_{-0.52}$	$0.60^{+0.19}_{-0.24}$	0.52	1.00	$1.00^{+0.01}_{-0.01}$	$6.6^{+0.8}_{-0.7}$
3441-8018	64.143390	−24.133838	$28.20^{+0.58}_{-0.58}$	$-18.50^{+0.58}_{-0.58}$	$0.59^{+0.46}_{-0.33}$	0.45	0.99	$0.99^{+0.00}_{-0.00}$	$1.3^{+5.2}_{-1.1}$
3602-7428	64.150087	−24.128578	$28.51^{+0.42}_{-0.34}$	$-18.18^{+0.42}_{-0.34}$	$0.34^{+0.28}_{-0.20}$	0.63	0.99	$0.99^{+0.00}_{-0.00}$	$6.0^{+0.8}_{-1.3}$
3418-6426	64.142432	−24.111851	$28.73^{+0.42}_{-0.33}$	$-17.96^{+0.42}_{-0.33}$	$0.27^{+0.22}_{-0.16}$	0.06	1.00	$1.00^{+0.01}_{-0.00}$	$1.4^{+5.4}_{-1.3}$
HFF3C									
3377-4319	109.390738	+37.742218	$29.84^{+0.13}_{-0.35}$	$-16.85^{+0.13}_{-0.35}$	$0.07^{+0.01}_{-0.03}$	0.90	63.39	$69.89^{+14.45}_{-11.72}$	$6.0^{+0.7}_{-0.7}$
3817-5168[s1]	109.409066	+37.754682	$27.73^{+0.09}_{-0.11}$	$-18.96^{+0.09}_{-0.11}$	$0.05^{+0.02}_{-0.02}$	0.47	4.63	$4.70^{+0.33}_{-0.25}$	$6.2^{+0.7}_{-0.7}$
3785-4338[s1]	109.407728	+37.742741	$28.65^{+0.10}_{-0.08}$	$-18.04^{+0.10}_{-0.08}$	$0.05^{+0.01}_{-0.01}$	0.62	9.25	$9.00^{+1.12}_{-1.31}$	$6.2^{+0.7}_{-0.7}$

Table C.1 (cont'd)

ID[a]	R.A.	Decl.	$m_{\rm UV}$[b,c]	$M_{\rm UV}$[c]	$r_{\rm e}$ / kpc[c,d]	e	$\mu_{\rm best}$[e]	μ[f]	$z_{\rm photo}$
3928-4047	109.413667	+37.734645	$29.21^{+0.10}_{-0.13}$	$-17.48^{+0.10}_{-0.13}$	$0.03^{+0.01}_{-0.01}$	0.66	12.34	$13.00^{+2.49}_{-2.00}$	$6.5^{+0.7}_{-0.8}$
3578-5538[s2]	109.399102	+37.764959	$27.65^{+0.17}_{-0.60}$	$-19.04^{+0.17}_{-0.60}$	$0.41^{+0.06}_{-0.16}$	0.04	6.30	$6.11^{+0.37}_{-0.43}$	$6.2^{+0.7}_{-0.7}$
3908-4016	109.412846	+37.733795	$29.58^{+0.09}_{-0.12}$	$-17.11^{+0.09}_{-0.12}$	$0.03^{+0.01}_{-0.01}$	0.80	17.95	$22.69^{+7.89}_{-7.35}$	$6.5^{+0.7}_{-0.7}$
3269-5069[s2]	109.386219	+37.751924	$27.81^{+0.17}_{-0.22}$	$-18.88^{+0.17}_{-0.22}$	$0.24^{+0.08}_{-0.09}$	0.76	3.17	$3.14^{+0.19}_{-0.19}$	$6.2^{+0.7}_{-0.7}$
3342-3294	109.389277	+37.724858	$27.44^{+0.17}_{-0.22}$	$-19.25^{+0.17}_{-0.22}$	$0.29^{+0.09}_{-0.10}$	0.78	2.31	$2.33^{+0.10}_{-0.07}$	$6.0^{+0.7}_{-0.6}$
3145-3537[s1]	109.381053	+37.731611	$28.43^{+0.06}_{-0.06}$	$-18.26^{+0.06}_{-0.06}$	$0.02^{+0.01}_{-0.01}$	0.86	3.42	$3.26^{+0.19}_{-0.21}$	$6.1^{+0.7}_{-0.7}$
3047-4112[s2]	109.376996	+37.736450	$28.31^{+0.10}_{-0.13}$	$-18.38^{+0.10}_{-0.13}$	$0.08^{+0.03}_{-0.03}$	0.90	4.05	$3.94^{+0.20}_{-0.31}$	$6.0^{+0.7}_{-0.6}$
3389-4210	109.391220	+37.739172	$30.36^{+0.30}_{-0.35}$	$-16.33^{+0.30}_{-0.35}$	$0.15^{+0.05}_{-0.05}$	0.72	27.22	$23.83^{+4.93}_{-7.00}$	$5.9^{+0.9}_{-5.1}$
3096-5100	109.379016	+37.752792	$29.25^{+0.29}_{-0.26}$	$-17.45^{+0.29}_{-0.26}$	$0.15^{+0.12}_{-0.09}$	0.61	5.15	$5.23^{+0.32}_{-0.26}$	$5.9^{+0.7}_{-0.7}$
3318-5132	109.388269	+37.753667	$29.56^{+0.25}_{-0.41}$	$-17.13^{+0.25}_{-0.41}$	$0.22^{+0.10}_{-0.08}$	0.77	5.73	$5.80^{+0.37}_{-0.51}$	$5.5^{+0.6}_{-4.8}$
4047-4196	109.418650	+37.738793	$29.93^{+0.10}_{-0.12}$	$-16.76^{+0.10}_{-0.12}$	$0.02^{+0.01}_{-0.01}$	0.33	8.29	$8.07^{+1.19}_{-1.32}$	$6.0^{+0.7}_{-0.7}$
3810-4541	109.408780	+37.748379	$32.53^{+0.31}_{-0.40}$	$-14.16^{+0.31}_{-0.40}$	$0.07^{+0.04}_{-0.03}$	0.90	145.08	$94.77^{+199.78}_{-44.40}$	$6.0^{+0.6}_{-0.7}$
3585-5491	109.399393	+37.763654	$28.65^{+0.64}_{-0.97}$	$-18.04^{+0.64}_{-0.97}$	$0.98^{+0.63}_{-0.32}$	0.79	6.77	$6.48^{+0.43}_{-0.66}$	$5.8^{+0.8}_{-5.1}$
3411-4573	109.392135	+37.749271	$30.17^{+0.24}_{-0.40}$	$-16.53^{+0.24}_{-0.40}$	$0.23^{+0.10}_{-0.09}$	0.83	8.50	$10.78^{+5.01}_{-2.81}$	$5.6^{+0.7}_{-5.2}$
2777-4506	109.365722	+37.747409	$29.49^{+0.25}_{-0.42}$	$-17.21^{+0.25}_{-0.42}$	$0.30^{+0.13}_{-0.11}$	0.79	4.47	$4.45^{+0.24}_{-0.23}$	$6.2^{+0.9}_{-5.0}$
3981-4481	109.415897	+37.746722	$30.54^{+0.27}_{-0.24}$	$-16.15^{+0.27}_{-0.24}$	$0.08^{+0.06}_{-0.05}$	0.79	12.74	$11.05^{+1.55}_{-1.16}$	$6.5^{+0.8}_{-0.7}$
3096-4181	109.379034	+37.738386	$29.97^{+0.10}_{-0.12}$	$-16.73^{+0.10}_{-0.12}$	$0.03^{+0.02}_{-0.01}$	0.89	5.87	$5.79^{+0.33}_{-0.44}$	$6.0^{+0.7}_{-0.7}$
3509-5294	109.396250	+37.758188	$28.86^{+0.63}_{-0.96}$	$-17.83^{+0.63}_{-0.96}$	$0.89^{+0.57}_{-0.29}$	0.27	8.65	$7.61^{+1.30}_{-0.82}$	$6.2^{+0.7}_{-1.2}$
3091-4467	109.378815	+37.746314	$30.75^{+0.10}_{-0.12}$	$-15.94^{+0.10}_{-0.12}$	$0.02^{+0.01}_{-0.01}$	0.45	10.91	$11.13^{+0.98}_{-1.13}$	$6.4^{+0.7}_{-0.7}$
HFF3P									
2342-9539	109.347598	+37.831665	$26.86^{+0.06}_{-0.07}$	$-19.83^{+0.06}_{-0.07}$	$0.06^{+0.03}_{-0.03}$	0.55	1.12	$1.16^{+0.02}_{-0.04}$	$6.5^{+0.7}_{-0.7}$
2252-9555	109.343857	+37.832092	$27.07^{+0.13}_{-0.11}$	$-19.63^{+0.13}_{-0.11}$	$0.27^{+0.08}_{-0.12}$	0.71	1.12	$1.15^{+0.02}_{-0.04}$	$6.2^{+0.7}_{-0.7}$
2427-9379	109.351141	+37.827198	$27.14^{+0.17}_{-0.23}$	$-19.55^{+0.17}_{-0.23}$	$0.33^{+0.10}_{-0.12}$	0.26	1.14	$1.18^{+0.02}_{-0.04}$	$6.6^{+0.7}_{-0.8}$
1410-0378	109.308787	+37.843848	$26.97^{+0.17}_{-0.23}$	$-19.72^{+0.17}_{-0.23}$	$0.44^{+0.14}_{-0.15}$	0.45	1.10	$1.13^{+0.02}_{-0.02}$	$7.1^{+0.8}_{-0.8}$
1604-9275	109.316835	+37.824319	$27.51^{+0.12}_{-0.14}$	$-19.18^{+0.12}_{-0.14}$	$0.06^{+0.04}_{-0.03}$	0.88	1.19	$1.21^{+0.02}_{-0.02}$	$6.8^{+0.8}_{-0.7}$
1906-8524	109.329441	+37.814580	$27.30^{+0.17}_{-0.22}$	$-19.39^{+0.17}_{-0.22}$	$0.41^{+0.13}_{-0.14}$	0.61	1.25	$1.28^{+0.02}_{-0.02}$	$7.2^{+0.8}_{-0.8}$
1778-9084	109.324122	+37.819016	$27.42^{+0.32}_{-0.28}$	$-19.27^{+0.32}_{-0.28}$	$0.26^{+0.21}_{-0.16}$	0.52	1.22	$1.24^{+0.02}_{-0.02}$	$5.8^{+0.7}_{-0.7}$
1705-9266	109.321068	+37.824061	$26.40^{+0.47}_{-0.52}$	$-20.30^{+0.47}_{-0.52}$	$1.01^{+0.36}_{-0.34}$	0.43	1.18	$1.21^{+0.02}_{-0.02}$	$5.9^{+1.1}_{-0.7}$
1519-8364	109.313303	+37.810113	$27.64^{+0.32}_{-0.28}$	$-19.06^{+0.32}_{-0.28}$	$0.29^{+0.23}_{-0.18}$	0.56	1.29	$1.30^{+0.02}_{-0.02}$	$6.8^{+0.7}_{-0.8}$
1837-9275	109.326543	+37.824306	$27.50^{+0.22}_{-0.17}$	$-19.19^{+0.22}_{-0.17}$	$0.42^{+0.12}_{-0.08}$	0.73	1.18	$1.20^{+0.02}_{-0.02}$	$6.1^{+0.7}_{-0.7}$
1881-1103	109.328390	+37.852863	$26.38^{+0.33}_{-0.30}$	$-20.32^{+0.33}_{-0.30}$	$0.61^{+0.23}_{-0.21}$	0.58	1.06	$1.09^{+0.02}_{-0.03}$	$6.2^{+0.7}_{-0.7}$
1844-9166	109.326863	+37.821291	$27.39^{+0.19}_{-0.14}$	$-19.31^{+0.19}_{-0.14}$	$0.70^{+0.13}_{-0.09}$	0.42	1.20	$1.22^{+0.02}_{-0.02}$	$4.6^{+1.1}_{-3.9}$
1855-8526	109.327331	+37.814632	$26.33^{+0.40}_{-0.54}$	$-20.36^{+0.40}_{-0.54}$	$0.99^{+0.30}_{-0.34}$	0.71	1.25	$1.28^{+0.02}_{-0.02}$	$5.8^{+0.7}_{-0.7}$
1977-9392	109.332398	+37.827567	$27.51^{+0.28}_{-0.46}$	$-19.19^{+0.28}_{-0.46}$	$0.47^{+0.21}_{-0.18}$	0.74	1.15	$1.18^{+0.02}_{-0.03}$	$6.5^{+0.8}_{-0.7}$
2364-9356	109.348503	+37.826578	$27.51^{+0.32}_{-0.53}$	$-19.18^{+0.32}_{-0.53}$	$0.56^{+0.18}_{-0.22}$	0.60	1.15	$1.18^{+0.02}_{-0.04}$	$7.3^{+0.8}_{-1.2}$
1762-0355	109.323430	+37.843220	$27.95^{+0.12}_{-0.12}$	$-18.74^{+0.12}_{-0.12}$	$0.05^{+0.03}_{-0.02}$	0.58	1.09	$1.12^{+0.02}_{-0.02}$	$6.4^{+0.9}_{-5.2}$
1696-0348	109.320698	+37.843017	$26.28^{+0.22}_{-0.24}$	$-20.42^{+0.22}_{-0.24}$	$1.20^{+0.16}_{-0.21}$	0.81	1.10	$1.12^{+0.02}_{-0.02}$	$5.9^{+0.7}_{-0.7}$
1892-9418	109.328836	+37.828302	$27.75^{+0.31}_{-0.28}$	$-18.94^{+0.31}_{-0.28}$	$0.20^{+0.16}_{-0.12}$	0.38	1.15	$1.18^{+0.02}_{-0.02}$	$6.5^{+0.7}_{-0.8}$
1188-9165	109.299505	+37.821260	$28.09^{+0.12}_{-0.13}$	$-18.60^{+0.12}_{-0.13}$	$0.07^{+0.04}_{-0.03}$	0.90	1.21	$1.22^{+0.01}_{-0.02}$	$5.8^{+0.7}_{-0.6}$
1399-9233	109.308292	+37.823145	$28.15^{+0.31}_{-0.27}$	$-18.54^{+0.31}_{-0.27}$	$0.12^{+0.10}_{-0.07}$	0.66	1.20	$1.21^{+0.01}_{-0.02}$	$5.7^{+0.7}_{-0.6}$
1527-9304	109.313633	+37.825128	$28.03^{+0.27}_{-0.45}$	$-18.66^{+0.27}_{-0.45}$	$0.45^{+0.19}_{-0.17}$	0.70	1.18	$1.20^{+0.02}_{-0.02}$	$6.1^{+0.7}_{-0.7}$
1840-9281	109.326706	+37.824478	$27.51^{+0.46}_{-0.60}$	$-19.18^{+0.46}_{-0.60}$	$0.66^{+0.29}_{-0.32}$	0.90	1.18	$1.20^{+0.02}_{-0.02}$	$5.7^{+0.6}_{-1.2}$
1263-9215	109.302636	+37.822653	$27.83^{+0.42}_{-0.56}$	$-18.87^{+0.42}_{-0.56}$	$0.56^{+0.33}_{-0.27}$	0.53	1.20	$1.21^{+0.01}_{-0.02}$	$6.5^{+0.8}_{-0.7}$
1949-0448	109.331212	+37.845805	$27.94^{+0.27}_{-0.45}$	$-18.75^{+0.27}_{-0.45}$	$0.57^{+0.25}_{-0.21}$	0.62	1.08	$1.11^{+0.02}_{-0.03}$	$6.0^{+1.1}_{-5.1}$
1319-0277	109.304963	+37.841038	$28.36^{+0.58}_{-0.57}$	$-18.33^{+0.58}_{-0.57}$	$0.37^{+0.29}_{-0.21}$	0.77	1.12	$1.14^{+0.01}_{-0.02}$	$5.8^{+0.8}_{-5.2}$
2208-9465	109.342009	+37.829593	$27.38^{+0.50}_{-0.78}$	$-19.31^{+0.50}_{-0.78}$	$0.72^{+0.29}_{-0.40}$	0.58	1.13	$1.17^{+0.02}_{-0.03}$	$5.6^{+0.6}_{-4.9}$
1307-9251	109.304485	+37.823649	$27.59^{+0.46}_{-0.60}$	$-19.10^{+0.46}_{-0.60}$	$0.54^{+0.23}_{-0.26}$	0.79	1.19	$1.21^{+0.01}_{-0.02}$	$1.2^{+4.7}_{-1.0}$
1477-9449	109.311563	+37.829163	$28.15^{+0.31}_{-0.27}$	$-18.55^{+0.31}_{-0.27}$	$0.34^{+0.27}_{-0.20}$	0.53	1.16	$1.18^{+0.02}_{-0.02}$	$6.1^{+0.9}_{-1.2}$
1538-9217	109.314090	+37.822717	$27.52^{+0.33}_{-0.46}$	$-19.17^{+0.33}_{-0.46}$	$0.95^{+0.37}_{-0.22}$	0.66	1.20	$1.22^{+0.02}_{-0.02}$	$6.6^{+0.9}_{-5.2}$
1375-9505	109.307304	+37.830722	$28.16^{+0.31}_{-0.27}$	$-18.53^{+0.31}_{-0.27}$	$0.27^{+0.21}_{-0.16}$	0.90	1.16	$1.18^{+0.01}_{-0.02}$	$1.4^{+2.4}_{-1.3}$
1373-9422	109.307224	+37.828402	$28.29^{+0.27}_{-0.45}$	$-18.41^{+0.27}_{-0.45}$	$0.52^{+0.23}_{-0.20}$	0.24	1.17	$1.19^{+0.01}_{-0.02}$	$6.5^{+0.7}_{-0.7}$
1489-0326	109.312053	+37.842390	$28.45^{+0.36}_{-0.32}$	$-18.25^{+0.36}_{-0.32}$	$0.24^{+0.18}_{-0.14}$	0.90	1.11	$1.13^{+0.02}_{-0.02}$	$6.9^{+0.8}_{-5.8}$
1810-0535	109.325457	+37.848217	$28.22^{+0.31}_{-0.27}$	$-18.47^{+0.31}_{-0.27}$	$0.18^{+0.14}_{-0.11}$	0.90	1.08	$1.11^{+0.02}_{-0.03}$	$6.8^{+0.8}_{-1.4}$
1151-9291	109.297969	+37.824773	$28.46^{+0.58}_{-0.57}$	$-18.23^{+0.58}_{-0.57}$	$0.42^{+0.33}_{-0.24}$	0.37	1.19	$1.20^{+0.01}_{-0.02}$	$1.4^{+5.4}_{-1.2}$

Table C.1 (cont'd)

ID[a]	R.A.	Decl.	$m_{\rm UV}$[b,c]	$M_{\rm UV}$[c]	$r_{\rm e}$ / kpc[c,d]	e	$\mu_{\rm best}$[e]	μ[f]	$z_{\rm photo}$
1813-0035	109.325574	+37.834310	$28.30^{+0.27}_{-0.45}$	$-18.40^{+0.27}_{-0.45}$	$0.48^{+0.21}_{-0.18}$	0.30	1.13	$1.15^{+0.02}_{-0.02}$	$5.6^{+0.6}_{-5.4}$
1776-8528	109.324018	+37.814689	$28.51^{+0.57}_{-0.57}$	$-18.18^{+0.57}_{-0.57}$	$0.36^{+0.28}_{-0.20}$	0.62	1.25	$1.28^{+0.02}_{-0.02}$	$5.7^{+0.9}_{-5.3}$
1853-9354	109.327214	+37.826505	$28.29^{+0.31}_{-0.27}$	$-18.41^{+0.31}_{-0.27}$	$0.21^{+0.17}_{-0.13}$	0.89	1.16	$1.19^{+0.02}_{-0.02}$	$5.6^{+0.7}_{-5.3}$
2010-0108	109.333783	+37.836335	$28.78^{+0.21}_{-0.21}$	$-17.91^{+0.21}_{-0.21}$	$0.09^{+0.08}_{-0.05}$	0.77	1.11	$1.14^{+0.02}_{-0.03}$	$5.6^{+0.7}_{-5.0}$
1628-9029	109.317874	+37.817496	$28.55^{+0.57}_{-0.57}$	$-18.14^{+0.57}_{-0.57}$	$0.42^{+0.33}_{-0.23}$	0.36	1.23	$1.25^{+0.02}_{-0.02}$	$5.6^{+0.7}_{-5.2}$
1936-9052	109.330680	+37.818119	$28.30^{+0.52}_{-0.41}$	$-18.40^{+0.52}_{-0.41}$	$0.30^{+0.24}_{-0.14}$	0.74	1.22	$1.25^{+0.02}_{-0.02}$	$5.6^{+0.7}_{-5.2}$
1494-9162	109.312291	+37.821185	$28.16^{+0.67}_{-0.71}$	$-18.53^{+0.67}_{-0.71}$	$0.38^{+0.23}_{-0.16}$	0.06	1.21	$1.23^{+0.02}_{-0.02}$	$6.3^{+1.0}_{-5.0}$
HFF4C									
4025-5027	177.417749	+22.417435	$25.73^{+0.06}_{-0.14}$	$-20.96^{+0.06}_{-0.14}$	$0.39^{+0.03}_{-0.09}$	0.64	1.55	$1.58^{+0.11}_{-0.12}$	$7.5^{+0.8}_{-0.8}$
3888-4567	177.412018	+22.415777	$25.55^{+0.05}_{-0.07}$	$-21.14^{+0.05}_{-0.07}$	$0.74^{+0.03}_{-0.04}$	0.66	1.92	$2.01^{+0.27}_{-0.24}$	$5.8^{+0.7}_{-0.6}$
3321-2566	177.388388	+22.382390	$26.94^{+0.11}_{-0.14}$	$-19.75^{+0.11}_{-0.14}$	$0.18^{+0.06}_{-0.08}$	0.11	1.72	$1.63^{+0.05}_{-0.05}$	$6.3^{+0.7}_{-0.7}$
3180-3434	177.382540	+22.395401	$26.56^{+0.18}_{-0.63}$	$-20.13^{+0.18}_{-0.63}$	$0.70^{+0.10}_{-0.28}$	0.34	2.25	$2.12^{+0.11}_{-0.11}$	$5.7^{+0.7}_{-0.6}$
3911-5079	177.412999	+22.418864	$26.80^{+0.17}_{-0.23}$	$-19.89^{+0.17}_{-0.23}$	$0.36^{+0.11}_{-0.13}$	0.50	1.69	$1.69^{+0.11}_{-0.12}$	$6.5^{+0.7}_{-0.8}$
3672-4342	177.403011	+22.409501	$27.93^{+0.16}_{-0.22}$	$-18.77^{+0.16}_{-0.22}$	$0.17^{+0.05}_{-0.06}$	0.46	3.58	$3.98^{+1.09}_{-0.55}$	$6.0^{+0.7}_{-0.7}$
4042-4205	177.418442	+22.405696	$27.76^{+0.13}_{-0.11}$	$-18.93^{+0.13}_{-0.11}$	$0.09^{+0.03}_{-0.04}$	0.87	1.75	$1.74^{+0.07}_{-0.06}$	$5.8^{+0.7}_{-0.6}$
3910-4491	177.412935	+22.413642	$27.61^{+0.05}_{-0.06}$	$-19.08^{+0.05}_{-0.06}$	$0.03^{+0.01}_{-0.01}$	0.35	1.85	$1.97^{+0.38}_{-0.22}$	$6.4^{+0.7}_{-0.7}$
4042-4207	177.418456	+22.405770	$27.33^{+0.13}_{-0.11}$	$-19.37^{+0.13}_{-0.11}$	$0.21^{+0.06}_{-0.09}$	0.90	1.75	$1.73^{+0.07}_{-0.06}$	$5.9^{+0.7}_{-0.7}$
4046-4231	177.418619	+22.406430	$27.82^{+0.21}_{-0.16}$	$-18.88^{+0.21}_{-0.16}$	$0.35^{+0.10}_{-0.07}$	0.42	1.71	$1.71^{+0.08}_{-0.07}$	$6.0^{+0.6}_{-0.7}$
3952-5014	177.414690	+22.417060	$27.50^{+0.17}_{-0.22}$	$-19.20^{+0.17}_{-0.22}$	$0.31^{+0.10}_{-0.11}$	0.73	1.69	$1.72^{+0.15}_{-0.15}$	$6.5^{+0.7}_{-0.8}$
4047-4228	177.418636	+22.406343	$28.05^{+0.12}_{-0.12}$	$-18.65^{+0.12}_{-0.12}$	$0.06^{+0.03}_{-0.02}$	0.90	1.72	$1.71^{+0.08}_{-0.07}$	$6.0^{+0.6}_{-0.7}$
3906-4324	177.412777	+22.409016	$27.95^{+0.31}_{-0.52}$	$-18.75^{+0.31}_{-0.52}$	$0.53^{+0.17}_{-0.21}$	0.51	1.93	$1.99^{+0.24}_{-0.13}$	$7.3^{+0.8}_{-1.1}$
3705-4446	177.404410	+22.412397	$28.89^{+0.11}_{-0.11}$	$-17.80^{+0.11}_{-0.11}$	$0.04^{+0.02}_{-0.02}$	0.89	3.41	$4.12^{+4.38}_{-1.04}$	$6.6^{+0.8}_{-0.8}$
3830-3120[s1]	177.409606	+22.386668	$29.91^{+0.28}_{-0.25}$	$-16.78^{+0.28}_{-0.25}$	$0.08^{+0.06}_{-0.05}$	0.84	6.80	$6.29^{+1.00}_{-1.08}$	$6.3^{+0.7}_{-0.7}$
3765-3173	177.406897	+22.388148	$28.21^{+0.33}_{-0.20}$	$-18.48^{+0.33}_{-0.20}$	$0.34^{+0.07}_{-0.07}$	0.28	5.48	$5.02^{+1.22}_{-1.13}$	$5.7^{+0.7}_{-4.8}$
3889-3206[s1]	177.412079	+22.389059	$29.88^{+0.11}_{-0.12}$	$-16.81^{+0.11}_{-0.12}$	$0.03^{+0.02}_{-0.01}$	0.63	7.88	$7.64^{+0.77}_{-0.63}$	$6.7^{+0.7}_{-0.8}$
3433-2527	177.393042	+22.381320	$28.19^{+0.31}_{-0.27}$	$-18.51^{+0.31}_{-0.27}$	$0.22^{+0.18}_{-0.13}$	0.53	1.74	$1.63^{+0.06}_{-0.06}$	$5.8^{+0.7}_{-0.6}$
4026-3382	177.417760	+22.393947	$28.24^{+0.30}_{-0.27}$	$-18.45^{+0.30}_{-0.27}$	$0.31^{+0.12}_{-0.11}$	0.59	3.08	$2.91^{+0.11}_{-0.10}$	$5.9^{+0.6}_{-0.7}$
3231-2579	177.384647	+22.382754	$28.21^{+0.12}_{-0.13}$	$-18.48^{+0.12}_{-0.13}$	$0.04^{+0.02}_{-0.02}$	0.70	1.67	$1.58^{+0.05}_{-0.05}$	$6.0^{+0.7}_{-0.7}$
3134-4050	177.380590	+22.401408	$28.82^{+0.26}_{-0.43}$	$-17.87^{+0.26}_{-0.43}$	$0.26^{+0.11}_{-0.10}$	0.67	2.83	$2.72^{+0.21}_{-0.17}$	$6.5^{+0.8}_{-0.7}$
3191-4433	177.382991	+22.412040	$30.05^{+0.10}_{-0.12}$	$-16.65^{+0.10}_{-0.12}$	$0.02^{+0.01}_{-0.01}$	0.46	6.49	$7.91^{+13.31}_{-2.89}$	$7.2^{+0.8}_{-1.3}$
3665-4526	177.402725	+22.414615	$29.40^{+0.29}_{-0.25}$	$-17.29^{+0.29}_{-0.25}$	$0.10^{+0.08}_{-0.06}$	0.90	4.89	$5.25^{+2.63}_{-1.53}$	$5.8^{+0.6}_{-0.7}$
4076-4033	177.419863	+22.400937	$28.90^{+0.11}_{-0.11}$	$-17.79^{+0.11}_{-0.11}$	$0.04^{+0.02}_{-0.01}$	0.66	2.05	$1.99^{+0.07}_{-0.06}$	$6.1^{+0.8}_{-0.7}$
3760-3035[s1]	177.406675	+22.384327	$29.98^{+0.10}_{-0.12}$	$-16.71^{+0.10}_{-0.12}$	$0.02^{+0.01}_{-0.01}$	0.67	6.14	$5.41^{+0.71}_{-0.96}$	$6.6^{+0.7}_{-0.8}$
3791-4415	177.407983	+22.411538	$28.35^{+0.44}_{-0.57}$	$-18.34^{+0.44}_{-0.57}$	$0.39^{+0.17}_{-0.19}$	0.75	2.32	$2.56^{+0.86}_{-0.34}$	$6.2^{+0.7}_{-0.7}$
3894-3418	177.412259	+22.394967	$30.02^{+0.10}_{-0.12}$	$-16.67^{+0.10}_{-0.12}$	$0.02^{+0.01}_{-0.01}$	0.85	6.64	$6.16^{+0.39}_{-0.33}$	$6.6^{+0.8}_{-0.7}$
3305-4210	177.387710	+22.405836	$30.45^{+0.27}_{-0.24}$	$-16.24^{+0.27}_{-0.24}$	$0.06^{+0.05}_{-0.04}$	0.44	10.29	$10.47^{+2.85}_{-1.73}$	$5.8^{+0.7}_{-0.6}$
3892-3416	177.412203	+22.394890	$29.10^{+0.28}_{-0.26}$	$-17.59^{+0.28}_{-0.26}$	$0.19^{+0.07}_{-0.07}$	0.78	6.79	$6.30^{+0.40}_{-0.35}$	$6.6^{+0.8}_{-0.7}$
3736-5005	177.405705	+22.416817	$29.74^{+0.20}_{-0.20}$	$-16.95^{+0.20}_{-0.20}$	$0.05^{+0.05}_{-0.03}$	0.72	2.53	$2.57^{+0.30}_{-0.31}$	$6.5^{+0.8}_{-1.2}$
4205-3155	177.425223	+22.387645	$26.92^{+0.69}_{-0.66}$	$-19.77^{+0.69}_{-0.66}$	$1.03^{+0.69}_{-0.30}$	0.62	2.22	$2.12^{+0.06}_{-0.05}$	$1.3^{+5.3}_{-0.4}$
3991-3123	177.416321	+22.386751	$29.64^{+0.20}_{-0.20}$	$-17.05^{+0.20}_{-0.20}$	$0.03^{+0.03}_{-0.01}$	0.84	3.45	$3.28^{+0.15}_{-0.13}$	$5.8^{+0.7}_{-4.8}$
3405-3155	177.391898	+22.387646	$28.80^{+0.26}_{-0.43}$	$-17.89^{+0.26}_{-0.43}$	$0.29^{+0.13}_{-0.11}$	0.89	2.34	$2.16^{+0.09}_{-0.09}$	$1.3^{+5.2}_{-1.1}$
3419-3006	177.392475	+22.383511	$28.66^{+0.30}_{-0.26}$	$-18.04^{+0.30}_{-0.26}$	$0.27^{+0.21}_{-0.16}$	0.55	1.90	$1.78^{+0.07}_{-0.06}$	$5.6^{+0.7}_{-4.5}$
3595-4157	177.399818	+22.404384	$34.45^{+0.39}_{-0.38}$	$-12.25^{+0.39}_{-0.38}$	$0.03^{+0.02}_{-0.02}$	0.90	157.63	$60.11^{+37.38}_{-18.69}$	$0.3^{+3.7}_{-0.2}$
4082-3192	177.420086	+22.388672	$29.15^{+0.29}_{-0.26}$	$-17.54^{+0.29}_{-0.26}$	$0.08^{+0.06}_{-0.05}$	0.90	2.94	$2.78^{+0.10}_{-0.10}$	$5.6^{+0.7}_{-4.9}$
3312-2565	177.388012	+22.382380	$28.30^{+0.31}_{-0.51}$	$-18.39^{+0.31}_{-0.51}$	$0.48^{+0.15}_{-0.19}$	0.77	1.72	$1.62^{+0.05}_{-0.05}$	$6.2^{+0.8}_{-0.9}$
3225-2532	177.384407	+22.381448	$27.76^{+0.41}_{-0.54}$	$-18.94^{+0.41}_{-0.54}$	$0.71^{+0.34}_{-0.27}$	0.59	1.61	$1.54^{+0.04}_{-0.04}$	$1.4^{+4.9}_{-1.3}$
3345-3553	177.389398	+22.398696	$29.37^{+0.38}_{-0.49}$	$-17.32^{+0.38}_{-0.49}$	$0.34^{+0.16}_{-0.13}$	0.73	6.03	$5.51^{+0.47}_{-0.49}$	$0.3^{+4.7}_{-0.2}$
3282-4046	177.386778	+22.401298	$29.59^{+0.25}_{-0.41}$	$-17.11^{+0.25}_{-0.41}$	$0.31^{+0.13}_{-0.12}$	0.51	5.01	$4.79^{+0.44}_{-0.37}$	$5.6^{+0.7}_{-0.6}$
3829-4199	177.409561	+22.405545	$29.58^{+0.20}_{-0.20}$	$-17.11^{+0.20}_{-0.20}$	$0.07^{+0.06}_{-0.03}$	0.90	2.41	$2.38^{+0.13}_{-0.12}$	$6.3^{+0.8}_{-1.6}$
HFF4P									
3938-8196	177.414121	+22.305448	$25.41^{+0.16}_{-0.57}$	$-21.28^{+0.16}_{-0.57}$	$0.76^{+0.11}_{-0.30}$	0.47	1.03	$1.01^{+0.01}_{-0.01}$	$6.8^{+0.7}_{-0.8}$
4461-7461	177.435880	+22.296142	$26.55^{+0.06}_{-0.07}$	$-20.15^{+0.06}_{-0.07}$	$0.06^{+0.03}_{-0.03}$	0.24	1.03	$1.01^{+0.01}_{-0.01}$	$7.5^{+0.9}_{-0.8}$
4423-8329	177.434292	+22.309155	$26.52^{+0.13}_{-0.12}$	$-20.17^{+0.13}_{-0.12}$	$0.25^{+0.07}_{-0.11}$	0.21	1.04	$1.03^{+0.01}_{-0.01}$	$7.1^{+0.8}_{-0.8}$
3681-7168	177.403385	+22.288000	$26.70^{+0.18}_{-0.23}$	$-19.99^{+0.18}_{-0.23}$	$0.31^{+0.10}_{-0.11}$	0.35	1.01	$1.00^{+0.01}_{-0.01}$	$6.2^{+0.7}_{-0.7}$

Table C.1 (cont'd)

ID[a]	R.A.	Decl.	$m_{\rm UV}$[b,c]	$M_{\rm UV}$[c]	$r_{\rm e}$ / kpc[c,d]	e	$\mu_{\rm best}$[e]	μ[f]	$z_{\rm photo}$
4005-7307	177.416916	+22.291875	$27.06^{+0.13}_{-0.11}$	$-19.63^{+0.13}_{-0.11}$	$0.31^{+0.09}_{-0.14}$	0.12	1.01	$1.00^{+0.01}_{-0.01}$	$6.8^{+0.8}_{-0.8}$
3742-7453	177.405922	+22.295927	$27.00^{+0.22}_{-0.17}$	$-19.70^{+0.22}_{-0.17}$	$0.46^{+0.13}_{-0.09}$	0.73	1.02	$1.01^{+0.01}_{-0.01}$	$6.0^{+0.7}_{-0.7}$
3815-7490	177.408969	+22.296968	$26.57^{+0.32}_{-0.29}$	$-20.13^{+0.32}_{-0.29}$	$0.60^{+0.22}_{-0.21}$	0.58	1.02	$1.01^{+0.01}_{-0.01}$	$6.0^{+0.6}_{-0.7}$
4208-8047	177.425354	+22.301318	$26.99^{+0.17}_{-0.23}$	$-19.70^{+0.17}_{-0.23}$	$0.34^{+0.11}_{-0.12}$	0.38	1.03	$1.01^{+0.01}_{-0.01}$	$6.2^{+0.7}_{-0.7}$
3678-7409	177.403268	+22.294703	$27.58^{+0.12}_{-0.12}$	$-19.12^{+0.12}_{-0.12}$	$0.06^{+0.03}_{-0.03}$	0.68	1.02	$1.01^{+0.01}_{-0.01}$	$7.2^{+0.8}_{-1.0}$
3695-7381	177.403979	+22.293922	$27.52^{+0.12}_{-0.12}$	$-19.17^{+0.12}_{-0.12}$	$0.06^{+0.04}_{-0.03}$	0.90	1.02	$1.01^{+0.01}_{-0.01}$	$7.2^{+0.8}_{-1.2}$
3832-7190	177.409706	+22.288622	$27.22^{+0.44}_{-0.57}$	$-19.47^{+0.44}_{-0.57}$	$0.47^{+0.28}_{-0.23}$	0.67	1.01	$1.00^{+0.01}_{-0.01}$	$6.4^{+0.7}_{-0.8}$
4539-7124	177.439130	+22.286794	$27.31^{+0.28}_{-0.47}$	$-19.39^{+0.28}_{-0.47}$	$0.66^{+0.29}_{-0.25}$	0.52	1.02	$1.01^{+0.01}_{-0.01}$	$6.2^{+0.7}_{-0.7}$
4497-8060	177.437411	+22.301678	$27.59^{+0.28}_{-0.46}$	$-19.11^{+0.28}_{-0.46}$	$0.59^{+0.25}_{-0.22}$	0.40	1.03	$1.02^{+0.01}_{-0.01}$	$6.9^{+0.8}_{-0.8}$
4269-8288	177.427882	+22.308025	$27.62^{+0.32}_{-0.28}$	$-19.07^{+0.32}_{-0.28}$	$0.36^{+0.28}_{-0.22}$	0.24	1.04	$1.02^{+0.01}_{-0.01}$	$6.0^{+0.7}_{-0.7}$
4045-8214	177.418575	+22.305965	$27.03^{+0.36}_{-0.42}$	$-19.67^{+0.36}_{-0.42}$	$0.79^{+0.28}_{-0.26}$	0.35	1.03	$1.02^{+0.01}_{-0.01}$	$5.8^{+1.0}_{-4.9}$
4194-8047	177.424789	+22.301318	$27.58^{+0.28}_{-0.46}$	$-19.12^{+0.28}_{-0.46}$	$0.51^{+0.22}_{-0.19}$	0.74	1.03	$1.01^{+0.01}_{-0.01}$	$5.9^{+0.6}_{-0.7}$
4372-7404	177.432202	+22.294558	$27.86^{+0.27}_{-0.46}$	$-18.83^{+0.27}_{-0.46}$	$0.45^{+0.19}_{-0.17}$	0.83	1.02	$1.01^{+0.01}_{-0.01}$	$7.1^{+0.8}_{-1.2}$
3881-7423	177.411719	+22.295094	$27.83^{+0.31}_{-0.28}$	$-18.87^{+0.31}_{-0.28}$	$0.13^{+0.10}_{-0.08}$	0.90	1.01	$1.01^{+0.01}_{-0.01}$	$6.8^{+0.7}_{-0.8}$
4133-6595	177.422215	+22.283195	$27.96^{+0.31}_{-0.28}$	$-18.74^{+0.31}_{-0.28}$	$0.37^{+0.29}_{-0.22}$	0.42	1.01	$1.00^{+0.01}_{-0.01}$	$6.1^{+0.7}_{-0.7}$
4005-7321	177.416898	+22.292273	$27.59^{+0.49}_{-0.77}$	$-19.10^{+0.49}_{-0.77}$	$0.76^{+0.31}_{-0.42}$	0.50	1.01	$1.00^{+0.01}_{-0.01}$	$6.6^{+0.8}_{-0.7}$
3549-8309	177.397916	+22.308605	$28.29^{+0.36}_{-0.32}$	$-18.41^{+0.36}_{-0.32}$	$0.12^{+0.09}_{-0.07}$	0.77	1.03	$1.02^{+0.01}_{-0.01}$	$6.5^{+0.7}_{-0.8}$
4459-7323	177.435824	+22.292329	$27.35^{+0.42}_{-0.55}$	$-19.34^{+0.42}_{-0.55}$	$0.75^{+0.36}_{-0.29}$	0.57	1.02	$1.01^{+0.01}_{-0.01}$	$5.5^{+0.6}_{-5.2}$
4399-8595	177.433312	+22.316552	$28.19^{+0.27}_{-0.45}$	$-18.50^{+0.27}_{-0.45}$	$0.55^{+0.24}_{-0.21}$	0.69	1.06	$1.04^{+0.02}_{-0.01}$	$5.7^{+1.1}_{-5.5}$
3860-7488	177.410866	+22.296898	$27.63^{+0.49}_{-0.77}$	$-19.06^{+0.49}_{-0.77}$	$0.75^{+0.30}_{-0.42}$	0.57	1.02	$1.01^{+0.01}_{-0.01}$	$5.7^{+0.8}_{-5.1}$
4529-8297	177.438743	+22.308266	$28.16^{+0.27}_{-0.45}$	$-18.54^{+0.27}_{-0.45}$	$0.47^{+0.21}_{-0.18}$	0.77	1.05	$1.03^{+0.01}_{-0.01}$	$6.5^{+0.8}_{-0.7}$
4250-7424	177.427107	+22.295124	$28.14^{+0.27}_{-0.45}$	$-18.55^{+0.27}_{-0.45}$	$0.51^{+0.22}_{-0.19}$	0.37	1.02	$1.01^{+0.01}_{-0.01}$	$6.5^{+0.7}_{-0.8}$
4163-8238	177.423498	+22.306622	$28.02^{+0.27}_{-0.45}$	$-18.67^{+0.27}_{-0.45}$	$0.47^{+0.20}_{-0.18}$	0.71	1.03	$1.02^{+0.01}_{-0.01}$	$6.1^{+0.7}_{-0.7}$
3731-7203	177.405479	+22.288982	$28.14^{+0.31}_{-0.27}$	$-18.56^{+0.31}_{-0.27}$	$0.17^{+0.13}_{-0.10}$	0.90	1.01	$1.00^{+0.01}_{-0.01}$	$6.1^{+0.7}_{-0.9}$
3841-8191	177.410083	+22.305310	$28.17^{+0.58}_{-0.58}$	$-18.52^{+0.58}_{-0.58}$	$0.46^{+0.36}_{-0.25}$	0.38	1.02	$1.01^{+0.01}_{-0.01}$	$1.3^{+4.8}_{-1.1}$
4380-7515	177.432540	+22.297653	$27.14^{+0.57}_{-0.68}$	$-19.55^{+0.57}_{-0.68}$	$1.01^{+0.64}_{-0.47}$	0.53	1.02	$1.01^{+0.01}_{-0.01}$	$1.2^{+4.7}_{-0.7}$
3653-8000	177.402242	+22.300011	$28.00^{+0.42}_{-0.55}$	$-18.70^{+0.42}_{-0.55}$	$0.54^{+0.32}_{-0.26}$	0.90	1.02	$1.01^{+0.01}_{-0.01}$	$6.5^{+0.7}_{-0.7}$
4110-8223	177.421272	+22.306214	$27.92^{+0.31}_{-0.52}$	$-18.77^{+0.31}_{-0.52}$	$0.77^{+0.24}_{-0.30}$	0.68	1.03	$1.02^{+0.01}_{-0.01}$	$6.1^{+0.8}_{-1.3}$
3924-7397	177.413514	+22.294386	$28.17^{+0.58}_{-0.58}$	$-18.53^{+0.58}_{-0.58}$	$0.41^{+0.32}_{-0.23}$	0.21	1.01	$1.01^{+0.01}_{-0.01}$	$6.4^{+0.7}_{-0.8}$
4417-9034	177.434056	+22.317617	$29.02^{+0.41}_{-0.33}$	$-17.67^{+0.41}_{-0.33}$	$0.16^{+0.14}_{-0.10}$	0.90	1.06	$1.05^{+0.02}_{-0.01}$	$1.3^{+4.7}_{-1.2}$
3614-8432	177.400593	+22.312020	$27.91^{+0.41}_{-0.53}$	$-18.78^{+0.41}_{-0.53}$	$0.76^{+0.36}_{-0.29}$	0.47	1.03	$1.02^{+0.01}_{-0.01}$	$1.4^{+4.9}_{-1.3}$
4579-7587	177.440827	+22.299656	$26.73^{+0.62}_{-0.52}$	$-19.96^{+0.62}_{-0.52}$	$1.33^{+0.53}_{-0.39}$	0.76	1.03	$1.02^{+0.01}_{-0.01}$	$1.3^{+4.8}_{-1.0}$
4380-7427	177.432518	+22.295210	$27.79^{+0.32}_{-0.52}$	$-18.91^{+0.32}_{-0.52}$	$0.70^{+0.22}_{-0.27}$	0.77	1.02	$1.01^{+0.01}_{-0.01}$	$6.1^{+0.7}_{-0.9}$
HFF5C									
4581-2148[s1]	342.190894	−44.537462	$26.69^{+0.03}_{-0.06}$	$-20.00^{+0.03}_{-0.06}$	$0.12^{+0.01}_{-0.05}$	0.46	5.84	$6.02^{+0.25}_{-0.28}$	$6.0^{+0.7}_{-0.7}$
4537-1480[s1]	342.189053	−44.530026	$26.41^{+0.08}_{-0.23}$	$-20.28^{+0.08}_{-0.23}$	$0.16^{+0.03}_{-0.04}$	0.64	4.29	$4.49^{+0.22}_{-0.25}$	$6.0^{+0.7}_{-0.7}$
4111-1112[s1]	342.171301	−44.519801	$26.82^{+0.04}_{-0.06}$	$-19.88^{+0.04}_{-0.06}$	$0.11^{+0.01}_{-0.04}$	0.54	2.44	$2.47^{+0.06}_{-0.06}$	$5.9^{+0.7}_{-0.6}$
4265-2489	342.177715	−44.546931	$27.53^{+0.31}_{-0.28}$	$-19.17^{+0.31}_{-0.28}$	$0.34^{+0.12}_{-0.12}$	0.64	3.22	$3.31^{+0.09}_{-0.11}$	$6.1^{+0.7}_{-0.7}$
4159-1333[s2]	342.173329	−44.525929	$28.87^{+0.10}_{-0.13}$	$-17.82^{+0.10}_{-0.13}$	$0.08^{+0.03}_{-0.04}$	0.40	5.92	$6.02^{+0.25}_{-0.27}$	$5.9^{+0.7}_{-0.6}$
4227-2335[s3]	342.176131	−44.542663	$29.15^{+0.15}_{-0.20}$	$-17.54^{+0.15}_{-0.20}$	$0.15^{+0.05}_{-0.05}$	0.59	9.56	$9.58^{+0.43}_{-0.40}$	$6.0^{+0.7}_{-0.7}$
4017-0457	342.167376	−44.512709	$27.29^{+0.31}_{-0.28}$	$-19.40^{+0.31}_{-0.28}$	$0.41^{+0.15}_{-0.14}$	0.71	1.71	$1.73^{+0.03}_{-0.03}$	$1.2^{+4.6}_{-0.6}$
3822-2382	342.159276	−44.543958	$28.97^{+0.29}_{-0.26}$	$-17.72^{+0.29}_{-0.26}$	$0.08^{+0.06}_{-0.05}$	0.90	4.27	$4.55^{+0.21}_{-0.22}$	$6.5^{+0.7}_{-0.8}$
4877-1209	342.203210	−44.522476	$28.82^{+0.41}_{-0.45}$	$-17.87^{+0.41}_{-0.45}$	$0.42^{+0.15}_{-0.14}$	0.54	8.91	$10.10^{+1.92}_{-1.31}$	$6.2^{+1.1}_{-4.9}$
3944-1488[s3]	342.164364	−44.530226	$29.18^{+0.29}_{-0.26}$	$-17.51^{+0.29}_{-0.26}$	$0.05^{+0.04}_{-0.03}$	0.90	5.68	$5.70^{+0.21}_{-0.23}$	$6.0^{+0.6}_{-0.7}$
3998-0372	342.166608	−44.510345	$27.78^{+0.45}_{-0.59}$	$-18.91^{+0.45}_{-0.59}$	$0.55^{+0.24}_{-0.27}$	0.84	1.59	$1.61^{+0.02}_{-0.02}$	$6.7^{+0.7}_{-0.9}$
4213-1414	342.175551	−44.528186	$31.35^{+0.33}_{-0.43}$	$-15.34^{+0.33}_{-0.43}$	$0.11^{+0.05}_{-0.04}$	0.89	47.88	$46.64^{+7.83}_{-7.07}$	$6.0^{+0.7}_{-0.7}$
4186-1141	342.174445	−44.520605	$28.92^{+0.43}_{-0.56}$	$-17.78^{+0.43}_{-0.56}$	$0.39^{+0.17}_{-0.19}$	0.60	2.98	$3.02^{+0.08}_{-0.08}$	$6.0^{+1.1}_{-5.5}$
4650-2338[s2]	342.193770	−44.542729	$29.19^{+0.11}_{-0.13}$	$-17.50^{+0.11}_{-0.13}$	$0.05^{+0.03}_{-0.02}$	0.90	2.52	$2.61^{+0.08}_{-0.09}$	$5.6^{+0.7}_{-5.4}$
3930-1274	342.163789	−44.524303	$29.35^{+0.21}_{-0.20}$	$-17.35^{+0.21}_{-0.20}$	$0.04^{+0.04}_{-0.02}$	0.37	2.53	$2.56^{+0.06}_{-0.06}$	$5.7^{+0.6}_{-0.7}$
4509-1101	342.187910	−44.519484	$30.81^{+0.19}_{-0.19}$	$-15.89^{+0.19}_{-0.19}$	$0.03^{+0.02}_{-0.01}$	0.48	8.85	$9.10^{+0.32}_{-0.31}$	$5.8^{+0.7}_{-0.8}$
3913-2297	342.163049	−44.541595	$29.74^{+0.28}_{-0.25}$	$-16.95^{+0.28}_{-0.25}$	$0.09^{+0.07}_{-0.05}$	0.90	8.19	$9.21^{+0.79}_{-0.76}$	$6.2^{+0.7}_{-0.7}$
4414-2071	342.183917	−44.535313	$31.01^{+0.39}_{-0.24}$	$-15.69^{+0.39}_{-0.24}$	$0.05^{+0.05}_{-0.03}$	0.90	17.05	$17.03^{+0.86}_{-0.70}$	$6.3^{+0.7}_{-0.8}$
4493-2466	342.187222	−44.546282	$29.31^{+0.40}_{-0.32}$	$-17.38^{+0.40}_{-0.32}$	$0.11^{+0.09}_{-0.06}$	0.50	2.47	$2.56^{+0.07}_{-0.09}$	$5.6^{+0.6}_{-5.5}$
3977-0487	342.165711	−44.513540	$28.41^{+0.41}_{-0.54}$	$-18.28^{+0.41}_{-0.54}$	$0.30^{+0.18}_{-0.15}$	0.89	1.74	$1.76^{+0.03}_{-0.03}$	$5.4^{+0.6}_{-5.1}$

Table C.1 (cont'd)

ID[a]	R.A.	Decl.	$m_{\rm UV}$[b,c]	$M_{\rm UV}$[c]	$r_{\rm e}$ / kpc[c,d]	e	$\mu_{\rm best}$[e]	μ[f]	$z_{\rm photo}$
3960-0509	342.165033	−44.514157	$27.48^{+0.44}_{-0.49}$	$-19.21^{+0.44}_{-0.49}$	$0.83^{+0.29}_{-0.28}$	0.65	1.77	$1.79^{+0.03}_{-0.03}$	$5.7^{+0.6}_{-4.7}$
4260-1364	342.177526	−44.526786	$31.47^{+0.35}_{-0.28}$	$-15.22^{+0.35}_{-0.28}$	$0.04^{+0.03}_{-0.02}$	0.81	19.12	$19.23^{+1.34}_{-1.43}$	$5.9^{+0.7}_{-5.2}$
4039-1566	342.168321	−44.532412	$33.04^{+0.32}_{-0.25}$	$-13.65^{+0.32}_{-0.25}$	$0.04^{+0.03}_{-0.02}$	0.90	77.69	$78.19^{+37.86}_{-17.60}$	$5.3^{+0.8}_{-5.1}$
HFF5P									
1436-3153	342.309861	−44.554260	$25.88^{+0.16}_{-0.43}$	$-20.82^{+0.16}_{-0.43}$	$0.55^{+0.08}_{-0.22}$	0.55	1.06	$1.06^{+0.00}_{-0.00}$	$6.3^{+0.7}_{-0.7}$
1475-2258	342.311462	−44.540502	$26.29^{+0.11}_{-0.15}$	$-20.41^{+0.11}_{-0.15}$	$0.17^{+0.06}_{-0.07}$	0.40	1.08	$1.08^{+0.00}_{-0.00}$	$6.3^{+0.7}_{-0.7}$
1436-3158	342.309845	−44.554390	$26.15^{+0.18}_{-0.24}$	$-20.55^{+0.18}_{-0.24}$	$0.39^{+0.12}_{-0.14}$	0.54	1.06	$1.06^{+0.00}_{-0.00}$	$6.2^{+0.7}_{-0.7}$
1554-3415	342.314784	−44.561531	$26.29^{+0.11}_{-0.15}$	$-20.41^{+0.11}_{-0.15}$	$0.10^{+0.04}_{-0.04}$	0.90	1.05	$1.05^{+0.00}_{-0.00}$	$6.4^{+0.8}_{-0.7}$
1915-3110	342.329812	−44.553074	$26.47^{+0.11}_{-0.15}$	$-20.23^{+0.11}_{-0.15}$	$0.23^{+0.08}_{-0.10}$	0.50	1.05	$1.05^{+0.00}_{-0.00}$	$6.5^{+0.7}_{-0.7}$
2129-2064	342.338729	−44.535120	$27.07^{+0.09}_{-0.09}$	$-19.62^{+0.09}_{-0.09}$	$0.05^{+0.03}_{-0.02}$	0.15	1.06	$1.06^{+0.00}_{-0.00}$	$7.5^{+0.8}_{-0.9}$
1929-2524	342.330388	−44.547896	$26.70^{+0.11}_{-0.14}$	$-20.00^{+0.11}_{-0.14}$	$0.24^{+0.09}_{-0.10}$	0.68	1.06	$1.06^{+0.00}_{-0.00}$	$6.8^{+0.8}_{-0.7}$
1550-3408	342.314621	−44.561337	$26.93^{+0.11}_{-0.14}$	$-19.76^{+0.11}_{-0.14}$	$0.17^{+0.06}_{-0.07}$	0.49	1.05	$1.05^{+0.00}_{-0.00}$	$6.5^{+0.7}_{-0.8}$
1742-2148	342.322622	−44.537447	$26.53^{+0.32}_{-0.29}$	$-20.17^{+0.32}_{-0.29}$	$0.54^{+0.20}_{-0.18}$	0.60	1.07	$1.07^{+0.00}_{-0.00}$	$6.9^{+0.7}_{-0.8}$
1200-3106	342.300031	−44.552972	$26.42^{+0.33}_{-0.29}$	$-20.27^{+0.33}_{-0.29}$	$0.54^{+0.20}_{-0.18}$	0.66	1.07	$1.07^{+0.00}_{-0.00}$	$6.3^{+0.7}_{-0.7}$
2195-1585	342.341480	−44.532925	$27.23^{+0.13}_{-0.11}$	$-19.47^{+0.13}_{-0.11}$	$0.20^{+0.06}_{-0.09}$	0.56	1.06	$1.06^{+0.00}_{-0.00}$	$6.4^{+0.7}_{-0.7}$
1375-1572	342.307308	−44.532566	$27.55^{+0.12}_{-0.14}$	$-19.14^{+0.12}_{-0.14}$	$0.07^{+0.04}_{-0.03}$	0.79	1.09	$1.09^{+0.00}_{-0.01}$	$7.3^{+0.8}_{-1.7}$
1545-2093	342.314400	−44.535944	$27.70^{+0.12}_{-0.14}$	$-19.00^{+0.12}_{-0.14}$	$0.07^{+0.04}_{-0.03}$	0.88	1.08	$1.08^{+0.00}_{-0.00}$	$6.4^{+0.7}_{-0.7}$
1587-2418	342.316159	−44.544962	$27.57^{+0.12}_{-0.14}$	$-19.12^{+0.12}_{-0.14}$	$0.08^{+0.05}_{-0.03}$	0.90	1.07	$1.07^{+0.00}_{-0.00}$	$5.8^{+0.7}_{-0.6}$
2100-3210	342.337526	−44.555841	$27.51^{+0.28}_{-0.46}$	$-19.18^{+0.28}_{-0.46}$	$0.44^{+0.19}_{-0.17}$	0.89	1.05	$1.05^{+0.00}_{-0.00}$	$6.0^{+0.7}_{-0.6}$
1653-1381	342.318878	−44.527252	$27.71^{+0.31}_{-0.28}$	$-18.99^{+0.31}_{-0.28}$	$0.26^{+0.21}_{-0.16}$	0.88	1.08	$1.09^{+0.00}_{-0.01}$	$6.0^{+0.7}_{-0.7}$
2357-2040	342.348226	−44.534471	$27.57^{+0.32}_{-0.53}$	$-19.13^{+0.32}_{-0.53}$	$0.77^{+0.24}_{-0.30}$	0.35	1.05	$1.05^{+0.00}_{-0.00}$	$5.8^{+0.7}_{-0.6}$
1512-3461	342.313007	−44.562829	$27.72^{+0.32}_{-0.52}$	$-18.97^{+0.32}_{-0.52}$	$0.61^{+0.19}_{-0.24}$	0.12	1.05	$1.05^{+0.00}_{-0.00}$	$6.3^{+0.7}_{-0.7}$
1200-3339	342.300002	−44.559444	$27.88^{+0.27}_{-0.46}$	$-18.81^{+0.27}_{-0.46}$	$0.50^{+0.22}_{-0.19}$	0.36	1.07	$1.07^{+0.00}_{-0.00}$	$6.2^{+0.7}_{-0.7}$
1537-2327	342.314047	−44.542428	$27.68^{+0.32}_{-0.52}$	$-19.01^{+0.32}_{-0.52}$	$0.73^{+0.23}_{-0.28}$	0.39	1.07	$1.07^{+0.00}_{-0.00}$	$5.8^{+1.0}_{-5.0}$
1372-3301	342.307200	−44.558381	$28.27^{+0.27}_{-0.45}$	$-18.42^{+0.27}_{-0.45}$	$0.44^{+0.19}_{-0.17}$	0.49	1.06	$1.06^{+0.00}_{-0.00}$	$6.6^{+0.7}_{-0.8}$
1870-3096	342.327941	−44.552684	$27.38^{+0.42}_{-0.55}$	$-19.31^{+0.42}_{-0.55}$	$0.80^{+0.38}_{-0.31}$	0.52	1.05	$1.05^{+0.00}_{-0.00}$	$1.4^{+2.5}_{-1.3}$
1423-3086	342.309306	−44.552396	$26.98^{+0.36}_{-0.42}$	$-19.71^{+0.36}_{-0.42}$	$0.81^{+0.28}_{-0.27}$	0.76	1.07	$1.07^{+0.00}_{-0.00}$	$6.3^{+0.7}_{-0.8}$
2243-2024	342.343497	−44.534020	$27.90^{+0.45}_{-0.59}$	$-18.79^{+0.45}_{-0.59}$	$0.70^{+0.30}_{-0.34}$	0.33	1.06	$1.06^{+0.00}_{-0.00}$	$5.9^{+0.6}_{-0.7}$
1545-2521	342.314409	−44.547811	$28.03^{+0.27}_{-0.45}$	$-18.67^{+0.27}_{-0.45}$	$0.64^{+0.28}_{-0.24}$	0.42	1.07	$1.07^{+0.00}_{-0.00}$	$6.1^{+0.7}_{-0.7}$
1255-3099	342.302320	−44.552755	$27.16^{+0.43}_{-0.55}$	$-19.53^{+0.43}_{-0.55}$	$0.77^{+0.37}_{-0.30}$	0.88	1.07	$1.07^{+0.00}_{-0.00}$	$5.9^{+0.7}_{-5.1}$
2068-3353	342.336177	−44.559817	$28.23^{+0.27}_{-0.45}$	$-18.46^{+0.27}_{-0.45}$	$0.55^{+0.24}_{-0.21}$	0.41	1.04	$1.04^{+0.00}_{-0.00}$	$6.4^{+0.7}_{-5.5}$
1449-2384	342.310396	−44.544023	$28.51^{+0.22}_{-0.21}$	$-18.18^{+0.22}_{-0.21}$	$0.06^{+0.05}_{-0.03}$	0.56	1.07	$1.07^{+0.00}_{-0.00}$	$6.1^{+0.7}_{-0.7}$
2116-2400	342.338198	−44.544472	$28.90^{+0.21}_{-0.21}$	$-17.80^{+0.21}_{-0.21}$	$0.06^{+0.05}_{-0.03}$	0.90	1.05	$1.05^{+0.00}_{-0.00}$	$5.7^{+0.6}_{-5.5}$
2227-3287	342.342824	−44.557990	$28.37^{+0.42}_{-0.34}$	$-18.32^{+0.42}_{-0.34}$	$0.17^{+0.14}_{-0.10}$	0.90	1.04	$1.04^{+0.00}_{-0.00}$	$5.6^{+0.6}_{-0.7}$
1957-1523	342.331571	−44.531212	$28.30^{+0.52}_{-0.41}$	$-18.40^{+0.52}_{-0.41}$	$0.39^{+0.31}_{-0.18}$	0.44	1.07	$1.07^{+0.00}_{-0.00}$	$5.8^{+0.7}_{-0.7}$
1908-3457	342.329506	−44.562705	$28.47^{+0.58}_{-0.57}$	$-18.23^{+0.58}_{-0.57}$	$0.42^{+0.33}_{-0.24}$	0.21	1.05	$1.05^{+0.00}_{-0.00}$	$0.3^{+5.8}_{-0.2}$
1949-2315	342.331243	−44.542096	$28.39^{+0.42}_{-0.34}$	$-18.31^{+0.42}_{-0.34}$	$0.21^{+0.18}_{-0.12}$	0.90	1.06	$1.06^{+0.00}_{-0.00}$	$5.6^{+0.7}_{-5.1}$
1940-3315	342.330870	−44.558773	$26.16^{+0.34}_{-0.38}$	$-20.53^{+0.34}_{-0.38}$	$4.36^{+1.16}_{-0.53}$	0.52	1.05	$1.05^{+0.00}_{-0.00}$	$5.7^{+1.1}_{-5.1}$
1716-2450	342.321503	−44.545838	$28.69^{+0.42}_{-0.33}$	$-18.00^{+0.42}_{-0.33}$	$0.28^{+0.24}_{-0.17}$	0.79	1.06	$1.06^{+0.00}_{-0.00}$	$5.7^{+0.8}_{-5.4}$
2055-2411	342.335663	−44.544751	$28.37^{+0.58}_{-0.57}$	$-18.32^{+0.58}_{-0.57}$	$0.52^{+0.41}_{-0.29}$	0.31	1.05	$1.05^{+0.00}_{-0.00}$	$1.4^{+3.0}_{-1.3}$
1992-3212	342.333018	−44.555916	$27.97^{+0.31}_{-0.52}$	$-18.72^{+0.31}_{-0.52}$	$0.68^{+0.22}_{-0.27}$	0.79	1.05	$1.05^{+0.00}_{-0.00}$	$6.5^{+0.7}_{-1.1}$
1226-3152	342.301115	−44.554238	$28.52^{+0.42}_{-0.34}$	$-18.18^{+0.42}_{-0.34}$	$0.24^{+0.20}_{-0.14}$	0.90	1.07	$1.07^{+0.00}_{-0.00}$	$5.9^{+0.7}_{-1.3}$
1542-1441	342.314282	−44.528924	$28.80^{+0.41}_{-0.33}$	$-17.90^{+0.41}_{-0.33}$	$0.34^{+0.29}_{-0.20}$	0.63	1.09	$1.09^{+0.00}_{-0.01}$	$5.9^{+1.0}_{-5.2}$
HFF6C									
5526-4003	39.980271	−1.566761	$28.70^{+0.06}_{-0.06}$	$-18.00^{+0.06}_{-0.06}$	$0.08^{+0.01}_{-0.02}$	0.36	12.43	$11.34^{+1.08}_{-1.21}$	$5.9^{+0.6}_{-0.7}$
5522-4002	39.980113	−1.566731	$28.79^{+0.10}_{-0.11}$	$-17.90^{+0.10}_{-0.11}$	$0.11^{+0.02}_{-0.02}$	0.62	11.63	$10.54^{+1.00}_{-1.07}$	$5.8^{+0.6}_{-0.7}$
5715-4130	39.988155	−1.570302	$28.06^{+0.21}_{-0.16}$	$-18.64^{+0.21}_{-0.16}$	$0.37^{+0.11}_{-0.07}$	0.57	3.30	$2.95^{+0.22}_{-0.22}$	$5.4^{+0.7}_{-1.1}$
5659-4166	39.985811	−1.571303	$28.49^{+0.10}_{-0.13}$	$-18.20^{+0.10}_{-0.13}$	$0.08^{+0.03}_{-0.04}$	0.71	4.25	$3.83^{+0.24}_{-0.28}$	$6.2^{+0.7}_{-0.7}$
4926-4158	39.955258	−1.571082	$28.47^{+0.21}_{-0.16}$	$-18.22^{+0.21}_{-0.16}$	$0.25^{+0.07}_{-0.05}$	0.66	3.55	$3.32^{+0.31}_{-0.21}$	$5.8^{+0.7}_{-0.6}$
5262-3591[s1]	39.969255	−1.566440	$29.04^{+0.11}_{-0.13}$	$-17.65^{+0.11}_{-0.13}$	$0.04^{+0.02}_{-0.02}$	0.90	4.35	$4.20^{+0.40}_{-0.33}$	$6.1^{+0.7}_{-0.7}$
5001-4358[s1]	39.958395	−1.576619	$29.11^{+0.30}_{-0.32}$	$-17.58^{+0.30}_{-0.32}$	$0.06^{+0.05}_{-0.04}$	0.82	4.16	$3.83^{+0.24}_{-0.18}$	$6.2^{+0.7}_{-0.7}$
HFF6P									
1557-6475	40.064896	−1.613212	$25.18^{+0.03}_{-0.07}$	$-21.52^{+0.03}_{-0.07}$	$0.13^{+0.01}_{-0.05}$	0.46	1.22	$1.14^{+0.03}_{-0.02}$	$6.1^{+0.7}_{-0.7}$
1405-7142	40.058557	−1.620628	$25.67^{+0.24}_{-0.15}$	$-21.03^{+0.24}_{-0.15}$	$0.27^{+0.11}_{-0.09}$	0.29	1.23	$1.15^{+0.03}_{-0.02}$	$7.1^{+0.8}_{-0.7}$

Table C.1 (cont'd)

ID[a]	R.A.	Decl.	$m_{\rm UV}$[b,c]	$M_{\rm UV}$[c]	$r_{\rm e}$ / kpc[c,d]	e	$\mu_{\rm best}$[e]	μ[f]	$z_{\rm photo}$
1422-8041	40.059266	−1.634499	$26.02^{+0.23}_{-0.15}$	$-20.68^{+0.23}_{-0.15}$	$0.29^{+0.12}_{-0.10}$	0.63	1.20	$1.14^{+0.03}_{-0.02}$	$6.3^{+0.7}_{-0.7}$
1512-7449	40.063019	−1.629156	$26.51^{+0.11}_{-0.15}$	$-20.18^{+0.11}_{-0.15}$	$0.17^{+0.06}_{-0.07}$	0.39	1.20	$1.14^{+0.03}_{-0.02}$	$6.4^{+0.7}_{-0.7}$
1066-7101	40.044451	−1.619499	$26.10^{+0.15}_{-0.56}$	$-20.59^{+0.15}_{-0.56}$	$0.83^{+0.12}_{-0.33}$	0.71	1.27	$1.19^{+0.04}_{-0.03}$	$6.0^{+0.7}_{-0.7}$
1553-6472	40.064711	−1.613127	$26.54^{+0.32}_{-0.29}$	$-20.15^{+0.32}_{-0.29}$	$0.55^{+0.20}_{-0.19}$	0.21	1.22	$1.14^{+0.03}_{-0.02}$	$6.3^{+0.7}_{-0.7}$
0962-7254	40.040086	−1.623732	$26.99^{+0.11}_{-0.14}$	$-19.71^{+0.11}_{-0.14}$	$0.19^{+0.07}_{-0.08}$	0.49	1.28	$1.20^{+0.04}_{-0.03}$	$6.2^{+0.7}_{-0.7}$
1112-8152	40.046339	−1.637564	$26.86^{+0.32}_{-0.29}$	$-19.84^{+0.32}_{-0.29}$	$0.43^{+0.16}_{-0.15}$	0.00	1.23	$1.16^{+0.03}_{-0.03}$	$5.2^{+0.7}_{-0.6}$
1365-7298	40.056894	−1.624969	$26.47^{+0.39}_{-0.53}$	$-20.23^{+0.39}_{-0.53}$	$0.99^{+0.30}_{-0.33}$	0.20	1.22	$1.15^{+0.03}_{-0.03}$	$1.1^{+0.3}_{-0.6}$
1338-7507	40.055776	−1.630760	$27.44^{+0.43}_{-0.57}$	$-19.26^{+0.43}_{-0.57}$	$0.36^{+0.21}_{-0.17}$	0.42	1.22	$1.15^{+0.03}_{-0.03}$	$6.5^{+0.7}_{-0.8}$
1443-8334	40.060155	−1.642617	$27.44^{+0.33}_{-0.35}$	$-19.26^{+0.33}_{-0.35}$	$0.13^{+0.11}_{-0.08}$	0.90	1.19	$1.13^{+0.03}_{-0.02}$	$5.9^{+0.7}_{-0.7}$
1496-6574	40.062337	−1.615954	$27.74^{+0.31}_{-0.28}$	$-18.96^{+0.31}_{-0.28}$	$0.19^{+0.15}_{-0.12}$	0.90	1.22	$1.15^{+0.03}_{-0.02}$	$7.1^{+0.8}_{-0.8}$
1135-6350	40.047325	−1.609737	$27.11^{+0.36}_{-0.41}$	$-19.59^{+0.36}_{-0.41}$	$0.75^{+0.26}_{-0.25}$	0.51	1.28	$1.19^{+0.04}_{-0.03}$	$6.3^{+0.8}_{-0.7}$
1233-7093	40.051408	−1.619257	$27.18^{+0.17}_{-0.23}$	$-19.51^{+0.17}_{-0.23}$	$0.40^{+0.12}_{-0.14}$	0.73	1.25	$1.17^{+0.03}_{-0.03}$	$6.5^{+0.8}_{-0.7}$
1242-7083	40.051751	−1.618990	$27.84^{+0.27}_{-0.46}$	$-18.85^{+0.27}_{-0.46}$	$0.38^{+0.17}_{-0.14}$	0.34	1.25	$1.17^{+0.03}_{-0.03}$	$6.3^{+0.7}_{-0.7}$
1203-7168	40.050146	−1.621356	$27.04^{+0.36}_{-0.42}$	$-19.65^{+0.36}_{-0.42}$	$0.67^{+0.24}_{-0.22}$	0.74	1.25	$1.17^{+0.03}_{-0.03}$	$6.5^{+0.7}_{-1.1}$
0954-7261	40.039781	−1.623926	$27.82^{+0.27}_{-0.46}$	$-18.87^{+0.27}_{-0.46}$	$0.46^{+0.20}_{-0.17}$	0.22	1.28	$1.20^{+0.04}_{-0.03}$	$6.1^{+0.7}_{-0.7}$
1339-7197	40.055810	−1.622150	$27.97^{+0.27}_{-0.45}$	$-18.73^{+0.27}_{-0.45}$	$0.56^{+0.24}_{-0.21}$	0.02	1.23	$1.16^{+0.03}_{-0.03}$	$6.3^{+0.7}_{-0.7}$
1619-8043	40.067498	−1.634549	$28.31^{+0.11}_{-0.13}$	$-18.38^{+0.11}_{-0.13}$	$0.06^{+0.03}_{-0.03}$	0.89	1.19	$1.12^{+0.03}_{-0.02}$	$6.2^{+0.7}_{-0.7}$
1406-8067	40.058588	−1.635205	$27.92^{+0.27}_{-0.45}$	$-18.78^{+0.27}_{-0.45}$	$0.46^{+0.20}_{-0.17}$	0.33	1.20	$1.14^{+0.03}_{-0.02}$	$6.4^{+0.8}_{-0.7}$
1120-6563	40.046698	−1.615649	$28.37^{+0.11}_{-0.13}$	$-18.32^{+0.11}_{-0.13}$	$0.06^{+0.03}_{-0.02}$	0.90	1.27	$1.19^{+0.04}_{-0.03}$	$6.3^{+0.7}_{-0.7}$
1404-6507	40.058514	−1.614092	$28.12^{+0.31}_{-0.27}$	$-18.57^{+0.31}_{-0.27}$	$0.15^{+0.12}_{-0.09}$	0.62	1.24	$1.15^{+0.03}_{-0.03}$	$6.0^{+0.6}_{-0.7}$
1111-8294	40.046301	−1.641520	$28.08^{+0.31}_{-0.27}$	$-18.62^{+0.31}_{-0.27}$	$0.20^{+0.16}_{-0.12}$	0.64	1.23	$1.16^{+0.03}_{-0.03}$	$6.1^{+0.7}_{-0.7}$
1650-7475	40.068770	−1.629867	$28.52^{+0.22}_{-0.21}$	$-18.18^{+0.22}_{-0.21}$	$0.07^{+0.07}_{-0.04}$	0.89	1.19	$1.13^{+0.03}_{-0.02}$	$6.1^{+0.7}_{-0.7}$
0940-7273	40.039181	−1.624271	$28.27^{+0.31}_{-0.27}$	$-18.42^{+0.31}_{-0.27}$	$0.18^{+0.14}_{-0.11}$	0.77	1.28	$1.20^{+0.04}_{-0.03}$	$6.1^{+0.7}_{-0.6}$
1631-7409	40.067987	−1.628035	$28.09^{+0.42}_{-0.55}$	$-18.60^{+0.42}_{-0.55}$	$0.52^{+0.31}_{-0.25}$	0.44	1.19	$1.13^{+0.03}_{-0.02}$	$6.2^{+0.7}_{-0.7}$
1513-6504	40.063047	−1.614000	$28.51^{+0.42}_{-0.34}$	$-18.18^{+0.42}_{-0.34}$	$0.24^{+0.21}_{-0.15}$	0.77	1.22	$1.14^{+0.03}_{-0.02}$	$5.9^{+0.7}_{-0.7}$
1282-8053	40.053420	−1.634833	$28.33^{+0.30}_{-0.27}$	$-18.36^{+0.30}_{-0.27}$	$0.23^{+0.18}_{-0.14}$	0.53	1.22	$1.15^{+0.03}_{-0.03}$	$5.8^{+0.7}_{-0.7}$
0963-7467	40.040146	−1.629650	$28.85^{+0.41}_{-0.33}$	$-17.84^{+0.41}_{-0.33}$	$0.28^{+0.23}_{-0.16}$	0.64	1.27	$1.19^{+0.04}_{-0.03}$	$6.5^{+0.7}_{-1.0}$
1352-6549	40.056353	−1.615251	$28.53^{+0.42}_{-0.34}$	$-18.17^{+0.42}_{-0.34}$	$0.33^{+0.27}_{-0.19}$	0.90	1.24	$1.16^{+0.03}_{-0.03}$	$6.0^{+0.9}_{-5.5}$
1352-8104	40.056373	−1.636246	$28.81^{+0.21}_{-0.21}$	$-17.88^{+0.21}_{-0.21}$	$0.06^{+0.05}_{-0.03}$	0.68	1.21	$1.14^{+0.03}_{-0.02}$	$5.7^{+0.6}_{-4.8}$
1636-7324	40.068190	−1.625671	$28.78^{+0.41}_{-0.33}$	$-17.91^{+0.41}_{-0.33}$	$0.16^{+0.14}_{-0.10}$	0.87	1.20	$1.13^{+0.03}_{-0.02}$	$6.5^{+0.7}_{-0.8}$
1197-8268	40.049891	−1.640781	$28.83^{+0.21}_{-0.21}$	$-17.87^{+0.21}_{-0.21}$	$0.09^{+0.08}_{-0.04}$	0.90	1.22	$1.15^{+0.03}_{-0.03}$	$6.4^{+0.7}_{-0.7}$
1485-8415	40.061875	−1.644873	$27.35^{+0.57}_{-0.67}$	$-19.34^{+0.57}_{-0.67}$	$0.89^{+0.57}_{-0.41}$	0.59	1.19	$1.13^{+0.03}_{-0.02}$	$5.7^{+0.6}_{-1.7}$
1346-7336	40.056107	−1.626010	$28.66^{+0.57}_{-0.56}$	$-18.03^{+0.57}_{-0.56}$	$0.40^{+0.31}_{-0.22}$	0.73	1.22	$1.15^{+0.03}_{-0.03}$	$6.1^{+0.8}_{-0.8}$
1534-8390	40.063919	−1.644192	$28.96^{+0.21}_{-0.21}$	$-17.74^{+0.21}_{-0.21}$	$0.05^{+0.04}_{-0.03}$	0.90	1.18	$1.12^{+0.03}_{-0.02}$	$5.8^{+0.7}_{-5.5}$
1105-8129	40.046060	−1.636942	$28.94^{+0.21}_{-0.21}$	$-17.75^{+0.21}_{-0.21}$	$0.06^{+0.05}_{-0.03}$	0.86	1.24	$1.17^{+0.03}_{-0.03}$	$5.7^{+0.6}_{-4.7}$
1437-6560	40.059896	−1.615568	$27.23^{+0.35}_{-0.41}$	$-19.46^{+0.35}_{-0.41}$	$0.80^{+0.28}_{-0.26}$	0.62	1.23	$1.15^{+0.03}_{-0.02}$	$5.8^{+0.6}_{-4.9}$
1197-8275	40.049900	−1.640993	$28.83^{+0.41}_{-0.33}$	$-17.86^{+0.41}_{-0.33}$	$0.15^{+0.12}_{-0.09}$	0.90	1.22	$1.15^{+0.03}_{-0.03}$	$6.2^{+0.7}_{-0.7}$
1554-7558	40.064752	−1.632167	$28.77^{+0.41}_{-0.33}$	$-17.93^{+0.41}_{-0.33}$	$0.17^{+0.14}_{-0.10}$	0.90	1.20	$1.13^{+0.03}_{-0.02}$	$1.2^{+3.8}_{-1.1}$

from light profile fitting with `glafic`.

[a]Asterisks indicate galaxies with multiple cores.

[b]Total apparent magnitude corrected for the gravitational lensing effects

[c]Errors are random errors in the fitting procedure.

[d]Circularized effective radius, $r_{\rm e}^{\rm maj}\sqrt{1-e}$, where $r_{\rm e}^{\rm maj}$ is the radius along the major axis and e the ellipticity.

[e]Best-fit value of magnification.

[f]Median value and 1σ error of the magnification factor from the MCMC posterior distribution.

[s1−−3]Dropout galaxy that composes a multiple image system.

Table C.2. Fitting results for dropouts at $z \sim 8$

ID[a]	R.A.	Decl.	$m_{\rm UV}$[b,c]	$M_{\rm UV}$[c]	$r_{\rm e}$ / kpc[c,d]	e	$\mu_{\rm best}$[e]	μ[f]	$z_{\rm photo}$
HFF1C									
2508-2496	3.604518	−30.380467	$26.40^{+0.07}_{-0.08}$	$-20.74^{+0.07}_{-0.08}$	$0.22^{+0.04}_{-0.07}$	0.74	1.34	$1.38^{+0.07}_{-0.05}$	$8.0^{+0.9}_{-0.9}$
2481-2561	3.603378	−30.382255	$26.66^{+0.16}_{-0.16}$	$-20.48^{+0.16}_{-0.16}$	$0.70^{+0.11}_{-0.10}$	0.60	1.42	$1.48^{+0.08}_{-0.06}$	$8.2^{+0.9}_{-0.9}$
2306-3089	3.596091	−30.385833	$27.40^{+0.21}_{-0.45}$	$-19.74^{+0.21}_{-0.45}$	$0.31^{+0.09}_{-0.15}$	0.43	2.13	$2.20^{+0.15}_{-0.12}$	$8.2^{+0.9}_{-0.9}$
2555-2515	3.606461	−30.380996	$27.41^{+0.18}_{-0.22}$	$-19.73^{+0.18}_{-0.22}$	$0.16^{+0.05}_{-0.07}$	0.89	1.33	$1.40^{+0.07}_{-0.05}$	$8.0^{+0.8}_{-0.9}$
2492-2561	3.603859	−30.382264	$27.23^{+0.36}_{-0.45}$	$-19.91^{+0.36}_{-0.45}$	$0.49^{+0.19}_{-0.19}$	0.49	1.41	$1.48^{+0.08}_{-0.06}$	$8.4^{+0.9}_{-0.9}$
2557-2513	3.606576	−30.380924	$26.79^{+0.30}_{-0.77}$	$-20.35^{+0.30}_{-0.77}$	$0.77^{+0.13}_{-0.43}$	0.32	1.33	$1.39^{+0.07}_{-0.05}$	$7.9^{+0.9}_{-6.1}$
2135-2432	3.588980	−30.378668	$29.21^{+0.20}_{-0.16}$	$-17.93^{+0.20}_{-0.16}$	$0.06^{+0.05}_{-0.03}$	0.76	1.98	$1.79^{+0.12}_{-0.09}$	$8.0^{+0.8}_{-0.9}$
2495-2562	3.603997	−30.382304	$27.20^{+0.32}_{-0.39}$	$-19.94^{+0.32}_{-0.39}$	$1.04^{+0.22}_{-0.33}$	0.57	1.41	$1.48^{+0.08}_{-0.06}$	$7.9^{+0.9}_{-6.1}$
2216-4356	3.592349	−30.409892	$29.35^{+0.31}_{-0.29}$	$-17.79^{+0.31}_{-0.29}$	$0.12^{+0.06}_{-0.04}$	0.89	10.81	$9.03^{+0.76}_{-0.70}$	$7.2^{+0.8}_{-2.0}$
2521-2532	3.605062	−30.381463	$28.25^{+0.55}_{-0.49}$	$-18.89^{+0.55}_{-0.49}$	$0.47^{+0.38}_{-0.20}$	0.45	1.36	$1.42^{+0.07}_{-0.06}$	$7.7^{+0.8}_{-6.4}$
HFF1P									
5398-1451	3.474918	−30.362542	$27.68^{+0.17}_{-0.18}$	$-19.46^{+0.17}_{-0.18}$	$0.11^{+0.04}_{-0.04}$	0.90	1.07	$1.05^{+0.01}_{-0.01}$	$7.5^{+0.8}_{-1.5}$
5021-2024	3.459246	−30.367360	$27.89^{+0.30}_{-0.27}$	$-19.25^{+0.30}_{-0.27}$	$0.21^{+0.11}_{-0.10}$	0.90	1.07	$1.03^{+0.01}_{-0.01}$	$7.6^{+0.8}_{-1.8}$
5512-1588	3.479685	−30.366359	$28.15^{+0.44}_{-0.39}$	$-19.00^{+0.44}_{-0.39}$	$0.42^{+0.29}_{-0.15}$	0.09	1.08	$1.06^{+0.01}_{-0.01}$	$7.8^{+0.8}_{-6.4}$
5530-3153	3.480419	−30.387608	$27.48^{+0.35}_{-0.32}$	$-19.66^{+0.35}_{-0.32}$	$0.46^{+0.23}_{-0.17}$	0.44	1.09	$1.03^{+0.01}_{-0.01}$	$7.3^{+0.8}_{-6.3}$
HFF2C									
1151-4540	64.047984	−24.081670	$27.07^{+0.34}_{-0.29}$	$-20.07^{+0.34}_{-0.29}$	$0.27^{+0.14}_{-0.09}$	0.57	1.44	$1.49^{+0.04}_{-0.03}$	$8.4^{+0.9}_{-0.9}$
0939-5354	64.039165	−24.093183	$26.05^{+0.31}_{-0.80}$	$-21.09^{+0.31}_{-0.80}$	$0.73^{+0.13}_{-0.40}$	0.37	1.38	$1.43^{+0.03}_{-0.03}$	$8.5^{+0.9}_{-0.9}$
1153-4531	64.048057	−24.081431	$27.09^{+0.37}_{-0.45}$	$-20.06^{+0.37}_{-0.45}$	$0.56^{+0.21}_{-0.22}$	0.28	1.44	$1.50^{+0.04}_{-0.03}$	$8.7^{+0.9}_{-1.0}$
0901-5171	64.037567	−24.088109	$28.49^{+0.28}_{-0.37}$	$-18.66^{+0.28}_{-0.37}$	$0.29^{+0.13}_{-0.12}$	0.64	1.70	$1.78^{+0.06}_{-0.05}$	$8.4^{+0.9}_{-0.9}$
1447-3538	64.060329	−24.064958	$28.82^{+0.26}_{-0.29}$	$-18.32^{+0.26}_{-0.29}$	$0.17^{+0.09}_{-0.07}$	0.35	1.79	$1.79^{+0.04}_{-0.04}$	$7.7^{+0.9}_{-0.8}$
HFF2P									
2912-7330	64.121366	−24.125856	$27.39^{+0.18}_{-0.22}$	$-19.75^{+0.18}_{-0.22}$	$0.12^{+0.04}_{-0.05}$	0.38	1.00	$1.00^{+0.00}_{-0.00}$	$7.6^{+0.9}_{-0.8}$
3286-6419	64.136930	−24.111643	$27.54^{+0.18}_{-0.22}$	$-19.60^{+0.18}_{-0.22}$	$0.19^{+0.06}_{-0.08}$	0.29	1.00	$1.00^{+0.01}_{-0.00}$	$7.8^{+0.9}_{-0.8}$
3596-6480	64.149865	−24.113352	$28.00^{+0.27}_{-0.30}$	$-19.15^{+0.27}_{-0.30}$	$0.31^{+0.16}_{-0.14}$	0.13	1.00	$0.99^{+0.01}_{-0.00}$	$8.5^{+1.0}_{-0.9}$
3044-6002	64.126862	−24.100067	$27.93^{+0.29}_{-0.39}$	$-19.22^{+0.29}_{-0.39}$	$0.34^{+0.15}_{-0.14}$	0.53	1.01	$1.00^{+0.01}_{-0.01}$	$1.8^{+6.4}_{-0.3}$
3042-6011	64.126779	−24.100323	$27.99^{+0.29}_{-0.38}$	$-19.15^{+0.29}_{-0.38}$	$0.44^{+0.19}_{-0.18}$	0.56	1.01	$1.00^{+0.01}_{-0.01}$	$8.2^{+0.9}_{-0.9}$
3549-6422	64.147904	−24.111729	$28.41^{+0.27}_{-0.29}$	$-18.73^{+0.27}_{-0.29}$	$0.13^{+0.07}_{-0.06}$	0.90	1.00	$1.00^{+0.01}_{-0.00}$	$8.4^{+0.9}_{-1.0}$
2862-7348	64.119271	−24.126357	$28.39^{+0.27}_{-0.29}$	$-18.75^{+0.27}_{-0.29}$	$0.18^{+0.09}_{-0.08}$	0.89	1.00	$1.00^{+0.00}_{-0.00}$	$5.8^{+2.1}_{-5.2}$
3642-6304	64.151758	−24.108450	$28.25^{+0.28}_{-0.38}$	$-18.89^{+0.28}_{-0.38}$	$0.32^{+0.14}_{-0.13}$	0.61	1.00	$1.00^{+0.01}_{-0.01}$	$8.6^{+1.0}_{-6.5}$
2871-7010	64.119662	−24.116954	$27.38^{+0.47}_{-0.42}$	$-19.77^{+0.47}_{-0.42}$	$0.61^{+0.29}_{-0.26}$	0.63	1.00	$1.00^{+0.00}_{-0.00}$	$7.7^{+0.9}_{-6.2}$
HFF3P									
2251-9452	109.343797	+37.829235	$27.67^{+0.17}_{-0.22}$	$-19.48^{+0.17}_{-0.22}$	$0.23^{+0.08}_{-0.10}$	0.26	1.14	$1.17^{+0.02}_{-0.04}$	$8.3^{+0.9}_{-0.9}$
1788-9254	109.324524	+37.823744	$27.77^{+0.17}_{-0.22}$	$-19.37^{+0.17}_{-0.22}$	$0.17^{+0.06}_{-0.08}$	0.24	1.19	$1.21^{+0.02}_{-0.02}$	$8.1^{+0.9}_{-0.9}$
1891-8538	109.328823	+37.814951	$27.97^{+0.29}_{-0.38}$	$-19.17^{+0.29}_{-0.38}$	$0.31^{+0.14}_{-0.13}$	0.17	1.26	$1.28^{+0.02}_{-0.02}$	$5.5^{+1.7}_{-4.8}$
1672-0089	109.319676	+37.835808	$27.92^{+0.29}_{-0.39}$	$-19.22^{+0.29}_{-0.39}$	$0.34^{+0.15}_{-0.14}$	0.64	1.13	$1.15^{+0.02}_{-0.02}$	$7.3^{+0.8}_{-2.2}$
1854-0446	109.327261	+37.845742	$28.25^{+0.27}_{-0.30}$	$-18.89^{+0.27}_{-0.30}$	$0.26^{+0.14}_{-0.12}$	0.63	1.09	$1.11^{+0.02}_{-0.03}$	$7.8^{+0.8}_{-2.8}$
2153-9369	109.339742	+37.826923	$28.23^{+0.28}_{-0.38}$	$-18.91^{+0.28}_{-0.38}$	$0.40^{+0.18}_{-0.17}$	0.41	1.15	$1.19^{+0.02}_{-0.03}$	$7.8^{+0.8}_{-6.0}$
HFF4C									
4025-5027	177.417749	+22.417435	$25.52^{+0.06}_{-0.15}$	$-21.62^{+0.06}_{-0.15}$	$0.27^{+0.02}_{-0.06}$	0.72	1.58	$1.60^{+0.12}_{-0.12}$	$7.5^{+0.8}_{-0.8}$
4024-4492	177.417702	+22.413687	$27.91^{+0.17}_{-0.22}$	$-19.23^{+0.17}_{-0.22}$	$0.09^{+0.03}_{-0.04}$	0.90	1.63	$1.68^{+0.22}_{-0.14}$	$8.4^{+1.0}_{-0.9}$
HFF4P									
3745-6484	177.406060	+22.280113	$26.68^{+0.28}_{-0.29}$	$-20.47^{+0.28}_{-0.29}$	$0.35^{+0.17}_{-0.12}$	0.72	1.01	$1.00^{+0.01}_{-0.01}$	$8.4^{+0.9}_{-0.9}$
3998-8560	177.416587	+22.315557	$27.09^{+0.18}_{-0.22}$	$-20.05^{+0.18}_{-0.22}$	$0.25^{+0.08}_{-0.11}$	0.60	1.04	$1.03^{+0.02}_{-0.01}$	$8.0^{+0.8}_{-0.9}$
3959-8115	177.414974	+22.303195	$27.37^{+0.27}_{-0.28}$	$-19.77^{+0.27}_{-0.28}$	$0.33^{+0.15}_{-0.11}$	0.52	1.02	$1.01^{+0.01}_{-0.01}$	$7.5^{+0.9}_{-2.0}$
3612-8473	177.400509	+22.313149	$27.91^{+0.29}_{-0.39}$	$-19.23^{+0.29}_{-0.39}$	$0.39^{+0.17}_{-0.16}$	0.34	1.04	$1.02^{+0.01}_{-0.01}$	$7.6^{+0.8}_{-6.3}$
4149-8180	177.422903	+22.305006	$26.62^{+0.60}_{-0.40}$	$-20.53^{+0.60}_{-0.40}$	$0.64^{+0.34}_{-0.28}$	0.53	1.03	$1.02^{+0.01}_{-0.01}$	$7.7^{+0.9}_{-6.6}$
3769-8456	177.407054	+22.312680	$27.94^{+0.27}_{-0.30}$	$-19.21^{+0.27}_{-0.30}$	$0.18^{+0.09}_{-0.08}$	0.89	1.03	$1.02^{+0.01}_{-0.01}$	$7.4^{+0.8}_{-1.5}$
4419-8349	177.434162	+22.309709	$28.18^{+0.19}_{-0.17}$	$-18.96^{+0.19}_{-0.17}$	$0.08^{+0.07}_{-0.04}$	0.90	1.05	$1.03^{+0.01}_{-0.01}$	$1.7^{+6.1}_{-1.2}$
4553-7304	177.439740	+22.291792	$27.04^{+0.47}_{-0.43}$	$-20.10^{+0.47}_{-0.43}$	$0.61^{+0.29}_{-0.26}$	0.84	1.02	$1.01^{+0.01}_{-0.01}$	$7.5^{+0.9}_{-6.4}$
3878-7079	177.411594	+22.285550	$28.28^{+0.43}_{-0.39}$	$-18.87^{+0.43}_{-0.39}$	$0.43^{+0.30}_{-0.15}$	0.75	1.01	$1.00^{+0.01}_{-0.01}$	$7.9^{+0.8}_{-6.7}$
3593-8440	177.399737	+22.312238	$27.86^{+0.51}_{-0.34}$	$-19.28^{+0.51}_{-0.34}$	$0.46^{+0.17}_{-0.17}$	0.32	1.04	$1.02^{+0.01}_{-0.01}$	$7.5^{+0.8}_{-6.7}$
HFF5C									

Table C.2 (cont'd)

ID[a]	R.A.	Decl.	$m_{\rm UV}$[b,c]	$M_{\rm UV}$[c]	$r_{\rm e}$ / kpc[c,d]	e	$\mu_{\rm best}$[e]	μ[f]	$z_{\rm photo}$
4316-1323[s1]	342.179848	−44.525661	$29.82^{+0.25}_{-0.65}$	$-17.32^{+0.25}_{-0.65}$	$0.17^{+0.03}_{-0.10}$	0.31	27.71	$28.32^{+2.05}_{-2.29}$	$8.2^{+0.9}_{-0.9}$
4374-1338[s1]	342.182266	−44.526074	$30.73^{+0.17}_{-0.24}$	$-16.41^{+0.17}_{-0.24}$	$0.08^{+0.02}_{-0.03}$	0.51	24.76	$25.32^{+1.41}_{-1.34}$	$8.5^{+1.0}_{-0.9}$
4111-2125	342.171304	−44.536810	$28.68^{+0.26}_{-0.27}$	$-18.46^{+0.26}_{-0.27}$	$0.20^{+0.09}_{-0.07}$	0.90	4.11	$4.15^{+0.12}_{-0.15}$	$1.6^{+0.5}_{-1.5}$
3935-1469	342.163986	−44.529704	$30.33^{+0.18}_{-0.15}$	$-16.81^{+0.18}_{-0.15}$	$0.03^{+0.02}_{-0.01}$	0.90	5.13	$5.17^{+0.18}_{-0.20}$	$7.9^{+0.9}_{-6.9}$
HFF5P									
2129-2064	342.338729	−44.535120	$26.96^{+0.09}_{-0.09}$	$-20.18^{+0.09}_{-0.09}$	$0.04^{+0.02}_{-0.02}$	0.32	1.06	$1.06^{+0.00}_{-0.00}$	$7.5^{+0.8}_{-0.9}$
1912-1491	342.329688	−44.530307	$26.79^{+0.17}_{-0.13}$	$-20.36^{+0.17}_{-0.13}$	$0.54^{+0.09}_{-0.08}$	0.66	1.07	$1.07^{+0.00}_{-0.00}$	$7.9^{+0.9}_{-0.9}$
1278-2047	342.303254	−44.534661	$28.36^{+0.27}_{-0.29}$	$-18.78^{+0.27}_{-0.29}$	$0.21^{+0.11}_{-0.09}$	0.44	1.10	$1.10^{+0.00}_{-0.01}$	$8.0^{+0.9}_{-6.4}$
2027-2472	342.334489	−44.546470	$27.48^{+0.35}_{-0.32}$	$-19.67^{+0.35}_{-0.32}$	$0.50^{+0.25}_{-0.18}$	0.85	1.05	$1.05^{+0.00}_{-0.00}$	$7.2^{+0.8}_{-6.1}$
1617-1544	342.317414	−44.531796	$26.94^{+0.22}_{-0.35}$	$-20.20^{+0.22}_{-0.35}$	$1.34^{+0.16}_{-0.18}$	0.31	1.08	$1.08^{+0.00}_{-0.01}$	$1.8^{+5.2}_{-1.5}$
1222-3093	342.300944	−44.552588	$28.32^{+0.28}_{-0.38}$	$-18.83^{+0.28}_{-0.38}$	$0.30^{+0.13}_{-0.12}$	0.69	1.07	$1.07^{+0.00}_{-0.00}$	$7.9^{+0.9}_{-6.5}$
HFF6C									
5058-4269[s1]	39.960762	−1.574159	$27.62^{+0.04}_{-0.03}$	$-19.52^{+0.04}_{-0.03}$	$0.14^{+0.01}_{-0.01}$	0.18	8.64	$7.90^{+0.70}_{-0.54}$	$7.8^{+0.9}_{-0.9}$
5131-4096[s1]	39.963821	−1.569361	$28.16^{+0.10}_{-0.13}$	$-18.98^{+0.10}_{-0.13}$	$0.04^{+0.01}_{-0.01}$	0.90	8.93	$8.38^{+0.93}_{-0.80}$	$7.9^{+0.9}_{-0.9}$
5578-4519[s2]	39.982425	−1.581097	$28.46^{+0.15}_{-0.28}$	$-18.69^{+0.15}_{-0.28}$	$0.11^{+0.03}_{-0.06}$	0.83	8.05	$7.58^{+0.49}_{-0.46}$	$8.2^{+0.9}_{-0.9}$
5420-5141[s2]	39.975874	−1.587261	$28.39^{+0.17}_{-0.21}$	$-18.75^{+0.17}_{-0.21}$	$0.07^{+0.02}_{-0.03}$	0.90	4.66	$4.56^{+0.31}_{-0.33}$	$8.2^{+0.9}_{-0.9}$
4926-4404	39.955279	−1.577912	$28.25^{+0.32}_{-0.28}$	$-18.90^{+0.32}_{-0.28}$	$0.20^{+0.11}_{-0.06}$	0.65	3.16	$2.92^{+0.18}_{-0.14}$	$8.3^{+1.0}_{-0.9}$
5187-5411	39.966133	−1.594771	$30.25^{+0.15}_{-0.16}$	$-16.89^{+0.15}_{-0.16}$	$0.07^{+0.03}_{-0.03}$	0.89	17.56	$10.31^{+1.83}_{-0.97}$	$7.4^{+0.8}_{-5.9}$
HFF6P									
1374-7002	40.057265	−1.616732	$28.63^{+0.20}_{-0.16}$	$-18.52^{+0.20}_{-0.16}$	$0.05^{+0.04}_{-0.03}$	0.90	1.24	$1.16^{+0.03}_{-0.03}$	$1.6^{+6.2}_{-0.5}$
1167-6515	40.048638	−1.614306	$29.32^{+0.38}_{-0.23}$	$-17.82^{+0.38}_{-0.23}$	$0.06^{+0.06}_{-0.04}$	0.89	1.27	$1.19^{+0.04}_{-0.03}$	$1.8^{+1.3}_{-1.6}$

from light profile fitting with `glafic`.

[a] Asterisks indicate galaxies with multiple cores.

[b] Total apparent magnitude corrected for the gravitational lensing effects

[c] Errors are random errors in the fitting procedure.

[d] Circularized effective radius, $r_{\rm e}^{\rm maj}\sqrt{1-e}$, where $r_{\rm e}^{\rm maj}$ is the radius along the major axis and e the ellipticity.

[e] Best-fit value of magnification.

[f] Median value and 1σ error of the magnification factor from the MCMC posterior distribution.

[s1−−2] Dropout galaxy that composes a multiple image system.

Table C.3. Fitting results for dropouts at $z \sim 9$

ID[a]	R.A.	Decl.	$m_{\rm UV}$[b,c]	$M_{\rm UV}$[c]	$r_{\rm e}$ / kpc[c,d]	e	$\mu_{\rm best}$[e]	μ[f]	$z_{\rm photo}$
HFF1C									
2481-2561	3.603379	−30.382255	$26.59^{+0.17}_{-0.34}$	$-20.73^{+0.17}_{-0.34}$	$0.67^{+0.12}_{-0.16}$	0.56	1.42	$1.49^{+0.08}_{-0.06}$	$8.2^{+0.9}_{-0.9}$
2492-2561	3.603859	−30.382262	$27.17^{+0.21}_{-0.21}$	$-20.15^{+0.21}_{-0.21}$	$0.50^{+0.12}_{-0.12}$	0.51	1.41	$1.48^{+0.08}_{-0.06}$	$8.4^{+0.9}_{-0.9}$
2220-4053	3.592512	−30.401486	$28.70^{+0.42}_{-0.31}$	$-18.62^{+0.42}_{-0.31}$	$0.21^{+0.09}_{-0.06}$	0.50	12.00	$14.37^{+1.22}_{-0.90}$	$9.5^{+1.1}_{-7.3}$
HFF1P									
5363-4016	3.473469	−30.400459	$28.67^{+0.18}_{-0.17}$	$-18.65^{+0.18}_{-0.17}$	$0.10^{+0.07}_{-0.05}$	0.75	1.08	$1.02^{+0.01}_{-0.01}$	$8.3^{+0.9}_{-6.6}$
5364-3024	3.473522	−30.384024	$28.46^{+0.32}_{-0.21}$	$-18.86^{+0.32}_{-0.21}$	$0.19^{+0.09}_{-0.07}$	0.71	1.09	$1.03^{+0.01}_{-0.01}$	$8.7^{+1.0}_{-6.3}$
5733-3462	3.488893	−30.396182	$27.82^{+0.24}_{-0.23}$	$-19.50^{+0.24}_{-0.23}$	$0.36^{+0.16}_{-0.12}$	0.60	1.10	$1.03^{+0.02}_{-0.01}$	$8.7^{+1.0}_{-0.9}$
5386-2074	3.474446	−30.368728	$28.17^{+0.32}_{-0.27}$	$-19.15^{+0.32}_{-0.27}$	$0.31^{+0.17}_{-0.15}$	0.90	1.08	$1.05^{+0.01}_{-0.01}$	$8.9^{+1.0}_{-6.9}$
HFF2C									
1151-4540	64.047984	−24.081671	$27.12^{+0.12}_{-0.17}$	$-20.20^{+0.12}_{-0.17}$	$0.25^{+0.05}_{-0.06}$	0.57	1.44	$1.50^{+0.04}_{-0.03}$	$8.4^{+0.9}_{-0.9}$
0939-5354	64.039161	−24.093184	$25.76^{+0.42}_{-0.45}$	$-21.56^{+0.42}_{-0.45}$	$0.50^{+0.20}_{-0.21}$	0.42	1.39	$1.43^{+0.03}_{-0.03}$	$8.5^{+1.0}_{-0.9}$
0901-5172	64.037566	−24.088113	$28.78^{+0.30}_{-0.24}$	$-18.54^{+0.30}_{-0.24}$	$0.40^{+0.17}_{-0.13}$	0.69	1.70	$1.79^{+0.06}_{-0.05}$	$8.3^{+1.0}_{-0.9}$
HFF2P									
3441-6014	64.143392	−24.100397	$27.79^{+0.18}_{-0.18}$	$-19.53^{+0.18}_{-0.18}$	$0.14^{+0.06}_{-0.06}$	0.56	1.00	$1.00^{+0.01}_{-0.01}$	$2.1^{+6.1}_{-0.5}$
3596-6480	64.149865	−24.113352	$27.83^{+0.18}_{-0.18}$	$-19.50^{+0.18}_{-0.18}$	$0.24^{+0.10}_{-0.09}$	0.17	1.00	$0.99^{+0.01}_{-0.00}$	$8.5^{+1.0}_{-0.9}$
3549-6422	64.147906	−24.111728	$28.45^{+0.32}_{-0.21}$	$-18.87^{+0.32}_{-0.21}$	$0.19^{+0.09}_{-0.07}$	0.90	1.00	$1.00^{+0.01}_{-0.00}$	$8.4^{+0.9}_{-1.0}$
3042-6011	64.126780	−24.100325	$28.39^{+0.31}_{-0.24}$	$-18.93^{+0.31}_{-0.24}$	$0.54^{+0.23}_{-0.17}$	0.46	1.01	$1.00^{+0.01}_{-0.01}$	$8.2^{+0.9}_{-0.9}$
3172-6467	64.132190	−24.112994	$28.53^{+0.32}_{-0.21}$	$-18.79^{+0.32}_{-0.21}$	$0.39^{+0.18}_{-0.15}$	0.64	1.00	$1.00^{+0.01}_{-0.00}$	$8.8^{+1.0}_{-2.0}$
3736-6107	64.155669	−24.102997	$28.43^{+0.19}_{-0.17}$	$-18.89^{+0.19}_{-0.17}$	$0.09^{+0.06}_{-0.05}$	0.90	1.00	$1.00^{+0.01}_{-0.01}$	$8.6^{+0.9}_{-6.8}$
HFF3P									
2251-9452	109.343799	+37.829235	$27.73^{+0.18}_{-0.18}$	$-19.60^{+0.18}_{-0.18}$	$0.15^{+0.07}_{-0.06}$	0.55	1.14	$1.18^{+0.02}_{-0.04}$	$8.3^{+0.9}_{-0.9}$
1821-9546	109.325904	+37.831848	$27.60^{+0.24}_{-0.23}$	$-19.72^{+0.24}_{-0.23}$	$0.34^{+0.15}_{-0.12}$	0.78	1.14	$1.17^{+0.02}_{-0.02}$	$2.2^{+6.2}_{-0.7}$
1762-9402	109.323423	+37.827843	$28.40^{+0.19}_{-0.17}$	$-18.92^{+0.19}_{-0.17}$	$0.08^{+0.06}_{-0.04}$	0.90	1.17	$1.19^{+0.02}_{-0.02}$	$7.6^{+1.1}_{-6.1}$
HFF4C									
3358-4457	177.389950	+22.412711	$28.58^{+0.06}_{-0.15}$	$-18.74^{+0.06}_{-0.15}$	$0.10^{+0.01}_{-0.02}$	0.53	17.51	$6.44^{+21.86}_{-3.64}$	$9.2^{+1.0}_{-1.0}$
4024-4492	177.417700	+22.413691	$27.82^{+0.18}_{-0.18}$	$-19.50^{+0.18}_{-0.18}$	$0.13^{+0.06}_{-0.05}$	0.90	1.63	$1.69^{+0.23}_{-0.14}$	$8.4^{+0.9}_{-0.9}$
3373-4483	177.390553	+22.413417	$31.90^{+0.21}_{-0.18}$	$-15.42^{+0.21}_{-0.18}$	$0.06^{+0.02}_{-0.02}$	0.90	63.34	$18.30^{+40.36}_{-12.02}$	$8.7^{+0.9}_{-6.9}$
3617-3327	177.400727	+22.392425	$31.58^{+0.22}_{-0.18}$	$-15.74^{+0.22}_{-0.18}$	$0.08^{+0.03}_{-0.02}$	0.90	35.85	$41.22^{+12.10}_{-7.02}$	$8.5^{+0.9}_{-6.2}$
HFF4P									
3745-6484	177.406058	+22.280112	$26.26^{+0.20}_{-0.23}$	$-21.06^{+0.20}_{-0.23}$	$0.34^{+0.11}_{-0.14}$	0.69	1.01	$1.00^{+0.01}_{-0.01}$	$8.4^{+0.9}_{-0.9}$
3994-7367	177.416441	+22.293541	$27.63^{+0.12}_{-0.11}$	$-19.69^{+0.12}_{-0.11}$	$0.04^{+0.03}_{-0.02}$	0.89	1.01	$1.01^{+0.01}_{-0.01}$	$9.2^{+1.0}_{-1.0}$
4205-8351	177.425216	+22.309763	$28.38^{+0.33}_{-0.21}$	$-18.94^{+0.33}_{-0.21}$	$0.41^{+0.19}_{-0.15}$	0.89	1.04	$1.02^{+0.01}_{-0.01}$	$2.1^{+7.2}_{-0.8}$
HFF5C									
4316-1323[s1]	342.179874	−44.525660	$29.28^{+0.42}_{-0.30}$	$-18.04^{+0.42}_{-0.30}$	$0.15^{+0.09}_{-0.03}$	0.12	29.57	$30.24^{+2.28}_{-2.54}$	$8.2^{+0.9}_{-0.9}$
4374-1338[s1]	342.182264	−44.526073	$30.45^{+0.23}_{-0.19}$	$-16.87^{+0.23}_{-0.19}$	$0.09^{+0.03}_{-0.03}$	0.46	24.15	$24.72^{+1.38}_{-1.30}$	$8.5^{+1.0}_{-0.9}$
HFF5P									
1975-2112	342.332299	−44.536446	$28.23^{+0.19}_{-0.17}$	$-19.09^{+0.19}_{-0.17}$	$0.05^{+0.03}_{-0.02}$	0.57	1.06	$1.06^{+0.00}_{-0.00}$	$2.1^{+6.6}_{-0.4}$
2042-2369	342.335117	−44.543602	$28.79^{+0.18}_{-0.17}$	$-18.53^{+0.18}_{-0.17}$	$0.11^{+0.08}_{-0.06}$	0.88	1.06	$1.06^{+0.00}_{-0.00}$	$8.3^{+1.0}_{-6.6}$
2092-3100	342.337187	−44.552795	$28.80^{+0.20}_{-0.19}$	$-18.52^{+0.20}_{-0.19}$	$0.06^{+0.06}_{-0.03}$	0.90	1.05	$1.05^{+0.00}_{-0.00}$	$8.2^{+0.9}_{-2.4}$
HFF6C									
5578-4519[s1]	39.982427	−1.581097	$28.42^{+0.18}_{-0.21}$	$-18.90^{+0.18}_{-0.21}$	$0.09^{+0.03}_{-0.04}$	0.81	8.26	$7.77^{+0.51}_{-0.49}$	$8.2^{+0.9}_{-0.9}$
5421-5141[s1]	39.975875	−1.587260	$28.23^{+0.12}_{-0.16}$	$-19.09^{+0.12}_{-0.16}$	$0.06^{+0.02}_{-0.03}$	0.90	4.55	$4.45^{+0.30}_{-0.32}$	$8.2^{+0.9}_{-0.9}$

Table C.3 (cont'd)

ID[a]	R.A.	Decl.	$m_{\rm UV}$[b,c]	$M_{\rm UV}$[c]	$r_{\rm e}$ / kpc[c,d]	e	$\mu_{\rm best}$[e]	μ[f]	$z_{\rm photo}$
HFF6P									
1247-6578	40.051970	−1.616066	$27.57^{+0.27}_{-0.23}$	$-19.76^{+0.27}_{-0.23}$	$0.44^{+0.14}_{-0.13}$	0.66	1.26	$1.18^{+0.03}_{-0.03}$	$2.1^{+5.7}_{-0.8}$
1350-7372	40.056259	−1.627015	$27.65^{+0.27}_{-0.23}$	$-19.67^{+0.27}_{-0.23}$	$0.42^{+0.14}_{-0.12}$	0.38	1.23	$1.16^{+0.03}_{-0.03}$	$8.3^{+1.2}_{-6.5}$
1194-8213	40.049784	−1.639252	$28.38^{+0.33}_{-0.21}$	$-18.94^{+0.33}_{-0.21}$	$0.24^{+0.11}_{-0.09}$	0.89	1.23	$1.16^{+0.03}_{-0.03}$	$8.9^{+1.0}_{-1.0}$
1311-7372	40.054627	−1.627015	$27.08^{+0.28}_{-0.46}$	$-20.24^{+0.28}_{-0.46}$	$0.73^{+0.44}_{-0.16}$	0.31	1.23	$1.16^{+0.03}_{-0.03}$	$8.5^{+0.9}_{-6.7}$
1293-6262	40.053900	−1.607296	$28.75^{+0.20}_{-0.19}$	$-18.57^{+0.20}_{-0.19}$	$0.06^{+0.06}_{-0.03}$	0.77	1.27	$1.18^{+0.04}_{-0.03}$	$8.9^{+1.0}_{-6.5}$
1514-7171	40.063097	−1.621433	$28.66^{+0.22}_{-0.32}$	$-18.66^{+0.22}_{-0.32}$	$0.55^{+0.14}_{-0.15}$	0.02	1.22	$1.14^{+0.03}_{-0.02}$	$8.6^{+1.1}_{-7.0}$

from light profile fitting with `glafic`.

[a] Asterisks indicate galaxies with multiple cores.

[b] Total apparent magnitude corrected for the gravitational lensing effects

[c] Errors are random errors in the fitting procedure.

[d] Circularized effective radius, $r_{\rm e}^{\rm maj}\sqrt{1-e}$, where $r_{\rm e}^{\rm maj}$ is the radius along the major axis and e the ellipticity.

[e] Best-fit value of magnification.

[f] Median value and 1σ error of the magnification factor from the MCMC posterior distribution.

[s1] Dropout galaxy that composes a multiple image system.

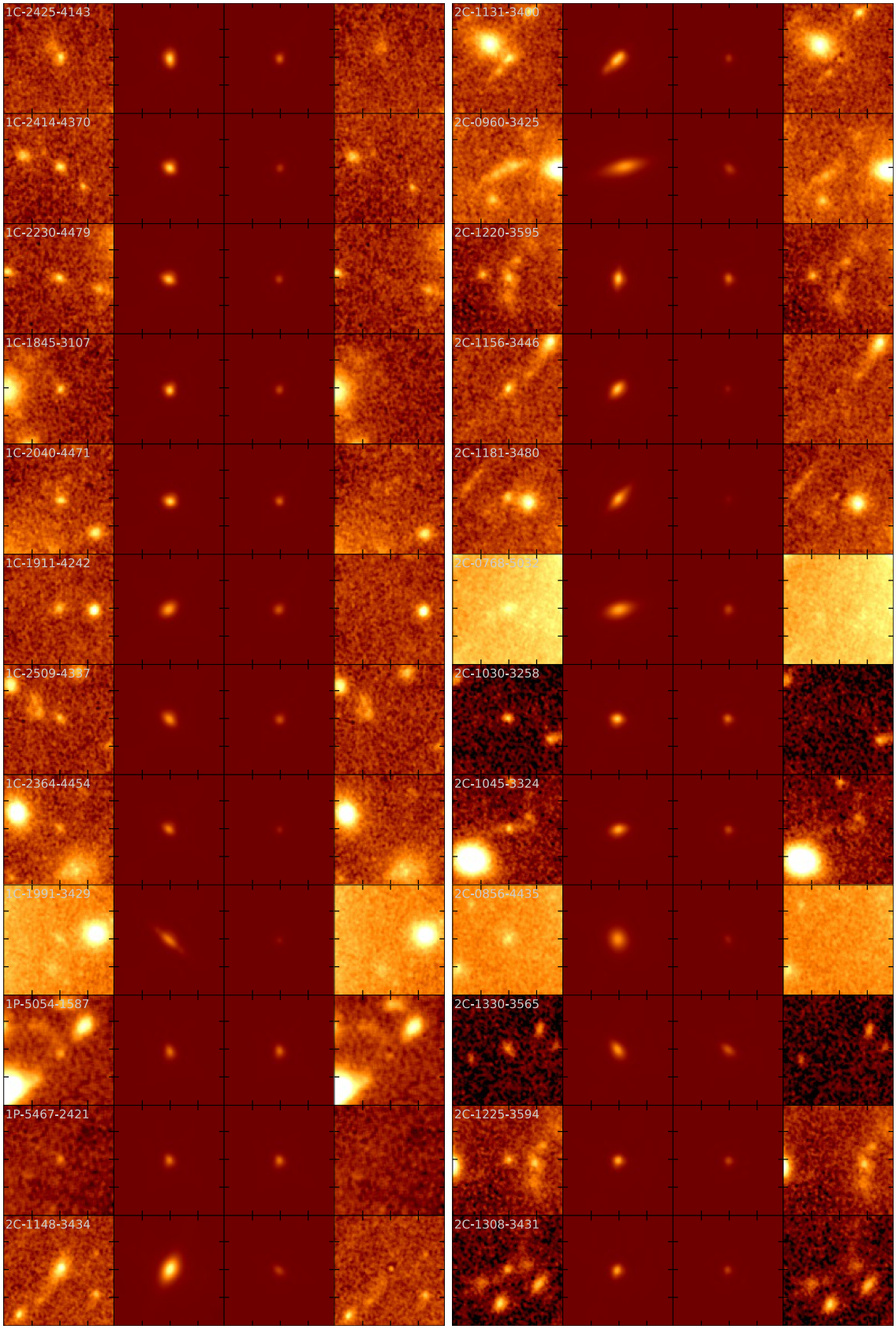

Figure C.1 Images for $z \sim 6-7$ faint galaxies at $M_{\rm UV} \gtrsim -18$. From left to right, $3'' \times 3''$ cutout images, best-fit Sérsic profiles on the image plane, best-fit Sérsic profiles on the source plane, and residual images on the image plane.

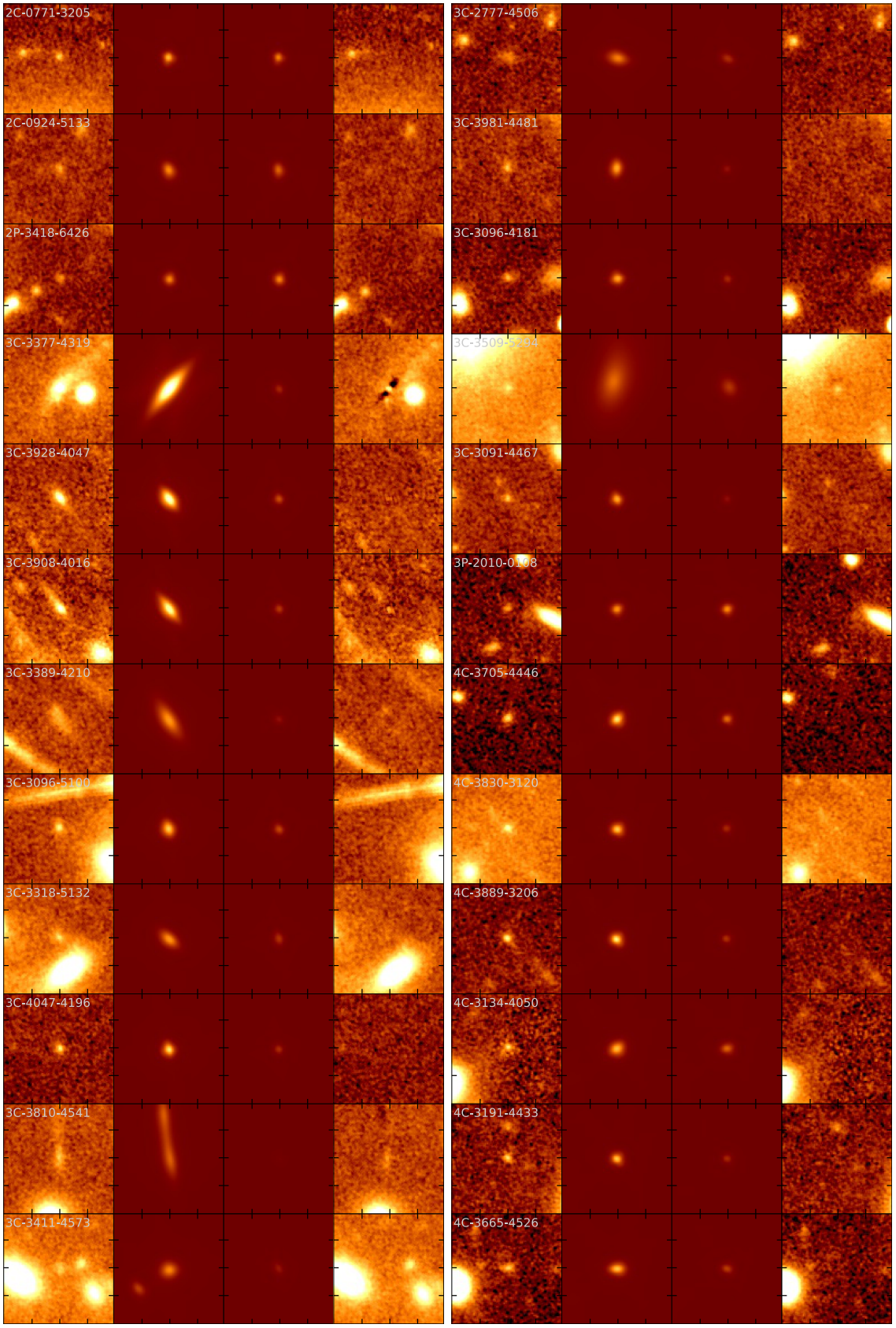

Figure C.1 Continued.

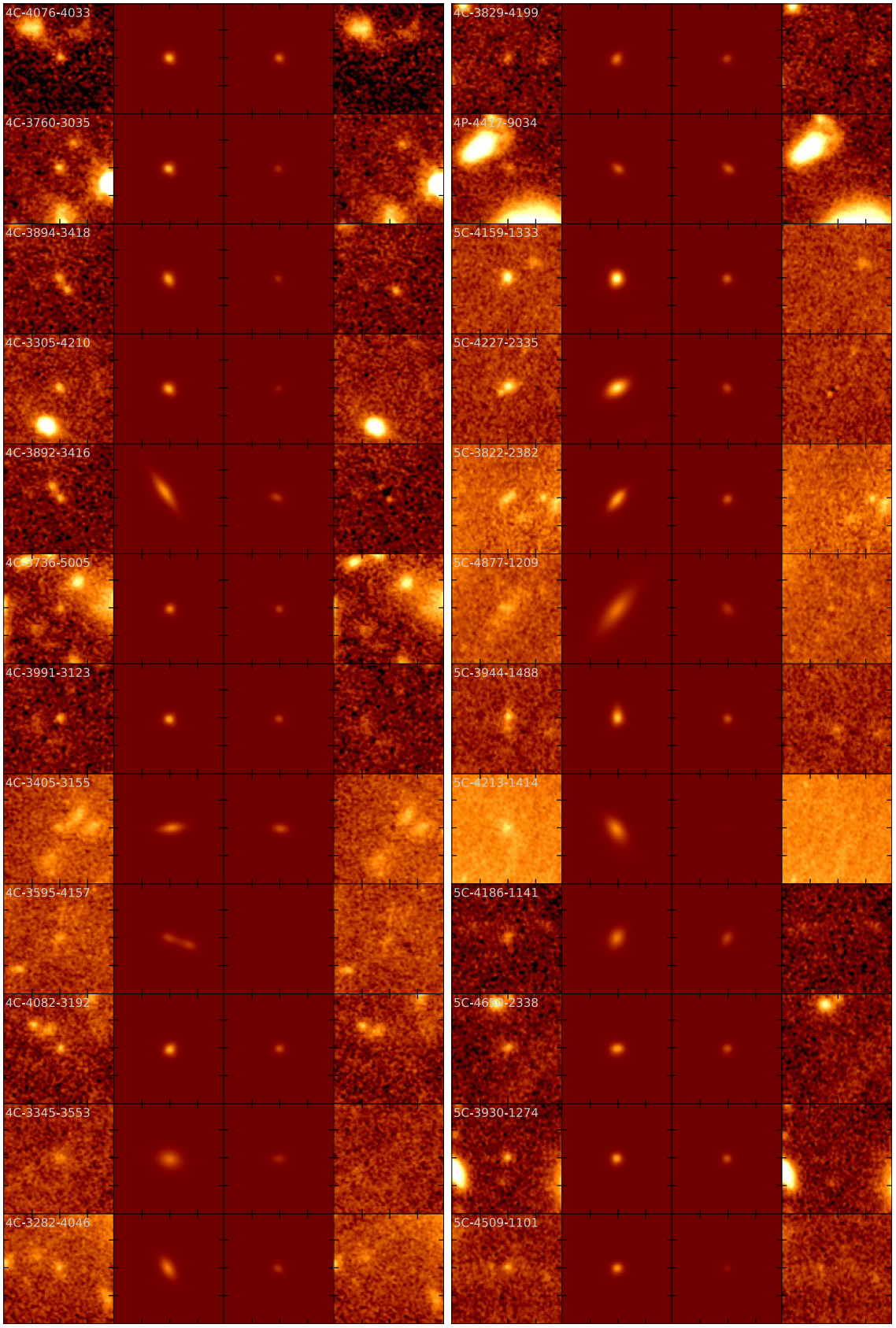

Figure C.1 Continued.

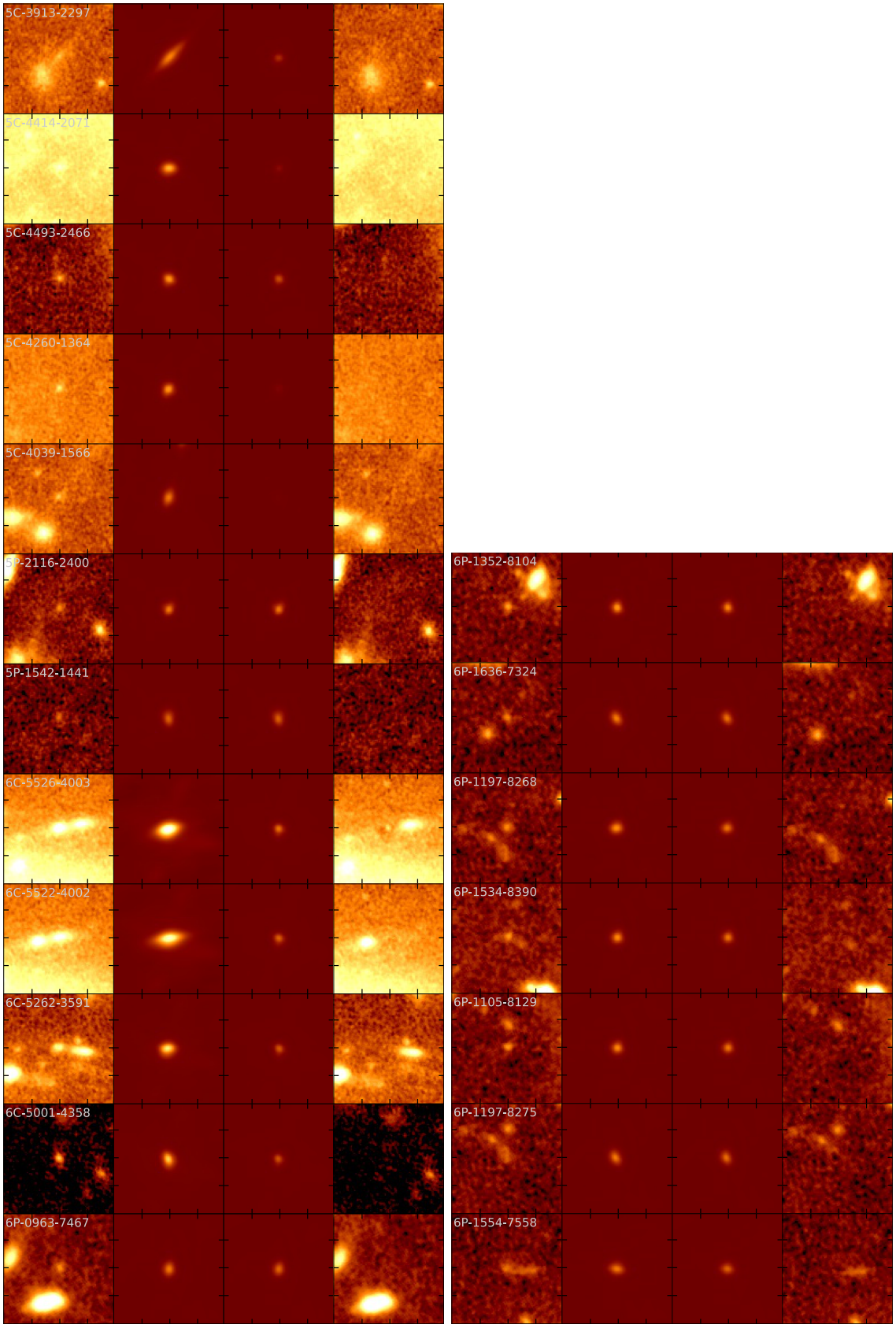

Figure C.1 Continued.

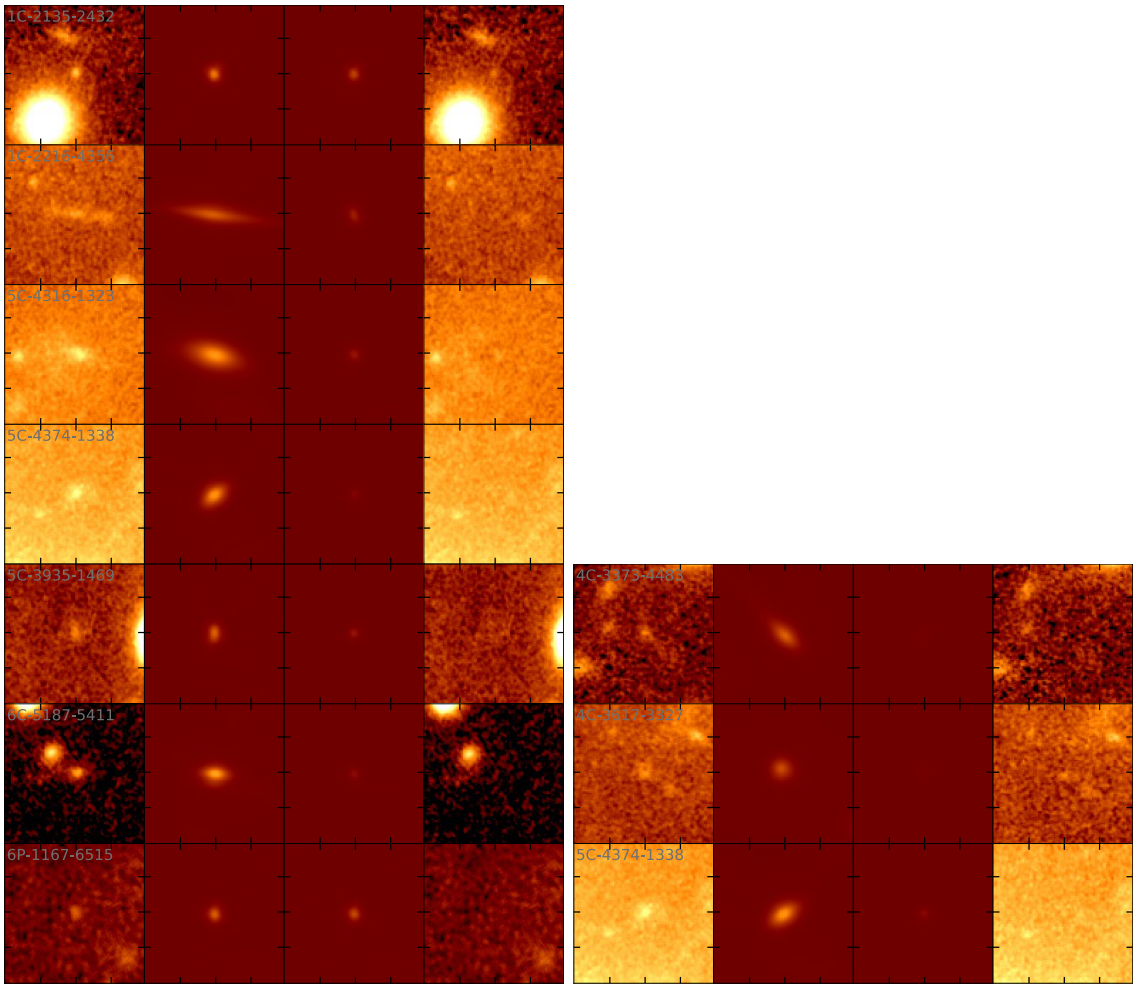

Figure C.2 Same as Figure C.1 but for $z \sim 8$ (*left*) and $z \sim 9$ (*right*).

Bibliography

Abell, G. O. 1958, The Astrophysical Journal, Supplement, 3, 211

Abell, G. O., Corwin, Jr., H. G., & Olowin, R. P. 1989, The Astrophysical Journal, Supplement, 70, 1

Allen, R. J., Kacprzak, G. G., Glazebrook, K., et al. 2017, The Astrophysical Journal, Letters, 834, L11

Atek, H., Richard, J., Kneib, J.-P., et al. 2014, The Astrophysical Journal, 786, 60

Atek, H., Richard, J., Jauzac, M., et al. 2015a, The Astrophysical Journal, 814, 69

Atek, H., Richard, J., Kneib, J.-P., et al. 2015b, The Astrophysical Journal, 800, 18

Balestra, I., Vanzella, E., Rosati, P., et al. 2013, Astronomy & Astrophysics, 559, L9

Beckwith, S. V. W., Stiavelli, M., Koekemoer, A. M., et al. 2006, The Astronomical Journal, 132, 1729

Behroozi, P. S., Wechsler, R. H., & Conroy, C. 2013, The Astrophysical Journal, 770, 57

Benítez, N. 2000, The Astrophysical Journal, 536, 571

Bertin, E., & Arnouts, S. 1996, Astronomy & Astrophysics Supplement Series, 117, 393

Bertin, E., Mellier, Y., Radovich, M., et al. 2002, in Astronomical Society of the Pacific Conference Series, Vol. 281, Astronomical Data Analysis Software and Systems XI, ed. D. A. Bohlender, D. Durand, & T. H. Handley, 228

Bouwens, R. J., Illingworth, G. D., Blakeslee, J. P., Broadhurst, T. J., & Franx, M. 2004, The Astrophysical Journal, Letters, 611, L1

Bouwens, R. J., Illingworth, G. D., Oesch, P. A., et al. 2017a, The Astrophysical Journal, 843, 41

Bouwens, R. J., Oesch, P. A., Illingworth, G. D., Ellis, R. S., & Stefanon, M. 2017b, The Astrophysical Journal, 843, 129

Bouwens, R. J., van Dokkum, P. G., Illingworth, G. D., et al. 2017c, ArXiv e-prints, arXiv:1711.02090

Bouwens, R. J., Illingworth, G. D., Oesch, P. A., et al. 2013, ArXiv e-prints, arXiv:1306.2950

—. 2014, The Astrophysical Journal, 793, 115

—. 2015, The Astrophysical Journal, 803, 34

Bowler, R. A. A., Dunlop, J. S., McLure, R. J., & McLeod, D. J. 2017, Monthly Notices of the Royal Astronomical Society, 466, 3612

Boylan-Kolchin, M., Springel, V., White, S. D. M., Jenkins, A., & Lemson, G. 2009, Monthly Notices of the Royal Astronomical Society, 398, 1150

Broadhurst, T., Benítez, N., Coe, D., et al. 2005, The Astrophysical Journal, 621, 53

Brook, C. B., Stinson, G., Gibson, B. K., et al. 2012, Monthly Notices of the Royal Astronomical Society, 419, 771

Brooks, A. M., Solomon, A. R., Governato, F., et al. 2011, The Astrophysical Journal, 728, 51

Bryan, G. L., & Norman, M. L. 1998, The Astrophysical Journal, 495, 80

Bullock, J. S., Kolatt, T. S., Sigad, Y., et al. 2001, Monthly Notices of the Royal Astronomical Society, 321, 559

Caminha, G. B., Grillo, C., Rosati, P., et al. 2016a, Astronomy & Astrophysics, 587, A80

Caminha, G. B., Karman, W., Rosati, P., et al. 2016b, Astronomy & Astrophysics, 595, A100

Caminha, G. B., Grillo, C., Rosati, P., et al. 2017, Astronomy & Astrophysics, 600, A90

Castellano, M., Yue, B., Ferrara, A., et al. 2016, The Astrophysical Journal, Letters, 823, L40

Charlton, P. J. L., Hudson, M. J., Balogh, M. L., & Khatri, S. 2017, Monthly Notices of the Royal Astronomical Society, 472, 2367

Christensen, L., Richard, J., Hjorth, J., et al. 2012, Monthly Notices of the Royal Astronomical Society, 427, 1953

Coe, D., Bradley, L., & Zitrin, A. 2015, The Astrophysical Journal, 800, 84

Correa, C. A., Wyithe, J. S. B., Schaye, J., & Duffy, A. R. 2015, Monthly Notices of the Royal Astronomical Society, 452, 1217

Curtis-Lake, E., McLure, R. J., Dunlop, J. S., et al. 2016, Monthly Notices of the Royal Astronomical Society, 457, 440

Danovich, M., Dekel, A., Hahn, O., Ceverino, D., & Primack, J. 2015, Monthly Notices of the Royal Astronomical Society, 449, 2087

Davis, A. J., & Natarajan, P. 2009, Monthly Notices of the Royal Astronomical Society, 393, 1498

de Jong, R. S., & Lacey, C. 2000, The Astrophysical Journal, 545, 781

DeFelippis, D., Genel, S., Bryan, G. L., & Fall, S. M. 2017, The Astrophysical Journal, 841, 16

Diego, J. M., Broadhurst, T., Molnar, S. M., Lam, D., & Lim, J. 2015a, Monthly Notices of the Royal Astronomical Society, 447, 3130

Diego, J. M., Broadhurst, T., Wong, J., et al. 2016a, Monthly Notices of the Royal Astronomical Society, 459, 3447

Diego, J. M., Broadhurst, T., Zitrin, A., et al. 2015b, Monthly Notices of the Royal Astronomical Society, 451, 3920

Diego, J. M., Schmidt, K. B., Broadhurst, T., et al. 2016b, ArXiv e-prints, arXiv:1609.04822

Dunlop, J. S., Rogers, A. B., McLure, R. J., et al. 2013, Monthly Notices of the Royal Astronomical Society, 432, 3520

Ebeling, H., Barrett, E., Donovan, D., et al. 2007, The Astrophysical Journal, Letters, 661, L33

Ebeling, H., Ma, C.-J., & Barrett, E. 2014, The Astrophysical Journal, Supplement, 211,

21
Ellis, R. S., McLure, R. J., Dunlop, J. S., et al. 2013, The Astrophysical Journal, Letters, 763, L7
Fall, S. M. 1983, in IAU Symposium, Vol. 100, Internal Kinematics and Dynamics of Galaxies, ed. E. Athanassoula, 391–398
Fall, S. M., & Efstathiou, G. 1980, Monthly Notices of the Royal Astronomical Society, 193, 189
Fall, S. M., & Romanowsky, A. J. 2013, The Astrophysical Journal, Letters, 769, L26
Ferguson, H. C., Dickinson, M., Giavalisco, M., et al. 2004, The Astrophysical Journal, Letters, 600, L107
Foreman-Mackey, D. 2016, The Journal of Open Source Software, 24, 1
Foreman-Mackey, D., Hogg, D. W., Lang, D., & Goodman, J. 2013, Publications of the Astronomical Society of the Pacific, 125, 306
Genel, S., Fall, S. M., Hernquist, L., et al. 2015, The Astrophysical Journal, Letters, 804, L40
Genzel, R., Newman, S., Jones, T., et al. 2011, The Astrophysical Journal, 733, 101
González, V., Labbé, I., Bouwens, R. J., et al. 2011, The Astrophysical Journal, Letters, 735, L34
Grazian, A., Castellano, M., Koekemoer, A. M., et al. 2011, Astronomy & Astrophysics, 532, A33
Grazian, A., Castellano, M., Fontana, A., et al. 2012, Astronomy & Astrophysics, 547, A51
Grillo, C., Suyu, S. H., Rosati, P., et al. 2015a, The Astrophysical Journal, 800, 38
Grillo, C., Karman, W., Suyu, S. H., et al. 2015b, ArXiv e-prints, arXiv:1511.04093
Grogin, N. A., Kocevski, D. D., Faber, S. M., et al. 2011, The Astrophysical Journal, Supplement, 197, 35
Guhathakurta, P., Tyson, J. A., & Majewski, S. R. 1990, The Astrophysical Journal, Letters, 357, L9
Guo, Q., Gonzalez-Perez, V., Guo, Q., et al. 2016, Monthly Notices of the Royal Astronomical Society, 461, 3457
Guo, Y., Giavalisco, M., Ferguson, H. C., Cassata, P., & Koekemoer, A. M. 2012, The Astrophysical Journal, 757, 120
Henriques, B. M. B., White, S. D. M., Thomas, P. A., et al. 2015, Monthly Notices of the Royal Astronomical Society, 451, 2663
Hoag, A., Huang, K.-H., Treu, T., et al. 2016, The Astrophysical Journal, 831, 182
Holwerda, B. W., Bouwens, R., Oesch, P., et al. 2015, The Astrophysical Journal, 808, 6
Hou, J., Lacey, C. G., & Frenk, C. S. 2017, ArXiv e-prints, arXiv:1708.02950
Huang, K.-H., Ferguson, H. C., Ravindranath, S., & Su, J. 2013, The Astrophysical Journal, 765, 68
Huang, K.-H., Fall, S. M., Ferguson, H. C., et al. 2017, The Astrophysical Journal, 838, 6
Illingworth, G. D., Magee, D., Oesch, P. A., et al. 2013, The Astrophysical Journal, Supplement, 209, 6

Ishigaki, M., Kawamata, R., Ouchi, M., Oguri, M., & Shimasaku, K. 2017, ArXiv e-prints, arXiv:1702.04867

Ishigaki, M., Kawamata, R., Ouchi, M., et al. 2015, The Astrophysical Journal, 799, 12

Jauzac, M., Clément, B., Limousin, M., et al. 2014, Monthly Notices of the Royal Astronomical Society, 443, 1549

Jauzac, M., Richard, J., Jullo, E., et al. 2015a, Monthly Notices of the Royal Astronomical Society, 452, 1437

Jauzac, M., Richard, J., Limousin, M., et al. 2015b, ArXiv e-prints, arXiv:1509.08914

Jiang, L., Egami, E., Fan, X., et al. 2013, The Astrophysical Journal, 773, 153

Jing, Y. P., & Suto, Y. 2002, The Astrophysical Journal, 574, 538

Johnson, T. L., Sharon, K., Bayliss, M. B., et al. 2014, The Astrophysical Journal, 797, 48

Karman, W., Caputi, K. I., Grillo, C., et al. 2015, Astronomy & Astrophysics, 574, A11

Karman, W., Caputi, K. I., Caminha, G. B., et al. 2017, Astronomy & Astrophysics, 599, A28

Kawamata, R., Ishigaki, M., Shimasaku, K., Oguri, M., & Ouchi, M. 2015, The Astrophysical Journal, 804, 103

Kawamata, R., Ishigaki, M., Shimasaku, K., et al. 2017, ArXiv e-prints, arXiv:1710.07301

Kawamata, R., Oguri, M., Ishigaki, M., Shimasaku, K., & Ouchi, M. 2016, The Astrophysical Journal, 819, 114

Keeton, C. R. 2001, ArXiv Astrophysics e-prints, astro-ph/0102341

Kelly, P. L., Rodney, S. A., Treu, T., et al. 2015, Science, 347, 1123

Kelly, P. L., Rodney, S. A., Treu, T., et al. 2016, The Astrophysical Journal Letters, 819, L8

Kennicutt, R. C., & Evans, N. J. 2012, Annual Review of Astronomy & Astrophysics, 50, 531

Kennicutt, Jr., R. C. 1998, The Astrophysical Journal, 498, 541

Koekemoer, A. M., Faber, S. M., Ferguson, H. C., et al. 2011, The Astrophysical Journal, Supplement, 197, 36

Koekemoer, A. M., Ellis, R. S., McLure, R. J., et al. 2013, The Astrophysical Journal, Supplement, 209, 3

Köhlinger, F., & Schmidt, R. W. 2014, Monthly Notices of the Royal Astronomical Society, 437, 1858

Lagattuta, D. J., Richard, J., Clément, B., et al. 2017, Monthly Notices of the Royal Astronomical Society, 469, 3946

Lam, D., Broadhurst, T., Diego, J. M., et al. 2014, The Astrophysical Journal, 797, 98

Laporte, N., Infante, L., Troncoso Iribarren, P., et al. 2016, The Astrophysical Journal, 820, 98

Law, D. R., Steidel, C. C., Shapley, A. E., et al. 2012, The Astrophysical Journal, 745, 85

Limousin, M., Ebeling, H., Richard, J., et al. 2012, Astronomy & Astrophysics, 544, A71

Limousin, M., Richard, J., Jullo, E., et al. 2015, ArXiv e-prints, arXiv:1510.08077

Liu, C., Mutch, S. J., Poole, G. B., et al. 2017, Monthly Notices of the Royal Astronomical

Society, 465, 3134
Livermore, R. C., Finkelstein, S. L., & Lotz, J. M. 2017, The Astrophysical Journal, 835, 113
Lotz, J. M., Jonsson, P., Cox, T. J., & Primack, J. R. 2008, Monthly Notices of the Royal Astronomical Society, 391, 1137
Lotz, J. M., Koekemoer, A., Coe, D., et al. 2017, The Astrophysical Journal, 837, 97
Ma, X., Hopkins, P. F., Boylan-Kolchin, M., et al. 2017, ArXiv e-prints, arXiv:1710.00008
Mahler, G., Richard, J., Clément, B., et al. 2018, Monthly Notices of the Royal Astronomical Society, 473, 663
Mann, A. W., & Ebeling, H. 2012, Monthly Notices of the Royal Astronomical Society, 420, 2120
McLeod, D. J., McLure, R. J., Dunlop, J. S., et al. 2015, Monthly Notices of the Royal Astronomical Society, 450, 3032
Meneghetti, M., Natarajan, P., Coe, D., et al. 2017, Monthly Notices of the Royal Astronomical Society, 472, 3177
Merten, J., Coe, D., Dupke, R., et al. 2011, Monthly Notices of the Royal Astronomical Society, 417, 333
Meurer, G. R., Heckman, T. M., & Calzetti, D. 1999, The Astrophysical Journal, 521, 64
Mo, H. J., Mao, S., & White, S. D. M. 1998, Monthly Notices of the Royal Astronomical Society, 295, 319
Monna, A., Seitz, S., Greisel, N., et al. 2014, Monthly Notices of the Royal Astronomical Society, 438, 1417
Mutch, S. J., Geil, P. M., Poole, G. B., et al. 2016, Monthly Notices of the Royal Astronomical Society, 462, 250
Navarro, J. F., Frenk, C. S., & White, S. D. M. 1997, The Astrophysical Journal, 490, 493
Newman, A. B., Ellis, R. S., & Treu, T. 2015, ArXiv e-prints, arXiv:1503.05282
Oesch, P. A., Bouwens, R. J., Illingworth, G. D., et al. 2015, The Astrophysical Journal, 808, 104
Oesch, P. A., Bouwens, R. J., Carollo, C. M., et al. 2010a, The Astrophysical Journal, Letters, 709, L21
Oesch, P. A., Bouwens, R. J., Illingworth, G. D., et al. 2010b, The Astrophysical Journal, Letters, 709, L16
—. 2013, The Astrophysical Journal, 773, 75
Oguri, M. 2010, Publications of the Astronomical Society of Japan, 62, 1017
—. 2015, Monthly Notices of the Royal Astronomical Society, 449, L86
Oguri, M., Bayliss, M. B., Dahle, H., et al. 2012, Monthly Notices of the Royal Astronomical Society, 420, 3213
Oguri, M., Schrabback, T., Jullo, E., et al. 2013, Monthly Notices of the Royal Astronomical Society, 429, 482
Okamura, T., Shimasaku, K., & Kawamata, R. 2017, ArXiv e-prints, arXiv:1709.03275
Oke, J. B., & Gunn, J. E. 1983, The Astrophysical Journal, 266, 713

Ono, Y., Ouchi, M., Curtis-Lake, E., et al. 2013, The Astrophysical Journal, 777, 155

Ono, Y., Ouchi, M., Harikane, Y., et al. 2017, ArXiv e-prints, arXiv:1704.06004

Owers, M. S., Randall, S. W., Nulsen, P. E. J., et al. 2011, The Astrophysical Journal, 728, 27

Peebles, P. J. E. 1969, The Astrophysical Journal, 155, 393

Peng, C. Y., Ho, L. C., Impey, C. D., & Rix, H.-W. 2002, The Astronomical Journal, 124, 266

—. 2010, The Astronomical Journal, 139, 2097

Postman, M., Coe, D., Benítez, N., et al. 2012, The Astrophysical Journal, Supplement, 199, 25

Prada, F., Klypin, A. A., Cuesta, A. J., Betancort-Rijo, J. E., & Primack, J. 2012, Monthly Notices of the Royal Astronomical Society, 423, 3018

Priewe, J., Williams, L. L. R., Liesenborgs, J., Coe, D., & Rodney, S. A. 2017, Monthly Notices of the Royal Astronomical Society, 465, 1030

Rau, S., Vegetti, S., & White, S. D. M. 2014, Monthly Notices of the Royal Astronomical Society, 443, 957

Ravindranath, S., Giavalisco, M., Ferguson, H. C., et al. 2006, The Astrophysical Journal, 652, 963

Reddy, N. A., & Steidel, C. C. 2009, The Astrophysical Journal, 692, 778

Richard, J., Kneib, J.-P., Limousin, M., Edge, A., & Jullo, E. 2010, Monthly Notices of the Royal Astronomical Society, 402, L44

Richard, J., Jauzac, M., Limousin, M., et al. 2014, Monthly Notices of the Royal Astronomical Society, 444, 268

Roche, N., Ratnatunga, K., Griffiths, R. E., Im, M., & Neuschaefer, L. 1996, Monthly Notices of the Royal Astronomical Society, 282, 1247

Rodney, S. A., Patel, B., Scolnic, D., et al. 2015, The Astrophysical Journal, 811, 70

Rodney, S. A., Strolger, L.-G., Kelly, P. L., et al. 2016, The Astrophysical Journal, 820, 50

Rodney, S. A., Balestra, I., Bradac, M., et al. 2017, ArXiv e-prints, arXiv:1707.02434

Romanowsky, A. J., & Fall, S. M. 2012, The Astrophysical Journal, Supplement, 203, 17

Sales, L. V., Navarro, J. F., Schaye, J., et al. 2010, Monthly Notices of the Royal Astronomical Society, 409, 1541

Schmidt, K. B., Treu, T., Trenti, M., et al. 2014a, The Astrophysical Journal, 786, 57

Schmidt, K. B., Treu, T., Brammer, G. B., et al. 2014b, The Astrophysical Journal, Letters, 782, L36

Schneider, P., Ehlers, J., & Falco, E. E. 1992, Gravitational Lenses

Schramm, T. 1990, Astronomy & Astrophysics, 231, 19

Sebesta, K., Williams, L. L. R., Mohammed, I., Saha, P., & Liesenborgs, J. 2015, ArXiv e-prints, arXiv:1507.08960

Sharon, K., & Johnson, T. L. 2015, The Astrophysical Journal, Letters, 800, L26

Shen, S., Mo, H. J., White, S. D. M., et al. 2003, Monthly Notices of the Royal Astronomical Society, 343, 978

Shibuya, T., Ouchi, M., & Harikane, Y. 2015, The Astrophysical Journal, Supplement, 219, 15

Smith, G. P., Ebeling, H., Limousin, M., et al. 2009, The Astrophysical Journal, Letters, 707, L163

Somerville, R. S., Behroozi, P., Pandya, V., et al. 2017, ArXiv e-prints, arXiv:1701.03526

Springel, V., White, S. D. M., Jenkins, A., et al. 2005, Nature, 435, 629

Steidel, C. C., Adelberger, K. L., Giavalisco, M., Dickinson, M., & Pettini, M. 1999, The Astrophysical Journal, 519, 1

Steidel, C. C., & Hamilton, D. 1992, The Astronomical Journal, 104, 941

Treu, T., Schmidt, K. B., Brammer, G. B., et al. 2015, The Astrophysical Journal, 812, 114

Treu, T., Brammer, G., Diego, J. M., et al. 2016, The Astrophysical Journal, 817, 60

Vanzella, E., Fontana, A., Zitrin, A., et al. 2014, The Astrophysical Journal, Letters, 783, L12

Vitvitska, M., Klypin, A. A., Kravtsov, A. V., et al. 2002, The Astrophysical Journal, 581, 799

Wang, X., Hoag, A., Huang, K.-H., et al. 2015, The Astrophysical Journal, 811, 29

Williams, L. L. R., Sebesta, K., & Liesenborgs, J. 2017, ArXiv e-prints, arXiv:1711.05265

Wyithe, J. S. B., & Loeb, A. 2011, Monthly Notices of the Royal Astronomical Society, 413, L38

Yue, B., Castellano, M., Ferrara, A., et al. 2017, ArXiv e-prints, arXiv:1711.05130

Zheng, W., Postman, M., Zitrin, A., et al. 2012, Nature, 489, 406

Zitrin, A., & Broadhurst, T. 2009, The Astrophysical Journal, Letters, 703, L132

Zitrin, A., Broadhurst, T., Rephaeli, Y., & Sadeh, S. 2009, The Astrophysical Journal, Letters, 707, L102

Zitrin, A., Ellis, R. S., Belli, S., & Stark, D. P. 2015a, The Astrophysical Journal, Letters, 805, L7

Zitrin, A., Meneghetti, M., Umetsu, K., et al. 2013, The Astrophysical Journal, Letters, 762, L30

Zitrin, A., Zheng, W., Broadhurst, T., et al. 2014, The Astrophysical Journal, Letters, 793, L12

Zitrin, A., Fabris, A., Merten, J., et al. 2015b, The Astrophysical Journal, 801, 44

Zjupa, J., & Springel, V. 2017, Monthly Notices of the Royal Astronomical Society, 466, 1625